international conference

FT 2025

conference proceedings

Darko Lovrec
Vito Tič
Editors

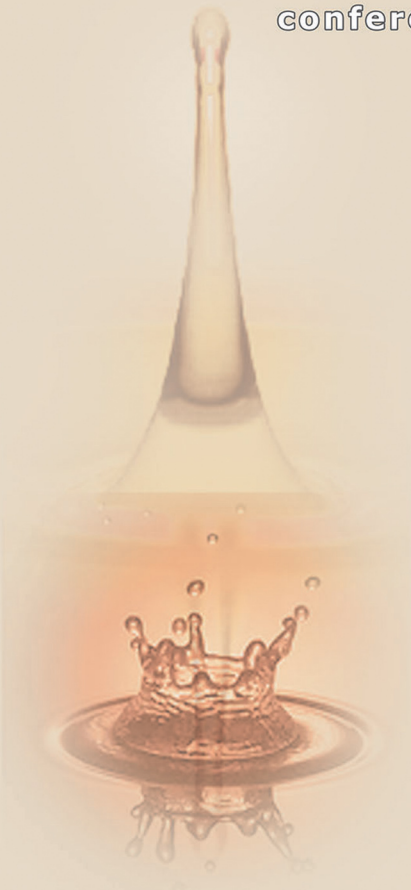

University of Maribor Press

Fluid Power 2025
Fluidna Tehnika 2025

MARIBOR, 17.–18. SEPTEMBER 2025

University of Maribor
Faculty of Mechanical Engineering

International Conference Fluid Power 2025

Conference Proceedings

Editors
Darko Lovrec
Vito Tič

September 2025

Title International Conference Fluid Power 2025

Subtitle Conference Proceedings

Editors Darko Lovrec
(University of Maribor, Faculty of Mechanical Engineering, Slovenia)

Vito Tič
(University of Maribor, Faculty of Mechanical Engineering, Slovenia)

Review Darko Lovrec (University of Maribor, Faculty of Mechanical Engineering, Slovenia), Vito Tič (University of Maribor, Faculty of Mechanical Engineering, Slovenia, Ana Trajkovski (University of Ljubljana, Faculty of Mechanical Engineering, Slovenia), Željko Šitum (University of Zagreb, Faculty of Mechanical Engineering and Naval Architecture, Croatia), Milan Kambič (OLMA d.o.o., Slovenia), Franc Majdič (University of Ljubljana, Faculty of Mechanical Engineering, Slovenia), Mihael Cipek (University of Zagreb, Faculty of Mechanical Engineering and Naval Architecture, Croatia), Joerg Edler (Technische Universität Graz, Austria), Marko Šimic (University of Ljubljana, Faculty of Mechanical Engineering, Slovenia), Riko Šafarič (University of Maribor, Faculty of Electrical Engineering and Computer Science), Almir Osmanović (University of Tuzla, Faculty of Mechanical Engineering Tuzla, Bosnia and Herzegovina), Ignacijo Biluš (University of Maribor, Faculty of Mechanical Engineering, Slovenia), Mitja Kastrevc (University of Maribor, Faculty of Mechanical Engineering, Slovenia)

Language editing Darko Lovrec
(University of Maribor, Faculty of Mechanical Engineering, Slovenia)

Technical editor Jan Perša
(University of Maribor, University of Maribor Press, Slovenia)

Cover designer Vito Tič
(University of Maribor, Faculty of Mechanical Engineering, Slovenia)

Graphic material Authors of proceedings & Lovrec, Tič (editors), 2025

Cover graphics Fluid Power conference,
University of Maribor, Faculty of Mechanical Engineering

Conference International conference Fluid Power 2025

Location and date Hotel Habakuk, Maribor, Slovenia, 17th – 18th September 2025

Organizing comittee Vito Tič (University of Maribor, Faculty of Mechanical Engineering, Slovenia), Darko Lovrec (University of Maribor, Faculty of Mechanical Engineering, Slovenia), Dušan Raner (University of Maribor, Faculty of Mechanical Engineering, Slovenia), Mitja Kastrevc (University of Maribor, Faculty of Mechanical Engineering, Slovenia), Eneja Kovačič (University of Maribor, Faculty of Mechanical Engineering, Slovenia), Tina Podkrajšek Kotnik (University of Maribor, Faculty of Mechanical Engineering, Slovenia)

Scientific comittee Darko Lovrec (University of Maribor, Faculty of Mechanical Engineering, Slovenia), Niko Herakovič (University of Ljubljana, Faculty of Mechanical Engineering, Slovenia), Željko Šitum (University of Zagreb, Faculty of Mechanical Engineering and Naval Architecture, Croatia), Franc Majdič (University of Ljubljana, Faculty of Mechanical Engineering, Slovenia), Joerg Edler (Technische Universität Graz, Austria), Riko Šafarič (University of Maribor, Faculty of Electrical Engineering and Computer Science, Slovenia), Aleš Bizjak (Chamber of Commerce Slovenia), Almir Osmanović (University of Tuzla, Faculty of Mechanical Engineering Tuzla, Bosnia and Herzegovina), Milan Kambič (Olma d.o.o., Slovenia), Mitar Jocanović (University of Novi Sad, Faculty of Technical Sciences, Serbia), Bernhard Manhartsgruber (Johannes Kepler University, Linz, Austria), Radovan Petrović (University of Kragujevac, Faculty of Mechanical Engineering, Serbia), Mihael Cipek (University of Zagreb, Faculty of Mechanical Engineering and Naval Architecture, Croatia), Marko Šimic (University of Ljubljana, Faculty of Mechanical Engineering, Slovenia), Ana Trajkovski (University of Ljubljana, Faculty of Mechanical Engineering, Slovenia)

Program committee Darko Lovrec (University of Maribor, Faculty of Mechanical Engineering, Slovenia), Vito Tič (University of Maribor, Faculty of Mechanical Engineering, Slovenia), Niko Herakovič (University of Ljubljana, Faculty of Mechanical Engineering, Slovenia), Željko Šitum (University of Zagreb, Faculty of Mechanical Engineering and Naval Architecture, Croatia), Milan Kambič (OLMA d.o.o., Slovenia), Franc Majdič (University of Ljubljana, Faculty of Mechanical Engineering, Slovenia)

Published by **University of Maribor**
University Press
Slomškov trg 15
2000 Maribor, Slovenia
https://press.um.si, zalozba@um.si

Issued by **University of Maribor**
Faculty of Mechanical Engineering
Smetanova ulica 17
2000 Maribor, Slovenia
https://fs.um.si, fs@um.si

Edition 1st

Publication type E-book

Available at http://press.um.si/index.php/ump/catalog/book/1042

Published at Maribor, Slovenia, September 2025

© University of Maribor, University of Maribor Press
/*Univerza v Mariboru, Univerzitetna založba*

Text © Authors of proceedings & Lovrec, Tič (editors), 2025

This book is published under a Creative Commons 4.0 International licence (CC BY 4.0). This license lets others remix, tweak, and build upon your work even for commercial purposes, as long as they credit you and license their new creations under the identical terms. This license is often compared to "copyleft" free and open source software licenses.

Any third-party material in this book is published under the book's Creative Commons licence unless indicated otherwise in the credit line to the material. If you would like to reuse any third-party material not covered by the book's Creative Commons licence, you will need to obtain permission directly from the copyright holder.

https://creativecommons.org/licenses/by/4.0/

CIP - Kataložni zapis o publikaciji
Univerzitetna knjižnica Maribor

621.51/.54(082)(0.034.2)
681.523(063)(082)(0.034.2)

MEDNARODNA konferenca Fluidna tehnika (2025 ; Maribor)
International Conference Fluid Power 2025 [Elektronski vir] : conference proceedings : [Hotel Habakuk, Maribor, Slovenia, 17th - 18th, September 2025] / editors Darko Lovrec, Vito Tič. - 1st ed. - E-publikacija. - Maribor : University of Maribor, University Press, 2025

Način dostopa (URL): https://press.um.si/index.php/ump/catalog/book/1042

ISBN 978-961-299-049-7 (PDF)
doi: 10.18690/um.fs.7.2025
COBISS.SI-ID 248505859

ISBN 978-961-299-049-7 (pdf)
978-961-299-051-0 (USB Flash Drive)

DOI https://doi.org/10.18690/um.fs.7.2025

Price Free copy

For publisher Prof. Dr. Zdravko Kačič,
Rector of University of Maribor

Attribution Lovrec, D., Tič, V. (eds.). (2025). *International conference Fluid Power 2025: Conference Proceedings*. Maribor: University Press.
doi: 10.18690/um.fs.7.2025

University of Maribor Press

Table of Contents

1	**Sustainability and Energy Efficiency in Fluid Power - Recent Advancements in Research and Industry** Katharina Schmitz	1
2	**Uniforest Connect - Digitalisation in Forestry Technology** Sandi Grobelnik, Robert Horvat	9
3	**A Self-Optimizing Hydraulic System Approach for Agile Metal Forming** Denis Jankovič, Marko Šimic, Tomaž Pepelnjak, Niko Herakovič	19
4	**Numerical Optimization of Internal Geometry for Additively Manufactured Hydraulic Manifolds** Jan Bartolj, Katharina Schmitz, Nikola Vukašinović, Franc Majdič	31
5	**Strategic Integration of Hydraulic Accumulators: Best Practices** Tadej Tašner	45
6	**Elika, Variable Flow With Fixed Displacement Helical Pump** Danilo Persici, Andrea Rimondi	61
7	**Designing Educational Systems to Illustrate Mechatronic Principles** Željko Šitum, Tomislav Drašković, Fran Hruškar, Lovro Meštrić, Mateo Šego, Eros Stemberger, Magdalena Antolković	79
8	**Pneumatics Today and Tomorrow: A Review of Technology and Development Trends** Marko Šimic, Niko Herakovič	93
9	**Static Properties Based Classification of Pneumatic Actuators - Potential of Progressive Effective Area Over the Stroke** Olivier Reinertz	111
10	**Implementation and Experimental Validation of a Time-Controlled Quick-Exhaust for Downstream Throttled Pneumatic Drives** Luca Päßler, Christian Reese, Olivier Reinertz, Katharina Schmitz	131

11	**Advanced Mechatronic Systems Featuring Pneumatic Actuation** Željko Šitum, Filip Čavić, Vid Pavlović, Lovro Zoričić, Ante Ivanković, Matija Čmelješević, Bernarda Galić, Mia Prgomet, Antonio Varović	**147**
12	**Pneumatically Powered Hydraulic Rescue Shears for Firefighter Operations** Borna Matkun, Mihael Cipek, Danijel Pavković, Željko Šitum	**163**
13	**Remote Control and Monitoring of a Pneumatic Workstation Using TwinCAT 3 and Beckhoff PLC** Vito Tič, Alfonz Muhič	**177**
14	**The Importance to Consider Advanced Fluid Properties in Flow Simulation of Positive Displacement Machines** Anže Čelik	**187**
15	**Research Into the Influence of Critical Hydraulic Tank Parameters When Using Two Pumps Simultaneously** Franc Majdič, Matevž Kramar, Ana Trajkovski, Jan Bartolj	**201**
16	**Upfront Simulations and (Their) Democratization – Where We Are?** Anže Čelik	**215**
17	**Presentation of a Mobile Testing Device for the Inspection of Micropiles of Rockfall Protection Nets in Alpine Terrain** Jörg Edler, Matthias Rebhan, Emanuel Troyer	**229**
18	**Contribution to the Research and Failure Analysis of the Geroler Hydraulic Motor** Almir Osmanović, Darko Lovrec, Jasmin Halilović, Salko Ćosić	**245**
19	**The Last 30 Years of Hydropower in the World and Slovenia** Andrej Predin, Mitja Kastrevc, Gorazd Hren	**261**
20	**Water Turbine Hydraulic Regulating System and Modifications To Meet Grid Stability Requirements** Marko Hrovat	**277**
21	**Factors Affecting the Accuracy of Operation of the Electrohydraulic Actuation Position System With Throttling Control** Dragan Nauparac, Nemanja Višnjić	**293**
22	**Experimental Study on Performance of Centrifugal Pump** Beena Baloni, Maitrik Shah, Salim Abbasbhai Channiwala	**313**
23	**Experimental Investigation of Ultrasonic Cavitation Erosion: Implications for Water Turbines and Hydraulic Machinery** Luka Kevorkijan, Tilen Jernejc, Luka Lešnik, Ignacijo Biluš	**325**

24 **Improving Energy Efficiency Through Using Modern Hydraulic Oil** 335
Aleš Hrobat, Jošt Mohorko, Vito Tič, Milan Kambič

25 **Wear Particles in the Hydraulic System and Their Impact on the Gear Pump Efficienc** 347
Nejc Novak, Ana Trajkovski, Jan Bartolj, Mitjan Kalin, Franc Majdič

26 **FTIR Changes of Differently Degraded Mineral and Turbine Oils** 359
Milan Kambič, Jošt Mohorko, Aleš Hrobat, Karin Pivec, Darko Lovrec

27 **Automated Detection of Compressed Air Leakage in Pneumatic Stations** 373
Vito Tič, Andrej Baligač


FT2025
30
YEARS

Sustainability and Energy Efficiency in Fluid Power - Recent Advancements in Research and Industry

Katharina Schmitz
RWTH Aachen University, Institute for Fluid Power Drives and Systems, Aachen, Germany
Katharina.Schmitz@ifas.rwth-aachen.de

Sustainability in all its three dimensions is a major driver for recent advancements in many sectors. In fluid power applications, sustainability and decarbonization are often linked to energy efficiency and reducing energy losses. Therefore, different new approaches and examples exist in research and in industry. Digital tools enable new advancements and additional methodology for developments. The paper gives an example of recent advancements and discusses the need for further developments in research and industrial development.

DOI
https://doi.org/10.18690/um.fs.7.2025.1

ISBN
978-961-299-049-7

Keywords:
sustainability, decarbonization, energy efficiency, research, industrial development

University of Maribor Press

1 Introduction

Fluid power systems are widely used in industrial and mobile applications. Since decades, it is a well-developed and mature technology with a high-power density, high forces and torques, good controllability, as well as a good reliability and robustness [1]. Nevertheless, energy consumption is rather high, compared to other technologies. However, in last years and decades the focus of industrial development mainly lied on cost issues rather than energy efficiency, where still a lot of potential can be found. Research institutions worldwide have shown several approaches for more energy efficiency and have a profound record of research on making systems and components better controllable and more efficient.

The importance of advancement and further development now comes to a new stage when discussion sustainability with its three dimensions: Society, Economy and Environment. Since its launch in 2019, the Green-Deal of European Commission sets a new target to transform Europe's economy, energy, transport, and industries for a more sustainable future [2]. It sets the clear goal of reaching climate neutrality in Europe in 2050 and a pathway towards it. This action plan relates to greenhouse gas (GHG) emissions and other climate merits but also means introducing new legislation on the circular economy, building renovation, biodiversity, farming and reporting obligation of companies. Therefore, many companies have started in including sustainability goals to their agenda and future development plans, including environmental footprint, economical numbers and considering the human factor.

To achieve Europe's climate goals, all industrial sectors need to contribute and to transform. Therefore, also fluid power researcher and companies need to answer the question, how a transformation into sustainable motion technology can be achieved.

2 Sustainable fluid power systems throughout the life cycle

The transformation towards climate neutral and decarbonized fluid power components and systems will be mainly driven by three key-enabler:

1. Electrification

   To achieve emission-free mobile machines, electrification (battery electric or hydrogen fuel cell electric) will be one of the most probable solutions to drive heavy duty machines in the future. This means, on the one hand, new boundary conditions for the fluid power system and on the other hand, a larger attention towards energy consumption of the system itself.

2. Digitalization (connectivity, "smart systems" and data algorithmic (AI))

   New digital solutions and the smart use of data are evolving rapidly in all fields of technology. For fluid power systems, data algorithmic and increasing connectivity will enable new system architectures, better controllability, energy savings, increasing robustness and higher productivity.

3. New paradigm: Circular Economy & Holistic Approach

   Starting with the Green-Deal, the topic circular economy is increasingly present nowadays. It requires awareness of the whole product life cycle from development, manufacturing, commissioning, usage, recycling / reconfiguration / reuse. In combination with a more holistic approach, this new paradigm will change the perspective of products and product development.

Right now, fluid power research and industry have started the transformation towards sustainable motion technology and fulfilling EUs goals [3], but there is still a long way to go until 2050. Selected recent advancements are discussed below, considering the various phases of the product life cycle.

2.1 Design and manufacturing

In the design process of fluid power components and systems, more digital tools help development and design engineers. Starting with standard tools like simulations and computer-aided calculations, artificial intelligence (AI-) or machine learning (ML-) based tools are now evolving and soon to be used in the development and designing process of technical systems as well as fluid power components and systems [4].

New manufacturing technologies are emerging and the concept of Industry 4.0 promises further improvements in manufacturing. Additive manufacturing might become increasingly important for fluid power components as it can save a lot of material during manufacturing, components can be lightweight and energy consumption during usage phase can be reduced due to smoother fluid flow through e.g. valve blocks [5], [6].

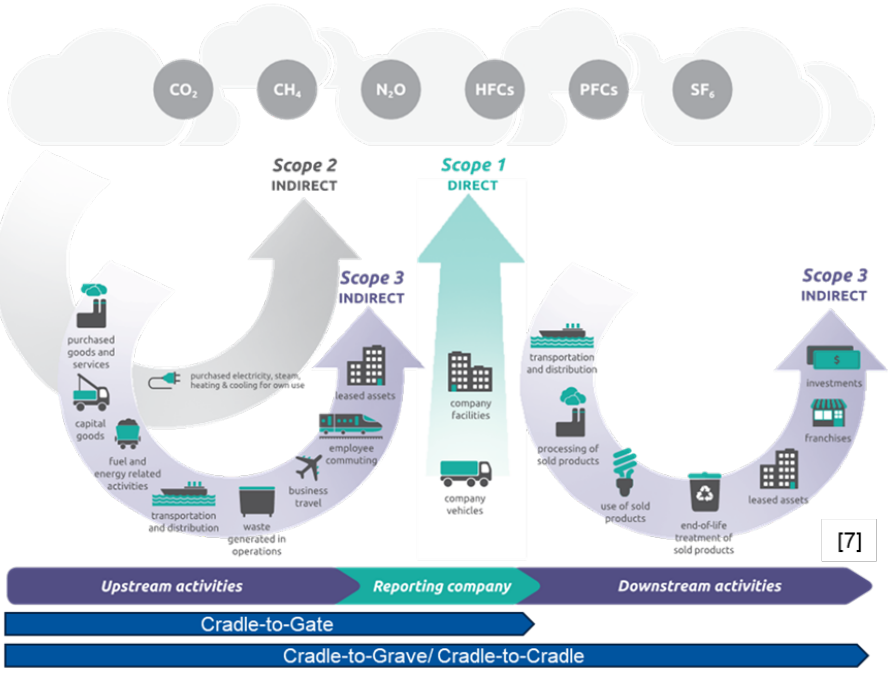

Figure 1: Greenhouse Gas Protocol: Scope 1, Scope 2 and Scope 3
Source: ifas & [7]

Next to new manufacturing technologies, current scope of interest for larger companies that contribute to ESG reporting is the reporting of their GHG emissions, e.g. according to the Greenhouse Gas Protocol [7], (Figure 1). Several companies report their emissions from Scope 1 (direct emissions of the reporting company) and Scope 2 (indirect emissions, mainly from purchased electricity, steam, heating and cooling) and set goals for reaching emission neutrality in Scope 1 and 2

within the next years. Next to the emissions on a company level, the product carbon footprint of single components and systems is of interest considering not only the upstream activities, but also the downstream activities including end of live consideration as well as the usage phase. The balancing of upstream activities for fluid power components is challenging [8], but especially for fluid power components that are widely used in many different applications and systems, the accounting of emissions during usage phase is an even more challenging task and not easy to calculate. Therefore, the basis of calculations for a product carbon footprint during usage phase is currently topic of discussion within a joint research project of a group of companies and universities [9].

One disadvantage of GHG emission monitoring is that ecological aspects are not covered in this reporting. Therefore, it is important to additionally consider environmental aspects. Legislation exists (e.g. REACH and possible future PFAS regulation), but companies and research need to further develop alternatives to environmental risky materials. However, this is a complex field of advancements. The reduction of environmental critical materials needs to be achieved by maintaining or improving current state of energy efficiency, robustness and should additionally consider recyclability or reparability.

Current research on different research facilities focuses, e.g., on new design of piston slippers of axial piston machines [10], [11] to enable lead-free slippers.

2.2 Commissioning

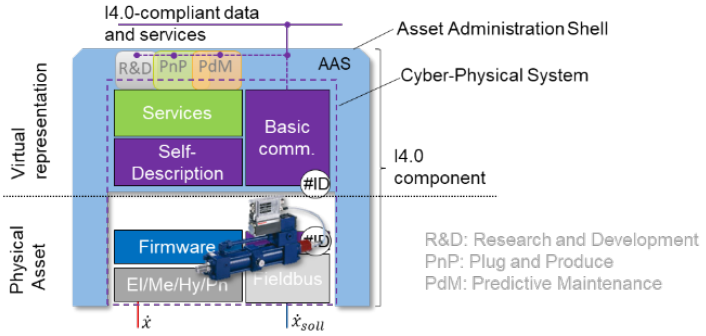

Figure 2: Asset Administration Shell (AAS).
Source: ifas & [12]

The commissioning of fluid power systems is a complex task due to a high number of different components, sometimes even from different suppliers by often an OEM and not the end customer. To facilitate the process, the interoperability of components and the consistent deposition of data plays an important role. The asset administration shell offers a tool to address this need during commissioning phase [12], and throughout the whole product life cycle [9], [13].

2.3 Usage

Main driver for emissions related to fluid power components is the usage phase. During power transmission, energy losses are unavoidable. But it is increasingly important to 1. decrease energy consumption (as it is directly linked to GHG emissions. In addition, total cost of ownership in electrified machines is highly dependent on energy consumption.) and to 2. increase productivity of machines using fluid power systems to decrease energy consumption per work cycle.

Several new approaches exist in research and industry to decrease energy consumption of fluid power components and systems during the usage phase. Especially, the collaborative research and development between universities and companies shows promising results, e.g. [14], [15], [16].

Figure 3: Examples of energy efficiency increase and increased productivity from bauma innovation awards 2025 in Munich, Germany
Source: ifas & [17]

An important field of current advancements lies in the increase of productivity of fluid power driven machines. Especially the construction sector develops further quickly in adapting automation technologies to their field of technology. Here, digital technologies and data algorithms will contribute to further advances in this area.

Three industrial examples in decreasing energy consumption and increasing productivity are shown in Figure 3 from 2025 Bauma Innovation Award [17].

2.4 End of life and repair

When discussion about the complete product life cycle, the end of life, repair and recycling need to be considered. Here, one advantage of fluid power components and systems comes into effect. The systems are modularly composed of different components and can be rearranged easily to new motion duties. In addition, most components are long lasting and robust and the steel base easy to repair. It is important to maintain this advantage even with improvements regarding new materials or new manufacturing technologies and with increasing use of digital technologies (especially integrated sensors). In addition, this advantage should be more clearly communicated in marketing and advertisement for fluid power technology.

3 Conclusion and Outlook

The transformation of our industry and society is unstoppable. Fluid power technology needs to further develop and is further developing with the help of new digital tools, the increased awareness of energy efficiency and the new paradigm of circular economy. Only by looking at the overall picture and considering all aspects, can an optimal solution for each individual case and task be found. A holistic approach is indispensable and requires involvement of all stakeholders, from component manufacturers to end users and common effort from industry and research institutions.

References

[1] Schmitz: *Fluidtechnik – Systeme und Komponenten*, Shaker, Aachen, 2022

[2] EU commission: https://commission.europa.eu/strategy-and-policy/priorities-2019-2024/story-von-der-leyen-commission/european-green-deal_en, visited on 01.08.2025

[3] Schmitz: *Potential for Fluid Power to Contribute to EU Climate Goal 2030*, International conference Fluid Power 2021, Slovenia, DOI: 10.18690/978-961-286-513-9.1

[4] ifas, current research project: *AutoPropVent – Automatisierte Vorauslegung proportionaler Einbauventile*, Forschungskuratorium Maschinenbau e.V., Forschungsfond Fluidtechnik im VDMA, 2025-2028

[5] BoschRexroth: *Whitepaper How manifolds produced using additive manufacturing reduce energy consumption and CO2 emissions*, 2022, https://www.boschrexroth.com/en/de/connected-hydraulics/sustainability/ (01.08.2025)

[6] Tappeiner, Donners, Schmid, Schmitz: *Additive manufacturing of hydraulic components - pressure loss comparison of different self-supporting channel geometries*, International Fluid Power Conference IFK, Dresden, Germany 2024, DOI: 10.13052/rp-9788770042222C20

[7] Greenhouse Gas Protocoll: *Corporate Value Chain (Scope 3) Standard,* 2025, avaibale online https://ghgprotocol.org/sites/default/files/standards/Corporate-Value-Chain-Accounting-Reporing-Standard_041613_2.pdf (01.08.2025)

[8] Sprink, Schmitz: *Product carbon footprint of hydraulic and pneumatic components - challenges in accounting and comparability*, International Fluid Power Conference IFK, Dresden, Germany 2024, DOI: 10.13052/rp-9788770042222C38

[9] Joint research project Fluid 4.0, www.Fluid40.de, visited on 01.08.2025

[10] Ivantysyn, Horn, Weber: *Design of a Lead-Free Slipper Bearing for Low Speed Axial Piston Pump Applications*, International Journal of Fluid Power, Vol. 25 2, 183–202., River Publishers, DOI: 10.13052/ijfp1439-9776.2524

[11] Schlegel, Schmitz: *Geometric design of axial piston machine slipper-bearings made of high-performance plastics*, Forschung im Ingenieurwesen (2025) 89:26, Springer, DOI: 10.1007/s10010-025-00813-2

[12] Alt: *Service-Oriented Architecture for Automated Commissioning of Fluid Power Systems*, Shaker, Aachen, 2023

[13] Ritz, Becker, Weber, Schmitz: *Accelerating Product Development: The Effort of Asset Administration Shells for aggregated Systems*, 19th Scandinavian International Conference on Fluid Power, SICFP'25

[14] Pan, Vacca, Manne, Gysling: *On the Volumetric Loss Caused by Incomplete Filling with Undissolved Gas in Positive Displacement Pumps: Lumped Parameter Modeling, CFD Comparisons, and Experimental Validations*, International Journal of Fluid Power (2025): Vol. 26-2, pp. 129–162, DOI: 10.13052/ijfp1439-9776.2622

[15] Schmidt, Binsbergen-Galán, Knöll, Riedmann, Schneider, and Heemskerk: *Energy Efficient Excavator Implement by Electro-Hydraulic/Mechanical Drive Network*, International Journal of Fluid Power (2024): pp. 413–438, DOI: 10.13052/ijfp1439-9776.2541

[16] Reddy, Ivantysyn, Rauschenberger, Weber: *Advanced micro-surfacing: tribological optimization for variable speed hydraulic drives*, ASME IDETC-CIE FPMC2025, Anaheim

[17] www.bauma-innovationspreis.de, visited 01.08.2025

UNIFOREST CONNECT - DIGITALISATION IN FORESTRY TECHNOLOGY

SANDI GROBELNIK, ROBERT HORVAT

Uniforest, d.o.o., Prebold, Slovenia
sandi.grobelnik@uniforest.si, robert.horvat@uniforest.si

DOI
https://doi.org/10.18690/um.fs.7.2025.2

ISBN
978-961-299-049-7

Keywords:
Uniforest Connect, machine servicing, smart way of working, service intervals,. work performance

As with most modern equipment, both for leisure and industrial purposes, there is an increasing demand for monitoring machine operating parameters via mobile devices. This allows for easy insight into the condition of the machine, monitoring of work performance, alerts about potential problems, and preventive maintenance. The aim of the project is to provide users of forestry machines with a very easy insight into the heart of the machine. All important parameters and data that end users, owners of multiple machines – companies and dealers – want to monitor are recorded there. Therefore, it is necessary to enable wireless connection of forestry machines with smart devices (phones, tablets, etc.), through which users will be able to access the machine's data. This will provide users with much better information about the machine's condition. It also makes it easier to diagnose faults on the machines. This helps the manufacturer, the service technicians, and, on the other hand, the user to minimise unwanted machine downtime.

University of Maribor Press

1 Introduction

As a manufacturer of forestry equipment, we are aware of the fact that a good machine with innovative solutions cannot satisfy users without good technical support and fast and responsive service in in case of problems. Therefore, if we want to satisfy our customers in this regard, we must be very familiar with user habits, their way of working, and the specifics of work in different markets. To this end, we have developed electronics that ensure the machine functions perfectly and at the same time stores all important events that occur on the machine, and can be sent to a smart device via a Bluetooth module.

For this purpose, an application suitable for smartphones was developed that recognizes the machine and displays important information to the user based on serial number (Figure 1).

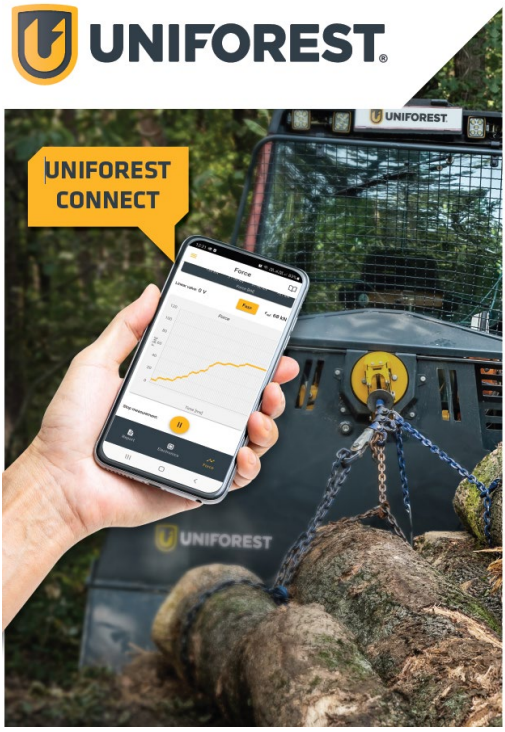

Figure 1: Smartphone app screen for controlling forestry machines »Uniforest Connect«.
Source: Uniforest, d.o.o.

This involves synchronizing two-way data flow between a smart device and electronics. Data security is of great importance in communication to ensure that data is reliable and usable. All data collected via the application is stored in the company's database. This contributes to much greater transparency of the machines on the manufacturer's side. The machine's serial number is used to record all of the machine's work cycles, usage times, and individual functions. On some models, the pulling force of the machine can also be monitored in real time, and the supply voltage is also displayed in real time. This data is presented to the user in a user-friendly graphical format.

2 How Uniforest Connect works

Users can install the app on their Android mobile phones via the Play Store/iTunes. It is also important that the smartphone has a Bluetooth connection, which the app uses to communicate with the winch electronics (Figure 2).

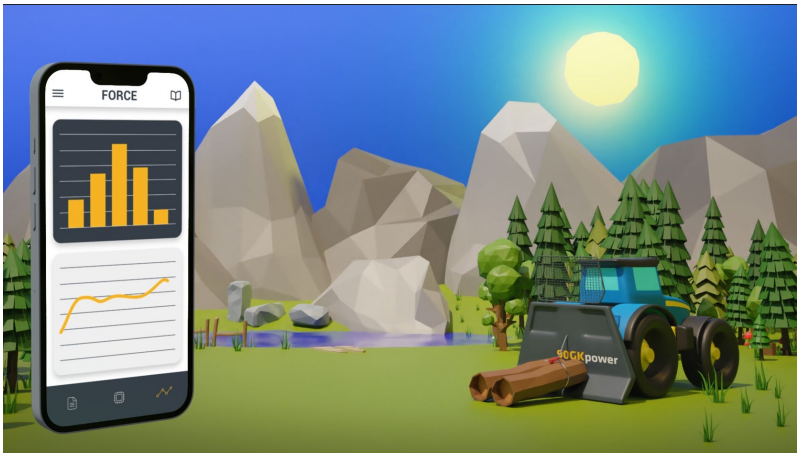

Figure 2: Connection of the Uniforest Connect app to a forestry winch via a wireless Bluetooth connection.
Source: Uniforest, d.o.o.

The functions offered by the "Uniforest Connect" system are described below.

- It can monitor the operation of the clutch, brakes, unwinding device, and limit switch.
- At the same time, the user has an overview of the service interval of the winch.

- Winch load monitoring: The electronics record the percentage of time the winch operates under load (Figure 3). This allows the user to determine whether the winch is suitable for their needs. At the same time, the user has an overview of the winch's service interval.
- Diagnostics: Power supply, pulling force (Figure 4), remote control signals, and inputs and outputs on valve coils are actively monitored at all times.

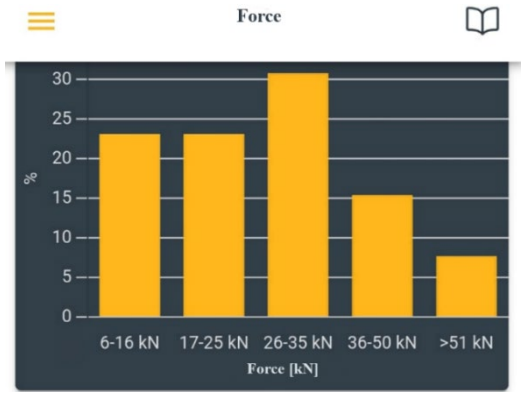

Figure 3: Recording the load percentage of the winch
Source: Uniforest, d.o.o.

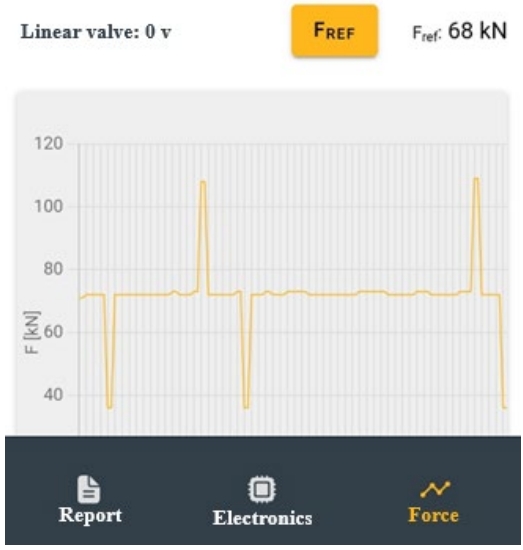

Figure 4: Recording the measured pulling force of the winch.
Source: Uniforest, d.o.o.

3 Benefits for the user

The newly developed application enables users to perform real-time diagnostics, monitor multiple machines simultaneously and optimise service cycles. The strong advantages of such applications are listed below: The user can perform basic diagnostics on site. Business users with multiple employees and multiple machines can monitor machine performance and efficiency on a daily basis. Service intervals help the user to optimise machine maintenance (reminders for regular maintenance). In tenders where Industry 4.0 or digital machine monitoring is required for tender funds, it will be possible to participate with our system.

This gives the user a real time insight into the operation of the device. It can later be saved and presented as a report, which can be useful for further analysing the operating regime of the individual winch. In case of a malfunction, the recorded history can provide valuable information for estimating the expected life of the machine, and with advanced knowledge and expertise in this field, appropriate preventive maintenance can be ensured.

4 Download. Connect. Extend. Warranty 2+1

Connect to the Uniforest Connect app and secure an additional year of warranty!

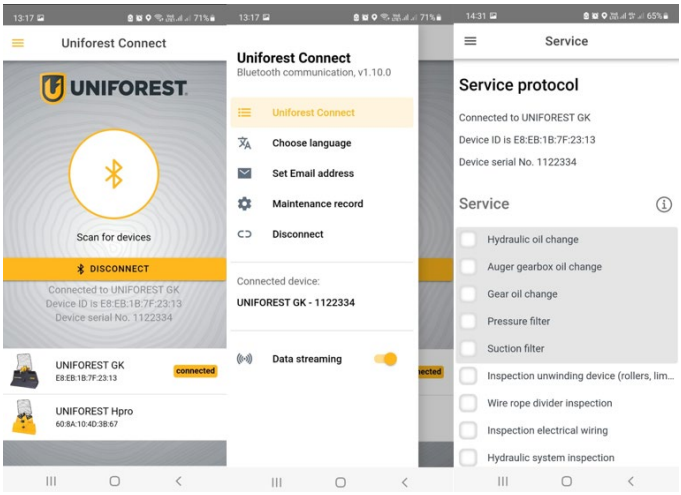

Figure 5: Settings screens of the "Uniforest connect" application.
Source: Uniforest, d.o.o.

– Well-maintained machines have a longer service life;
– If the service intervals are adhered to, an extended warranty period of 2+1 year is guaranteed.

Uniforest is the first forestry winch manufacturer to enable digital diagnostics and take the user experience to another level! In this way, we can not only maintain our competitive advantage, but above all we want to implement further solutions to improve the user experience for end customers, vendors and service providers.

5 How Uniforest Connect works on cutting and splitting machines

Figure 6 shows the settings screen of the "Uniforest Connect" application for cutting and splitting machines [1]. There are several options from which the user can select the optimum settings for their needs.

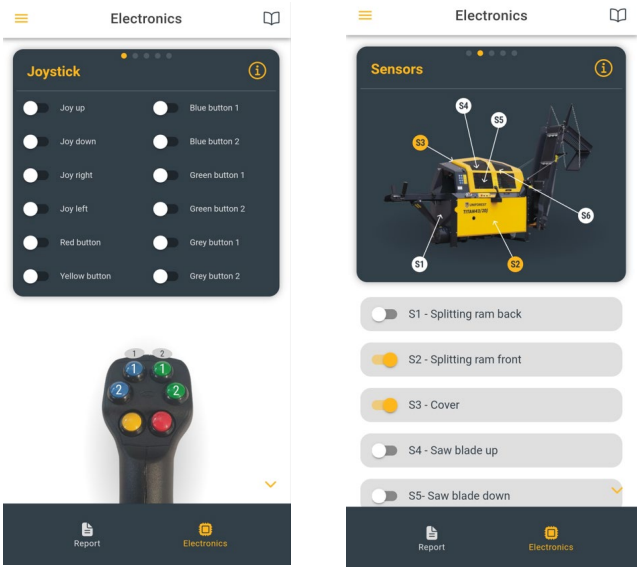

Figure 6: Settings screens of the "Uniforest Connect" application on cutting and splitting machines.
Source: Uniforest, d.o.o.

Cutting and splitting machines, provide the user with:

– a complete diagnosis of the electronics,

- an overview of the inputs and outputs of the control unit, an overview of the operation of the sensors, measurements of the machine temperature, measurements of the machine speed, and if the instructions are not followed (tractor PTO speed too high or too low), the application warns the user,
- measurements of the control signal voltage,

With Log measurement setting, you can easily calculate the total quantity of logs by measuring the length, diameter, and volume of the logs or the chopped wood (Figure 7).

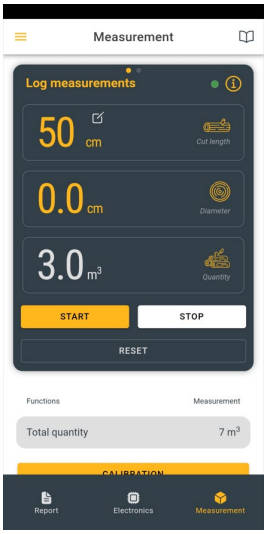

Figure 7: Diagnostic display of completed work – split logs on a cutting and splitting machine
Source: Uniforest, d.o.o.

6 The significance of Industry 4.0 and Industry 5.0 for users and the positioning of "Uniforest Connect"

Technological developments in recent years have brought about the increasing introduction of artificial intelligence into the operation of machines, production, storage and other systems, the creation and dissemination of information, and, finally, into people's everyday use in the form of "smart" devices, cars and homes. Automation, device connectivity, and artificial intelligence are the foundations of Industry 4.0.

However, the independent operation and learning of software in various forms and its response to real-world circumstances is not always ideal, which is why the next stage of development has brought about Industry 5.0. This puts people back at the centre and focuses on safe and ergonomic working and the optimisation of work processes for optimum efficiency, considering the reduction of the negative effects of modern work on people.

The most widespread forms of Industry 5.0 include: generative artificial intelligence, which interacts with humans and thus develops according to the user's needs, augmented reality, which combines virtual and real reality with the aim of promoting creativity and efficiency, digital twins for the continuous monitoring, simulation, and optimisation of industrial processes, the use of blockchain as a data tracking system for greater security and transparency in industrial processes.

6.1 Connectivity and smart maintenance with Uniforest Connect

Uniforest machines are connected to the central Uniforest database via the Uniforest Connect app (Figure 8), which enables tracking of the service cycle, predictive maintenance, and timely notification of service centres. Thanks to this technology, spare parts are always available, and the work process remains uninterrupted. Industry 4.0 in practice – integration of IoT and data analytics [2].

Figure 8: Connect diagnostic and monitoring system
Source: Uniforest, d.o.o.

6.2 Real-time diagnostics and remote control

Solutions at your fingertips – anywhere, anytime. With advanced remote machine diagnostics and a response time of 0.3 seconds, operators and service technicians can monitor machine loads live, check input signals, and quickly troubleshoot faults (Figure 9). Industry 4.0 – advanced monitoring of machine performance in line with the EU strategy [3].

Figure 9: Uniforest connect - response in 0.3 s
Source: Uniforest, d.o.o.

6.3 Machine traceability and safety

System provides all machine information in one place. Every Uniforest machine is traceable via its serial number, which is stored in the electronics and on the declaration plate. The service history is available, at any time and provides a complete overview of past interventions and future maintenance work (Figure 10). Industry 4.0 – transparency and intelligent data management in line with EU directives [4].

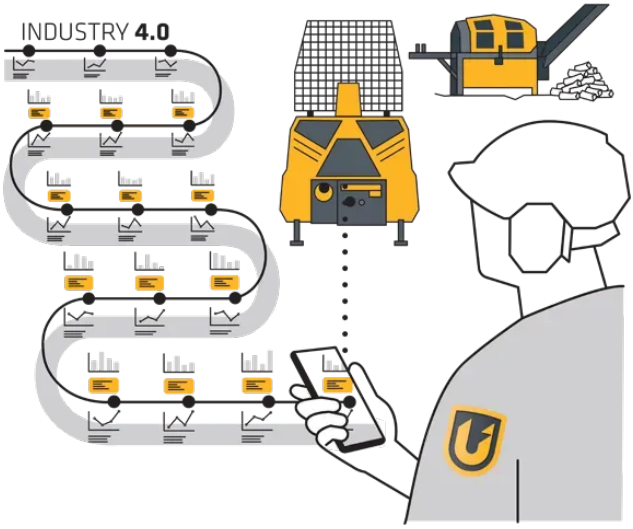

Figure 10: Machine traceability via the Uniforet Connect app.
Source: Uniforest, d.o.o.

6.4 Ergonomic design according to EU standards

The system features a less-effort approach with more security. Uniforest machines are designed in accordance with EU ergonomic guidelines, including ISO 12100, which reduces operator fatigue and improves the working environment. Customized control systems and user-friendly applications enable easy operation in multiple languages. Industry 5.0 – people and a safe working environment at the centre [5]. Reference to the EU Directive: Directive 89/391/EEC on safety and health at work.

References

[1] Uniforet Connect, Katalog, 2025, Slovenija.
[2] Europian Union: Direktiva 2006/42/ES Evropskega parlamenta in Sveta z dne 17. maja 2006 o strojih in spremembah Direktive 95/16/ES (preoblikovano), 2025.
[3] European Union: Shaping Europe's digital future, source: https://commission.europa.eu/strategy-and-policy/priorities-2019-2024/europe-fit-digital-age/shaping-europes-digital-future_en , available on: 19th August 2025.
[4] European Union: Industrial research and innovation, source: https://research-and-innovation.ec.europa.eu/research-area/industrial-research-and-innovation_en, available on: 19th August 2025.
[5] Europian Union: "Direktiva Sveta z dne 12. junija 1989 o uvajanju ukrepov za spodbujanje izboljšav varnosti in zdravja delavcev pri delu, 2025

A Self-Optimizing Hydraulic System Approach for Agile Metal Forming

Denis Jankovič, Marko Šimic, Tomaž Pepelnjak, Niko Herakovič

University of Ljubljana, Faculty of Mechanical Engineering, Ljubljana, Slovenia
denis.jankovic@fs.uni-lj.si, marko.simic@fs.uni-lj.si, tomaz.pepelnjak@fs.uni-lj.si, niko.herakovic@fs.uni-lj.si

This research presents a novel concept of a smart hydraulic press system, enhanced with an expert system and a multi-objective optimization loop, aimed at flexible metal forming in agile manufacturing. Unlike traditional forming systems designed for mass production, the proposed solution enables adaptive, multi-phase control for producing a variety of products. By integrating AI-driven data analytics and real-time adaptive control, the system supports predictive decision-making, anomaly detection, and self-optimization of the forming process. The expert system utilizes historical datasets and machine learning models to minimize response error and adapt to process variations. Experimental validation demonstrates over 95% improvement in hydraulic system performance. The study also highlights the potential for further enhancement through an additional control loop focusing on product dimensional accuracy based on material properties and tool geometry. This approach aligns with Industry 4.0 and 5.0 goals for flexible, efficient, and sustainable manufacturing.

DOI
https://doi.org/10.18690/um.fs.7.2025.3

ISBN
978-961-299-049-7

Keywords:
hydraulic press, flexible manufacturing, adaptive control, self-optimizing,. agile manufacturing

University of Maribor Press

1 Introduction

Manufacturing companies are undergoing a paradigm shift, transitioning from traditional production-centric operations toward service-oriented, intelligent manufacturing systems. In this context, hydraulic presses, widely used in metal forming, are evolving into smart systems that integrate expert knowledge, sensor data, and optimization algorithms to enhance flexibility and performance in agile manufacturing environments [1].

This paper focuses on the development and implementation of smart hydraulic press systems, specifically designed to support flexible metal forming processes such as incremental forming, deep drawing, and other advanced processes [2]. The integration of expert systems (ES) in such machines enables real-time process adaptation, fault diagnosis, and parameter tuning, while a multi-objective optimization loop supports decision-making to balance conflicting goals such as forming accuracy, energy efficiency, and cycle time.

The key research challenge is to establish a systematic design methodology for such smart systems, bridging the gap between market demands for flexibility (servtization) and technological enablers such as Cyber-Physical Systems (CPS) and data-driven control [3].

This contribution presents a modular framework composed of building optimization control loops for smart hydraulic press integration. These control loops serve two main purposes: (1) to reduce the hydraulic press instability by identifying real-time data patterns observed in real environment, and (2) to improve the final product quality.

2 Self-optimizing hydraulic system

Manufacturing processes typically follow the behaviour of Gaussian (normal) distributions, where it is common for the majority of process variation to fall within a 95 % probability range [4]. This level of repeatability is generally considered adequate for most production environments. However, in high-performance required environments, such as lean manufacturing, stricter requirements are imposed, often demanding process probability range above 98 %.

In this context, the proposed concept of a self-optimizing hydraulic system highlights the necessity of integrating various research domains, including simulation tools, machine learning techniques in order to designate the services for flexible manufacturing [5]. These are essential for the development of a purpose-built expert system capable of recognizing deviations, reconfiguring parameters, and adapting in real time i.e. when the hydraulic system operates outside the 95 % confidence range or when product specifications deviate from target requirements.

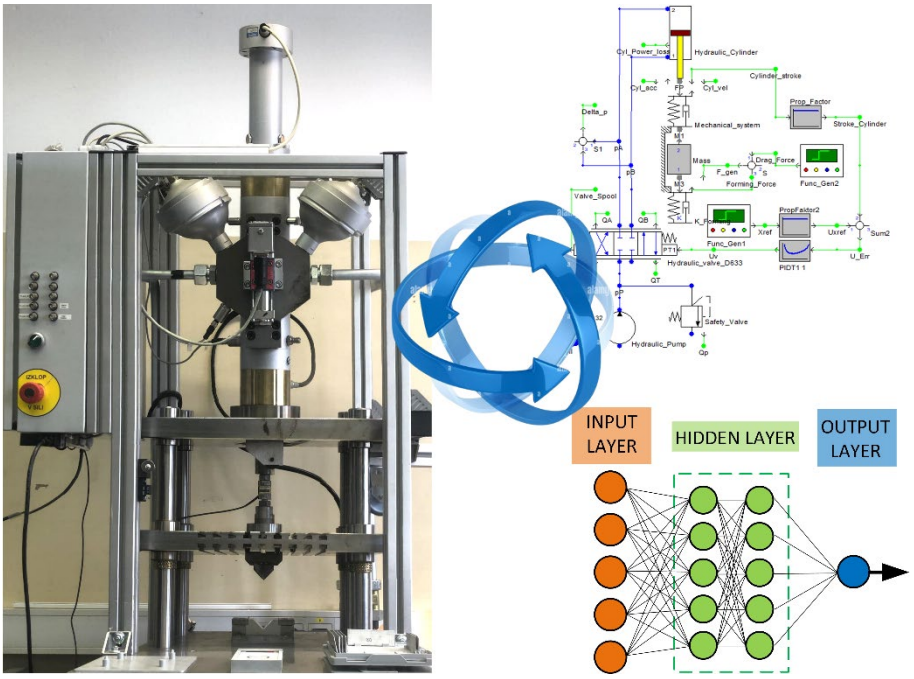

Figure 1: Hydraulic press analysis approach and data exchange.

The behaviour of any manufacturing system, including hydraulic systems, which play a key role in forming processes, can be predicted using well-established physical principles implemented in simulation models. The simulation tools replicate the system's physical behaviour within a virtual environment, enabling detailed analysis and optimization before real-world implementation [6].

In this context, the proposed concept emphasizes the importance of using multiple specialized tools designed to analyse the performance of distinct subsystems. This includes the simulation of hydraulic systems using tools such as DSHPlus, and the

simulation of forming processes using advanced finite element software such as Abaqus. Moreover, data-driven models have gained significant popularity and are increasingly becoming a core element in integrating intelligent decision-making into the system. The results obtained from both domains are later integrated and interpreted in conjunction with expert knowledge to develop a comprehensive understanding of overall system behaviour and performance, as illustrated in the Figure 1.

The hydraulic press system is interpreted as a multi-node structure, consisting of key hydraulic components such as the hydraulic cylinder, PI controller, hydraulic power unit, hydraulic oil, pressure accumulators, hydraulic valves. Moreover, the studied hydraulic system is part of manufacturing process of sheet metal bending. Here, the forming process is described as subsystem. Each node must be accurately represented within the simulation model to ensure realistic results.

Specifically, the forming process can be modelled using Abaqus, a simulation environment purposely designed for analysing complex forming operations. This enables detailed insight into material deformation, stress distribution, and tool-workpiece interactions, which are critical for evaluating and optimizing the performance of the hydraulic press system.

Recent research shows that the accuracy of real-environment systems is best achieved using data-driven models [7]. A wide range of modelling techniques in the area of Machine Learning and Artificial Intelligence is available, including high-performance models such as Gaussian Process Regression (GPR) and Neural Networks (NN), as well as simpler models such as Polynomial Regression and Support Vector Regression (SVR).

In previous research, aiming at modelling the hydraulic press, a Polynomial Regression has proven to be sufficiently effective. It offers several advantages: it is computationally efficient, fast to train, and quick in prediction, while still providing high prediction accuracy in modelling the behaviour of the investigated system [8], [9].

Smart services are a combination of physical and digital services that are based on gathered data from a physical system. As a result, smart services are integrated product-service systems with a focus on digital, data-based service components. The

challenge in our research is to combine theoretical considerations in the field of hydraulic systems operation, cyber-physical systems (technology push) and the predetermined requirements (hydraulic press stability, product quality). Our approach shows steps required to designate multi-objective optimisation loop for hydraulic presses, which can be used to plan new smart services based on an existing product and to implement them based on reference solutions.

3 Multi-objective optimization concept for hydraulic press

3.1 Hydraulic system optimisation loop

Hydraulic system optimization loop aims to align the actual movement of the hydraulic cylinder with its desired movement, which is pre-defined based on the hydraulic press cycle required for the forming operation. Expert systems are effective tools for supporting this process by autonomously identifying deviations, inefficiencies, and optimization potentials in the hydraulic press control logic as shown on Figure 2. These systems not only monitor and analyse the dynamic behaviour of the press but also assist in:

- reducing energy consumption,
- reducing cycle time,
- and increasing process stability.

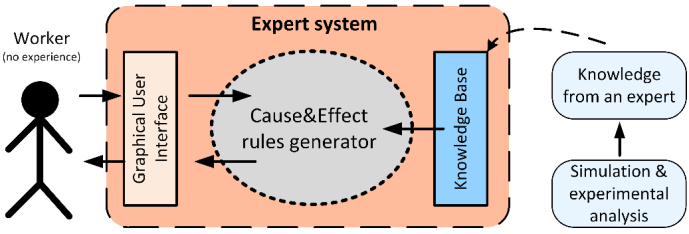

Figure 2: Expert system integration.

3.1.1 Knowledge integration into the expert system

By leveraging real-time and historical data, the designated expert system detects patterns in system responses, suggest parameter adjustments, and adapt control strategies accordingly. This data-driven optimization is particularly valuable in

modern manufacturing, where sustainability and energy efficiency are key priorities beside product quality. The integration of expert systems into hydraulic press operations contributes to operational stability and indirectly to product quality requirements. Here the hearth of the expert system is cause & effect rules generator, which is set up by hydraulic system experts required to perform in depth simulation and experimental analysis.

The knowledge base describes the behaviour of the hydraulic press under various loading conditions, which are determined by different hydraulic cylinder velocities and the intensity of the forming process (different forming materials, products require different forming cycles). An observer i.e. worker accompanies the hydraulic press operation and monitors the response error reduction of hydraulic press to confirm the hydraulic system operational stability during the manufacturing process.

Furthermore, a detailed analysis was conducted in a simulation environment, achieving an average similarity of 80.3 % compared to the behaviour of the hydraulic press under various loading conditions in real environment, as illustrated in Figure 3. In contrast, learnt models using machine learning and artificial intelligence techniques, based on polynomial regression analysis demonstrated a significantly higher prediction accuracy of 98.3% compared to hydraulic press system behaviour.

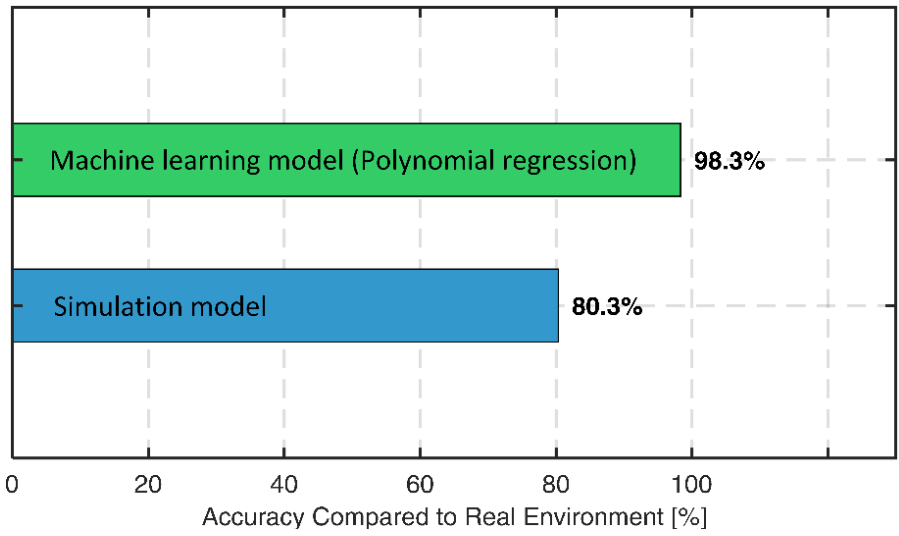

Figure 3: Comparison of system modelling accuracy between simulation environment and machine learning approach.

This notable improvement highlights the strong potential of data-driven approaches for capturing complex nonlinear system behaviour with high fidelity [7]. The achieved prediction accuracy of the ML model not only surpasses traditional simulation models but also confirms the scientific relevance and robustness of using AI techniques for predictive modelling in advanced manufacturing systems. Such results contribute meaningfully to the development of intelligent control architectures and position the methodology at the forefront of current research in smart forming technologies.

However, beyond sophisticated diagnostic capabilities, the practical and user-friendly software tools MATLAB are used to develop ML and AI tools which enable rapid implementation of expert knowledge into the control environment. The presented expert system simplicity shows fast development and deployment of expert logic, that emerged as essential enablers in this context. A standardized interface for rule-based reasoning, simplify integration into existing hydraulic press control systems and enables improvement in hydraulic press behaviour.

This paper presents a comparative evaluation of the proposed expert system with respect to its applicability in hydraulic press optimization, with a particular focus on forming processes. Based on the limitations identified in existing solutions, we introduce a novel expert system framework implemented within the TwinCAT environment. This implementation provides enhanced flexibility, transparency, and seamless integration into both research and industrial settings.

3.1.2 Improvement in operational stability of hydraulic press

Operational stability of a hydraulic press is determined by its ability to minimize the absolute mean error $\measuredangle X_C$ in the hydraulic cylinder displacement response. Figure 4 illustrates the improvement in the hydraulic press position accuracy, where the implementation of the proposed intelligent methodology resulted in a reduction of the absolute displacement error $\measuredangle X_C$ by up to 3.5 mm. This significant improvement validates the effectiveness of the developed approach in enhancing system control fidelity. By integrating machine learning models into the control processing unit, the system is able to dynamically adapt to changing operating conditions, reducing the error range across various phases of hydraulic press cycle.

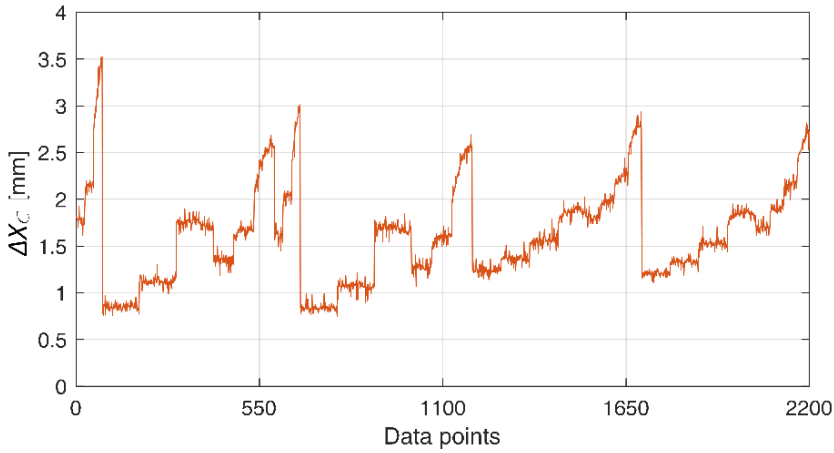

Figure 4: Hydraulic press response error reduction.

The operating conditions represent different load scenarios of the hydraulic press, where variations in specimen cross-sections directly affect the magnitude of force required by the hydraulic cylinder, as well as the cylinder's movement velocity. Larger cross-sections result in increased resistance of the material, requiring higher forces to be applied by the hydraulic cylinder. Additionally, at higher movement velocities, the hydraulic cylinder must overcome material resistance within a shorter time interval, which further stresses the system. Conversely, smaller specimen cross-sections and lower movement velocities reduce material resistance, resulting in lower force demands and more stable system response.

Regression models represent the core intelligence of the expert system, where the capability of predicting system states with sufficient accuracy based on the data used for training. However, improper learning strategies often lead to degraded model performance, particularly when exposed to previously unseen operational states. Despite this, the proposed expert system demonstrated robust generalization capability during validation in the context of various scenarios, where the hydraulic system operated under unfamiliar conditions.

Overall, the integration of AI-driven regression models into the hydraulic press control logic significantly improves system responsiveness and robustness, offering a scalable and scientifically grounded solution for next-generation forming technologies.

3.2 End user product optimisation loop

In the context of flexible manufacturing, where products vary in shape, size, and material properties, diverse operational requirements are addressed within the concept of the multi-objective optimisation loop, as illustrated in Figure 5.

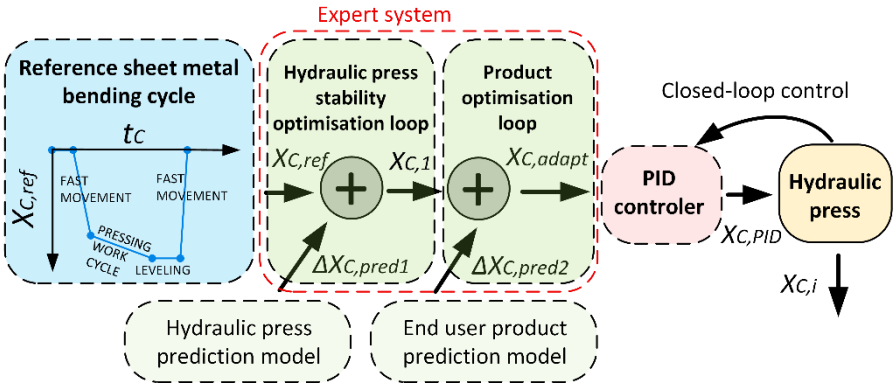

Figure 5: Multi-objective optimisation loop.

The operation of the hydraulic press is dynamically adapted to $X_{C,adapt}$ through a purpose-built optimisation framework tailored to the specific demands of each forming scenario given by the hydraulic press cycle (reference movement $X_{C,ref}$).

Within the proposed multi-objective optimisation loop integrated into the expert system, two primary objectives are considered:

1. In the first step hydraulic press stability optimisation loop focuses on the dynamic behaviour of the hydraulic system (hydraulic cylinder properties, internal and external leakages, hydraulic oil properties such as viscosity, temperature, pressure etc.) [10]. A dedicated optimisation model predicts the response error $\Delta X_{C,pred1}$ of the hydraulic press and actively corrects its behaviour (X_{C1}) to maintain operational stability under varying system dynamics.
2. In the second step the adapted signal from hydraulic press stability optimisation loop, the product optimisation loop targets the correction of hydraulic press response error $\Delta X_{C,pred2}$ resulting from variations in material properties, product geometry, dimensional tolerances, forming speed, temperature effects, lubrication conditions, and tool wear. This loop relies on a product prediction

model that estimates the expected deviation in forming outcomes and adjusts the control signal accordingly, after the hydraulic stability correction.

In the final step, a robust PID controller ensures precise execution of the optimised control signal $X_{C,\,PID}$. It compensates for any residual uncertainties and disturbances in the system, maintaining both process stability and product quality. The PID controller operates within a closed feedback loop, continuously aligning press performance with the desired forming results.

This layered approach enables real-time adaptability in agile production environment, where the interplay between system dynamics and product-specific requirements must be managed with high precision.

4 Discussion

The integration of expert systems and predictive models into hydraulic press control opens new possibilities for intelligent forming systems. The high accuracy achieved by the regression models demonstrates that data-driven approaches can effectively capture nonlinear system behaviour in real-world production environments.

The multi-objective optimization strategy enables a coordinated balance between internal system dynamics and product quality requirements. This is especially relevant in agile manufacturing contexts, where forming parameters must adapt in real time to disturbances. The combination of predictive logic and corrective control (via the PID layer) contributes to overall process robustness, yet its performance still depends on the quality and representativeness of the training data.

One of the advantages of the developed system is its modular design and compatibility with existing industrial platforms, allowing practical deployment without major retrofits. However, further research is needed to evaluate long-term system performance under varying production conditions, including tool wear, fluid degradation, and system fatigue.

In future developments, integrating additional sensory inputs (e.g., acoustic emission, vibration analysis) and exploring deep learning methods could further enhance the system's adaptive capabilities.

5 Conclusions

In this study we developed a smart hydraulic press system for flexible sheet metal forming, designed for agile production environments.
The key achievements are:

- Implementation of an expert system with real-time and historical data integration,
- Predictive modelling using polynomial regression with accuracy up to 98.3 %,
- Development of a dual-loop control structure combining optimization and PID regulation,
- Modular system architecture, tested in MATLAB and TwinCAT environments,
- Demonstrated reduction in force fluctuation and improved press stability.

The system lays the foundation for adaptive, intelligent forming processes aligned with Industry 4.0 and 5.0 goals.

Acknowledgments

The work was carried out in the framework of several research programs: Innovative manufacturing systems and process (P2-0248); Research on the reliability and efficiency of edge computing in the smart factory using 5G technologies (J2-4470); research program for young researchers (53512), which are financed by the Republic of Slovenia – Ministry of Education, Science and Sport. We would like to thank the German company FLUIDON GmbH who support us with DSH^{plus} simulation tool licence.

References

[1] Xin, C., Motz, T., Fuhl, W., Hartel, A. & Kasneci, E. (2023). *Deep learning-based position detection for hydraulic cylinders using scattering parameters*. Expert Systems with Applications, Vol. 232,.

[2] Trzepieciński, T. (2020). *Recent developments and trends in sheet metal forming*. Metals, Vol. 10, pp. 1–53.

[3] Xu, L. Da, Xu, E. L. & Li, L. (2018). *Industry 4.0: State of the art and future trends*. International Journal of Production Research, Vol. 56, pp. 2941–2962.

[4] Brun, M., Ghiotti, A., Bruschi, S. & Filippi, S. (2021). *Active control of blankholder in sheet metal stamping*. Procedia CIRP, Vol. 100, pp. 151–156.

[5] Quatrini, E., Costantino, F., Pocci, C. & Tronci, M. (2020). *Predictive model for the degradation state of a hydraulic system with dimensionality reduction*. Procedia Manufacturing, Vol. 42, pp. 516–523.

[6] Zhang, X., Yin, Y. & Huang, W. (2010). *Influence of temperature on null position pressure characteristics of flapper-nozzle servo valve*. 2010 International Conference on Computer Design and Applications, ICCDA 2010, Vol. 3, pp. 257–261.

[7] Guo, W., Pan, T. & Li, Z. (2016). *Development of a soft sensor for processes with multiple operating regimes using adaptive multi-state partial least squares regression*. Journal of the Taiwan Institute of Chemical Engineers, Vol. 67, pp. 20–28.

[8] Jankovič, D., Šimic, M. & Herakovič, N. (2024). *A comparative study of machine learning regression models for production systems condition monitoring.* Advances in Production Engineering And Management, Vol. 19, pp. 78–92.

[9] Jankovič, D., Pipan, M., Šimic, M. & Herakovič, N. (2024). *Polynomial Regression-Based Predictive Expert System for Enhancing Hydraulic Press Performance over a 5G Network*. Applied Sciences (Switzerland), Vol. 14,.

[10] Feuchtmüller, O., Hörl, L. & Bauer, F. (2021). *Oil film generation of a hydraulic rod seal: an experimental study using ellipsometry*. Tribology International, Vol. 162, pp. 0–3.

Numerical Optimization of Internal Geometry for Additively Manufactured Hydraulic Manifolds

Jan Bartolj,[1] Katharina Schmitz,[2]
Nikola Vukašinović,[1] Franc Majdič[1]

[1] University of Ljubljana, Faculty of Mechanical Engineering, Ljubljana, Slovenia
jan.bartolj@fs.uni-lj.si, nikola.vukasinovic@fs.uni-lj.si, franc.majdic@fs.uni-lj.si
[2] RWTH Aachen University, Institute for Fluid Power Drives and Systems, Aachen, Germany
Katharina.Schmitz@ifas.rwth-aachen.de

This study presents a novel approach for the design and optimisation of hydraulic manifolds with self-supporting geometries that are compatible with additive manufacturing. Conventional manifolds with a circular cross-section often require complex post-processing as the internal channels are not supported. In this work, configurations of cross-sectional shapes that do not require support structures are investigated. A parametric optimisation and an adjoint gradient algorithm strategy were implemented to refine the cross-sectional geometry of the internal channels with the aim of minimising pressure loss while ensuring manufacturability. Use of CFD simulations to analyse the flow behaviour and pressure losses for different design variants. The integration of self-supporting features not only improves flow efficiency but also realises the full potential of AM by reducing manufacturing time and post-processing requirements. This research contributes to the development of more efficient, production-ready hydraulic systems through simulation-based design methods that take cross-sectional geometry into account.

DOI
https://doi.org/10.18690/um.fs.7.2025.4

ISBN
978-961-299-049-7

Keywords:
hydraulic manifold, additive manufacturing, internal cross-section, parametrical optimization, CFD simulation

University of Maribor Press

1 Introduction

The European Union's legislative framework, particularly the Energy Efficiency Directive (EU 2023/1791) and the Ecodesign Directive (2009/125/EC), sets increasingly strict targets for reducing energy consumption in industry. These policies not only drive improvements in components like pumps and hydraulic systems but also push for new design methods that prioritize energy performance across a product's lifecycle.

In hydraulic systems, internal flow losses in manifolds represent a non-negligible source of inefficiency. Traditional design methods are largely constrained by manufacturing limits, resulting in geometries that are rarely optimal from a fluid dynamics standpoint. With the rise of Additive Manufacturing (AM), and particularly metal-based techniques such as SLM (Selective Laser Melting) or DMLS (Direct Metal Laser Sintering), designers are no longer limited to planar drilling or simple intersections [3]. Instead, AM allows for the fabrication of fully three-dimensional internal channels, opening up the design space for true geometry-driven optimization [1], [2], [4].

The work presented here combines numerical methods for shape optimisation, in particular parametric optimisation and adjoint gradient techniques, with the design freedom offered by AM. Whilst AM allows for complex geometries[5, 6], it also brings its own limitations, such as the need for support structures during manufacture. For applications with internal flow, such as manifolds, it can be difficult or impossible to remove these supports and must therefore be considered early in the design process. Despite these challenges, AM remains an important enabler, allowing flow paths to be designed according to performance rather than manufacturing constraints.

2 Background & Motivation

2.1 Energy consumption in hydraulics

In hydraulics energy consumption is usually defined by the input energy needed to generate and maintain flow of the fluid under pressure. So basically, energy consumption is a sum of all losses in the hydraulic circuit. Mainly, losses occur where

mechanical or electrical power is used to drive hydraulic pumps, losses caused by friction, turbulence and changes in fluid flow direction, pressure drops and heat generation.

2.2 Numerical simulations

The flow simulations were based on the incompressible, stationary Navier–Stokes equations, which were solved using the finite volume method. The fluid was assumed to be a Newtonian fluid with constant properties. Turbulence was modelled using the realisable k-ω SST model, which is suitable for internal flows with moderate curvature and separation. The governing equations include conservation of mass (1):

$$\nabla \cdot \mathbf{u} = 0 \tag{1}$$

and momentum conservation (2):

$$\rho(\mathbf{u} \cdot \nabla)\mathbf{u} = -\nabla p + \nabla \cdot \bar{\boldsymbol{\tau}} + \mathbf{F} \tag{2}$$

where $\mathbf{u}$ is the velocity vector, p the pressure, ρ the density, $\bar{\boldsymbol{\tau}}$ Newtonian viscous stress tensor and $\mathbf{F}$ represents additional body forces.

Pressure-velocity coupling was handled using the SIMPLE algorithm. Boundary conditions were defined as velocity inlets and pressure outlets, with no-slip conditions on all walls. Meshes were unstructured with refined boundary layers; y+ values were monitored to maintain compatibility with wall functions. Simulation outputs primarily pressure drop served as the objective function for optimization in both parametric and adjoint-based workflows.

2.3 Gradient Adjoint method

The Gradient Adjoint method (GA-method) efficiently calculates how an objective function changes in relation to shape variations (Figure 1).

Unlike finite differences, which require many flow simulations, the GA-method solves a single additional system, regardless of the number of design variables. This makes it ideal for optimising complex geometries with many parameters. The

method provides accurate gradients at low cost, enabling effective workflows for shape optimisation.

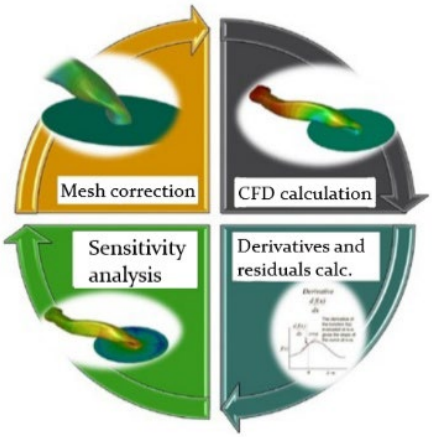

Figure 1: Gradient Adjoint method workflow.

The GA-method in ANSYS Fluent computes sensitivities of an objective function J with respect to shape changes by solving the adjoint form of the flow equations. Starting from the primal residual (3):

$$\mathbf{R}(\mathbf{U}) = 0\,. \tag{3}$$

where $\mathbf{U}$ is the flow solution vector, the adjoint variables $\boldsymbol{\lambda}$ are found by solving equation (4):

$$\left(\frac{\partial \mathbf{R}}{\partial \mathbf{U}}\right)^{\mathrm{T}} \boldsymbol{\lambda} = \frac{\partial J}{\partial \mathbf{U}}\,. \tag{4}$$

The shape derivative, which represents the gradient of the objective function with respect to boundary displacement $\delta\mathbf{x}$, is then obtained from equation (5):

$$\frac{dJ}{d\mathbf{x}} = \frac{\partial J}{\partial \mathbf{x}} - \boldsymbol{\lambda}^{\mathrm{T}} \frac{\partial \mathbf{R}}{\partial \mathbf{x}}\,. \tag{5}$$

This expression allows efficient calculation of gradients for complex geometries without repeating full flow simulations for each parameter. The computed gradients are used to drive mesh deformation and guide shape optimization, relying on steady-state RANS flow solutions and consistent turbulence modelling.

3 Methodology

Research is divided into two case studies. Both are based on the geometry you can see in the Figure 2.

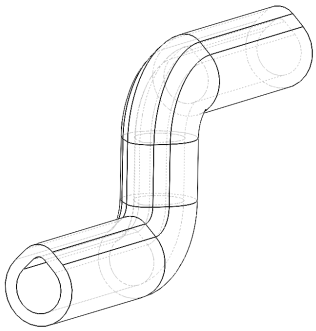

Figure 2: Base S-bend channel geometry for optimisation.

It is a simple S-shaped channel, as often found in hydraulic manifolds. We wanted this geometry to be simple, so we chose to have both bends in the same reference plane. Overall simulations of this S-bent shape are L = 115 mm, H = 70 mm, W = 20 mm.

The first case study is fully parametric and tied to the basic dimension of the geometry, while the second case study is based on the fluid-filled cavity within the channel itself.

3.1 Parametric optimization case 1

A basic teardrop shape with a cross-section of 120 mm^2 was used and 3 measurements were used for parameter optimization. The measurements selected are shown in Figure 3. The top measurement is the upper radius. This is defined as

2 mm, while the second measurement is defined as the angle of the conical upper part of the teardrop and is 90°. The last measurement is again the radius, but this time the lower circular part is defined and is shown in Figure 3 as 6 mm.

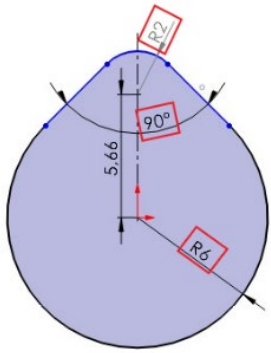

Figure 3: Case study 1. Parametrical optimization of the teardrop shape.

3.2 Gradient adjoint simulation case

The optimisation process using the GA-method is slightly different from the parametric simulation in the previous case. This time we need to define the actual fluid domain as this process optimises the entire fluid geometry within a channel and is not limited to different dimensionally defined sketches. We have the geometry in Figure 4.

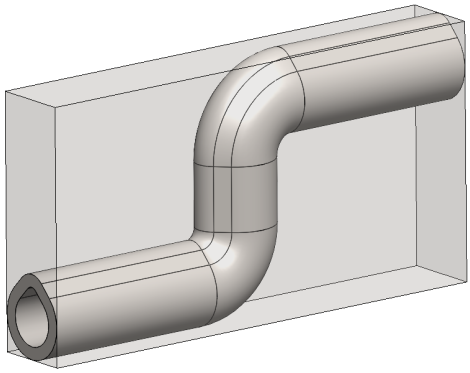

Figure 4: Case study 2. GA-method base geometry with defined optimization space.

4 Implementation

4.1 Mesh

The mesh we used was unstructured with polyhedral elements across the entire geometry. We used boundary layers near the walls of the fluid region as a refinement to better understand the conditions that occur near the fluid-wall interface. This study confirmed that a cell number of about 550 thousand was sufficient in our case to efficiently describe the flow conditions without wasting computation time.

4.2 Solvers and governing equations

The Ansys Fluent solver was used in all cases to calculate the CFD results. This is a CFD solver based on the finite volume method. The numerical formulation used was calculated for incompressible, steady state, Newtonian, isothermal, single-phase, turbulent flow. This meant that two Navier-Stokes equations for mass and momentum conservation were used in combination with the k-ω SST turbulence model.

4.3 Boundary conditions

In the calculations, we have used water as the hydraulic fluid, with a density of 998 kg/m^3 at room temperature. The fluid we have defined has a kinematic viscosity of $0.993 * 10^{-6}$ m^2/s. Since we did not calculate thermodynamic effects such as heat transfer between the fluid and solid walls, the material of the pipe was not defined.

Calculation domain can be divided into three parts. Main calculation domain of the defined S-bend with two appendices, one per inlet and outlet (see Figure 5). The attachments were added to ensure that the flow at the inlet is fully developed in the actual geometry and the results are not influenced by the boundary surface at the outlet.

At the inlet (yellow in Figure 5) we have defined an inlet velocity of the hydraulic fluid corresponding to the flow rate of 70 l/min. An atmospheric pressure of 101.3 MPa was defined at the outlet (red area in Figure 5). At the interfaces of the fluid area and the attachments at the inlet and outlet (blue and green areas in Figure 5),

we inserted measurement points to effectively calculate the pressure losses and other parameters at the actual inlet and outlet of the observed area.

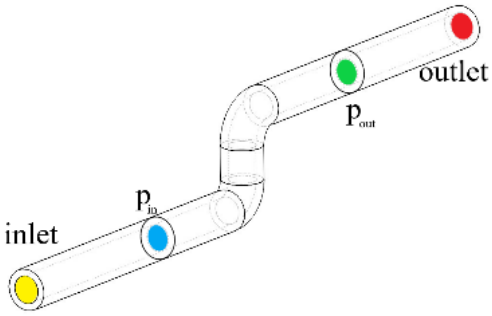

Figure 5: Definition of base geometry appendices with inlet, outlet and measuring areas defined.

5 Results

5.1 Case study 1

It was expected that the result of the first case study would be an enlargement of the fluid area and the elimination of the upper conical edges that define the teardrop shape. As can be seen in Figure 6, this was the case. The optimisation software attempted to make the base circle of the teardrop slightly larger and the upper edges lower. This larger cross-sectional area reduces the velocity through the channel while simultaneously reducing the pressure drop. The resulting change in geometry can be seen in Figure 6 where grey area represents the non-optimized shape, while blue outline, enhanced with the green and red arrows, represents recommended geometry change.

Looking at the flow velocity profiles, it can be seen that this case study slightly improves the channel properties. This becomes clear after the first bend, where a reduced recirculation area can be observed. Less recirculation means less turbulence and a lower pressure drop as the fluid flow is better controlled. The upper velocity profile in Figure 7, profile a) represents the original, non-optimised shape of the teardrop channel, while the lower profile b) represents the optimised shape of the

teardrop channel with an increased angle of the conical part and an upper radius of approx. 4 mm, which is almost twice as large as the initial value.

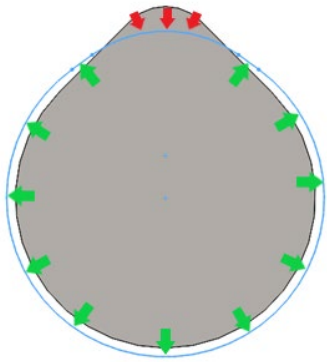

Figure 6: Case study 1 resulting geometry.

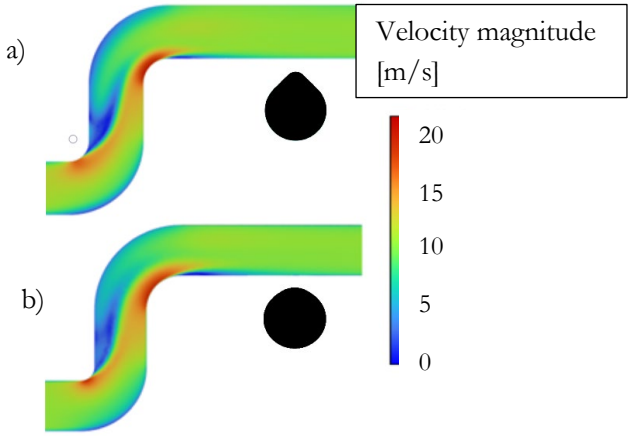

Figure 7: CS1 – Velocity longitudinal profiles comparison with a) non-optimized and b) optimized geometries.

Looking at the parameter of turbulent kinetic energy dissipation, we can compare a) the original and b) the optimised shape of the channel in Figure 8. We can observe the difference in flow behaviour, which confirms the statement obtained from the velocity profiles that the amount of fluid that is recirculating after the first bend decreases.

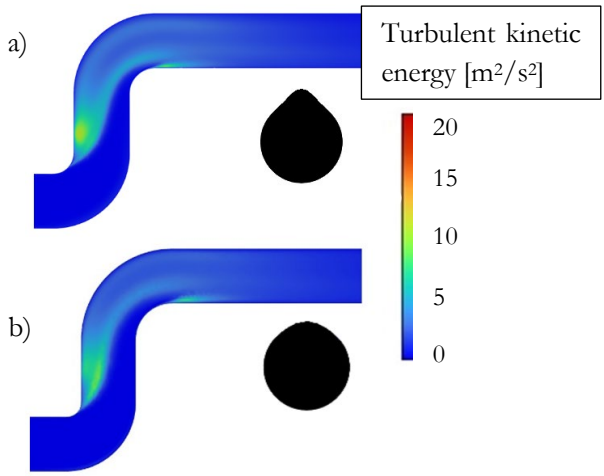

Figure 8: CS1 – Turbulent kinetic energy dissipation longitudinal profiles comparison with a) non-optimized and b) optimized geometries.

If we look at the result of the optimisation itself, we can observe how the different parameters chosen for the optimisation affect the resulting pressure drop on the Figure 9. The first graph represents the response surface that was calculated using the angle of the conical tip of the teardrop and the upper radius and its effect on the resulting pressure drop. It is interesting to note that we can see the local minimum of the response surface. This means that there is a local minimum in the observed set of parameters. At 70 l/min, the original teardrop had a pressure drop of 39412.52 Pa, while the optimised variant has a pressure drop of 33839.58 Pa. By optimising the cross-sectional shape of the geometry alone, a 15 % reduction in pressure loss can be achieved. It is interesting to note that the duct with a circular shape and a cross-sectional area of 120 mm² has a pressure loss of 34697.08 Pa and therefore performs slightly worse than the optimised shape. However, this is not a fair comparison, as the optimisation has increased the cross-sectional area by around 11 %, as already mentioned.

Comparing the response surface diagram for the conical upper angle and the lower radius in Figure 10, we can see that a local minimum is reached again. What is interesting in this case is that the gradients located around the local minimum are much higher than those observed in the previous graph, which makes the local minimum even clearer.

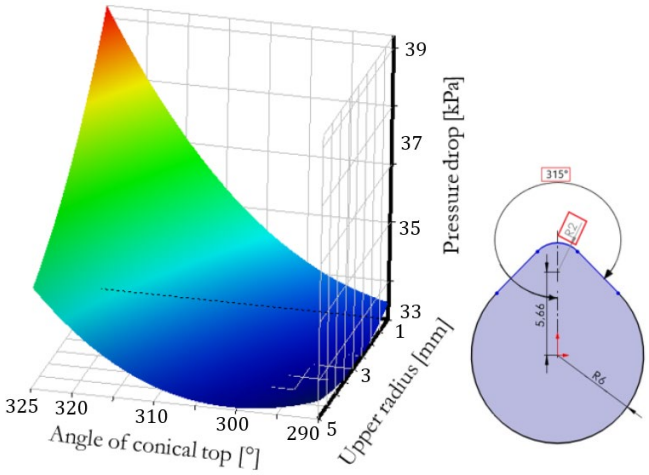

Figure 9: CS1 – Response surface of the parametric study combining angled conical top and upper radius and their effect on pressure drop.

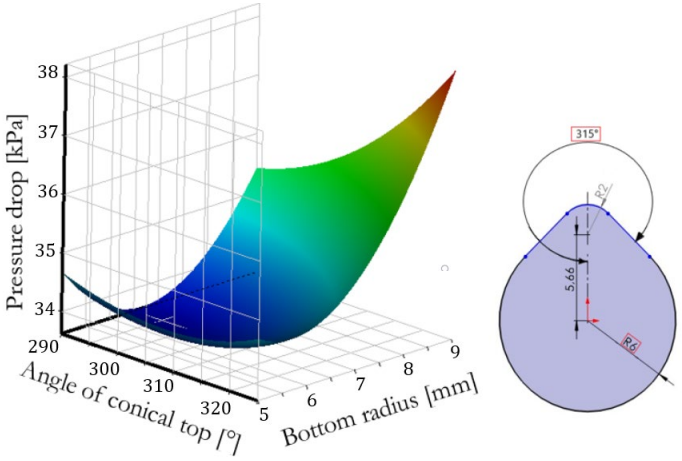

Figure 10: CS1 – Response surface of the parametric study combining angled conical top and bottom radius and their effect on pressure drop.

At the end of case study 1, we have effectively reduced the pressure drop from 39.41 kPa to 33.83 kPa and Turbulent kinetic energy dissipation. With these values, we have reached the local minimum in the response surface and thus the point that gives us the optimal shape of the geometry.

5.3 Case study 2

In this case the optimisation was not purely parametric, but changed the mesh while the CFD results were calculated. Interestingly, the shape obtained with the GA-method has an extremely optimised and almost organic shape. The resulting geometry is shown in green colour in Figure 11, while the transparent grey colour represents the non-optimised geometry.

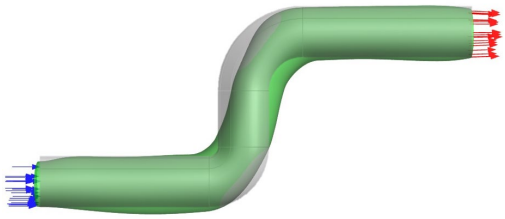

Figure 11: CS2 – Recommended geometry changes as the result of the GA study.

If we look at the velocity profiles of the optimised b) and the non-optimised a) velocity profiles in Figure 12, we can clearly see that the geometry optimisation has effectively reduced the velocity.

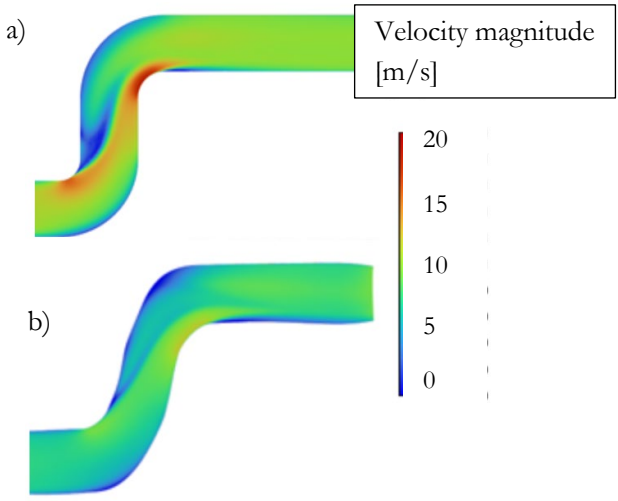

Figure 12: CS2 - Velocity longitudinal profiles comparison with a) non-optimized and b) optimized geometries.

This is mainly due to the increase in the overall circumference of the pipe and the bending of the vertical section to control the flow impact.

Turbulent kinetic energy dissipation that was obtained through this study has shown drastically lower values compared to original geometry. This is why we decided to show the results by themselves in the Figure 13. Maximum calculated value is 3 m^2/s^2. Small amount of recirculation can be spotted at such a smaller scale and the highest value is clearly depicted in red after the second bend where we were expecting some flow separation.

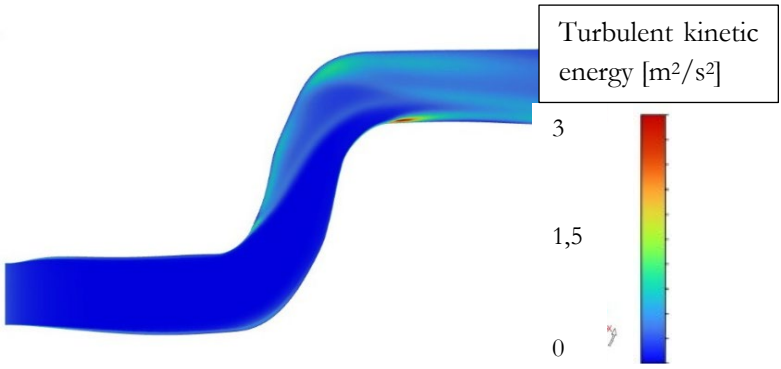

Figure 13: CS2 – Turbulent kinetic energy dissipation longitudinal profile of GA optimized geometry.

In case study 2, the pressure drop was reduced from 39.41 kPa to 30.32 kPa. If this study were to be run further, the result could be even better, but at the expense of extremely morphed mesh elements. It is also very interesting that in this study it was possible for different parts to have different shapes across the entire geometry. This can be seen at the beginning, where the channel must be self-supporting to fulfil the printability criteria, but not self-supporting in the vertical section, where this is not mandatory.

6 Discussion

In this article, we present two case studies in which we effectively improved the flow properties of the simple S-bend channel geometry. One study was parametric and one was performed using the gradient adjoint method. In both studies, we reduced

the pressure drop by about 25 % by changing the geometry of the pipe. In the second case study, we demonstrated the use of the Gradient Adjoint method, which reshapes the elements of the mesh after each design iteration to achieve a more efficient result by determining the critical parts of the geometry. This leads to an optimised shape of the geometry, but also to some shapes that are difficult to produce without the use of additive manufacturing.

All in all, this article shows the great potential that numerical optimisation has in industry. Sometimes optimisation should only be used to get an idea for further development, but in some cases these optimised designs could be used directly in a new and improved generation of fluid power components.

References

[1] Arena, M., Ambrogiani, P., Raiola, V., Bocchetto, F., Tirelli, T., & Castaldo, M. (2023). Design and qualification of an additively manufactured manifold for aircraft landing gears applications. *Aerospace, 10*(69), 1–18. https://doi.org/10.3390/aerospace10010069

[2] Biedermann, M. (2022). *Automated design of additive manufactured flow components* (Doctoral thesis, ETH Zurich). https://doi.org/10.3929/ethz-b-000587405

[3] Diegel, O., Nordin, A., & Motte, D. (2019). *A practical guide to design for additive manufacturing.* Springer Singapore. https://doi.org/10.1007/978-981-13-8282-6

[4] Hofmann, U., Fankhauser, M., Willen, S., Inniger, D., Klahn, C., Löffel, K., & Meboldt, M. (2023). Design of an additively manufactured hydraulic directional spool valve: An industrial case study. *Virtual and Physical Prototyping, 18*(1), 1–18. https://doi.org/10.1080/17452759.2023.2166634

[5] Matthiesen, G., Merget, D., Rückert, M., Schmitz, K., & Schleifenbaum, J. H. (2018). Additive manufacturing processes in fluid power – properties and opportunities demonstrated at a flow-optimized fitting. In *Proceedings of the International Conference on Hydraulics and Pneumatics – HERVEX* (pp. 1–6). ISSN 1454-8003

[6] Tappeiner, Z., Donners, M., Schmid, M., & Schmitz, K. (2014, October). Resource saving process route for integrated hydraulic components. *HyRess Project poster*, RWTH Aachen University. Retrieved July 30, 2025, from https://acam.rwth-campus.com/wp-content/uploads/sites/11/2014/10/HyRess-Resource-saving-Process-Route-for-Integrated-Hydraulic-Components.pdf

Strategic Integration of Hydraulic Accumulators: Best Practices

Tadej Tašner
HAWE Hidravlični sistemi d.o.o., Štore, Slovenia
t.tasner@hawe.si

Hydraulic accumulators are indispensable in fluid power systems, providing critical functions such as energy storage, pressure holding or stabilization, and load balancing. However, their effectiveness heavily depends on correct application and circuit integration. This paper explores the principles guiding the proper use of hydraulic accumulators, emphasizing selection criteria, sizing, pre-charge pressure considerations, and safety protocols. It presents strategies for incorporating accumulators into hydraulic circuits to achieve specific functional objectives–such as energy storage, load levelling, and response enhancement–while utilizing the accumulator volume as much as possible and avoiding common pitfalls like exceeding pressure ratio, fluid compatibility issues and lifetime limitations. Through analytical modelling and application-based case studies, the paper illustrates how thoughtful accumulator integration can elevate system efficiency, reliability, and longevity. The findings aim to equip engineers with practical guidelines to make accumulators not just an add-on, but a performance enhancing element within their designs.

DOI
https://doi.org/10.18690/um.fs.7.2025.5

ISBN
978-961-299-049-7

Keywords:
hydraulic accumulators, task, circuit integration, selection criteria, safety protocols, engineering guidelines

University of Maribor Press

1 Introduction

Hydraulic accumulators are indispensable components in modern fluid power systems, serving as energy storage devices that enhance system efficiency, stability, and responsiveness. Functionally analogous to electrical capacitors, accumulators store energy in the form of pressurized fluid, which can be released on demand to supplement pump flow, dampen pressure fluctuations, or provide emergency power in case of system failure [1]. Their integration into hydraulic circuits allows for improved dynamic performance, reduced energy consumption, and extended component lifespan, particularly in applications involving cyclic loads or transient pressure spikes.

The most prevalent type of accumulator in industrial and mobile applications is the gas-loaded or hydropneumatic accumulator, which utilizes a compressible gas—typically nitrogen—as a spring medium to exert pressure on the hydraulic fluid. The thermodynamic behavior of the gas, whether isothermal or adiabatic, significantly influences the accumulator's energy storage capacity and response characteristics [2]. Accurate modeling of this behavior is essential for optimizing accumulator performance, especially in high-frequency or high-pressure environments. Moreover, accumulators are increasingly being used in energy recovery systems, such as hydraulic hybrids and renewable energy platforms, where their ability to store and release energy efficiently plays a pivotal role in sustainable operation [3].

Given their multifaceted utility, hydraulic accumulators continue to evolve as critical elements in fluid-mechatronic systems. This paper presents hydraulic accumulators and verifies engineering practices for their use in the most common hydraulic applications. It outlines the fundamental operating principles of accumulator types such as bladder, piston, and diaphragm, and examines their roles in energy storage, pressure regulation, and shock absorption. Drawing from field-tested implementations and industry standards, the study highlights best practices for selection, sizing, and integration of accumulators into hydraulic circuits. Emphasis is placed on optimizing system reliability, improving energy efficiency, and extending component lifespan through proper accumulator usage. The findings serve as a practical reference for engineers and technicians seeking to enhance hydraulic system performance across mobile and industrial platforms.

2 Hydraulic accumulator types

Hydraulic accumulators are broadly categorized into two types based on their loading mechanism: mechanically loaded and gas loaded. Mechanically loaded accumulators use either springs or weights to exert pressure on the hydraulic fluid, while gas loaded accumulators rely on compressed gas — typically nitrogen — separated from the fluid by a bladder, diaphragm, or piston [1].

Spring-loaded accumulators operate by compressing a spring as fluid enters the chamber. This stored mechanical energy is released when the fluid is needed again. Their compact design and rapid response make them suitable for small-scale applications, but they suffer from a variable pressure output that depends on the spring's compression. Additionally, their limited stroke restricts fluid volume, making them unsuitable for high-pressure or large-volume systems. Weight-loaded accumulators, on the other hand, maintain constant pressure throughout the stroke by using a heavy mass to pressurize the fluid. While they offer excellent pressure stability and can handle large volumes, their size and weight make them impractical for mobile applications and require substantial structural support [1].

Table 1: Comparison of different accumulator types [1]

Group	Mechanically Loaded		Gas Loaded		
Type	**Weight**	**Spring**	**Bladder**	**Diaphragm**	**Piston**
Pressure	low	low	high	medium	high
Output Pressure	constant	linear	hyperbolic (isotherm) or steeper (polytropic/adiabatic)		
Friction Losses	yes	yes	no	no	yes
Energy Density	-	0	+	0	+
Storage Capacity	+	-	0	-	+
Placement	vertical	any	any	any	any
Response Time	slow	medium	fast	fast	medium

Gas loaded accumulators are more commonly used due to their versatility and efficiency. Bladder accumulators feature a flexible bladder that separates the gas from the fluid. They are lightweight, respond quickly, and are ideal for mobile hydraulic systems. However, they are limited to moderate pressure ranges and can degrade over time due to bladder fatigue or contamination. Diaphragm accumulators

use an elastomeric diaphragm to separate the gas and fluid. They are well-suited for high-pressure applications and offer a simple, low-maintenance design, though their fluid capacity is generally lower than bladder types. Piston accumulators, which use a solid piston to separate the gas and fluid, are robust and capable of handling both high pressures and large volumes. They maintain consistent pressure and are highly durable, but they require regular maintenance and are more expensive to manufacture and install [1].

3 Hydraulic vs. electric energy storage

According to a comparative study published in Energies, the specific energy of a bladder hydraulic accumulator was found to be 9.4 times lower than that of an ultracapacitor under equivalent conditions. While this highlights the limitations of hydraulic systems in compact energy storage, it also underscores their advantages in power density and cost-effectiveness, especially for high-force, short-duration tasks [4].

Table 2: Comparison of energy and power density of different energy storage systems [4]

	Energy			Power		
Energy Storage System	**Vol.** $\frac{\text{Wh}}{\text{m}^3}$	**Specific** $\frac{\text{Wh}}{\text{kg}}$	**Cost** $\frac{\text{US\$}}{\text{Wh}}$	**Vol.** $\frac{\text{kW}}{\text{m}^3}$	**Specific** $\frac{\text{kW}}{\text{kg}}$	**Cost** $\frac{\text{US\$}}{\text{kW}}$
$LiFePO_4$ Battery	**195144**	**115.2**	**0.45**	325.24	0.192	270.83
Ultracapacitor	2539.7	2.72	138.67	2588	2.21	217
Bladder Accumulator	1227	0.29	404.68	**7548**	**2.69**	**75**

4 Basic Accumulator Calculations

Brief accumulator calculations are also presented for user reference. Such calculations include calculation of precharge pressure and available volumes at different pressures for different use cases. The following variables will be used in calculations:

p_0 ... gas precharge pressure [bar]
p_1 ... min working pressure [bar]

p_2 ... max working pressure [bar]
V_0 ... effective gas volume (accumulator volume incl. gas bottles) [l]
V_1 ... gas volume at p_1 [l]
V_2 ... gas volume at p_2 [l]
T_0 ... gas precharge temperature (normally 20°C) [°C]
T_{min} ... min working temperature of the gas [°C]
T_{max} ... max working temperature of the gas [°C]
n_c ... polytropic index for charging accumulator [-]
n_d ... polytropic index for discharging accumulator [-]

4.1 Gas working temperatures

Estimating working gas temperatures is challenging. The minimum is usually the lowest ambient temperature, while the maximum falls between the highest ambient and fluid temperatures. Factors influencing the maximum include accumulator function, type, ambient and fluid temperatures, and fluid exchange volume. In accumulators where gas is mostly in contact with fresh fluid (such as bladder types), or in pump support roles with high fluid exchange and hot oil, fluid temperature has greater influence than ambient air.

Fluid temperature should be factored into shock absorption and pulsation dampening, but volume exchange remains minimal in these two applications. The maximum working gas temperature can therefore typically be estimated by averaging the highest fluid and ambient temperatures.

For energy storage applications in which pumps operate solely to charge the accumulator, the maximum anticipated ambient temperature may be used. This is because accumulators are filled with oil at ambient temperature, and the gas temperature remains nearly equivalent to the ambient temperature.

4.2 Precharge pressure

Typically, precharge pressure is set to about 90 % of the system's minimum operating pressure (for energy storage), striking a balance that allows fluid to enter the accumulator without compromising its ability to discharge when needed. Setting the precharge too high prevents fluid from entering the accumulator, while setting it too low risks bottoming out the gas chamber, reducing the accumulator's lifespan and effectiveness. Proper selection of precharge pressure is essential for maintaining

pressure stability and ensuring reliable hydraulic performance. Care must be taken, that the ratio between maximum pressure and precharge pressure doesn't exceed accumulators' compression ratio. Typical compression ratio for bladder accumulators is 4, while diaphragm accumulators can go up to 8.

Recommended precharge pressure:

- Energy storage and pump support: 90 % of minimum working pressure
- Shock adsorption: 60 % to90 % of average working pressure
- Pulsation damping: 60 % of average working pressure

Precharge pressure is always calculated for maximum working gas temperature (see previous chapter). If we take an example for energy storage, we can calculate precharge pressure at maximum temperature with (1) and then convert to precharge pressure at 20 °C with isochoric relation for ideal gas (2). [5]

$$p_{0@T_{max}} = 0{,}9 \cdot p_1 \tag{1}$$

$$p_0 = p_{0@T_{max}} \frac{T_0+273}{T_{max}+273} \tag{2}$$

4.3 Calculation of available fluid volume in accumulator

A key parameter in energy storage is the amount of hydraulic medium stored in the accumulator. This can be calculated by combining the general gas equations for polytropic compression (3) - charging and decompression (4) - discharging, resulting in equation (5) [6].

$$p_0 V_0^{n_c} = p_2 V_2^{n_c} \tag{3}$$

$$p_2 V_2^{n_d} = p_1 V_1^{n_d} \tag{4}$$

$$\Delta V = V_1 - V_2 = V_0 \cdot \left(\frac{p_0}{p_2}\right)^{\frac{1}{n_c}} \cdot \left(\left(\frac{p_2}{p_1}\right)^{\frac{1}{n_d}} - 1\right) \tag{5}$$

Polytropic index values reflect how heat transferred during compression/expansion [7]:

- isothermal (slow > 3 min, with full heat exchange) $n = 1$
- adiabatic (fast < 1 min, with no heat exchange) $n = \kappa = 1{,}4$ (for diatomic gases)
- polytropic (partial heat exchange) $1 < n < \kappa$

Examples of different processes:

- accumulation of energy (pump support): adiabatic charge and discharge
- emergency, safety functions: isothermal charge and adiabatic discharge
- leakage and volume compensation: isothermal charge and discharge

Some calculators add additional correction factor to the results [8].

4.4 Calculating required accumulator size for pulsation dampening

The use of accumulators as pulsation dampeners is particularly suitable for constant pressure systems, since their effectiveness diminishes below and does not perform optimally at pressures significantly above the operating pressure. Nevertheless, in hydraulic applications, the necessary volumes for effective pulsation dampening are relatively small (typically within the deciliter range). Consequently, it is possible to cover a broad pressure range by utilizing high compression ratio diaphragm accumulators, precharged to comparatively low precharge pressures.

To determine the required accumulator size for a piston pump, it is necessary to identify its operating pressure p and define maximum allowed pulsation α [%]. The fluctuating fluid volume produced by the pump, which the accumulator must absorb can be calculated out of the piston volume V_p [l] and the pump type coefficient K [-] [8]. Since the process is adiabatic, a value of 1,4 is used for n. If the recommended precharge pressure of 0,6 is applied for pulsation dampening, the equation can be further simplified to (6):

$$V_0 = \frac{K \cdot V_p}{\left(\frac{p_0}{p_1}\right)^{\frac{1}{n}} - \left(\frac{p_0}{p_2}\right)^{\frac{1}{n}}} = \frac{K \cdot V_p}{\left(\frac{p_0}{p \cdot (1-\alpha)}\right)^{\frac{1}{n}} - \left(\frac{p_0}{p \cdot (1+\alpha)}\right)^{\frac{1}{n}}} = \frac{K \cdot V_p}{\left(\frac{0{,}6}{(1-\alpha)}\right)^{\frac{1}{1{,}4}} - \left(\frac{0{,}6}{(1+\alpha)}\right)^{\frac{1}{1{,}4}}} \quad (6)$$

For pulsation dampening it is crucial that the accumulator is mounted close to the pump and that the flow is directed to the accumulator using a T-piece as shown in Figure 1, where use a special T-piece (shown on the left) is shown in the middle and use of a normal T-piece is shown on the right.

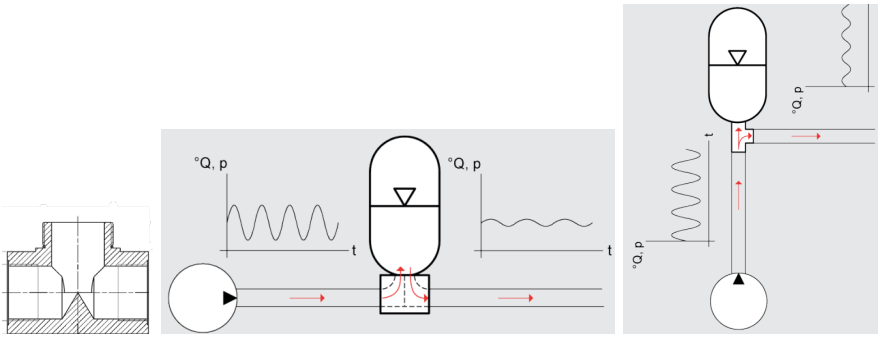

Figure 1: Mounting of accumulators for pulsation dampening
Source: [8], [9]

4.5 Calculating required accumulator size for shock adsorption

Shock adsorption is required when high flow in long pipelines is suddenly stopped, such as when a hydraulic valve closes quickly. The fluid's inertia creates a pressure surge that must be absorbed by converting its kinetic energy into gas (adiabatic compression). Therefore, the equation (7) applies [10]. In this case p_1 represents pressure in fluid line before closing a valve and p_2 is the maximum allowable line pressure during the shock

$$\frac{mv^2}{2} = -\int p\mathrm{d}V = -\frac{p_2V_2 - p_1V_1}{1-n}\,(\text{adiabatic compression}) \quad (7)$$

If we combine this with first isothermal compression from V_0p_0 to V_1p_1 and then adiabatic compression from V_1p_1 to V_2p_2 and solve for effective gas volume V_0 we get (8).

$$V_0 = \frac{m v^2 \cdot (1-n)}{2 \cdot p_0 \cdot 10^5 \cdot \left(\left(\frac{p_2}{p_1} \right)^{1-\frac{1}{n}} - 1 \right)} \tag{8}$$

Mass m [kg] of the fluid can be calculated out of fluid density ρ [$\frac{\text{kg}}{\text{m}^3}$], pipe length l [m] and pipe diameter d [mm]. Fluid velocity can be calculated out of flow Q [$\frac{\text{l}}{\text{min}}$] and pipe diameter. Considering non-SI conversions we get equation (9).

$$V_0 = \frac{\rho \cdot l \cdot Q^2 \cdot (1-n)}{1{,}8 \cdot 10^8 \cdot \pi \cdot d^2 \cdot p_0 \cdot \left(\left(\frac{p_2}{p_1} \right)^{1-\frac{1}{n}} - 1 \right)} \tag{9}$$

As with pulsation dampening, the required volumes for shock absorption in hydraulic systems typically fall within the deciliter range, making diaphragm accumulators particularly suitable for these applications. Conversely, in water supply systems and hydropower plants - where pipelines are extensive and diameters substantial - the accumulator stations needed for shock absorption generally require capacities in the range of 1000 liters.

4.6 Other Caveats when Choosing Hydraulic Accumulators

- **Hydraulic medium compatibility:** Accumulator elastomers (bladder/diaphragm/seals) and accumulator shell have to be compatible with the hydraulic medium.
- **Temperature compatibility:** Accumulator elastomers and shell have to withstand highest and lowest operating temperatures.
- **Max compression ratio:** must not be exceeded $\left(\frac{p_2}{p_0} \right)$
- **Certificate:** Correct certificate for destination country / place of installation has to be chosen:
  - PED – Europe
  - ASME – America
  - DNV, BV, … - ships
  - EAC – Russia
  - ML – China
  - …

- **Gas valve adapter:** Correct gas valve adapter for destination country has to be chosen.
- **Lifetime:** If pressure is in a certain range, it has "infinite" cycle life of 2M cycles, when outside of this range, cycle number could be as low as few thousand. This parameter has to be requested from the manufacturer and should be on the PED certificate of the accumulator.

5 Practical applications of hydraulic accumulators

Before digging into practical examples, we must be familiar with the correct protection of hydraulic accumulators, as outlined in **EN 14359**. This standard emphasizes the importance of integrating appropriate safety mechanisms (safety pressure relief valves, gas safety valves, and burst discs) to prevent overpressure, gas leakage, and structural failure. These protective measures must be tailored to the operating conditions of the hydraulic accumulator, ensuring compliance with the **Pressure Equipment Directive (PED) 2014/68/EU**. Once properly safeguarded, hydraulic accumulators can be confidently deployed across a wide range of applications [11].

5.1 Safe use of hydraulic accumulators

How to properly protect the hydraulic accumulators is described in EN 14359 with circuit examples in Annex C [11] and summarized in [12]. Hydraulic accumulators which will be used in Europe require a PED certificate when they meet specific criteria related to pressure and volume. The key threshold is when the product of pressure and volume exceeds 50 bar·liters, and when the accumulator volume is greater than 1 liter—both conditions apply to fluid group 2, which includes mineral oil and nitrogen. In rare cases, even piping on the gas side may fall under PED if it exceeds certain dimensions and pressure combinations (e.g., DN > 32 mm and P × DN > 1000 bar·mm). It is similar with ASME, but there is no minimum pressure limit defined.

When an accumulator falls under PED/ASME:

- It must be purchased with a valid PED/ASME certificate.
- It must be protected according to EN 14359, including:

- a manual isolation valve,
- a ball valve to drain back to tank,
- a dedicated PED/ASME certified safety pressure relief valve (not shared with the main system), and
- a non-isolatable pressure gauge for monitoring accumulator pressure.

For systems with multiple accumulators in parallel, shared protection components may be used, provided the configuration still meets PED/ASME safety requirements.

Certified safety pressure relief valve must be correctly dimensioned, to ensure safe operation. It has to handle entire flow that could be causing the pressure rise (typically flow of all the pumps connected to the accumulator; attention has to be paid to external forces acting on cylinders/hydromotors as well), so that maximum allowable pressure of the accumulator is not exceeded by more than 10 % taking back pressure in the tank line into account.

When an accumulator doesn't fall under PED or ASME, sound engineering practices must be used to protect it, therefore following EN 14359 is always recommended at least with pressure gauge and non-certified pressure relief valve.

5.2 Practical Examples of Safety Equipment Configuration

This chapter outlines typical protection methods following EN 14359, detailed in annex C [11]. The most common is a safety block (Figure 2), which combines an isolation valve, discharge valve, and safety pressure relief valve, with ports for the hydraulic system, accumulator, tank, and pressure gauge. Use of individual components is also permitted. The pressure gauge must connect directly to the accumulator (without isolation device) or via quick coupling; otherwise, a gauge check port should be included to ensure proper function. A check valve on the pump side is advised to guard against pressure release towards the pump (during pump maintenance or when changing the pressure filter).

When using multiple accumulators each individual accumulator can have its own safety block. But there is an exception that allows using only one safety pressure relief valve for all accumulators (Figure 3), while still allowing individual isolation

and discharge of each accumulator, easing maintenance on the system. Care must be taken that fully charged accumulators don't remain isolated for too long, as ambient temperature rise may increase gas pressure, exceeding max pressure of the accumulator. This can be avoided using burst discs on the gas side.

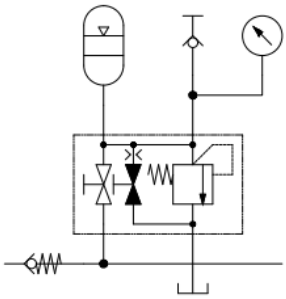

Figure 2: Protecting single accumulator using accumulator safety block
Source: [own work]

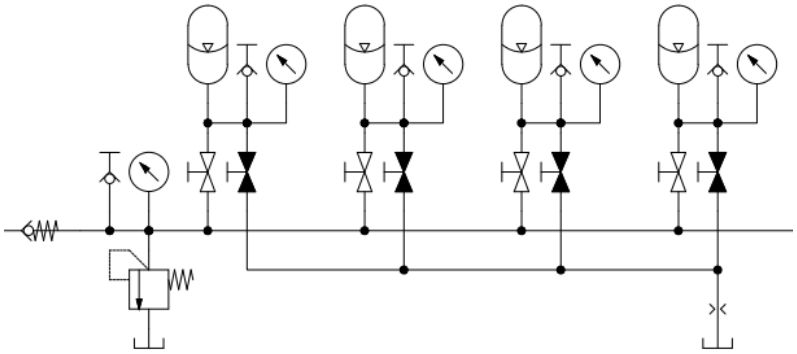

Figure 3: Protecting multiple accumulators using individual components [own work]
Source: [own work]

5.3 Practical example of using hydraulic accumulators for safe operation of a Pelton hydraulic power plant

The Pelton turbine (Figure 4) typically features three primary actuators requiring control: a jet deflector, which redirects the jet away from the turbine; a main inlet or shut-off valve, utilized to halt water flow through the turbine; and needle adjustment cylinders, designed to accurately regulate the flow through each individual nozzles [13].

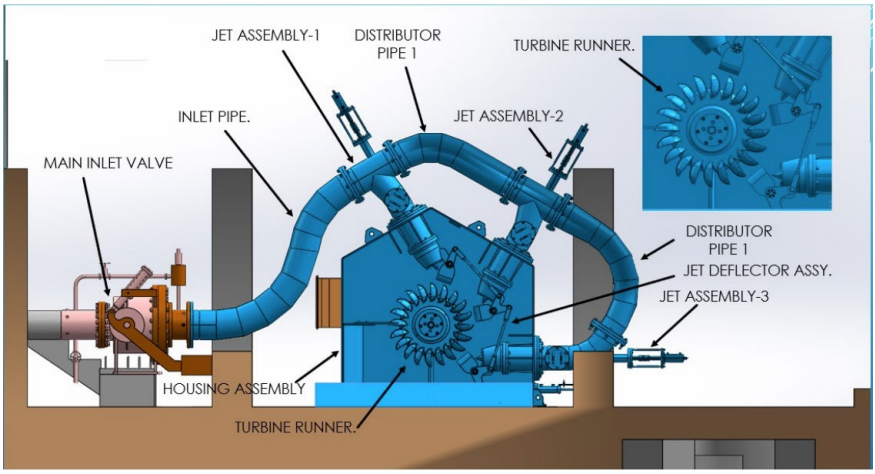

Figure 4: Pelton turbine with three nozzles
Source: [13]

During power plant operation, the hydraulic unit is responsible for adjusting the nozzle needles and jet deflector to ensure the generator output matches grid power demand. The hydraulic power unit (HPU) supplies actuators via the accumulator; when accumulator pressure decreases, the hydraulic pump replenishes it. It is essential to ensure that the pump does not start excessively frequently and that the accumulator is refilled within an appropriate period.

In emergency situations, such as when the hydraulic pump fails to start as anticipated, the generator should be shut down promptly. The jet deflector must retract to redirect the jets away from the turbine, and all nozzles need to be closed. Therefore, sufficient pressurized fluid should be stored in the accumulator to stop the turbine safely. The cylinder sizes, closing times and minimum required pressures are different for different turbine sizes.

Accumulator design steps:

- Calculate cylinder volumes and emergency directions.
- Calculate volumes needed for normal operation and emergency.
- Adjust accumulator volume, emergency, pump turn on, and pump turn off pressures while iterating equation (5) which calculates available fluid volume in

normal operation (Figure 5) and emergency operation (Figure 6) and compare it to available volume in accumulator.

– Define required pump size and motor power based on charging time of the hydraulic accumulator.

		system pressure when pump turns off		psys=	230 bar
		system pressure when pump turns on		pmin=	120 bar
cylinder	qty	larger side of cylinder volume		number of strokes	needed volume
Jet deflector	1	0,16 l		1,5	0,24 l
Shut-off valve	1	0,53 l		0	0,00 l
Needle adjustment 1	1	0,31 l		1	0,31 l
Needle adjustment 2	1	0,31 l		1	0,31 l
SUM	4	1,32 l			0,86 l
accumulator	qty	rated volume	precharge pressure	worst case total working volume max	min
main accumulator	1	10,0 l	45 bar	1,28 l	1,13 l
SUM	1	10,0 l		1,28 l	1,13 l
pump		flow rate		accumulator charge time max	min
pump flow rate		10,9 l/min		7 s	6 s

Figure 5: HPU Calculation – Normal Operation Evaluation

Source: [own work].

		system pressure when emergency stop procedure starts		p_{em}=	110 bar
		system pressure when emergency stop procedure ends		p_{emmin}=	50 bar
cylinder	qty	direction	full stroke emergency volume	safety factor / sicherheitsfactor	needed volume
Jet deflector	1	Retraction	0,11 l	1,5	0,16 l
Shut-off valve	1	Gravity	0,00 l	0	0,00 l
Needle adjustment 1	1	Extension	0,31 l	1,5	0,47 l
Needle adjustment 2	1	Extension	0,31 l	1,5	0,47 l
SUM	4		0,74 l		1,10 l
accumulator	qty	rated volume	precharge pressure		WC total avail. volume
main accumulator	1	10,0 l	45 bar		2,75 l
SUM	1	10,0 l			2,75 l

Figure 6: HPU Calculation – Emergency Stop Evaluation

Source: [own work]

Each HPU is tested after assembly where volumes are measured. Comparison of results is presented in Table 3. Please note that the calculations shown above are for minimum ambient temperature (0 °C), but they were made also for 20 °C making them comparable to measurements which were made at ca. 20 °C.

Table 3: Comparison of different accumulator types

	Calculation 0°C	Calculation 20°C	Measurement ~20°C
Recharge Time $(p_{min} \rightarrow p_{max})$	7 s	8 s	11 s
Available Volume $(p_{max} \rightarrow p_{min})$	1.13 l	1.28 l	1.37 l
Available Volume $(p_{em} \rightarrow p_{emmin})$	2.75 l	3.11 l	3.22 l

The HPU was already commissioned in Guyana at a 0,8 MW power plant (water flow 200 l/s with 207 m head; 488 mm turbine runner diameter).

6 Conclusion

Hydraulic accumulators become safe dynamic enhancers of system performance, when strategically integrated. This paper has outlined the critical parameters—selection, sizing, and safety measures—that govern their effective use. By applying thermodynamic principles and engineering calculations, designers can tailor accumulator configurations to meet specific functional goals such as energy storage, pulsation dampening, and shock absorption. Moreover, adherence to safety standards like EN 14359 and PED ensure not only regulatory compliance but also operational reliability. Through practical examples, including the Pelton turbine application, it becomes evident that accumulators are not merely auxiliary devices but essential contributors to system resilience and efficiency.

Engineers who embrace these best practices will unlock the full potential of hydraulic accumulators, driving reliability across fluid power systems.

References

[1] Costa, G. K., & Sepehri, N. (2023). Hydraulic accumulators in energy efficient circuits. *Frontiers in Mechanical Engineering, 9*, Article 1163293. https://www.frontiersin.org/articles/10.3389/fmech.2023.1163293/full

[2] Dindorf, R., Takosoglu, J., & Wos, P. (2023). Review of hydro-pneumatic accumulator models for the study of the energy efficiency of hydraulic systems. *Energies, 16*(18), 6472. https://www.mdpi.com/1996-1073/16/18/6472

[3] Zhu, Jianxin & Shen, Chao & He, Qinghua & Li, Saibai & Dai, Peng & Li, Xiang. (2024). Boom Potential Energy Regeneration Method for Hybrid Hydraulic Excavators. IEEE Access. http://dx.doi.org/10.1109/ACCESS.2024.3386741.

[4] Leon-Quiroga, J., Newell, B., Krishnamurthy, M., Gonzalez-Mancera, A., & Garcia-Bravo, J. (2020). Energy efficiency comparison of hydraulic accumulators and ultracapacitors. *Energies*, 13(7), 1632. MDPI Journal

[5] HYDAC. (2001). Bladder accumulators. https://rodavigo.net/datos/articulos/130/vejiga-para-acumulador-235290-hydac-(1).pdf

[6] Majdič, F. (2021). Matematični model za hidravlične akumulatorje. *Ventil*, 27(4), 246–250. https://revija-ventil.si/wp-content/uploads/2021.11-majdic.pdf

[7] Majdič, F. (2021). Hidravlični akumulatorji: Dodatni vir hidravlične tlačne energije v hidravličnih sistemih z neenakomerno porabo. *Ventil*, 27(3), 192–196. https://revija-ventil.si/wp-content/uploads/2021.08_majdic.pdf

[8] EPE Italiana. (2019). Catalogo generale EPE 2019. https://www.epeitaliana.it/wp-content/uploads/2020/06/Catalogo-Generale-EPE-2019.pdf

[9] HYDAC. (2021). *Hydraulic dampers and accumulator applications* https://www.hidro-norm.com.tr/panel/Sayfalar/urunler/prd-doc-pro-3701-00001-sen-ain-v17-625.pdf

[10] LibreTexts PHYSICS. (n.d.). 3.7: Adiabatic processes for an ideal gas. *University Physics II – Thermodynamics, Electricity, and Magnetism (OpenStax).* https://phys.libretexts.org/Bookshelves/University_Physics/University_Physics_(OpenStax)/University_Physics_II_-Thermodynamics_Electricity_and_Magnetism(OpenStax)/03%3A_The_First_Law_of_Thermodynamics/3.07%3A_Adiabatic_Processes_for_an_Ideal_Gas

[11] European Committee for Standardization. (2017). EN 14359:2017 – Gas-loaded accumulators for fluid power applications.

[12] Tašner, T. (2022). Legal requirements of hydraulic power units. *International Conference Fluid Power 2023*. https://press.um.si/index.php/ump/catalog/view/811/1155/3408

[13] Biswas, C., & Pandey, P. (2023). Pelton turbine runner material selection through FEM structural analysis. *International Research Journal of Modernization in Engineering, Technology and Science,* 5(9). https://www.irjmets.com/uploadedfiles/paper//issue_9_september_2023/44892/final/fin_irjmets1695813897.pdf

[14] Gugler GmbH. (n.d.). Worldwide references. *Gugler Water Turbines.* https://www.gugler.com/worldwide-references/

Elika, Variable Flow With Fixed Displacement Helical Pump

Danilo Persici, Andrea Rimondi

Marzocchi Pompe S.p.A., Zola Predosa, Italy
danilo.persici@marzocchipompe.com, andrea.rimondi@marzocchipompe.com

Electrification and hybridization have reduced engine noise in industrial vehicles, making hydraulic circuit noise the dominant source. Variable displacement pumps can lower noise but often at the cost of efficiency. The Elika gear pump, developed with the University of Bologna, uses patented helical gear technology to deliver low noise and high efficiency across a wide speed range, particularly when paired with Variable Frequency Drive brushless motors. Recent Marzocchi R&D tests showed it can deliver flows from 1 l/min to 20 l/min with the same displacement, maintaining over 90 % volumetric efficiency. These characteristics enable variable flow from a fixed displacement pump, offering a cost-effective, energy-efficient alternative to variable displacement designs, especially for electrified powertrains where noise reduction and efficiency are critical.

DOI
https://doi.org/10.18690/um.fs.7.2025.6

ISBN
978-961-299-049-7

Keywords:
gear pump,
helical rotors,
Elika,
low noise,
Variable Frequency Drive

University of Maribor Press

1 Introduction

Standard external gear pumps provide high flows with high pressure and more over they can be small, lightweight and highly customizable. Their main issue is as the pressure and the speed rise then their noise becomes intrusive. Many new and modern applications are in high demand for low noise solutions; the main technical solutions developed over the years to reduce the noise of gear pumps are summarized below.

2 Development of external gear pumps

2.1 Standard external gear pump

It's well known that the major sources of noise of a gear pump are due to two different factors: a mechanical one, generated by the transmission of motion between the gear wheels, and the hydraulic one due to the volume of oil entrapped in the area in which the gears meshing (red area on Figure 1).

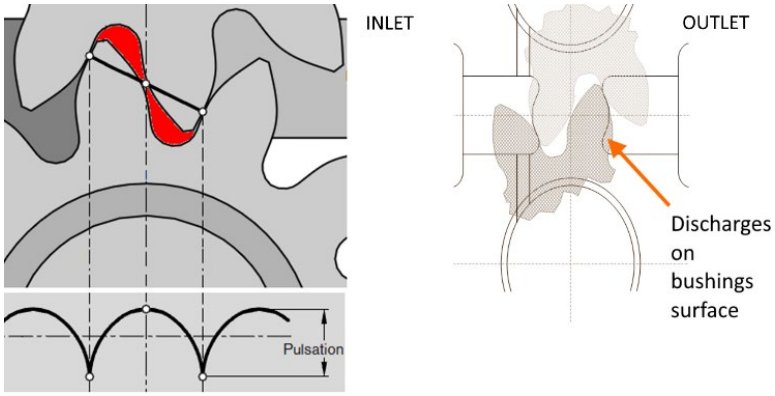

Figure 1: Standard external gear pump.

The encapsulation of this volume of oil generates high pressure pulsations and noise. The frequency of this phenomenon depends not only on the entity of the trapped volume, but also on the number of teeth of the wheels and their rotation speed; consequently, if the speed working range are wide, the frequencies with which these phenomena arise can be high, and noise generated can reach particularly annoying frequencies (>3000 Hz). In the standard external gear pumps, Figure 1, in order to

reduce noise and pulsations, the optimization of gears and discharges on bushings surfaces gives only limited benefits.

2.2 Dual flank external gear pump

In order to reduce the volume trapped between the gear wheels, a technical solution is to use "double flank" profiles, Figure 2. Using this solution, thanks to the reduction of the trapped volume (red area on Figure 2), a considerable reduction of the pressure pulsation up to 75 %, and noise are reduced of about 3 dBA.

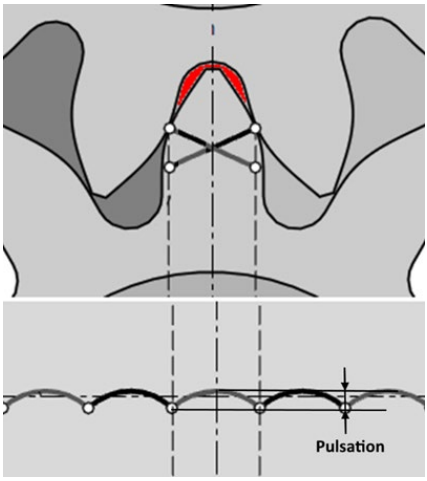

Figure 2: Dual flank external gear pump.

However, the double contact transmission has the effect of doubling the fundamental frequency of gear meshing, consequently the frequency spectrum of the emitted noise shifts towards higher, and consequently, more annoying frequencies.

2.3 Gear pump with helical gears

The mechanical noise of meshing of the gear wheels can be reduced using helical gears, Figure 3. Using this technical solution is a partial improvement, as it does not solve the problem related to the volume of oil trapped between the gear wheels. The helix angle used in any case is low to avoid oil seepage from the helical shaft in the meshing position; consequently, in order to limit the helix angle, these pumps often

have to have a large number of teeth. This factor significantly limits the specific displacement of helical pumps, making them bulkier than the corresponding straight tooth pumps. Using this solution, a considerable reduction of the pressure pulsation up to 75 %, and noise are reduced by about 2 dBA to 10 dBA.

Figure 3: Gear pump with helical gears.

2.4 Gear pump with conjugated helical gears

This solution is able to eliminate both the hydraulic noise caused by the volume of oil that remains trapped between the wheels, which in this case is practically zero, and the noise typical of straight tooth transmissions. The absence of the trapped volume also removes any constraint on the helix angles, as the fluid can no longer seep between the gear wheels in the meshing area, Figure 4.

This technical solution, having eliminated the two main sources of noise (mechanical and hydraulic), is able to reduce the pressure pulsation up to 80 %, and the pump noise up to 15 dBA.

The idea of reducing the pump noise through elimination of the encapsulated volume, thanks to a special shape of tooth profile is not new. The idea was born precisely in the mobile market. His first documented application dates back to the power steering inventor Francis W. Davis. The inventor studied and applied, for the

first time, a gear pump without encapsulation in order to reduce the noise in hydraulic power steering Figure 5.

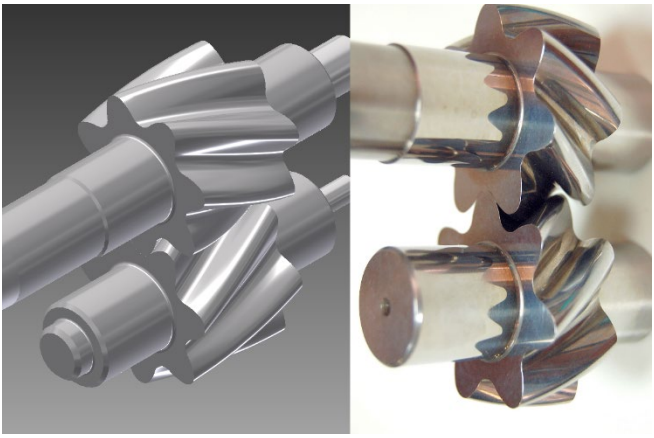

Figure 4: Gear pump with conjugated helical gears.

Figure 5: Drawings of the Pat. US2261143 – Gears - 18/08/1939 – Francis W. Davis.

A pump using a special tooth profile design was installed with success on the Pierce-Arrow in 1928 and moved to a Buick in 1932. In the original power steering the working pressures reached 70 to 100 bar, and the maximum rotation speed was about 1800 rpm. Despite the difficulty of manufacturing these special toothed wheels, in the following years, Francis W. Davis continued to study low noise hydraulic power steering and economic methods to produce non-encapsulated tooth profiles, collaborating with the major American automotive companies, and filing numerous patents. Unfortunately, in 1934 the Great Depression forced the inventor to suspend his research because of the high production costs. Later, the advent of Second World War moved the inventor attention towards military applications where low noise and comfort were not a priority. The interesting story of this American inventor is described in the book "The unreasonable American" published

in 1968 by the academy of Applied Science. The profiles of the toothed wheels described in the patents were conceptually very simple, essentially composed of circular and involute arcs and obtained with shaped tools (Pat.US.US2261143, US2206079). The degree of accuracy obtained once, was just sufficient for applications at low to medium speeds and pressures.

Now, after more than 90 years, Marzocchi Pompe intends to bring again this technology in high pressure and mobile applications. The development of tooth grinding technology makes possible the economical production of high precision toothed wheels.

Analyzing the pump features globally, this is the pump that is able to allow the best performance in terms of pulsation noise and performance Table 1, making it competitive also with respect to internal gear pumps.

Table 1: Pump features

Features:	EXTENAL GEAR PUMP	DUAL FLANK GEAR PUMP	HELICAL GEARS not conjugated PUMP	HELICAL GEARS Conjugated PUMP
NOISE	☹	☹	☻ ☻	☺ ☺ ☺ ☺
PULSATIONS	☹	☹	☻ ☻	☺ ☺ ☺ ☺
EFFICIENCY	☺ ☺ ☺	☻ ☻	☻ ☻	☺ ☺ ☺ ☺
Contamination RESISTENCE	☺ ☺ ☺	☻ ☻	☻ ☻	☻ ☻
SIMPLICITY constructive	☺ ☺ ☺ ☺	☻ ☻	☺ ☺ ☺	☻ ☻
COST	☺ ☺ ☺ ☺	☺ ☺ ☺	☺ ☺ ☺	☻ ☻

3 The Elika Pump

It is well known that the major source of noise of a gear pump is due to pressure pulsations and that the main source of this phenomenon is the area in which the gears mesh. Here the pressure pulsations originate from the encapsulated oil between the teeth of the pump's gears. In that small vein, symbolized by the red zone in Figure 1, the oil gets trapped, compressed and then makes noise at every engagement of the gear. Elika Pump was conceived and designed to be a low noise and low pulsation pump.

The heart of the Elika Pump is the particular patented shape of the tooth profile without encapsulation, which reduces considerably the pressure oscillations and vibrations produced by the pump, producing many advantages on the final application (Pat. EP2352921).

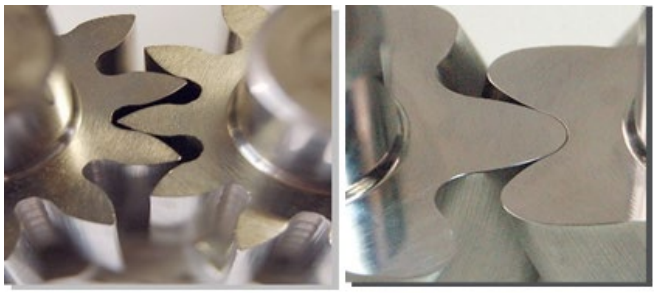

Figure 6: Left - traditional tooth profile (conventional external gear pump); right - Elika tooth profile (helical shape) with not trapping zone.

As can be seen from Figure 6, there is no space for the oil to get trapped between the teeth of the gear as the helically shaped teeth are completely matching each other. This helps to get rid of much of the hydro-mechanical noise coming from that encapsulation. The helical gear also has a lower number of teeth. The helical toothing ensures the continuity of motion despite the low number of teeth. The low number of teeth greatly reduces the fundamental frequencies of the pump noise and makes the sound particularly pleasant.

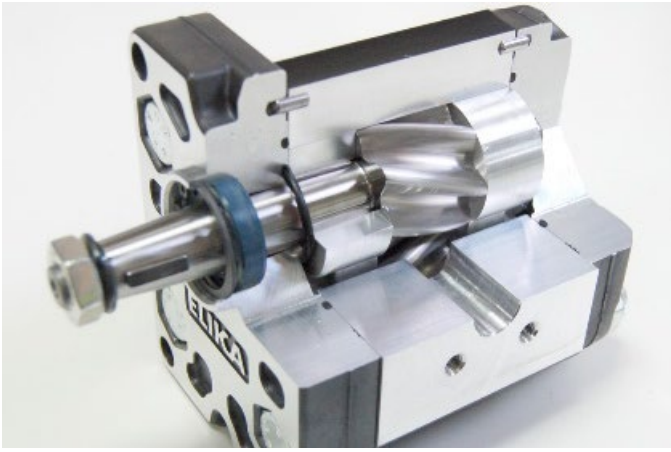

Figure 7: Elika Pump sectioned.

Elika is Marzocchi Pompe's response for all those applications that require low noise levels. It was designed to be completely interchangeable with a conventional Gear Pump. This pump reduces the noise emission up to 15 dBA compared to a conventional external gear pump. The maximum operating pressures are similar to those of the series Marzocchi GHP Series Pump (Cast-Iron Flange and cover Pumps) and reach up to 300 bar. From the outside Elika looks very similar to a standard Gear Pump. The difference is inside, Figure 7.

To ensure the correct continuity of motion with this special tooth profile without encapsulation, it was necessary to generate a helical toothing. Each pump has a gear with a right helix and another with left helix. The use of helical gears generates axial forces of magnitude proportional to the working pressure, which must always be balanced. The resulting of axial force is due to two different type of components: transmission components, due to the transmission of motion between the driving gear and the driven gear, that are opposite; pressure components due to the axial reaction of the pressure on the surface of the gear wheels on in the pump outlet area, that are in the same direction. The resultant forces of the axial thrusts induced by helical teeth are always hydraulically balanced in an optimal way, in every operating condition, by the axial compensation system integrated in the pump cover, Figure 8. The problem of axial thrust generated in pumps with helical gears was already studied in 1972 by Yasuo Kita (US3658452).

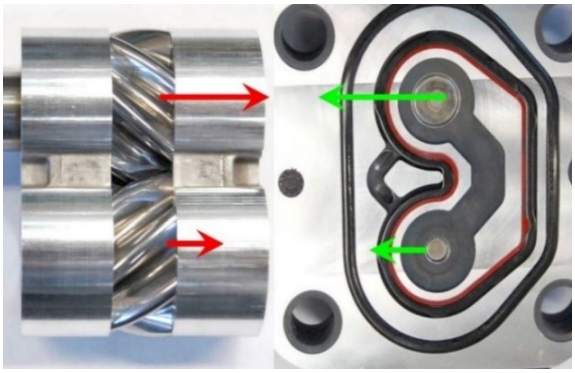

Figure 8: Hydraulic compensation system.

On the driving shaft, the components of the axial and hydraulic forces are concordant, on the driven shaft instead they are discordant, consequently the resulting forces are different, but both are directed towards the cover (red arrows).

The components are hydraulically balanced through compensating cylinders (green arrows).

Today the Elika pump is available in 5 groups: Elika1P, ElikaK1P, Elika2, Elika3, Elika4. These groups range from 2.1 cm^3/rev all the way to 200 cm^3/rev. Elika is also available as multiple stack pumps. Elika's versatility and low-noise, low-ripple and high efficiency characteristics project this pump into many different end applications. Powerpacks and mini powerpacks, material handling machines, automotive, agricultural machines, municipality etc. In addition to the particular low-noise, there are other characteristics of this pump to be discovered. Due to the peculiar design, Elika pumps are capable of maintaining high overall efficiency over a high range of speeds. The high range on speeds translate into a high range of flows. The pump Type ELI1P-D-3.7-G (displacement 3.72 cm^3/rev), tested in Marzocchi R&D lab, allowed to deliver flow from 1 l/min to 20 l/min using the same displacement and maintaining high volumetric efficiency (>90 %) throughout.

4 Developing a new application

This feature, coupled with the ever-increasing diffusion of VFD brushless motors, leads to the possibility of obtaining a variable flow from a fixed displacement pump. This pump is particularly suited for electric vehicles (thanks to its high overall efficiency) where energy saving is a main driver. In these applications, it is required that even in the phases in which the vehicles operate only in electric mode, the hydraulic applications such as the steering that must remain in operation, must not be audible. This feature is particularly important in public transport to ensure maximum interior comfort.

Its features make this product very useful against variable displacement pumps. Marzocchi Pompe R&D Department has tested the following Elika Pump and Brushless Motor (Figure 9 Description of test circuit, Figure 10 Pump on test).

Marzocchi started testing the pump and then the pump and motor together. Starting from 250 rpm, the pump maintains a volumetric efficiency of more than 90 %. The Figure 11 graph shows that the pump could go all the way up to 5,000 rpm and achieve very high efficiency. The conclusion is that Elika's volumetric efficiency is almost independent of pressure.

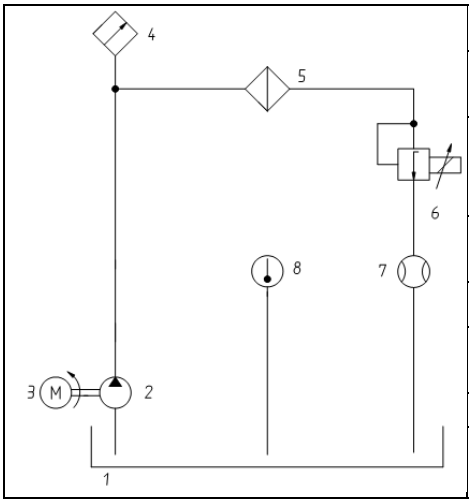

1-Oil Tank, 80 l ISO VG 46
2-Elika ELI1P-D-3.7-G Pump; displacement 3.72 cm^3/rev
3-BLDC Motor; 4 kW max. power; voltage 24V DC; Max current 160A; Max speed 5000 rpm.
4-Pressure transducer Druck PTX 611 (max 400 bar)
5-High pressure filter 12 μm
6- Proportional valve Vickers KACG 3 L350D (max 350 bar)
7- Flowmeter VSE type VS 04 (max 40 l/min)
8-Thermocouple PT100

Figure 9: Test circuit.

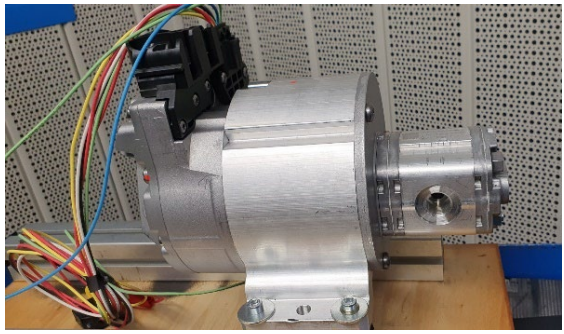

Figure 10: Motor – Pump on test.

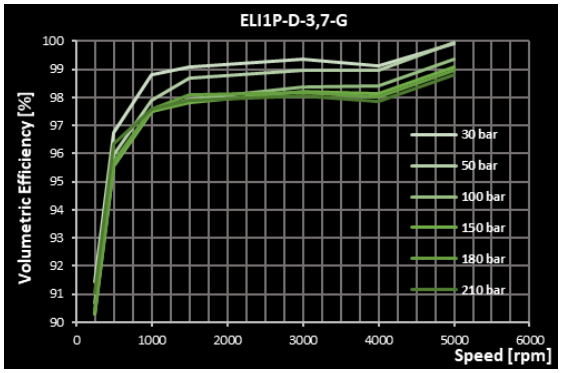

Figure 11: ELI1P volumetric efficiency vs. speed.

Starting from 50 bar, the pump maintains mechanical efficiency in excess of 80 %. At higher pressures, the mechanical efficiency is almost independent of speed (Figure 12).

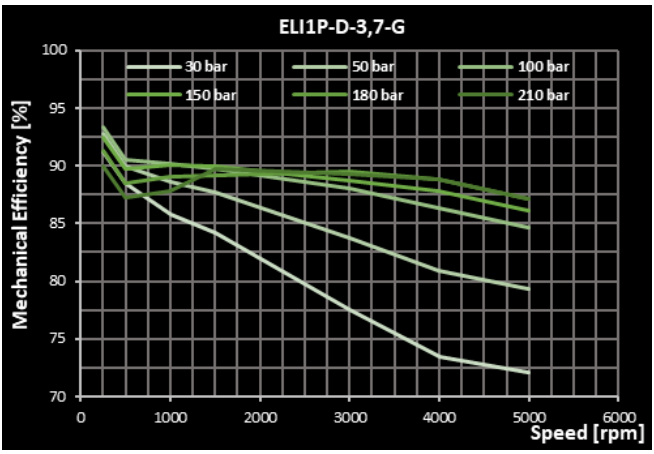

Figure 12: ELI1P mechanical efficiency vs. speed.

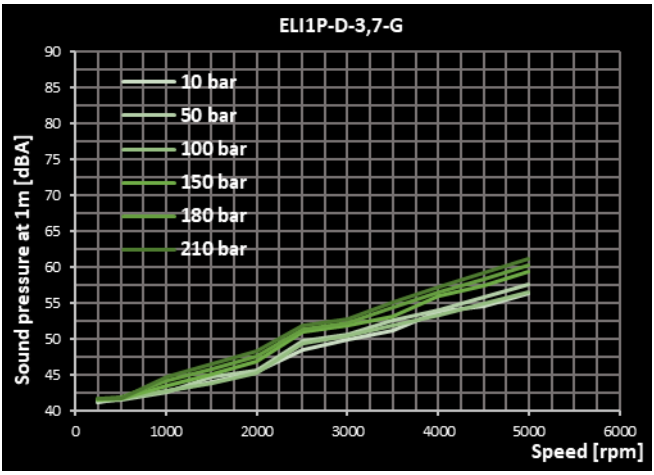

Figure 13: Elika ELI1P-D-3.7 pump sound pressure in dBA vs. speed.

The following two charts (Figure13 and Figure 14) show the noise comparison data between the Elika Pump and its corresponding, same displacement, Standard Gear Marzocchi Pump that has straight teeth and comes from the 1P Family of pumps (Figures 13 to 15). The noise tests were performed in a soundproofed chamber, with

a background noise lower than 32 dBA, according to ISO 4412 standards, with a integrating sound level meter Type Delta Ohm HD 2110 L.

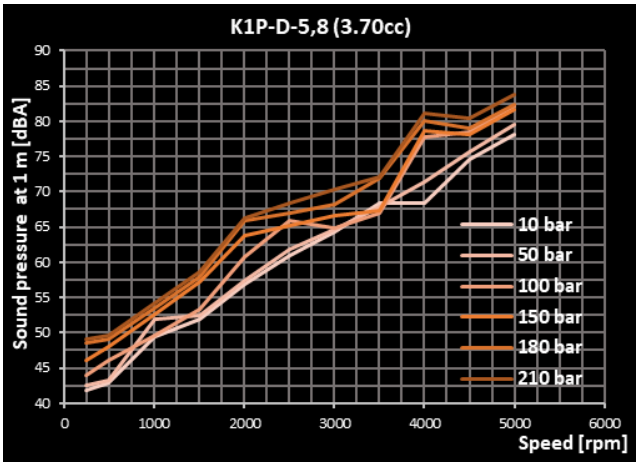

Figure 14: Standard straight teeth gear pump K1P-D-5.8 sound pressure in dBA vs. rpm.

At 5,000 rpm and at the highest pressure Elika Pump hardly reaches 62.5 dBA, on the other side the conventional Pump, K1P, reaches the mentioned peak at 2,000 rpm and 150 bar. Elika low-noise advantage on conventional straight gears pumps is even more evident in the following graphic showing their average data comparison.

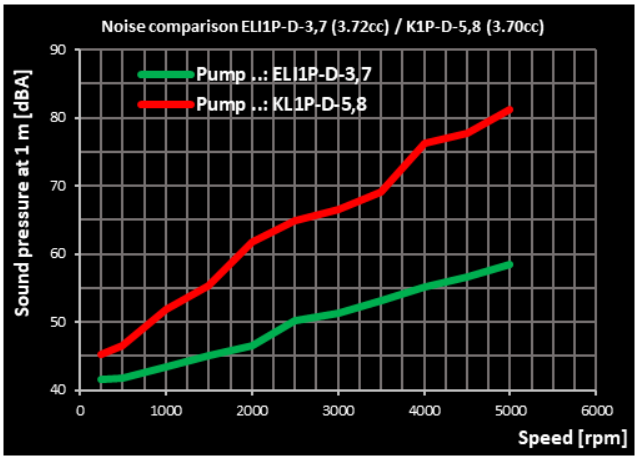

Figure 15: Average noise comparison between ELI1P (green) and K1P (red).

Elika is not only quieter but also the noise increases less steep. One particular aspect of the noise of this pump is its frequency. Looking at the graph in Figure 16 the Elika Pump in green shows the frequency spectrum shifted toward the lower frequencies. The lower frequency spectrum means that the noise is more pleasant. Standard gear pump has a pitch on high frequency which is, on the other hand, particularly unpleasant.

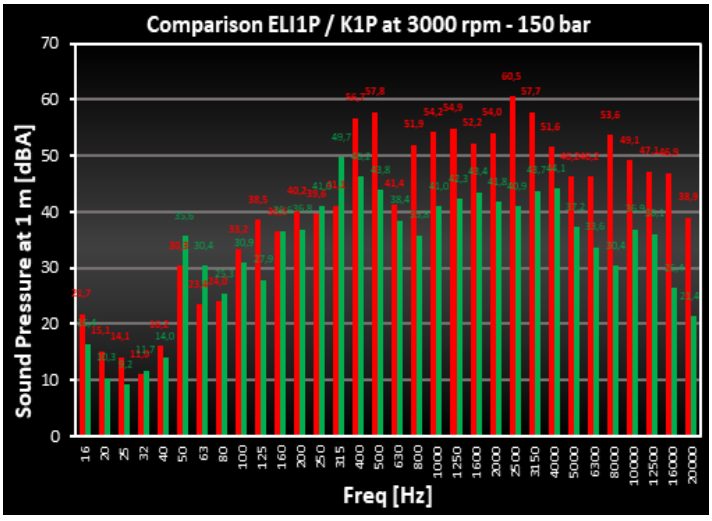

Figure 16: Noise spectrum comparison ELI1P (green) / K1P (red) at 3000 rpm and 150 bar.

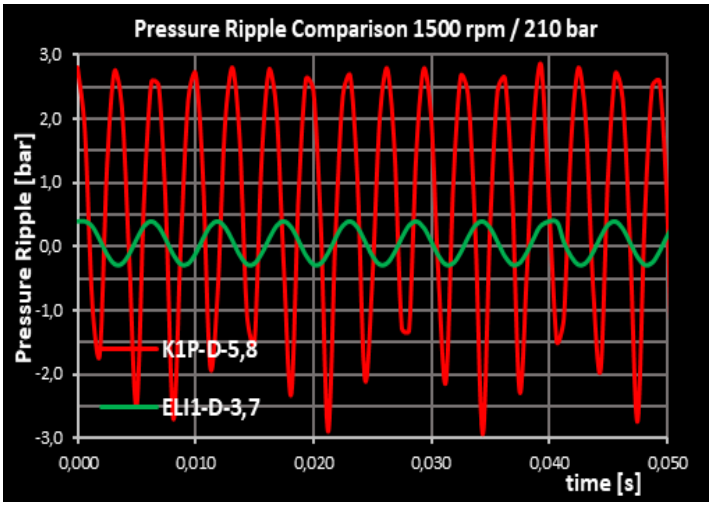

Figure 17: Pressure ripple comparison ELI1P (green) / K1P (red) at 1,500 rpm / 210 bar.

Looking at the chart in Figure 17, the Elika Pump has lower amplitude of the pressure ripple but also a lower frequency.

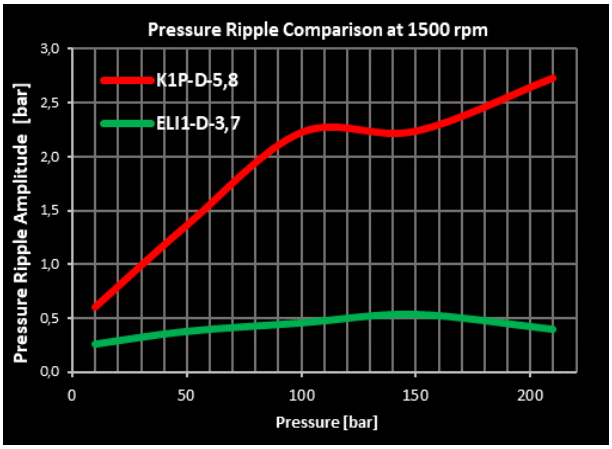

Figure 18: Comparison ELI1P (green) / K1P (red), pressure ripple comparison at 1,500 rpm.

The green line in Figure 18 shows us the summary of all the testing on the Elika range of pressures. The ripple, as the pressure increases, becomes a lot different between the two pumps showing its great distance from the standard pump and its red line. The Elika Pump is consistently lower than 0.5 bar.

5 Pump and motor combination

The chart on Figure 19 shows the relation between flow and current of the motor-pump combination at different pressures. It is clear how the relation is close to linear.

Figure 20 shows the combined Overall efficiency ηovr of the motor + pump calculated as:

$$\eta_{ovr} = \frac{\text{Hydraulic Power}}{\text{Electrical power}} \quad (1)$$

By looking at the graph in Figure 20, the efficiencies stay in the range of 60 % to 70 %.

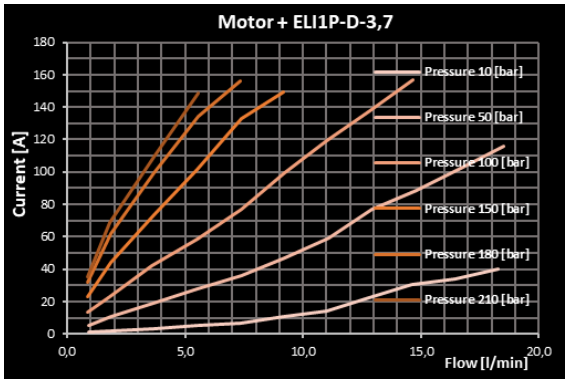

Figure 19: Relation between flow and current of the motor-pump.

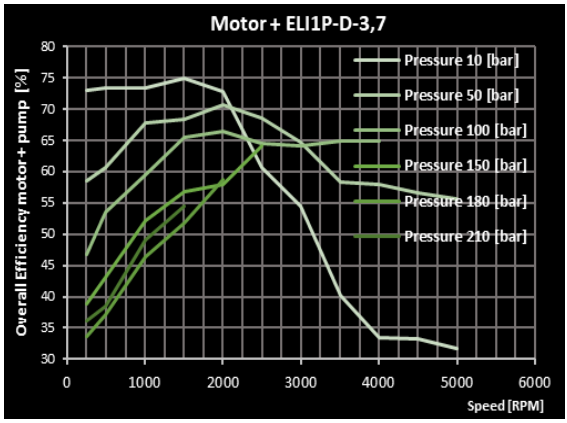

Figure 20: Overall motor-pump efficiency.

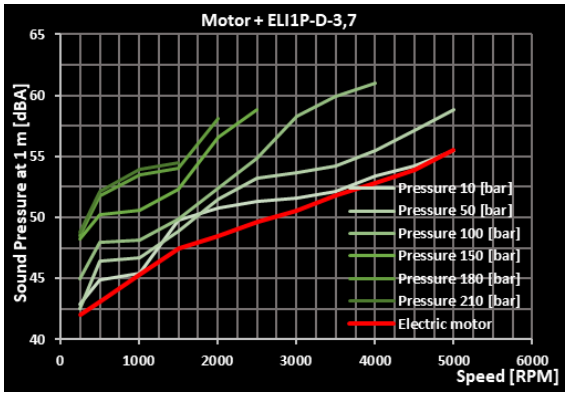

Figure 21: Motor-pump combined noise.

Figure 21 shows in green the overall sound pressure of the motor + pump combination. Red line shows the motor alone. It's clear that the pump adds just a small amount of noise over the motor which is already very silent. All the way to 150 bars the pump just adds 3 dBA to 5 dBA. The whole combination, pump plus motor, always stays below 60 dBA which is a very good target.

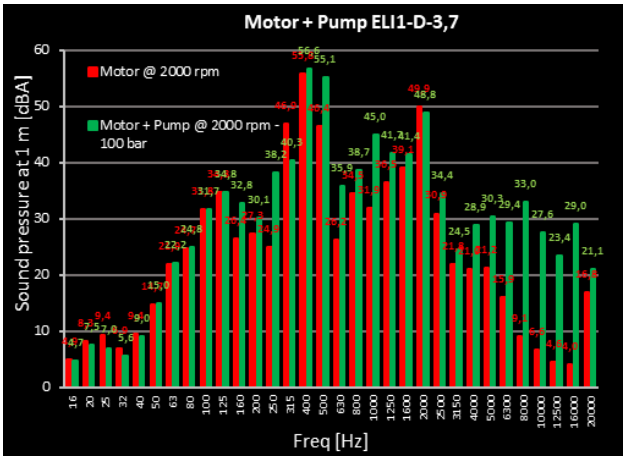

Figure 22: Frequency spectrum comparison with motor only (red) vs. motor+pump (green) at 2000 rpm, 100 bar.

6 Benefit of a VFD pump drive

Electrification and hybridization have dramatically reduced engine noise from industrial vehicles, making hydraulic circuit noise predominant. This feature, coupled with the ever-increasing diffusion of VFD brushless motors, leads to the possibility of obtaining a variable flow from a fixed displacement pump. In these applications, it is required that even in the phases in which the vehicles operate only in electric mode, the hydraulic applications such as the steering that must remain in operation, must not be audible. This feature is particularly important in public transport to ensure maximum interior comfort.

Elika pumps are particularly suited for electric vehicles (thanks to its high overall efficiency) where energy saving is a main driver. Its features make this product very useful against variable displacement pumps. The Elika gear pump has been co-developed with the Faculty of Engineering at the University of Bologna, using helical gear technology (Pat. EP2352921).

This technology delivers low noise with high efficiency across a high range of speeds and is particularly efficient when coupled with VFD brushless motors. Recent tests at the Marzocchi R&D lab demonstrated flow from 1 l/min to 20 l/min using the same displacement and maintaining high volumetric efficiency (>90 %) throughout. This presentation demonstrates how recently discovered additional benefits of helical gear technology can increase efficiency and reduce cost when deployed in electrified powertrains.

Major benefits both for the final user and the system of a Variable flow with fixed displacement helical pump Elika Drive are:

- Possibility to obtain high flow variation using variable speed.
- Less expensive than variable displacement pump solution.
- Higher efficiency reduces energy consumption (smaller pump displacement).
- Higher efficiency reduces oil heating (smaller reservoirs and coolers).
- Low noise thanks to the inherent design of Elika (-15 dBA on average).

References

[1] Claudio Bonacini – "Sulla portata delle pompe ad ingranaggi" L'INGEGNERE N.9 1961
[2] Claudio Bonacini – "Sulle pompe ad ingranaggi a dentatura elicoidale" TECNICA ITALIANA – RIVISTA DI INGEGNERIA 03/03/1965
[3] Houston Brantch & Wendell Smith – "The unreasonable American" Francis W. Davis, inventor of Power Steering – Academy of Applied Science 1968
[4] Pat. US2261143 "GEAR" 18/08/1939 - Francis W. Davis
[5] Pat. US2206079 "PUMP" 28/07/1936 - Francis W. Davis
[6] Pat. US3209611 "TEETH PROFILES OF ROTORS FOR GEAR PUMPS OF ROTARY TYPE" 05/10/1965 – Hitosi Iyoi
[7] Pat. US3658452 "GEAR PUMP OR MOTOR" 25/04/1972 – Yasuo Kita
[8] Pat. EP2352921 "TOOTH PROFILE FOR ROTORS OF POSITIVE DISPLACEMENT EXTERNAL GEAR PUMPS" – 21/05/2014 Catania Giuseppe
[9] Pat. EP2859237 "GEAR PUMP OR HYDRAULIC GEAR MOTOR WITH HELICAL TOOTHING PROVIDED WITH HYDRAULIC SYSTEM FOR AXIAL THRUST BALANCE" – 04/05/2016 Ferretti Stefano, Persici Danilo

Designing Educational Systems to Illustrate Mechatronic Principles

Željko Šitum, Tomislav Drašković, Fran Hruškar, Lovro Meštrić, Mateo Šego, Eros Stemberger, Magdalena Antolković

[1] University of Zagreb, Faculty of Mechanical Engineering and Naval Architecture, Zagreb, Croatia
zeljko.situm@fsb.unizg.hr, td206264@stud.fsb.unizg.hr, fh239918@stud.fsb.unizg.hr, lm227775@stud.fsb.unizg.hr, ms23475@stud.fsb.unizg.hr, es214728@stud.fsb.unizg.hr, ma242350@stud.fsb.unizg.hr

This article presents six innovative laboratory mechatronic systems developed as educational prototypes to illustrate fundamental mechatronic principles to engineering students. The first prototype is an oncooscillator that generates oscillating magnetic fields via a rotating magnet driven by a DC motor, potentially demonstrating biomedical applications such as tumour cell disruption. The second is a robotic fire-fighting system ("firebot") connected to a water tanker for fire suppression. The third prototype models a cargo transport vehicle facing challenges of load instability on uneven terrain. The fourth is a mini-vessel equipped with a gyroscopic stabilization mechanism to minimize lateral rolling during navigation. The fifth is an automated chessboard capable of autonomous gameplay, piece movement, and board state recognition. The final system is a compact underwater vehicle (submarine) designed for submerged exploration and operational tasks. These prototypes serve as practical tools for bridging theoretical knowledge with hands-on learning in mechatronics education.

DOI
https://doi.org/10.18690/um.fs.7.2025.7

ISBN
978-961-299-049-7

Keywords:
mechatronic models, automatic control, biomedical engineering, underwater robotics, gyroscopic stabilization

University of Maribor Press

1 Introduction

Mechatronics is an interdisciplinary field combining mechanical, electrical, computer, and control engineering, with applications expanding beyond traditional industrial automation into biomedical, environmental, transportation, and interactive systems [1], [2]. As mechatronic systems grow in complexity and scope, engineering education must evolve accordingly, emphasizing both theoretical foundations and hands-on experience through practical learning platforms [3]. One of the main challenges in teaching mechatronics is translating abstract theoretical concepts into real systems. Conventional instruction often falls short in conveying the integrated, multidisciplinary nature of real-world engineering tasks [4]. To address this gap, educational laboratory prototypes have become essential tools in teaching. These systems promote active learning, critical thinking, and innovation by allowing students to work directly with sensors, actuators, microcontrollers, and feedback systems in real applications [5]. This article presents six such educational prototypes developed to illustrate fundamental mechatronic principles. These include: an oncooscillator generating oscillating magnetic fields for biomedical research; a robotic fire-fighting platform (firebot); a vehicle stabilization system for transporting liquid cargo; a gyroscopically stabilized mini-vessel simulating dynamic marine balance; an automated chessboard capable of autonomous play; and a compact underwater vehicle for submerged exploration. These prototypes serve both as didactic tools and as foundations for advanced research in robotics and intelligent system design.

2 Biomedical and environmental mechatronic prototypes

2.1 Oncooscillator for the treatment of tumour diseases

The oncooscillator is an innovative medical device developed for non-invasive cancer treatment using oscillating magnetic fields (OMF). Based on recent research, particularly in the form of spinning oscillating magnetic fields (sOMF), these devices have shown the potential to selectively disrupt mitochondrial activity in tumour cells, leading to their death without affecting healthy cells [6]. This approach targets the electron transport chain in mitochondria, increasing reactive oxygen species and causing energy failure in malignant cells. The therapeutic system consists of three oscillators that generate dynamic magnetic fields through the rapid rotation of strong permanent magnets. The rotation is achieved using 24 V brushed DC motors

without gear transmission, providing high torque and suitable speeds. The motors are controlled by an Arduino Mega 2560 using PWM signals, with a DC-DC converter and IC driver (up to 1.5 A) ensuring stable voltage and current. Key mechanical components are constructed from industrial plastics and polymer-based materials, chosen for their excellent thermal and mechanical properties, as well as non-magnetic behaviour. This prevents interference with magnetic fields and ensures system safety. Ceramic bearings are used to support the rotating magnets due to their low friction and non-magnetic characteristics, preventing heat buildup and maintaining mechanical integrity during extended use. The magnets used in the system are of type DX0X0-N52, known for their extremely high magnetic strength. These magnets must be handled with care due to their strong attractive force, which poses a risk of damage or injury if not properly secured. Their high magnetic induction and relatively low mass make them ideal for OMF therapy applications. An important design strategy in the oncooscillator is the use of inertial motion. Motors accelerate the magnets to the desired rotational frequency, after which power is reduced, and the system relies on the inertia of the rotating mass to maintain consistent motion. This eliminates the need for mechanical braking and reduces power consumption, improving overall efficiency. Speed monitoring is enabled by Hall-effect sensors, which detect variations in magnetic fields and provide feedback to the control system. This allows real-time adjustment of the motor drive signals, ensuring synchronized operation of all three oscillators (Figure 1). Because the system uses a common PWM signal, all motors operate at the same speed, assuming identical mechanical loads.

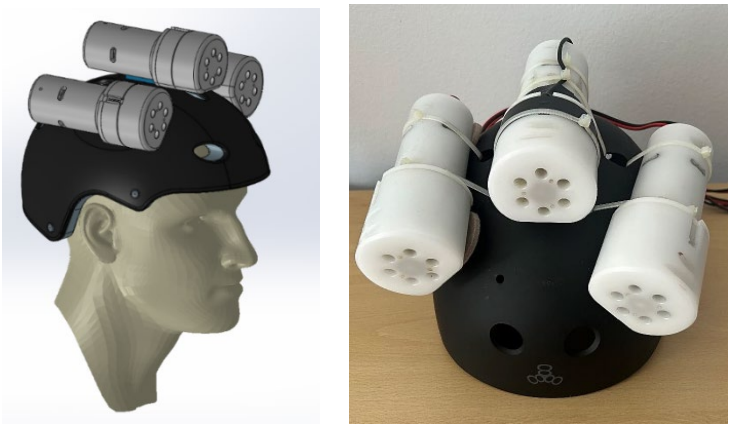

Figure 1: CAD model and assembled OMF helmet.
Source: https://repozitorij.fsb.unizg.hr/islandora/object/fsb:10889 [7]

Figure 2: Application of OMF: a) wearable helmet, b) configuration for reclining patient.
Source: https://repozitorij.fsb.unizg.hr/islandora/object/fsb:10889 [7]

The device is implemented in two configurations: a wearable helmet and a version adapted for patients in a reclined position (Figure 2). Both are designed to provide localized treatment, particularly for brain tumours such as glioblastoma. Preliminary reports and findings from existing studies show that OMF exposure can trigger selective cancer cell death in GBM and lung cancer cells, while sparing normal tissues. This selectivity is believed to be linked to the bioenergetic vulnerabilities of tumour mitochondria and the radical pair mechanism.

With its non-invasive nature, low energy consumption, and precise control, the oncooscillator represents a promising addition to the field of cancer therapy. Its potential applications extend beyond oncology to include mental health and rehabilitation treatments, where magnetic stimulation is already in use.

2.2 Mobile fire-fighting robot (firebot)

A compact, mobile fire-fighting robot has been designed and built for indoor and outdoor intervention in hazardous environments. Its primary function is water-based fire suppression, with water supplied via connection to a fire truck or water tank. Its compact dimensions enable operation in narrow and confined spaces, including stairways and steep terrain, where human access may be limited or dangerous. Additionally, the robot integrates environmental sensors to measure gas concentrations and an infrared sensor to detect the hottest point in the area. A camera mounted on a rotating turret allows for remote visual inspection and control via network connection. To ensure the robot's mobility and performance, a tracked chassis system was developed. Tracks allow climbing stairs and traversing uneven ground. The chassis consists of hollow steel square tubes (30x30 mm, 5 mm thick)

for structural integrity, and PETG polymer joints manufactured via 3D printing for the prototype stage. Lightweight aluminium checker plates are used as protective covers, with the option of mounting standard wheels on axles for simplified assembly and improved load capacity. The robot is powered by electric motors due to their robustness and reliability in oxygen-deficient environments. Each track is driven by a DC motor via a gear system, while shafts are supported by bearings press-fitted into the chassis. The drivetrain was built using PETG-printed sprockets and track links, with future versions planned in metal for improved durability. The drive assembly also includes commercially available wheels and standardized steel axles to reduce production complexity. The fire-fighting turret mounted on top of the chassis enables two degrees of rotational freedom using two Nema 17 stepper motors. One motor controls horizontal rotation, while the other, equipped with a planetary gearbox (32:1), handles vertical movement. The turret's components are also 3D-printed. A high-definition camera is fixed on the turret for real-time visual feedback, connected via LAN and powered by a 12V supply. The control system is built on a Raspberry Pi 4 using Python scripts. Wireless communication over the network ensures reliable remote control. All electronic components, including motor drivers (BTS7960 and TB6600), a DC-DC voltage regulator, and batteries, are housed in a waterproof enclosure inside the robot chassis, Figure 3.

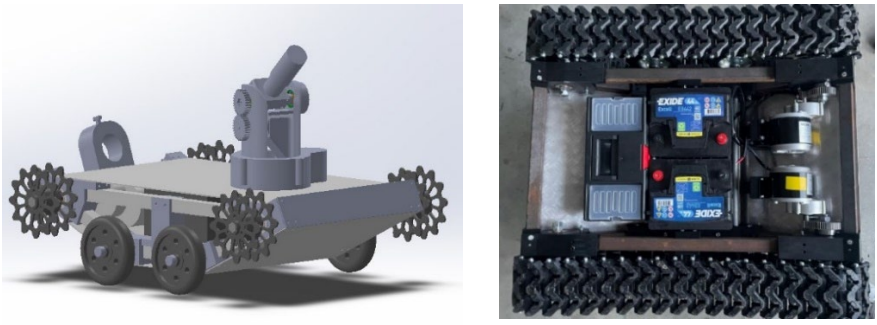

(a) (b)

Figure 3: a) CAD model of firebot, b) drive assembly with mounted components.
Source: https://repozitorij.fsb.unizg.hr/islandora/object/fsb:10889 [8]

The robot's low centre of gravity, with batteries placed at the base, ensures stability. Tests showed it can climb obstacles (e.g., standard-sized steps), pull heavy objects (e.g., sandbags), and endure mechanical stress. The turret rotation system and camera positioning enhance hazard and potential casualty detection. The final mobile fire-

fighting robot is shown in Figure 4. Future upgrades may include LIDAR, gas sensors, and semi-autonomous navigation for low-visibility conditions.

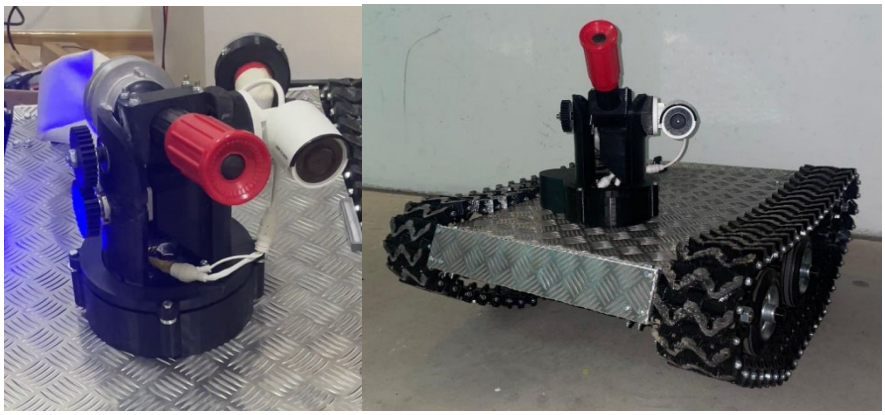

Figure 4: Mobile fire-fighting robot with mounted rotating turret.
Source: https://repozitorij.fsb.unizg.hr/islandora/object/fsb:10889 [8]

3 Mobility and stability systems in mechatronics

3.1 Electronic stability control of liquid transport vehicles

A model of a transport vehicle designed for carrying liquids or low-density materials was developed to address common stability issues encountered during operation on uneven or inclined surfaces. The proposed solution includes an active suspension system that dynamically maintains vehicle stability by controlling chassis inclination in real time. The aim of this project is to demonstrate, through an educational prototype, the benefits of electronically controlled suspension in mitigating vehicle oscillations due to road surface irregularities. Figure 5 shows the CAD model of the transport vehicle and the created conveyor belt with surface bumps. The system integrates two MPU6050 gyroscopic sensors placed at the front and rear axles to measure angular displacement. Their data is processed by an Arduino Nano, which sends corrective signals to MG995 servo motors. These motors adjust the axle positions to counteract tilting. A plexiglass container holding 400 ml of water is mounted on the chassis to simulate a real load. To simulate road disturbances, a motorized conveyor belt with surface bumps was built. The belt is powered by a Nema 17 stepper motor with gear reduction and controlled via an Arduino Nano and A4988 driver housed in a control unit with an LCD display. The setup allows

controlled and repeatable testing of suspension response. A Simulink dynamic model was created, incorporating road input and a sliding PID controller. This controller generates voltage outputs to stabilize the vehicle. Based on simulation results, parts were modelled in CAD and produced using FDM 3D printing with PET-G filament. The chassis, axles, and joints were assembled using U-profiles, springs, and servos. A custom two-layer PCB designed in Altium Designer processes signals and realizes motor control.

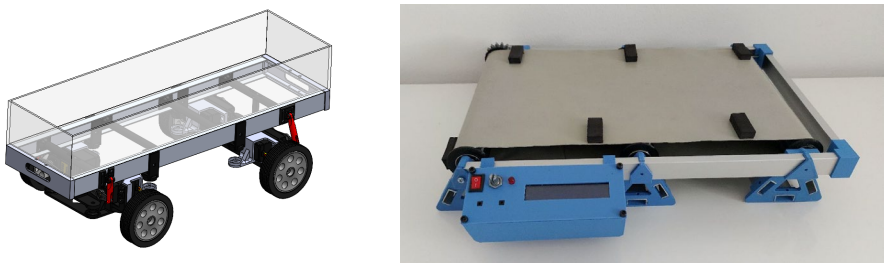

(a) (b)

Figure 5: a) CAD model of the transport vehicle, b) conveyor belt with surface bumps.
Source: https://repozitorij.fsb.unizg.hr/islandora/object/fsb:10871 [9]

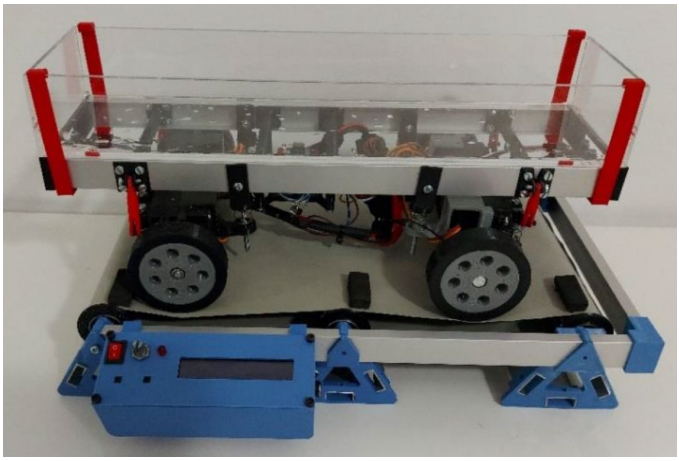

Figure 6: Vehicle prototype equipped with electronic stability control system.
Source: https://repozitorij.fsb.unizg.hr/islandora/object/fsb:10871 [9]

Figure 6 shows the completed vehicle prototype equipped with electronic stability control system. Testing involved both static and dynamic conditions. In static tests, the vehicle-maintained stability over a 7 mm obstacle, even when loaded. During

dynamic tests on the moving belt (0.04 m/s), angular data was collected, showing fast sensor and servo motors response that kept the chassis nearly horizontal. Stabilization occurred within 8 seconds. The final model demonstrates effective real-time tilt correction via active suspension and provides a valuable educational tool for studying electronic stability in liquid transport systems.

3.2 Mini-vessel with gyroscopic stabilization

A scale model of a vessel equipped with a gyroscopic stabilization system was designed to reduce lateral rolling caused by wave action or side forces. In modern maritime engineering, improving vessel stability enhances safety, comfort and manoeuvrability. Among available stabilization methods, gyroscopic stabilizers stand out for their compactness, mechanical simplicity, and ability to produce required stabilizing torques by using the law of conservation of angular momentum. The goal of this project was to show a way to reduce the amplitude of the roll angle, and the number of free roll oscillations within a range of ±2°. The basic component of the system is a high-speed spinning rotor. When subjected to external torques, the rotor exhibits precession, producing a stabilizing force perpendicular to the rolling motion. The vessel stabilization system integrates several components: a rotor (which is extracted from a lightweight RC aircraft motor), a NEMA 17 stepper motor for achieving precession, a Dasduino CORE microcontroller for signal processing and control, and a six-axis IMU sensor to estimate the vessel's roll angle. The entire assembly was modelled in SolidWorks, with the flywheel as the central element around which the system was compactly designed. The CAD model of the gyroscopic stabilization system is shown in Figure 7.

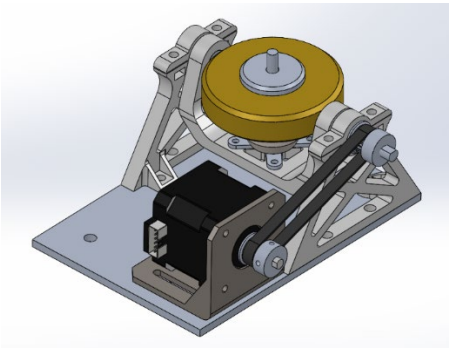

Figure 7: CAD model of the gyroscopic stabilizer.
Source: https://repozitorij.fsb.unizg.hr/islandora/object/fsb:11058 [10]

Practical production of the system was carried out using available technologies including turning, milling, FDM, and 3D printing. Most parts were printed using FDM for ease of manufacture and geometric flexibility. After assembling all the parts, the system was tested in a controlled environment, i.e. a water basin simulating calm sea conditions. Validation of simulation results with experimental data is a key element in engineering development. Simulations used simplified rolling motion equations, and experiments were designed to match these scenarios by manually tilting the vessel and observing its free oscillation. Figure 8 shows the mini-vessel model during its in-water testing. Real-time data acquisition was performed using the "data streamer" function in Excel, collecting sensor signals on a laptop. Matlab was used for post-processing and comparing simulated and experimental results. Initial testing without stabilization confirmed that the simplified dynamic model accurately reflected real-world behaviour. Subsequent testing with the gyroscopic system (passive mode, without active control) showed a significant reduction in oscillations. Starting from a 13° tilt, the unstabilized vessel needed 11 oscillations to settle within ±2°, while the gyroscopic stabilizer reduced this to just 2 oscillations (82 % improvement). Although active control could enhance performance further, the actuator system's weight exceeds the mini-vessel's capacity, making full active testing impractical in this setup.

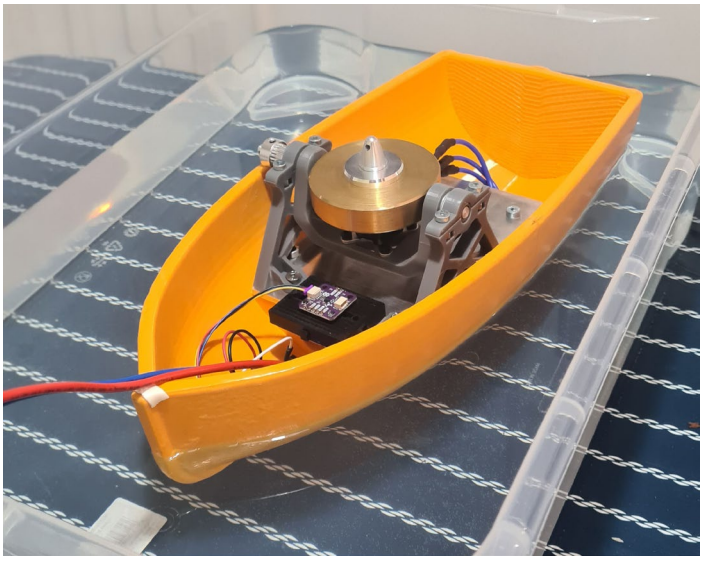

Figure 8: Mini-vessel model during water-based testing.
Source: https://repozitorij.fsb.unizg.hr/islandora/object/fsb:11058 [10]

This project confirms the feasibility and effectiveness of gyroscopic stabilization in small marine vessels. The system significantly improved roll damping even without active control, validating both the simulation and design. Future work may focus on reducing mass and adding active control to improve the stabilization response of the vessel.

4 Autonomous and underwater mechatronic platforms

4.1 Automated chess board with autonomous gameplay

The design and development of an automated chess board capable of autonomous gameplay represents an interesting intersection of embedded systems, mechanics, and artificial intelligence. The system can detect the player's moves, compute its own responses using a chess engine, and physically move the pieces using an XY-axis magnetic actuator. This allows the board to act as a real, physical chess opponent. The game begins in the standard initial position, whereby the human player always playing with white pieces to simplify programming logic. The detection system uses 64 reed switches, one beneath each square. Each switch contains two ferromagnetic contacts in a sealed, inert gas-filled tube. When a magnetic piece is near, the contacts close, signalling its presence. Since reed switches can't distinguish piece colour, all 64 squares are scanned twice per second to detect piece movement, including captures. The magnets embedded in the pieces are vertically aligned, which poses detection challenges due to reed switch geometry. This was resolved by offsetting the placement of the switches from the centre of each square. To connect all switches with limited input pins, four multiplexers are used to address and read the 64 switches efficiently. A display connected via I2C protocol provides user feedback, shows allowed player timers, and alerts about illegal moves or game status. Upon powering up, the board automatically calibrates using end-stop limit switches to locate the electromagnet's home position. The board is powered by an Arduino Nano with ESP32 microcontroller, programmed via the Arduino IDE. The gameplay engine is Micro-Max, a lightweight chess engine of only 133 lines of C code, developed by Harm Geert Muller. It uses the minimax algorithm with alpha-beta pruning technique to optimize move generation. Minimax simulates future game states by assuming both players play optimally, evaluating positions based on balance of figures, king safety, pawn structure, and possibilities of playing the next move. A key innovation is real-time move evaluation assistance. When a player lifts a piece, all legal destination squares light up using embedded multi-coloured LEDs.

The colours reflect the engine's evaluation of each possible move, helping players of all levels understand strategic consequences and learn in real time. Figure 9 illustrates the electronic schematic connecting the reed switch, address multiplexer, stepper motor driver (TMC2208) and display to the Arduino.

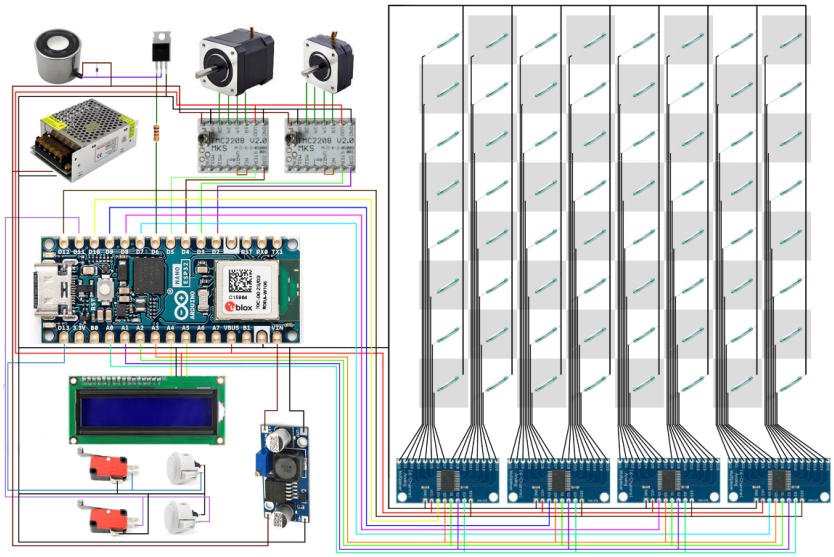

Figure 9: Electronic schematic connecting of chess board.
Source: https://repozitorij.fsb.unizg.hr/islandora/object/fsb:10599 [11]

Figure 10: Automated chess board.
Source: https://repozitorij.fsb.unizg.hr/islandora/object/fsb:10599 [11]

Figure 10 shows an assembled automated chessboard consisting of a game board with pieces, a drive mechanism, a piece disposal zone, and a visual feedback interface. By combining intuitive physical interaction, smart move generation, and online connectivity, this project not only revives the tactile experience of traditional chess but also uses modern technologies to enhance player engagement, education, and fun.

4.2 Underwater vehicle (submarine) for submerged exploration

This project presents the design and construction of a small-scale underwater vehicle (submarine) intended for underwater research. Unlike ground-based or aerial robotics, underwater vehicles must address challenges like waterproofing under hydrostatic pressure and maintaining buoyancy control at varying depths. The developed submarine is pressure-resistant up to 10 meters and utilizes ballast tanks and electric propulsion for depth and movement control. The submarine's frame is built from a 95 mm diameter, 550 mm long acrylic tube, offering both a lightweight structure and sufficient resistance to pressure up to 8 bar. Acrylic was chosen for its transparency, strength, and low weight. Sealing is achieved using O-rings and silicone sealant to ensure watertight integrity. Buoyancy regulation is based on Archimedes' principle. When the buoyant force exceeds the vehicle's weight, it ascends; when lower, it descends. This principle is exploited via a custom-designed ballast system with ten piston-driven cylinders that intake or expel water using motorized actuators. Figure 11 shows the location of the ballast tanks and the design of the submarine's rudder and propeller.

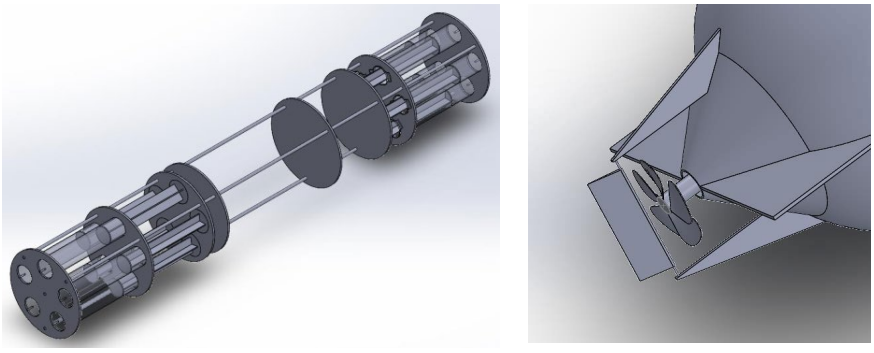

(a) (b)

Figure 11: a) ballast tanks, b) rudder and propeller.
Source: https://repozitorij.fsb.unizg.hr/islandora/object/fsb:12022 [12]

Motor torque was calculated including piston friction and the force required to displace water, based on internal and hydrostatic pressures. The propulsion system uses a DC motor (RS-385) driving a custom 3D-printed propeller, generating a pressure difference to create thrust that moves the submarine forward. Steering is achieved by a servo-controlled rudder (SG90), also made by 3D printing. A custom PCB controller, built with an Adafruit Pro Trinket (ATmega328) and nRF24L01 radio module, enables wireless control. Due to radio signal attenuation underwater, communication is relayed via a surface buoy with an antenna, connected to the vehicle through a wired link. Onboard control is handled by an Arduino UNO R3, which processes joystick and switch inputs to operate motors, ballast systems, and servo-controlled rudder (Figure 12). The system is powered by a 6000 mAh Li-ion battery, with motor control via an L298N dual H-bridge driver. Communication stability is maintained through configuration of the radio module. Testing in controlled water environments confirmed effective propulsion and depth control. However, sealing remains a weak point, and long-range signal reliability needs improvement. Future developments will focus on better sealing, adding cameras, and modular hardware. The project confirmed the educational possibilities of building a functional, low-cost ROV using accessible tools and components for underwater exploration.

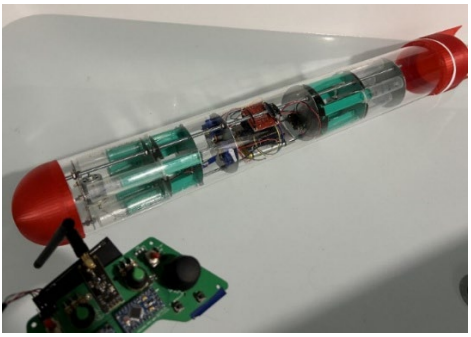

Figure 12: Underwater vehicle (submarine).
Source: https://repozitorij.fsb.unizg.hr/islandora/object/fsb:12022 [12]

5 Conclusion

Laboratory-based learning plays a vital role in engineering education, particularly in fields such as mechatronics and robotics where interdisciplinary integration is essential. The six presented prototypes demonstrate how theoretical concepts,

ranging from kinematics and control systems to sensor integration and embedded programming, can be effectively applied into hands-on applications. Through constructing and testing these systems, students actively engage with real-world design challenges, developing critical thinking and problem-solving skills. These educational platforms not only enhance conceptual understanding but also inspire creativity and innovation. As is well known, laboratory work remains necessary in preparing future engineers for the complexities of modern mechatronic systems.

Acknowledgments

This research was funded by the University of Zagreb, through tenders for short-term annual financial support for scientific research in the period 2022–2024.

References

[1] Bolton, W. (2018). Mechatronics: Electronic control systems in mechanical and electrical engineering. 7th edn. Harlow: Pearson, ISBN 978-1-292-25097-7.

[2] Singh, M. and Joshi, A. (2020). Emerging trends in mechatronics engineering: A review. *International Journal of Engineering Research and Technology*, 13(6), 1454–1461.

[3] Habib, M.K. (2013). Mechatronics: A unifying and integrating engineering science paradigm. *IEEE Industrial Electronics Magazine*, 7(2), 20–27. https://doi.org/10.1109/MIE.2013.2253134.

[4] Aung, W. and Miller, R.K. (2020). Mechatronics education: Challenges and opportunities. *International Journal of Engineering Education*, 36(4), 1025–1032.

[5] Gonzalez, R., Khamis, A. and Nunez, P. (2021). Hands-on mechatronics education through project-based learning: A case study. *IEEE Transactions on Education*, 64(2), 123–130. https://doi.org/10.1109/TE.2020.3008721.

[6] Sharpe, M. A., Baskin, D. S., Pichumani, K., Ijare, O. B., & Helekar, S. A. (2021). Rotating Magnetic Fields Inhibit Mitochondrial Respiration, Promote Oxidative Stress and Produce Loss of Mitochondrial Integrity in Cancer Cells. *Frontiers in oncology*, *11*, 768758. https://doi.org/10.3389/fonc.2021.768758

[7] Drašković, T. (2024). Application of oscillating magnetic fields for treating tumors**.** Master's thesis, (in Croatian), University of Zagreb, Fac. of Mech. Eng. and Naval Arch.

[8] Hruškar, F. (2024). Mobile fire-fighting robot. Undergraduate thesis (in Croatian), University of Zagreb, Fac. of Mech. Eng. and Naval Arch. https://repozitorij.fsb.unizg.hr/islandora/object/fsb:11085

[9] Meštrić, L. (2024). Electronic stability control of liquid transport vehicles. Master's thesis, (in Croatian), University of Zagreb, Fac. of Mech. Eng. and Naval Arch. https://repozitorij.fsb.unizg.hr/islandora/object/fsb:10871

[10] Šego, M. (2024). Design of a vessel stabilization device. Undergraduate thesis (in Croatian), University of Zagreb, Fac. of Mech. Eng. and Naval Arch. https://repozitorij.fsb.unizg.hr/islandora/object/fsb:11058

[11] Stemberger, E. (2024). Automated chess board. Master's thesis, (in Croatian), University of Zagreb, Fac. of Mech. Eng. and Naval Arch. https://repozitorij.fsb.unizg.hr/islandora/object/fsb:10599

[12] Antolković, M. (2025). Designing a remotely controlled underwater vehicle. Undergraduate thesis (in Croatian), University of Zagreb, Fac. of Mech. Eng. and Naval Arch. https://repozitorij.fsb.unizg.hr/islandora/object/fsb:12022

Pneumatics Today and Tomorrow: A Review of Technology and Development Trends

Marko Šimic, Niko Herakovič
University of Ljubljana, Faculty of Mechanical Engineering, Ljubljana, Slovenia
marko.simic@fs.uni-lj.si, niko.herakovic@fs.uni-lj.si

This paper reviews recent innovations and trends in pneumatics, highlighting advances in actuator design, energy efficiency, and intelligent control. Developments in miniature 3D-printed and soft pneumatic actuators offer lightweight, customizable, and safe solutions for robotics and biomedical applications. Proportional and digital pneumatics continue to evolve for Industry 4.0, with reinforcement learning improving controller adaptability. Energy-saving methods-including intermittent air supply, pressure-based cut-off circuits, optimized sizing, and novel throttling-enable up to 71 % efficiency gains and short payback times. Trajectory-based gripping force calculation and product carbon footprint analysis support sustainable practices. Soft robotics contributes with novel actuator designs, data-driven modelling, and nonlinear control strategies. Experimental validations confirm these technologies' practicality and effectiveness. Overall, this review presents pneumatics as a versatile, efficient, and eco-conscious platform for modern automation, integrating IoT, digital twins, and hybrid systems for future-ready fluid power solutions.

DOI
https://doi.org/10.18690/um.fs.7.2025.8

ISBN
978-961-299-049-7

Keywords:
pneumatics,
energy efficiency,
soft robotics,
intelligent control,
sustainable automation

University of Maribor Press

1 Introduction

Pneumatics has long been a cornerstone of industrial automation due to its simplicity, robustness, and cost-effectiveness. Pneumatic systems are widely used in manufacturing, packaging, robotics, and process industries for tasks such as actuation, assembly, gripping, and material handling. Their advantages include simple distribution and transfer of air energy across industrial environments, a favourable power-to-weight ratio, fast response times, and inherent safety in explosive or hygienic settings. Pneumatic systems are also easy to maintain, with cost-effective spare parts and straightforward transformation between linear and rotary motion. Their compliance and softness make them particularly suitable for collaborative and human-safe applications [1], [2].

1.1 State of the art

Compared to hydraulic and electric drives, pneumatic systems offer several distinct advantages that make them highly suitable for a wide range of industrial and commercial applications. Unlike hydraulic systems, which depend on potentially flammable and environmentally hazardous fluids, pneumatic systems operate using compressed air, a clean, abundant, and renewable energy source. This makes them inherently safer, especially in explosive or hygienic environments, and eliminates the risk of toxic leaks or fire hazards. While electric drives are known for their precision and programmability, they are often more complex, sensitive to overloads, and less robust in harsh or vibration-prone settings. Pneumatic systems, by contrast, are mechanically simple, overload-resistant, and capable of continuing operation during brief power outages due to stored compressed air in the system. Modern pneumatic systems are also modular and easy to maintain, making them ideal for both large-scale industrial automation and smaller, mobile, or start-up operations. Their widespread use across industries such as automotive manufacturing, electronics, food and beverage processing, petrochemicals, pharmaceuticals, HVAC, and transportation, particularly in air brake systems, demonstrates their versatility and reliability. Despite lingering misconceptions about noise, leakage, or operational complexity, properly designed pneumatic systems are clean, efficient, and relatively quiet. Their mechanical simplicity allows for quick troubleshooting and reconfiguration, and their compact, lightweight components make them especially advantageous in applications where space and mobility are critical [1], [2].

However, pneumatic systems are not without limitations. The compressibility of air can lead to reduced precision and stick-slip effects, particularly at low speeds. Pressure limitations often necessitate larger components to achieve the same force output as hydraulic or electric systems. Effective air preparation is essential to prevent moisture, oil, and particulate contamination, and the performance of seals and other components can be sensitive to temperature fluctuations. Pneumatic systems are also vulnerable to air leakage, which can reduce efficiency and increase energy costs, especially given the relatively high energy demand of air compression. Additionally, they may be less suitable for applications requiring highly accurate motion or force control, as their speed and position regulation is generally less precise than that of electric drives. Noise from compressors and valves can also be a concern if not properly managed, and the systems may be sensitive to dust and vibration in certain environments [1], [2].

1.2 Industrial pneumatics and recent trends

Every industrial pneumatic system includes essential components such as air generation, pressure control, storage tanks, distribution networks, and end-use devices (Figure 1). Each part must be well-designed to ensure efficiency, stability, and long-term, sustainable operation.

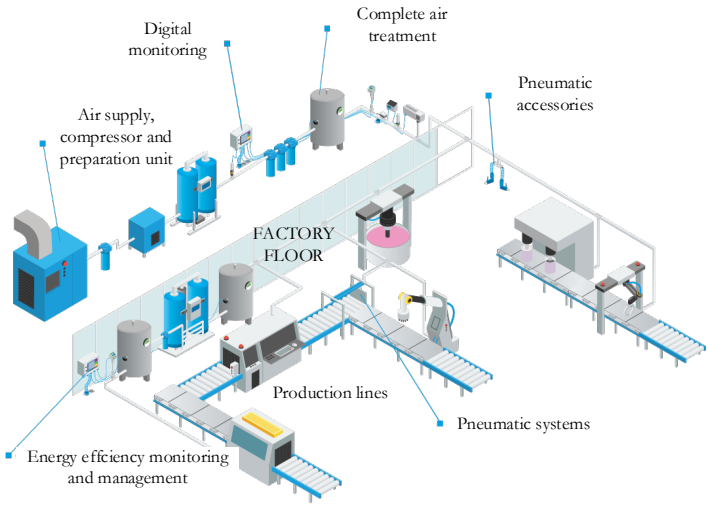

Figure 1: Industrial pneumatics: compressed air chain with main pneumatic subsystems [3].

Recent technological advancements are significantly reshaping the landscape of pneumatic systems. Innovations in actuator design, intelligent control, and energy-saving strategies are helping to overcome long-standing limitations traditionally associated with pneumatics [4]. The integration of these systems with Industry 4.0 technologies, such as the Internet of Things (IoT), digital twins, and machine learning, has opened new possibilities for creating adaptive, efficient, and sustainable automation solutions [5], [6], [7]. Modern pneumatic platforms now support seamless integration with advanced components like multifunctional island valves and flowmeters that are compatible with PLC controllers. These developments enable centralized and streamlined management of multiple pneumatic valves and actuators, while also facilitating real-time data acquisition at the machine level. This data can be used for operational analysis, predictive diagnostics, and performance optimization. Furthermore, the interconnection of pneumatic system data with higher-level IT infrastructures such as ERP (Enterprise Resource Planning), MES (Manufacturing Execution Systems), and other digital platforms enhance transparency and enable more effective decision-making across production environments [8].

This review aims to synthesize these technological developments, highlight emerging trends, and identify opportunities for further research and industrial application in the evolving field of pneumatic automation.

2 Advanced approaches

2.1 Pneumatic actuators

Recent developments in pneumatic actuators have significantly expanded their capabilities, particularly in terms of miniaturization, customization, and integration with soft materials. These advances are enabling new applications in robotics, biomedical devices, and lightweight automation systems.

One of the most promising directions is the use of additive manufacturing to create compact, lightweight pneumatic actuators. Nall and Bhounsule [5] demonstrated a 3D-printed, double-acting linear pneumatic actuator with a power-to-weight ratio comparable to commercial alternatives (Figure 2). Their actuator, weighing only 12 grams, achieved a peak output power of 2 W at 40 psi and was successfully integrated

into a hopping robot inspired by the Pixar Luxo lamp. Such actuators offer several advantages such as rapid prototyping and customization, integration of structural and functional components, and low-cost fabrication using hobby-grade printers and therefore are ideal for educational robotics, wearable devices, and exploratory research in soft robotics.

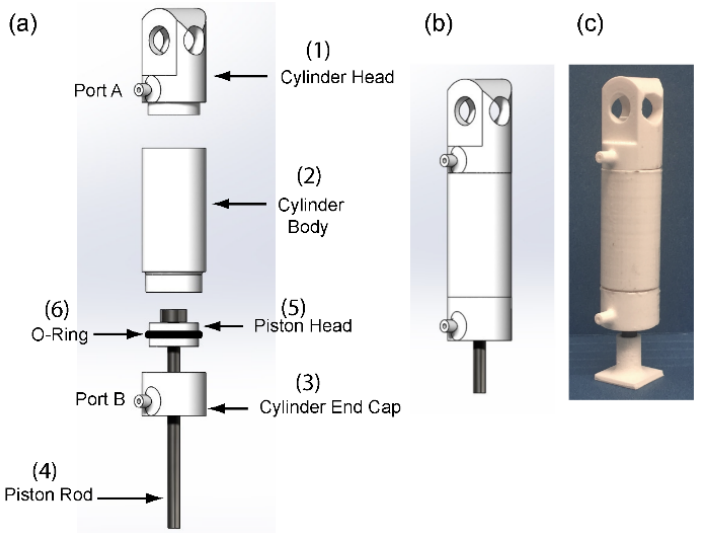

Figure 2: An Overview of the 3D printed actuator: (a) an exploded view, (b) assembled view, and (c) 3d printed and assembled [5].

Soft robotics and biomedical applications have emerged as a key area where pneumatics and pneumatic actuators plays a central role. Soft pneumatic actuators, often made from elastomers or textiles, provide safe and adaptive interaction with humans and unstructured environments (Figure 3) [6].

They are particularly suited for biomedical applications, such as assistive devices and surgical tools. Recent work has focused on functionally graded materials for variable stiffness, antagonistic actuator systems using stereolithography and combustion-powered soft robots for high-thrust applications. These actuators benefit from the inherent compliance of soft materials, enabling complex motions and safe physical interaction. However, challenges remain in modelling their nonlinear behaviour and achieving precise control.

The integration of miniature and soft actuators into robotic systems has led to novel applications such as jumping and hopping robots with high energy efficiency [5] and bioinspired tentacle-like manipulators as well as compact actuators for wearable exoskeletons and prosthetics [6]. These applications highlight the versatility of pneumatic actuation in domains where weight, safety, and adaptability are critical.

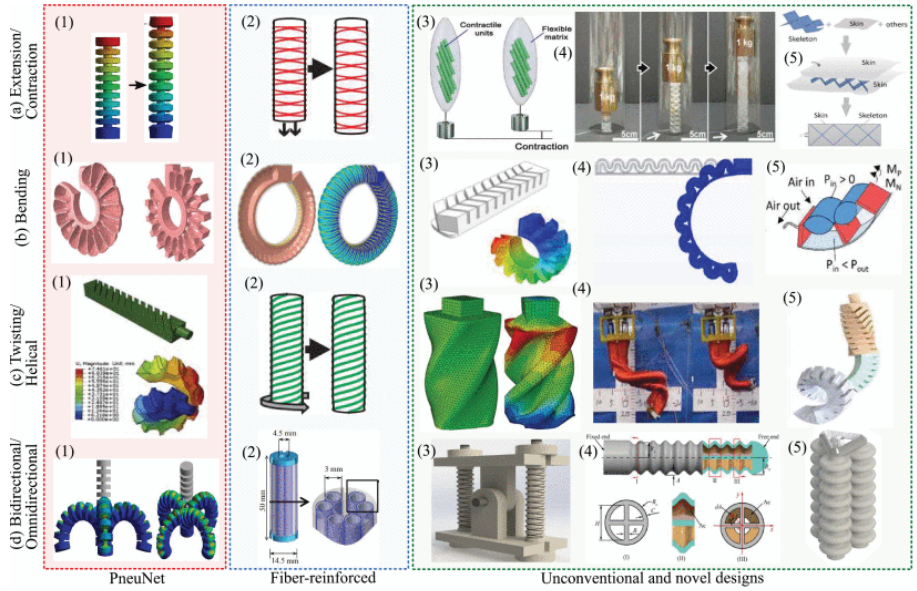

Figure 3: Soft pneumatic actuator designs: (a) Extension and contraction SPAs: (1), (2), (3), (4) and (5). (b) Bending SPAs: (1), (2), (3), (4) and (5). (c) Twisting and helical SPAs: (1), (2), (3), (4) and (5). (d) Bidirectional and Omnidirectional SPAs: (1), (2), (3), (4) and (5) [6].

To address the complexity of soft and miniature actuators, researchers are increasingly turning to data-driven modelling and advanced control strategies. Reinforcement learning and neural networks are being explored to improve adaptability and performance.

2.2 Intelligent control and Industry 4.0 integration

The integration of intelligent control strategies and digital technologies is transforming pneumatic systems into adaptive, efficient, and interconnected components of modern automation. These advancements are driven by the need for

higher precision, energy efficiency, and seamless integration with Industry 4.0 frameworks.

2.2.1 Proportional and Digital Pneumatics

Traditional on/off pneumatic control is increasingly being replaced by proportional and digital control systems that offer finer regulation of pressure and flow. Proportional valves, often controlled via analogue or pulse-width modulation (PWM) signals, enable continuous adjustment of actuator force and speed. Recent developments include the use of modulated pulse control for proportional flow regulation, offering high-speed switching (up to 1500 Hz) and compact modular designs [9].

One of the potential alternatives to hydraulic systems presents the pneumatic system designed for dynamic material strength testing, particularly for low-strength materials such as natural fibres (Figure 4). The system uses a pneumatic cylinder to apply cyclic loads, with force controlled via a proportional pressure valve and a PID controller implemented on an Arduino-compatible PLC. A touchscreen interface allows intuitive operation and real-time monitoring. Experimental tests confirm accurate force control up to 11 kN, with reliable performance in low-frequency fatigue testing. The system offers a cost-effective and portable solution for laboratories focused on testing low-strength or natural materials [10].

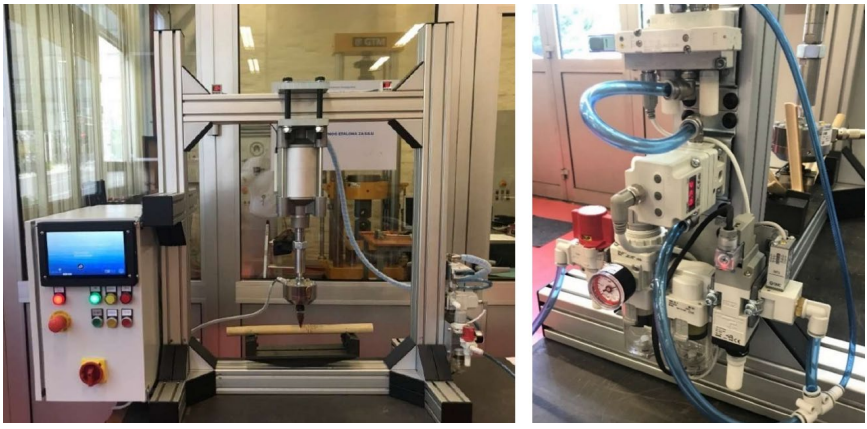

Figure 4: Fatigue testing machine driven by pneumatic system [10].

Digital pneumatics in combination with piezo technology, characterized by the use of binary-controlled microvalves and smart valve terminals, allows for precise and programmable control of pneumatic circuits. These systems are often integrated with embedded sensors and microcontrollers, enabling real-time feedback and diagnostics [11], [12].

2.2.2 Reinforcement learning and Adaptive control

One of the most promising trends in intelligent control is the application of reinforcement learning (RL) and neural networks to pneumatic systems. Allmendinger and Erhard [13] demonstrated a hybrid control approach where a deep deterministic policy gradient (DDPG) agent was trained in a virtual environment to enhance the performance of a conventional PID controller for mass flow regulation (Figure 5). The RL-enhanced controller achieved faster settling times and better adaptability to varying environmental conditions, such as changes in inlet pressure and coil temperature (Figure 6).

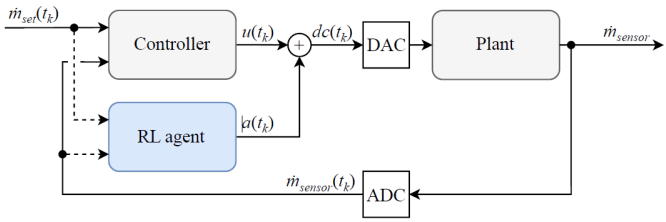

Figure 5: Structure and main components of training model [13].

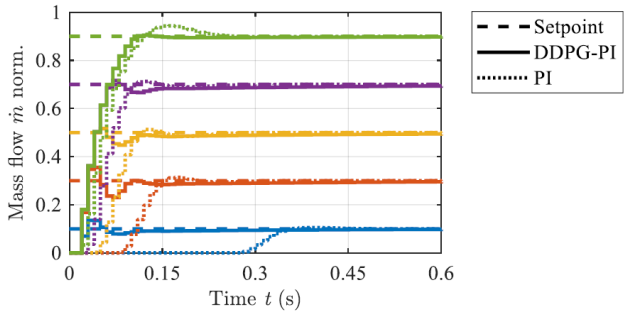

Figure 6: Comparison of the control performance between DDPG-PI and conventional PI controller [13].

This approach highlights the potential of data-driven control to compensate nonlinearities and uncertainties, improve robustness and adaptability and enable self-tuning and predictive behaviour of pneumatic system.

2.3 IoT, Digital twins, and Smart pneumatics

The convergence of pneumatics with the Industrial Internet of Things (IIoT) and digital twin technologies is enabling predictive maintenance, remote monitoring, and system optimization. Smart pneumatic systems are equipped with embedded sensors for pressure, flow, temperature, and position, which feed data into cloud-based analytics platforms with the help of new 5G and 6G technology [14]. Especially 5G and 6G technology is important for modular production systems and distributed control networks [15]. The main players in the pneumatics such as FESTO and SMC proposed and developed Smart pneumatic platforms representing several automations and IIoT layers (intelligent devices with embedded sensors and edge computers; motion and machine control layer with PLC, I/O devices and management and cloud-based analytic layer to perform real-time monitoring an diagnostics, predictive maintenance and energy optimization [16].

Key benefits include:

- Early detection of leaks and component wear
- Optimization of energy consumption
- Real-time performance monitoring and diagnostics

Digital twins, virtual replicas of physical pneumatic systems, allow for simulation, testing, and optimization of control strategies before deployment. This reduces commissioning time and enhances system reliability. Modern pneumatic systems are increasingly being integrated into cyber-physical systems (CPS), where they interact with digital controllers, sensors, and actuators in a closed-loop architecture. Hybrid systems combining pneumatic and electric actuation are also gaining traction, offering the benefits of both technologies in terms of force density, precision, and energy efficiency. These integrations support the broader goals of Industry 4.0, including modular and reconfigurable automation, decentralized control and edge computing, enhanced human-machine collaboration [8], [16], [17], [18], [19].

2.4 Energy efficiency in pneumatic systems

Energy efficiency has become a central concern in pneumatic system design, driven by rising energy costs, sustainability goals, and the need for competitive industrial automation. Traditional pneumatic systems are often criticized for their low energy efficiency, typically ranging between 5 to 20 % [20], [21], [22], [23], [24], [25]. However, recent research has introduced several innovative strategies to significantly reduce air consumption and improve overall system performance. One possible and simple solution presents energy saving circuits (Figure 7). Energy-saving circuits include all the circuits that deviate from standard meter-in or meter-out pneumatic circuits in terms of their structure and whose purpose is to reduce the amount of compressed air supplied to the system [21].

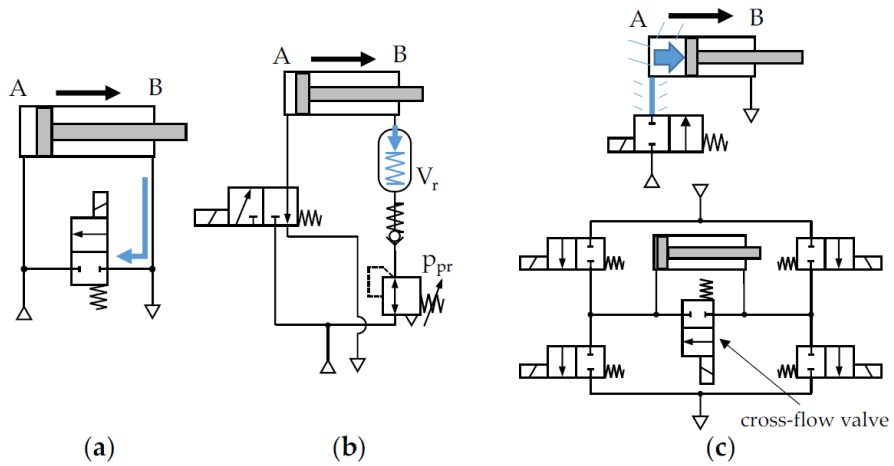

Figure 7: Basic principles of energy-saving circuits: (a) short (cross-flow) circuit; (b) exhaust air storage circuit; and (c) above: cut-off (expansion) principle, below: expansion bridge circuit with an additional cross-flow valve [21].

One of the most effective methods for improving energy efficiency is the use of intermittent air supply. Instead of continuously supplying compressed air throughout the actuator stroke, this method introduces controlled air pulses, allowing the actuator to utilize expansion energy more effectively. Gryboś and Leszczyński [22] demonstrated through exergy analysis that intermittent air supply can reduce exergy consumption by over 60 % compared to conventional systems.

This approach not only minimizes energy losses but also maintains actuator performance. The authors developed a dynamic model and validated it experimentally, showing that actuator speed and force profiles remain within acceptable limits while significantly reducing energy input. Figure 8 illustrates the exergy flow in classical and intermittent air supply systems, highlighting the shift in energy losses from the muffler to the distributed pneumatic line.

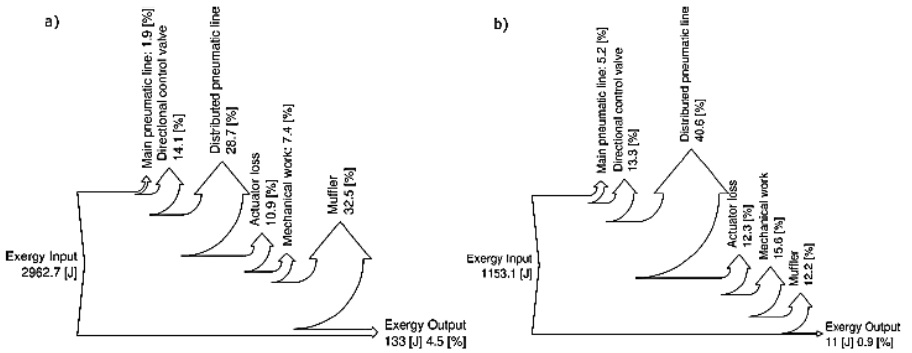

Figure 8: Sankey diagram: (a) exergy flow in classical and (b) intermittent air supply of pneumatic systems [22].

Proper sizing of pneumatic actuators and valves is another critical factor in reducing energy waste. Oversized actuators consume more air than necessary, especially in motion tasks. Doll et al. [7] introduced the Pneumatic Frequency Ratio (PFR) as a design metric to optimize actuator sizing based on stroke length, load, and transition time. Their method ensures that the actuator operates within an efficient dynamic range, avoiding excessive air consumption while maintaining performance.

Additionally, combined throttling strategies, such as adaptive upstream and downstream throttling, have shown promise in experimental studies. Reese et al. [26] developed a novel circuit combining quick exhaust valves and proportional control, achieving substantial air savings without compromising cycle time (Figure 9).

Other strategies, presented in [22] include the use of back pressure regulation and energy recovery systems. By introducing controlled back pressure in the exhaust line, it is possible to recover part of the expansion energy and reduce the net air

consumption. These methods are particularly effective in systems with high-frequency actuation or long stroke lengths.

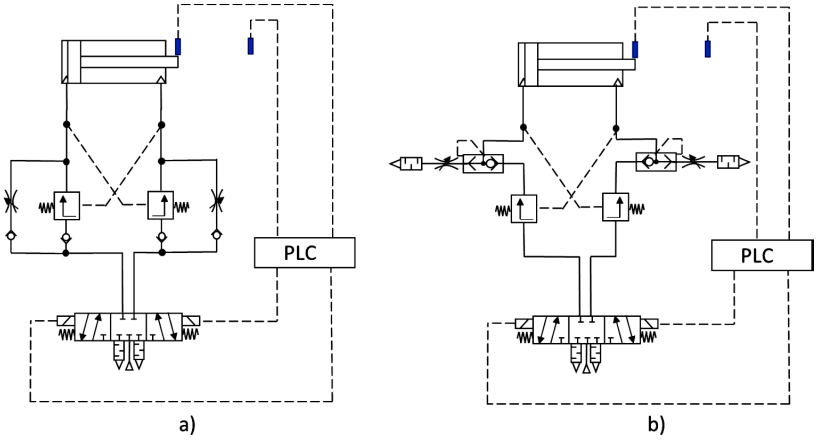

Figure 9: Adaptive upstream throttling configurations: a) original circuit and b) circuit with quick exhaust [26].

Recent trend, which is supported by all major players in the field of pneumatics is focused on reduction of delivery pressure from traditional 6 bar to 4 bar (4-bar factory) [23], [24], [25]. This shift targets significant reductions in energy consumption, operating costs, and CO_2 emissions. Since compressed air generation is a major industrial energy burden, even modest pressure reductions can lead to substantial efficiency gains (for every 1 bar reduction in delivery pressure, an average of 6 to 8 % less specific power is consumed.).

Implementing a 4-bar system requires a phased approach, beginning with an assessment of pressure and flow demands across the facility and detail check of working principles of all pneumatic component under lower 4-bar pressure. Localized control, air storage, and minor component changes often enable existing equipment to operate effectively at lower pressures. Once stability is confirmed at the machine level, the factory-wide supply pressure can be gradually lowered, reducing compressor duty and associated energy use.

This transition also involves redefining design standards to ensure future machinery supports lower pressure operation. Where higher pressure is occasionally needed, local boosters can be used. The 4-bar factory is not only a technical upgrade but a strategic move toward more sustainable and efficient manufacturing [23], [24], [27].

3 Future trends and outlook

The evolution of pneumatic systems is being shaped by a convergence of technological, environmental, and economic drivers. As industries transition toward smarter, more sustainable, and digitally integrated operations, pneumatics is poised to play a renewed role in next-generation automation systems. Here are two typical examples focused on sustainability and eco-conscious design of pneumatic system.

The first approach to sustainability involves quantifying the greenhouse gas emissions associated with pneumatic components. Sprink and Schmitz [28] conducted a cradle-to-gate Product Carbon Footprint (PCF) analysis of various pneumatic actuators and valves. Their study revealed significant variability in emissions depending on material sourcing, manufacturing processes, and data quality. To ensure comparability, the authors emphasized the need for standardized system boundaries, transparent reporting of assumptions and use of primary data where possible. Figure 10 illustrates the system boundary used in their PCF analysis, covering raw material extraction, component manufacturing, and assembly. This framework supports sustainability assessments and digital integration strategies.

The integration of PCF analysis with digital tools such as digital twins and IoT platforms enables real-time monitoring of environmental performance. This supports informed decision-making in design, procurement, and operation. Moreover, manufacturers are increasingly offering low-carbon alternatives, such as components made from recycled materials or produced using renewable energy.

The second potential approach to sustainability is optimizing the gripping force (required holding force) in pneumatic handling systems. Eberhardt et al. [29] proposed a trajectory-specific method for calculating the required holding force of surface (vacuum) grippers (Figure 11).

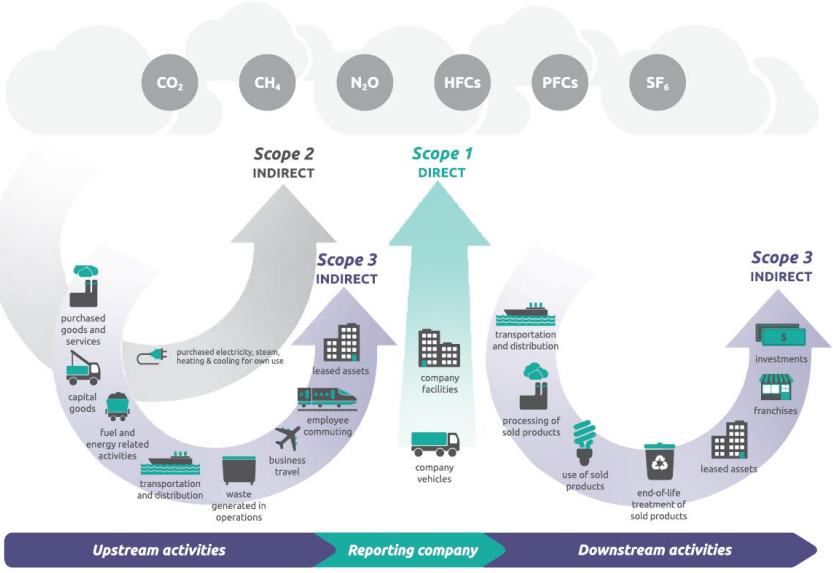

Figure 10: System boundary for cradle-to-gate Product Carbon Footprint (PCF) analysis of pneumatic components [28].

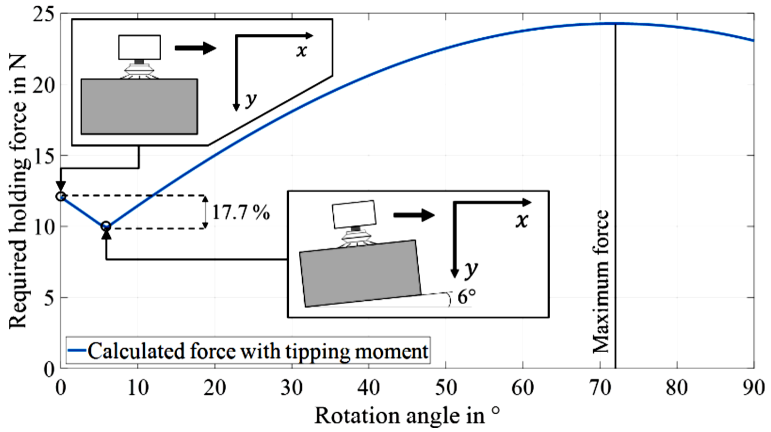

Figure 11: Reduce required holding force through clever alignment of the gripping object [29].

By tailoring the gripping force to the actual dynamic load along the robot path or any other handling device, unnecessary air consumption can be avoided, leading to both energy savings and reduced wear of pneumatic components. This method

supports sustainable automation by minimizing overdesign and oversizing of grippers, reducing compressed air usage and extending component lifespan. The major challenge represents the real-time adaptive control of required air supply or control of vacuum pump.

Based on presented advanced approaches from section 2 and some other trends and developments in pneumatics described in [30], [31], [32] we can summarize:

- Miniaturization, supported by soft robotics and microfabrication, is expanding pneumatics into wearable and biomedical fields, with a focus on low-pressure, compact, and safe actuation.
- New strategies have been developed to improve pneumatic system efficiency, such as preventing leaks, using properly sized components, and performing regular maintenance. These also emphasize the role of smart monitoring tools like FLUX flowmeters and IoT-enabled valves in reducing energy waste and enabling predictive maintenance.
- New smart pneumatic grippers that integrate valves, absolute position sensors, and part detection within a compact IO-Link-controlled package are now used in robotics. These units deliver high cycle rates (up to 500 grips/min for RPG), consume up to 90 % less compressed air than conventional systems, and support predictive maintenance through onboard diagnostics.
- The use of airflow sensors, in combination with modular IIoT-enabled systems, 5G technology, enables simple integration and allows real-time monitoring to reduce compressed air waste (saving 10 to 20 % in energy and emissions).
- The use of advanced materials and coatings is significantly improving the durability and performance of pneumatic components.
- Current approaches focus on integrating pneumatics into cyber-physical systems through digital twins, enabling real-time monitoring, simulation, and predictive maintenance. These digital tools enhance performance and align with Industry 4.0 goals.
- Hybrid pneumatic-electric systems are emerging to combine the power density of pneumatics with the precision of electric actuators, particularly in collaborative robots and modular automation.

- Artificial intelligence is advancing pneumatic control through self-optimizing algorithms that adapt in real time, enabling smarter fault detection, autonomous tuning, and efficient system design.
- Sustainability is driving the use of recycled or bio-based materials and circular design principles, supported by growing demands for transparent carbon footprint reporting.

4 Conclusions

This review has outlined the transformative developments shaping modern pneumatic systems. The integration of miniature 3D-printed and soft actuators has extended pneumatics into fields such as robotics, biomedicine, and wearable devices, where lightweight and adaptive actuation is essential. Intelligent control strategies, particularly those based on reinforcement learning and digital pneumatics, are enhancing system adaptability, precision, and efficiency.

Energy efficiency remains a central challenge and opportunity, with approaches such as intermittent air supply, optimized actuator sizing, combined throttling circuits, and reduced operating pressures (e.g., 4-bar systems) demonstrating substantial air and energy savings. These methods not only lower operational costs but also contribute to sustainability goals.

Digitalization is driving the evolution of pneumatics into smart, cyber-physical systems. The integration of IioT sensors, 5G, digital twins, and AI enables predictive maintenance, real-time monitoring, and data-driven optimization. Moreover, sustainability is emerging as a key design driver, exemplified by lifecycle assessments like Product Carbon Footprint (PCF) analysis and innovations in eco-friendly materials and energy-conscious control strategies.

Looking ahead, pneumatic systems are poised to become an essential component of Industry 4.0-characterized by hybrid actuation, smart diagnostics, modular architectures, and environmentally responsible designs. These advancements underscore pneumatics not as a legacy technology, but as a versatile, scalable, and sustainable platform ready to meet the demands of next-generation automation.

Acknowledgments

The work was carried out in the framework of the research program: Innovative manufacturing systems and process, funding No. (P2-0248); research project: Research on the reliability and efficiency of edge computing in the smart factory using 5G technologies, funding No. (J2-4470), which are financed by the Republic of Slovenia – Ministry of Education, Science and Sport. This work was also carried out within the Horizon Europe Grant N°101087348 (project INNO2MARE) and Grant N°101058693 (project STAGE).

References

[1] SMC (2019). 8 Advantages of Pneumatic Systems, *SMC Pneumatics USA- Orange Coast Pneumatics*. https://www.smcpneumatics.com/8-Advantages-of-Pneumatic-Systems_b_31.html.

[2] Nuryasin, A. (2025). Advantages and Disadvantages of Pneumatic Systems in Industrial Automation. *PT Bawalaksana Central Industrial*. https://bawalaksana.co/advantages-and-disadvantages-of-pneumatic-systems/.

[3] MADER (2018). Optimale Druckluftechnik und Pneumatik in der Lebensmittel- und Getränkeindustrie. https://www.mader.eu/aktuell/2018/branchenpaket-leitfaden-fuer-effiziente-druckluft-der-lebensmittel-und.

[4] Singh, A. P. A., Gameti, N., Gupta, S. (2024). Future Trends in Industrial Hydraulics and Pneumatics: Implications for Operations and Maintenance. *International Journal of Technical Innovation in Modern Engineering and Science, 10* (10), 15-25. doi: https://ijtimes.com/index.php/ijtimes/article/view/3442.

[5] Nall, C. L., & Bhounsule, P. A. (2019). A Miniature 3D Printed On-Off Linear Pneumatic Actuator and Its Demonstration into a Cartoon Character of a Hopping Lamp. *Actuators*, *8*(4), 72. doi: https://doi.org/10.3390/act8040072.

[6] Xavier, M. S. *et al.* (2022). Soft Pneumatic Actuators: A Review of Design, Fabrication, Modeling, Sensing, Control and Applications, *IEEE Access*, vol. 10, pp. 59442-59485, 2022, doi: 10.1109/ACCESS.2022.3179589.

[7] Doll, M., Neumann, R., Gauchel, W. (2024). Sizing of pneumatic drives under energy efficiency aspects. *4th International Fluid Power Conference*, Dresden 2024.

[8] SMC (2019). Factory Automation Trends. *SMC Corporation*. https://www.smc.eu/da-dk/focus-articles/trends.

[9] Avram, M., et al. (2020). Trends and perspectives in proportional pneumatics. *IOP Conf. Ser.: Mater. Sci. Eng.* doi: 10.1088/1757-899X/997/1/012034.

[10] Šitum, Ž., Bača, M. M., Benić, J., Alar, Ž. (2024). Control of a Pneumatic System for Material Strength Testing. *4th International Fluid Power Conference*, Dresden 2024.

[11] FESTO (2024). Pneumatics Makes a Technological Leap with Piezo. https://press.festo.com/en-US/node/4679.

[12] FESTO (2015). Piezo technology in pneumatic valves. https://www.festo.com/tw/en/e/solutions/piezo-technology-shape-the-future-of-automation-id_1519983/.

[13] Allmendinger, M., Erhard, M. (2024). Reinforcement learning-based PID controller design for mass flow. *Control of a Pneumatic System for Material Strength Testing.* 4th International Fluid Power Conference, Dresden 2024.

[14] Rowse, T. (2022). What is Smart Pneumatics? *Rowse Pneumatics*. https://www.rowse-pneumatics.co.uk/blog/post/what-is-smart-pneumatics?srsltid=AfmBOoogVomE8SmMzk24lA6gfSINFcIOUgdpKekImgajTcLP7tJGo5Y.

[15] Sotiris, M., Lenz, S., Vogt, T., Henze, M. (2025). Secure integration of 5G in industrial networks: State of the art, challenges and opportunities, *Future Generation Computer Systems*, Volume 166. doi: https://doi.org/10.1016/j.future.2024.107645.
[16] EMERSON (2019). Improve Machine Performance with IIoT Solutions. *Emerson Electric Co. AVENTICS*.
[17] Weiss Robotics (2025). Smart Pneumatics - Hybrid technologies provides advantages. https://weiss-robotics.com/smart-pneumatics/.
[18] SPS Pneumatic Tools. (2025). The Future of Pneumatic Technology: Trends to Watch in 2025. *SPS Enterprises*. https://www.spspneumatictools.com/future-of-pneumatic-technology-trends-2025.
[19] Hufnagl, H., Čebular, A., Stemler, M. (2021). Trends in pneumatics - digitalization. *International conference Fluid Power 2021*. doi: https://doi.org/10.18690/978-961-286-513-9.
[20] Nuryasin, A. (2024). How to improve pneumatic system efficiency for green manufacturing. *PT. Bawalaksana Central Industrial*. https://bawalaksana.co/how-to-improve-pneumatic-system-efficiency/
[21] Boyko, V, Wener, J. (2023). Energy Efficiency of Pneumatic Actuating Systems with Pressure-Based Air Supply Cut-Off. *Actuators*, *13*, 44. doi: https://doi.org/10.3390/act13010044.
[22] Gryboś, D., Leszczyński, J. (2024). Exergy analysis for the intermittent air supply in pneumatic machines. *4th International Fluid Power Conference*, Dresden 2024.
[23] SMC (2024). 4-Bar Factory - Accept the Challenge. *SMC Corporation* https://www.smc.eu/fi-fi/solutions/energy-efficiency/4-bar-factory.
[24] SMC (2024). Energy efficiency - Energy Optimization with SMC strategy. *SMC Corporation*. https://www.smc.eu/fi-fi/solutions/energy-efficiency.
[25] FESTO (2025). Compressed Air Energy Efficiency Audit. *FESTO Corporation*. https://www.festo.com/us/en/e/support/additional-services/compressed-air-energy-efficiency-audit-id_2012747/.
[26] Reese, C., Reinertz, O., Schmitz, K. (2024). Feasibility study and experimental validation of a novel combined throttling approach. *4th International Fluid Power Conference*, Dresden 2024.
[27] Schipiour, S. (2024). Transformative Advancements in Pneumatic Systems - Trends, Technologies, and Industry Applications. *Fluid Power Journal*. https://fluidpowerjournal.com/transformative-advancements-in-pneumatic-systems/.
[28] Sprink, J., Schmitz, K. (2024). Product carbon footprint of hydraulic and pneumatic components – challenges in accounting and comparability. *4th International Fluid Power Conference*, Dresden 2024.
[29] Eberhardt, T., Stegmaier, V., Schaaf, W., Verl, A. (2024). A trajectory-specific approach for calculating the required holding force for surface grippers. *4th International Fluid Power Conference*, Dresden 2024.
[30] Brezni, R. (2022). On the Air: How Smart Pneumatics Saves Costs and Helps the Planet, *Fluid Power Journal*. https://fluidpowerjournal.com/on-the-air-how-smart-pneumatics-saves-costs-and-helps-the-planet/.
[31] Melzer, F. (2022). When the Future of Robotics Becomes Pneumatics. *Tech Briefs - Engineering Solutions for Design & Manufacturing*. https://www.techbriefs.com/component/content/article/46682-when-the-future-of-robotics-becomes-pneumatics.
[32] Motion Control & Drives (2024). Latest trends in pneumatics systems. *South African Instrumentation and control*. https://www.instrumentation.co.za/21217r.

Static Properties Based Classification of Pneumatic Actuators - Potential of Progressive Effective Area Over the Stroke

Olivier Reinertz
RWTH Aachen University, Institute for Fluid Power Drives and Systems, Aachen, Germany
Olivier.reinertz@ifas.rwth-aachen.de

A variety of pneumatic actuator principles coexist on the market. The different designs are each dedicated to selected applications due to their specific properties and requirements. This paper aims to analyze the existing solutions by means of their static properties, to reveal innovation potential for new designs with enhanced operational behavior. It is based on a thorough investigation of the underlying physical correlations of force and stiffness. Thereof, a classification of existing principles is achieved, and a barely realized class of actuators with progressive effective area over the stroke is unveiled. A further analysis of the operational behavior of these actuators shows huge potential in selected applications. They are predicted to be superior in terms of performance and efficiency compared to existing solutions. A further analysis of the requirements on the design emphasizes the need for completely different realization concepts in comparison to the existing solutions. Finally, the paper closes by showing possible pathways to solve the actual challenges by incorporating new design methods.

DOI
https://doi.org/10.18690/um.fs.7.2025.9

ISBN
978-961-299-049-7

Keywords:
pneumatic,
actuators,
design,
actuator stiffness,
progressive force actuators

University of Maribor Press

1 Introduction

Pneumatic drives are widely used in mobile and industrial applications. While robustness and simple overload protection are key features of all fluid power actuators, open-loop controlled pneumatics additionally benefit from its simplicity in implementation and maintenance as well as low procurement costs. This makes technology especially relevant for automation tasks with low to medium power requirements. Other fields of application are mobile suspension systems and vibration isolating machine foundations, which benefit from the low stiffness of compressed air and the possibility of simple height adjustment during load changes. [1]

Different classes of pneumatic actuators can be distinguished by their design. The selection of a specific design for an application is usually driven by its robustness and geometric integratability. Furthermore, the curse of force and stiffness over the stroke and pressure and the friction induced hysteresis can be decisive parameters.

Usually, actuator sizing relies on the required stroke and the before-mentioned characteristics. Meanwhile, if standard control schemes are implemented to pneumatic drives, actuator sizing has a direct influence on the compressed air demand in operation. [2] Hence, the stroke and pressure dependent curse of force and stiffness of pneumatic actuators defines their sizing and directly influences the efficiency of the driven machines.

In the scope of this paper, the fundamental correlations of the static properties of pneumatic actuators are first deduced and then applied to the different actuator schemes on the market. Therewith, a new class of barely used actuators with progressive force over the stroke is unveiled and discussed by means of its usability in advantageous applications and its realizability. It will be shown that significant optimization in performance and efficiency is feasible by adapting the drive characteristics.

2 Fundamental static properties of pneumatic actuators

The fundamentals for calculating the main descriptive parameters for the operational behavior of pneumatic actuators, exerted force and stiffness, are briefly deduced in the following.

2.1 Fluidic force

For ideal actuators, which are free of friction and material hysteresis, a direct correlation between relative pressure(s), position, and the exerted fluidic force F_{fluid} exists. Hence, the force is independent from the fluid properties and the actuator's history.

The simplest load case for investigation of the actuator's force characteristic is the assumption of an incompressible fluid and an isobaric movement of the drive. Under these conditions the first law of thermodynamics can be easily applied. It requires that the fluidic energy provided to the actuator with volume V_A to hold its pressure p_{rel} constant during motion equals the mechanical work performed, which is given by the exerted force F_{fluid} and the stroke s in equation (1). This equation can be simplified to equation (2), which is generally applicable to all kinds of fluidic actuators.

$$p_{rel} \cdot \Delta V_A = p_{rel} \int_1^2 \frac{\partial V_A}{\partial s} ds = \int_1^2 F_{fluid}\, ds \tag{1}$$

$$F_{fluid} = p_{rel} \cdot \frac{\partial V_A}{\partial s} \tag{2}$$

It is obvious that the partial derivative of the volume over the stroke in the above-mentioned equation represents the fictitious active area of the actuator. Especially for non-linear systems, such as diaphragms, bellows and pneumatic muscles, this general relationship provides interesting insights into the actuator's fluid-mechanical properties, as will be shown in the following chapters. It should be noted that all forces, which result from the fluid pressure acting against the actuator chamber walls, which are transmitted through these walls or adjacent parts to the output, e.g., tensile forces in diaphragm walls, are included in the above calculation. Nevertheless, mechanical forces resulting from the mechanical stiffness of the actuator wall in the

working direction and/or friction forces at sliding seals need to be superimposed to the fluidic forces calculated with equation (2) for realistic results.

2.2 Actuator stiffness

The fluidic stiffness of an actuator can be expressed by the spring rate $k_{fluidic}$, which is defined by the local change in fluidic force F_{fluid} over the stroke with enclosed fluid. For a single actuator chamber, the fluidic stiffness results from equation (2) and is given by:

$$k_{fluidic} = -\frac{dF_{fluid}}{ds} = -\frac{dp_{rel}}{ds} \cdot \frac{\partial V_A}{\partial s} - p_{rel} \frac{d}{ds}\left(\frac{\partial V_A}{\partial s}\right) \tag{3}$$

Herein, the left term represents the portion of the actuator's stiffness, which results from a pressure change in the enclosed fluid due to the movement. Meanwhile, the right term covers stiffness, which results from a change in fictitious active area during displacement. Hence, the left term cannot be regarded without taking the compressibility of the enclosed fluid into account. To allow for fluid model integration, the change in fluid pressure needs to be a function of the fluid volume V_f, which equals the chamber volume V_A. Therefore, the equation is rearranged as follows:

$$k_{fluidic} = -\frac{dp_{rel}}{dV_f} \cdot \frac{dV_A}{ds} \cdot \frac{\partial V_A}{\partial s} - p_{rel} \frac{d}{ds}\left(\frac{\partial V_A}{\partial s}\right) \tag{4}$$

For soft actuators, the chamber volume changes not only with stroke but also with pressure. Therefore, partial derivatives of the volume with respect to the pressure and stroke need to be considered for a general stiffness equation:

$$dV_A = \frac{\partial V_A}{\partial s} ds + \frac{\partial V_A}{\partial p_{rel}} dp_{rel} = \frac{\partial V_A}{\partial s} ds + \frac{\partial V_A}{\partial p_{rel}} \cdot \frac{dp_{rel}}{dV_f} dV_A \tag{5}$$

Thereof, the volume change of the actuator over the stroke results:

$$\frac{dV_A}{ds} = \frac{\frac{\partial V_A}{\partial s}}{1 - \frac{\partial V_A}{\partial p_{rel}} \cdot \frac{dp_{rel}}{dV_f}} \tag{6}$$

The denominator of equation (6) shows that the pressure build-up in the fluid due to a reduction in volume and the wall strain caused by this pressure have an opposite effect on the stiffness. Stepping back to the right term of equation (4), the influence of the pressure on the partial derivative of the volume over the stroke needs to be considered for soft actuators. This leads to the following total derivative:

$$\frac{d}{ds}\left(\frac{\partial V_A}{\partial s}\right) = \frac{\partial^2 V_A}{\partial s^2} + \frac{\partial^2 V_A}{\partial s \partial p_{rel}} \cdot \frac{dp_{rel}}{ds} = \frac{\partial^2 V_A}{\partial s^2} + \frac{\partial^2 V_A}{\partial s \partial p_{rel}} \cdot \frac{dp_{rel}}{dV_f} \cdot \frac{dV_A}{ds} \tag{7}$$

Herein, the influence of the geometrical change in active area over the stroke is covered by the left term, while the right term describes the change in active area due to the stroke induced pressure fluctuation. Inserting equations (6) and (7) into equation (4) yields the general stiffness formulation for all kinds of actuators and arbitrary fluids:

$$k_{fluidic} = \frac{-\left(\frac{\partial V_A}{\partial s}\right)^2}{\frac{dV_f}{dp_{rel}} - \frac{\partial V_A}{\partial p_{rel}}} - p_{rel}\left(\frac{\partial^2 V_A}{\partial s^2} + \frac{\frac{\partial^2 V_A}{\partial s \partial p_{rel}} \cdot \frac{\partial V_A}{\partial s}}{\frac{dV_f}{dp_{rel}} - \frac{\partial V_A}{\partial p_{rel}}}\right) \tag{8}$$

A further assessment of the stiffness in pneumatic applications requires an approximation of the pressure/volume correlation of the gaseous fluid. Under the assumption that no change in air mass occurs during actuator motion, a polytropic change of state with the polytropic exponent n is used to describe the actuator's internal absolute pressure p_A:

$$p_A V_f^n = const. \quad \Rightarrow \quad \frac{dV_f}{dp_{rel}} = \frac{dV_f}{dp_A} = \frac{V_A}{-n \cdot p_A} \tag{9}$$

Under the assumption of a neglectable pressure-induced volume change and under consideration of the ambient pressure p_{amb} the stiffness calculates to:

$$k_{pneu} = \frac{n \cdot p_A}{V_A}\left(\frac{\partial V_A}{\partial s}\right)^2 - (p_A - p_{amb}) \cdot \frac{\partial^2 V_A}{\partial s^2} \tag{10}$$

The stroke dependent mechanical stiffness of the actuator housing, internal springs, etc. are neglected in the following, but can be superimposed to the result of the fluidic spring stiffness $k_{fluidic}$ or k_{pneu}. In the case of double acting drives, the stiffnesses of both chambers need to be considered.

3 Classification of existing pneumatic actuators

In the following, relevant existing design schemes of pneumatic actuators are described and classified according to the stroke dependence of their force. Therefore, positive stroke direction is chosen to raise the actuator's volume. Therewith all actuators move in positive direction during pressurization. To allow for better comparability, single acting devices are investigated. However, the results can be extrapolated to double-acting systems without any restrictions. For stiffness-evaluation of double acting devices, the stiffness of both chambers at the corresponding pressures needs to be taken into account.

3.1 Cylinders

The pneumatic cylinder is the primary actuator for automation purposes. Due to its rigid structure, volume increases linearly with the stroke and the differential in equation (2), which equals the fictitious active area, corresponds to the geometric piston area. Unavoidable seal friction needs to be considered and can pose a challenge in servo-controlled systems, low pressure applications or strongly miniaturized designs.

3.2 Membrane and diaphragm actuators

The sealing of the drive chamber by means of a flexible part allows to circumvent friction forces and leakages of translational seals of conventional cylinders. Depending on the shape of the used elastic part and piston, different designs with specific properties can be distinguished. The most relevant are briefly discussed in the following and depicted in Figure 1.

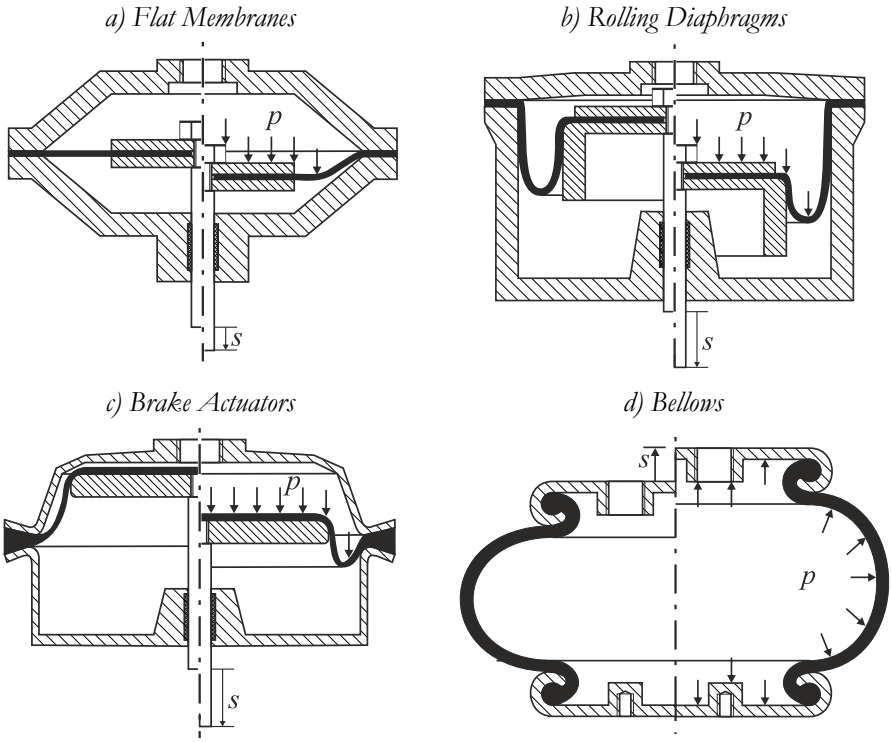

Figure 1: Investigated membrane actuators;
left: depressurized in neutral position, right: pressurized at stroke *s*;
Source: own

By using membranes or diaphragms for sealing, stick-slip effects at slow motion and hysteresis in force control can be avoided. This makes these actuators well suited as pneumatic springs in machine suspensions and actuators in control applications, e.g. for pneumatically controlled valves and brakes. Nevertheless, due to the viscoelastic material properties of the elastomeric parts used, some force hysteresis in cyclic motion is unavoidable [3].

3.2.1 Flat membranes

In Figure 1, a), a sketch of a typical realization of a flat membrane actuator is shown. To allow for sufficient mechanical stress distribution in the membrane, a rigid piston is connected to the load bearing rod, which holds the inner part of the membrane.

The membrane needs to allow for elastic deformation, as radial elongation is required for the piston stroke. Therefore, the stroke of flat membranes is usually very limited. If the piston moves out of its neutral position and pressure-induced deformation of the membrane is neglected, the membrane is deformed into a conical shape. Hence, the actuator's chamber volume can be described by the volume of a truncated cone, as given in equation (11). Herein the membrane geometry factor β equals the quotient of inner to outer diameter of the flexible part of the membrane and lies between zero and one.

$$\frac{\partial V_{dia}}{\partial s} = \frac{\pi R_{dia}^2}{3}(1 + \beta + \beta^2) \tag{11}$$

This equation obviously shows a stroke independent behavior, which is rarely achieved in real applications. Due to the elasticity of the membrane, the pressure leads to a convex shape of the membrane and therefore increases the chamber volume. According to *Yakovlev et al.* [4], the volume change of the drive chamber can be described by the semi-empirically deduced so called Liktan equation:

$$\frac{\partial V_{cyl}}{\partial s} = \frac{\pi R_{Cyl}^2}{3}\left(1 + \beta + \beta^2 - \frac{s}{\sqrt{5s_{max}(p)^2 - 5s^2}} \cdot (1 - \beta)\sqrt{4 + 7\beta + 4\beta^2}\right) \tag{12}$$

It is important to note that the design specific and pressure dependent imaginary stroke s_{max} cannot be reached by the actuator. The additional term of the Liktan equation is monotonically falling for constant pressure, which implies that the force of the actuator behaves accordingly.

3.2.2 Rolling diaphragm cylinders

The rolling diaphragm principle is widely used in applications requiring low friction and higher strokes compared to the flat membrane principle. The task of the rolling diaphragm is to seal the significant gap between piston and cylinder wall, as shown in Figure 1, b).

Therefore, it sticks on both the cylinder and the piston circumference and rolls from one surface to the other during piston motion. The rolling diaphragm is only pressurized from one side and its length in an axial cut plane stays constant over the

stroke. Hence, the bulge of the diaphragm curvature moves at half the piston speed. This leads to equation (13) for the description of the rolling diaphragm actuator's volume with cylinder wall radius R_{cyl} and piston radius R_{piston}. It is obvious that the actuator's force is, in analogy to a conventional cylinder, stroke independently. [5]

$$\frac{\partial V_{roll}}{\partial s} = \left(\frac{R_{cyl} + R_{piston}}{2}\right)^2 \cdot \pi \tag{13}$$

A drawback of this solution is, that the piston axial length, which directly influences the length of the actuator, needs to be at least half the stroke length. Therefore, rolling diaphragm actuators are suboptimal for higher stroke length especially in applications with strong demands on building space and weight.

In pneumatic suspension of mobile equipment, so called air bags are frequently used, which represent a special design of rolling diaphragms. The diaphragm is designed to withstand the tangential tensile forces generated by the pressurization, so that the outer support cylinder required for conventional rolling diaphragm devices can be omitted. A nearly constant force is achieved for isobaric conditions over the usual stroke regime. In the second stroke half, the exerted force usually decreases, as the diameter of the air bag decreases over its length to match the piston diameter at its end. Exemplary information on design and corresponding force characteristics can be found e.g. in [6].

3.2.3 Brake actuators

The demand for low costs, long lifetime, and reduced building space has led to the development of multiple designs of brake actuators, which differ among others in the shape of the membrane and piston. Besides rolling diaphragm designs there are also top hat membranes on the market [7]. A top-hat membrane is frequently used with a reduced piston length, ending up in a piston design being only a flat plate with rounded corners [8], as shown in Figure 1, c). Meanwhile, the diaphragm form stays comparable to a rolling diaphragm with the only difference in operating behavior, that a radial deformation of the diaphragm arises, which leads to additional chamber volume. As this chamber extension is very pronounced at stroke begin, the force in this regime is amplified. For symmetry reasons, the force reduces also at stroke end

accordingly, as the diaphragm is tensioned again by the axial piston movement and chamber volume increase is limited thereby. Mathematical description of the volume stroke correlation of such actuators is rather complex due to the pressure and stroke dependent deformation of the elastic diaphragm and the multiple geometry parameters, which need to be considered [9]. However, a rough approximation of the force can be achieved by using equation (12).

3.2.4 Bellows

Pneumatic bellows are primarily used in machine or vehicle suspension systems and as pneumatic actuators, if side and angular movements are unavoidable. They consist of two rigid plates, which are connected by one or multiple elastomeric bellows, as shown in Figure 1, d). The benefit of stacking multiple convolutions lies in the higher strokes feasible without excessive material deformation, while the total length to diameter ratio of such systems is limited by buckling effects. Therefore, the number of convolutions lies usually between one and three. [10]

The force characteristics have been investigated by *Quaglia and Guala* [11]. An exact analytical solution is not feasible, but good approximation is achieved by the following equation (14). Therein, the radius of the end plate R_{plate} and the longitudinal fixed length of the fiber reinforced elastic wall L_F define the actuator geometry and thus its force capability. The stroke is measured between the upper and lower end plate and is always smaller than the longitudinal wall length.

$$\frac{\partial V_{roll}}{\partial s} = R_{plate}^2 \cdot \pi \cdot \left(1 - \frac{L_F}{R_{plate}} \cdot \frac{\cos\left(a\sqrt{1-\frac{s}{L_F}}\right)}{a\sqrt{1-\frac{s}{L_F}}} \right) \quad \text{with} \quad a = \sqrt{\frac{\pi^3}{4\pi-8}} \tag{14}$$

The resulting equation describes a continuously decreasing force over the stroke at constant pressure.

3.3 Pneumatic artificial muscles

While common membrane and diaphragm actuators are built to push the load, pneumatic muscles are designed to pull the load during pressurization. Depending on the technical realization, different designs of pneumatic artificial muscles (PAMs) are distinguished. An overview is given in Figure 2.

These consist at least of two rigid end cups, which allow for their mechanical integration, and an interconnecting elastic wall. This wall contains or is wrapped by fibers that connect the two ends. The different designs differ in the geometry of the sealing wall and the arrangement of the fibers. The common working principle is that the radial pressure load on the elastic wall tends to raise the radius of the assembly. As the elasticity of the fibers is negligible, the distance of the end pieces must decrease as the radius increases while the pressure force on the end cups counteracts the fiber forces. As the surface of the end faces is usually very limited and the pressure force exerted by the elastic housing is amplified through the fiber arrangement, the fiber forces in axial direction are dominant and the device shortens during pressurization. In order to avoid the generation of torques at the end pieces, the fibers are usually symmetrically wound in both directions of rotation so that the resulting torques compensate for each other.

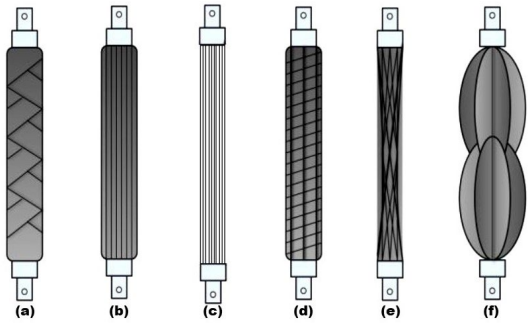

Figure 2: Overview of PAMs: (a) McKibben Muscle/Braided Muscle; (b) Pleated Muscle; (c) PAM reinforced by Kevlar Fiber; (d) Yarlott Netted Muscle; (e) Paynter Hyperboloid Muscle; (f) ROMAC Muscle;

Source: [11]

The only available design on the market is the McKibben PAM. According to *Takosoglu et al.* its static force/stroke characteristic can be modeled by equation (15) [13]. The parameters *b*, *n*, and *c* are positive numbers and need to be empirically adjusted by means of measurement data. For higher model accuracy these can be tuned as a function of the pressure.

$$\frac{\partial V_{PAM}}{\partial s} = R_i^2 \cdot \pi \cdot \left(b \cdot \left(1 - \left(\frac{s}{L_{max}}\right)^n\right) - c\right) \tag{15}$$

Thereof, it can be concluded that also for PAMs, which generate tensile forces, the force decreases over the stroke.

3.4 Summary of existing designs

The before-mentioned actuator designs and the stroke dependence of their force are summarized in Table 1. This overview demonstrates that actuators with stroke independent and decreasing force over the stroke exist. Actuators with continuously increasing force over the stroke at constant pressurization are non-existent on the market to date. The following chapter is dedicated to this non-existent class of actuators.

Table 1: Overview of existing designs

Actuator Design	Force characteristics	Force direction
Cylinder	stroke-independent	Single or double acting
Flat Membrane	mostly stroke-independent	Single or double acting
Rolling diaphragm	stroke-independent	Single acting
Brake actuator	mostly stroke-independent	Single or double acting
Bellow	Falling over the stroke	Only Extension
PAM	Falling over the stroke	Only Retraction

source: own

4 Actuators with increasing force over the stroke

The volumetric constraints to achieve actuators with significantly increasing force over the stroke at constant pressurization are achieved through differentiating equation (2), which leads to equation (16).

$$\frac{dF_{fluid}}{ds} > 0 \Rightarrow \frac{\partial^2 V_A}{\partial s^2} > 0 \tag{16}$$

It shows that the actuator volume needs to follow a progressively increasing function over the stroke. In the following, the potential of such actuators, their design challenges, which hinder their industrialization, and possible solutions are investigated.

4.1 Potential

Pneumatic actuators are widely used in many different applications with their own special demands on actuator performance. Therefore, in this chapter, only selected applications will be focused to highlight opportunities resulting from a progressive force/stroke characteristic.

4.1.1 Suspension systems

A closer look at the stiffness equations in chapter 2 unveils the potential to realize actuators, with outstanding stiffness properties. Therefore, at first, an actuator with parabolic volume stroke correlation, as given in equation (17), is investigated. Its force can be easily deduced, as shown in equation (18) Moreover, equation (10) is applicable and, due to its specific design, the resulting stiffness of the actuator in equation (19) is stroke independent.

$$V = \frac{A^2}{4B} + A \cdot s + B \cdot s^2 \tag{17}$$

$$F = (p_A - p_{amb}) \cdot (A + 2B \cdot s) \tag{18}$$

$$k = (2n - 1) \cdot 2B \cdot p_A + 2B \cdot p_{amb} \tag{19}$$

Another interesting application is to realize actuators, which allow for stiffness minimization while maintaining sufficient load bearing capability and small dead volumes. This is especially interesting for machine suspensions aiming to decouple the machine from the building structure by suspending the machine mass with the lowest possible eigenfrequency. A promising approach is an exponential volume/stroke characteristic, which results in the properties in equations (20) to (22).

$$V_{exp} = K \cdot \mathrm{e}^{(L \cdot s)} \tag{20}$$

$$F_{exp} = (p_A - p_{amb}) \cdot K \cdot L \cdot \mathrm{e}^{(L \cdot s)} \tag{21}$$

$$k_{exp} = ((n - 1) \cdot p_A + p_{amb}) \cdot K \cdot L^2 \cdot \mathrm{e}^{(L \cdot s)} \tag{22}$$

When comparing the operating behavior with the properties of a conventional actuator, e.g., a cylinder or a rolling diaphragm, a significant reduction in stiffness gets apparent. For comparison, the effective area A_{cyl} and position s_{cyl} of the cylinder can be determined in such a way that pressure, force, and volume are equal to the exponential actuator for a specific position s_0. This leads to the following equations:

$$F_{exp} = F_{cyl} = (p_A - p_{amb}) \cdot A_{cyl} \quad \Rightarrow \quad A_{cyl} = K \cdot L \cdot \mathrm{e}^{(L \cdot s_0)} \tag{23}$$

$$V_{exp} = V_{cyl} = s_{cyl} \cdot A_{cyl} \quad \Rightarrow \quad s_{cyl} = \frac{1}{L} \tag{24}$$

Thereof, the stiffness of the reference actuator in equation (25) results.

$$k_{cyl} = \frac{n \cdot p_A}{V_{cyl}} \left(\frac{\partial V_{cyl}}{\partial s_{cyl}} \right)^2 = n \cdot p_A \cdot K \cdot L^2 \cdot \mathrm{e}^{(L \cdot s_0)} \tag{25}$$

The comparison of equations (22) and (25) leads to equation (26). It demonstrates the strongly reduced stiffness in comparison to commonly used designs at significant chamber pressures for all polytropic coefficients between 1 and 1.4, as shown in in equation (27).

$$\frac{k_{exp}}{k_{cyl}} = \frac{n-1}{n} + \frac{p_{amb}}{n \cdot p_A} \tag{26}$$

$$\frac{p_{amb}}{p_A} < \frac{k_{exp}}{k_{cyl}} < 0.286 + 0.714 \cdot \frac{p_{amb}}{p_A} \tag{27}$$

Vice versa, a strongly reduced volume at the same stiffness in comparison to conventional actuators is achievable. Especially in the case of servo-controlled suspension systems, e.g. for position control or active damping, the volume reduction at constant stiffness can lead to significant improvements in control dynamics and compressed air demand.

4.1.2 Energy savings in automation

Compressed air consumption of pneumatic actuators with conventional control schemes, as e.g. downstream throttling or direct pressurization with the control-valve, is defined by the actuator chamber's volume at stroke end $V_A(s_{max})$, the specific

gas constant R and the pressure p_S and temperature T_S of the air supply, as shown in equation (28).

$$m_{Air} = \frac{p_S}{R \cdot T_S} \cdot V_A(s_{max}) \tag{28}$$

To fulfill the task, the actuator needs to overcome the force demand over the stroke $F_{Load}(s)$ in all positions, as shown in equation (29). Thereof, the minimum required compressed air mass to fulfill the task in equation (30) is achieved.

$$F_{Load}(s_A) < (p_S - p_{amb}) \cdot \frac{\partial V_A}{\partial s} \tag{29}$$

$$m_{Air,min} = \frac{p_S}{R \cdot T_S} \cdot \frac{\int_0^{s_{max}} F_{Load}(s_A) ds_A}{(p_S - p_{amb})} \tag{30}$$

If the application requires the highest force only at stroke end, which is the case in many clamping and pressing operations, the partial derivative of the volume over the stroke at stroke end needs to match the force demand. In the previous chapter, it has been shown that the volume change over the stroke of all existing actuators is either constant or decreases. This means, that in the entire stroke regime with lower force demand, strong oversizing of the actuator occurs. Therewith, for all existing actuators, the real air mass demand is given by equation (31).

$$m_{Air,conv} > \frac{p_S \cdot s_{max}}{R \cdot T_S} \cdot \frac{max\{F_{Laod}(s)\}}{(p_S - p_{amb})} \tag{31}$$

In contrast to this, if an exemplary drive with parabolic volume stroke correlation (see equation (17)) is used, which has only half of the maximum force at stroke begin and, in analogy to the before stated calculations, no dead volume, its stroke dependent volume and the resulting compressed air demand are given by equation (32) and (33). Thus, a 25 % reduction in air consumption is achieved simply by changing the actuator characteristic to a more application specific design.

$$V_{A,parab} = \frac{max\{F_{Laod}(s)\}}{2(p_S - p_{amb})} \cdot \left(s + \frac{s^2}{2s_{max}}\right) \tag{32}$$

$$m_{Air,parab} = \frac{3}{4} \frac{p_S \cdot s_{max}}{R \cdot T_S} \cdot \frac{max\{F_{Laod}(s)\}}{p_S - p_{amb}} \tag{33}$$

The optimization potential is application and actuator specific, as the load force needs to be overcome in all stroke positions and an actuator principle allowing for the optimal force/stroke correlation needs to be found.

4.2 Design challenges and solution approaches

The force of sliding-seal free actuators can be split into two parts: the stroke invariable pressure force, which acts directly on the movable rigid surface of the actuator chamber in direction of motion and the force contribution of the pressure forces acting against the actuator's wall and thus indirectly contributing to the actuator's force. The requirement of an increasing force over the stroke can therefore only be realized by changing the axial force of the side walls. It can be met either by a side wall, which decreasingly counteracts the pressure force on the moving end face over the stroke or by a side wall, which increasingly enforces the movement. In the following, due to the inherent reduction of the power density in the first case, only wall designs enforcing the actuator force are considered.

4.2.1 Tensile wall forces

Common nonlinear actuators possess elastic walls, which transmit primarily tensile forces on the moving end cap. The elasticity allows for a stroke variable cross-section of the actuator while the actuators' geometry is defined usually by integrated fibers with significant Young's modulus. To assist the drive's motion, these tensile forces need at least to act partially in moving direction. Theoretically, increasing assistance of these forces over the stroke can be achieved either by changing the forces' direction and/or its magnitude. Nevertheless, a design achieving the functionality mainly by changing the force direction has not been found to date. Instead, a change in assisting force magnitude can be achieved by the design proposed in Figure 3.

The main challenge in realization is to allow the pronounced tangential elongation of the elastic wall over the stroke without damage. A possible solution, which needs to be investigated in future, could be the use of a pumpkin inspired wall design in analogy to pleated muscles, with significantly higher stiffness in longitudinal compared to tangential direction.

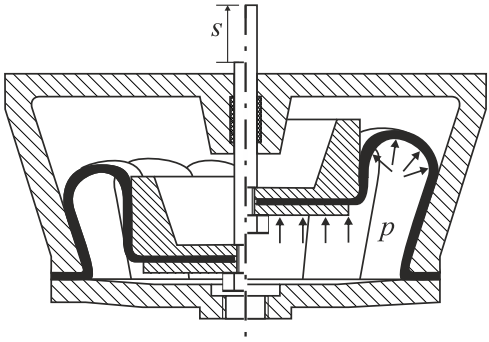

Figure 3: Rolling diaphragm in pumpkin inspired design
Source: own

4.2.2 Compressive wall forces

To allow for progressively increasing volume during elongation of the actuator a design with central constriction in analogy to an hourglass could be theoretically used, as it fulfills the volumetric requirements, see Figure 4, left. The constriction of the actuator shell is widened as the actuator elongates in axial direction. This leads to an additional volume increase over the stroke in comparison to conventional designs. However, the realization of such actuators would suffer from a compromise between rigidity of the wall for the compressive force transmission and elasticity of the wall for diameter and length change during motion. The same limitations apply to all elasticity-based design, if no additional rigid elements for force transmission are introduced.

A possible solution can be found by integrating rigid bars into the elastic wall of the hourglass design, which then represents a rotational hyperboloid, as shown in Figure 4, right. By allowing relative rotation of the two end caps, the central diameter increases at elongation of the actuator. Therewith, the elastic wall seals the system only between the rigid bars and is relieved from transmitting compressive forces. Unfortunately, strong angular distortions of the resulting facets between the rotating bars occur, which makes membrane design still a huge challenge.

An alternative to the above-mentioned designs is the introduction of an origami inspired actuator with rigid sealing facets, which are connected by sealed rotational joints. Despite the fact that such actuators cannot exist from a mathematical point

of view, as the bellows constriction prohibits the existence of a deformable polyhedron with a variable closed volume, the design in Figure 5 demonstrates that small deviations from a mathematically exact polyhedron by means of slight elasticity in selected segments (marked in blue in Figure 5) is sufficient for realization.

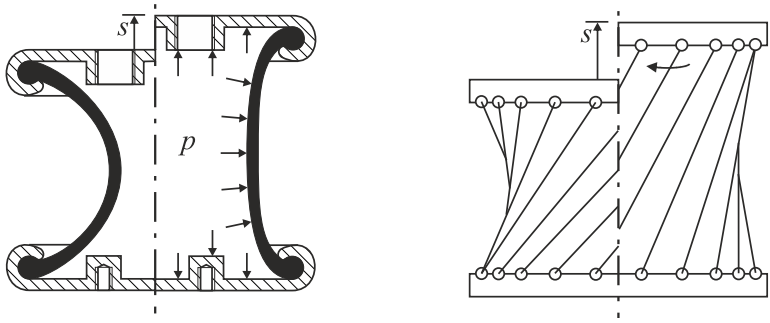

Figure 4: Hourglass actuator designs
Source: own

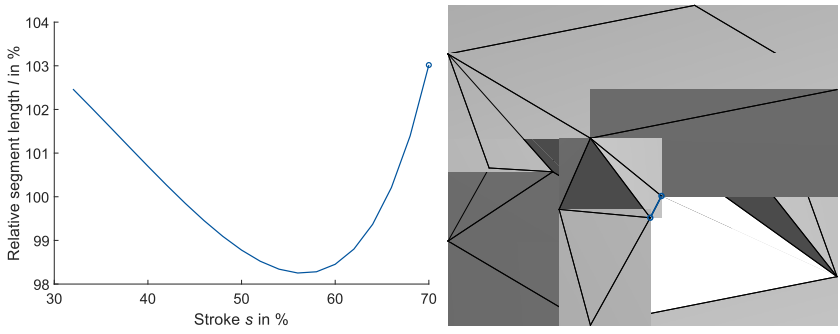

Figure 5: Origami inspired design and segment elongation during motion
Source: own

Obvious challenges are the implementation of the sealing system at all joints, the tolerance management to couple multiple facets to allow for a single degree of freedom in assembled state, the slight elasticity implementation and the fact, that a real actuator will have significant wall thickness to withstand internal pressure and compressive forces, which demands for significant design changes compared to the proposed principle.

5 Conclusion and Outlook

In the scope of this paper, a generalized form of the force and stiffness calculation for pneumatic actuators, which bases solely on the description of their internal volume in operation has been deduced. These fundamentals are not only relevant for the description of conventional pneumatic drives but can also enable fluidic stiffness calculation of soft actuators in early design stages by means of model-based calculation of the volume under deformation and pressurization.

Furthermore, these equations enable the classification of all relevant existing solutions of industrial pneumatic drives by their static characteristics. The result shows a whole class of actuators with progressive effective area over the stroke, which are neither available on the market nor systematically researched.

A first investigation of the potential of such actuators unveils different applications – clamping, pressing and machine suspension – that can be significantly optimized by replacing conventional actuators with devices of this new class. Consequently, the main arising design challenges are investigated and possible solutions discussed. Three different promising designs were elaborated, the conical rolling diaphragm in pumpkin design, the rotational hyperboloid actuator with push bars and the origami inspired actuator. Further studies on the realizability, arising challenges and the measured operational behavior of prototypical realizations are aspired in future.

References

[1] Murrenhoff, H., Reinertz, O.: *Fundamentals of Fluid Power - Part 2: Pneumatics*, 2nd edition, Shaker, Aachen, Germany, ISBN: 978-3-8440-3213-0

[2] Doll, M., Neumann, R., Sawodny, O.: *Dimensioning of pneumatic cylinders for motion tasks*, International Journal of Fluid Power, 2015, 16(1), pp. 11–24, doi: 10.1080/14399776.2015.1012437

[3] Gong, Y., Guo, H.: *Measurement and Modeling of Hysteresis in Pneumatic Actuator Under Different Loading Rate*, Proceedings of China SAE Congress 2018: Selected Papers, Lecture Notes in Electrical Engineering 574, Springer Nature Singapore, 2020, doi: 10.1007/978-981-13-9718-9_4

[4] Yakovlev et al.: *Static Characteristic of a Membrane Pneumatic Actuator*, Russian Engineering Research, 2022, 42(4), pp. 391–394, doi: 10.3103/S1068798X22040323

[5] N.N.: *Diaphragm Design Guidebook*, DiaCom Corporation, 2018

[6] N.N.: *Axle Guide – Running Gears for Commercial Vehicles: Selection, Design, Installation*, 1st edition, BPW Bergische Achsen KG, 2023

[7] N.N.: *Spring Brake Actuators for Air Disc Brakes*, Service Manual, Rev. 001, Knorr-Bremse Systeme für Nutzfahrzeuge GmbH, 2015
[8] Moni, Arangarason, A.: *Brake Chamber Type 12*, Specification Drawing, WABCO, 2021
[9] Fojtášek, K., Dvořák, L.: *Mathematical Modeling of Diaphragm Pneumatic Motors*, EPJ Web of Conferences, 2014, doi: 10.1051/epjconf/20146702028
[10] Chen, J.-J., et al.: *Theoretical modelling and experimental analysis of the vertical stiffness of a convoluted air spring including the effect of the stiffness of the bellows*, Proceedings of the Institution of Mechanical Engineers, Part D: Journal of Automobile Engineering, 2018, Vol. 232(4), pp. 547–561, doi: 10.1177/0954407017704589
[11] Quaglia, G., Guala, A.: *Evaluation and Validation of an Air Spring Analytical Model*, International Journal of Fluid Power, 2003, 4(2), pp. 43-54
[12] Kalita, B., Leonessa, A., Dwivedy, S. K.: *A Review on the Development of Pneumatic Artificial Muscle Actuators: Force Model and Application*, Actuators, 2022, 11, 288, doi: 10.3390/act11100288
[13] Takosoglu, J. E. et al.: *Determining the Static Characteristics of Pneumatic Muscles*, Measurement and Control, 2016, 49(2), doi: 10.1177/0020294016629176

Implementation and Experimental Validation of a Time-Controlled Quick-Exhaust for Downstream Throttled Pneumatic Drives

Luca Päßler, Christian Reese, Olivier Reinertz, Katharina Schmitz

RWTH Aachen University, Institute for Fluid Power Drives and Systems, Aachen, Germany
luca.paessler@ifas.rwth-aachen.de, christian.reese@ifas.rwth-aachen.de
Olivier.reinertz@ifas.rwth-aachen.de, katharina.schmitz@ifas.rwth-aachen.de

Downstream-throttled pneumatic cylinders are frequently utilized as actuators for motion tasks due to their cost-effectiveness, durability, and robustness. However, they are often regarded as energy-inefficient. This paper presents a novel approach to enhance efficiency by focusing solely on controlling the exhaust air. The proposed system utilizes a time-controlled pneumatic-mechanical quick-exhaust valve, which allows high acceleration at the start of the stroke and subsequent deceleration via conventional downstream throttling. Building on a previous lumped-parameter simulation study, this work details the technical implementation of the concept and provides experimental results that assess its performance and robustness. Comparative tests with a conventional downstream-throttled system demonstrate that the cylinder can be downsized by at least one size, thereby substantially reducing air consumption. However, this improvement comes at the cost of reduced robustness, which necessitates further investigation. The paper covers the entire development process from the initial concept, over the component design, robustness studies and improvements up to a final experimental validation of its dynamic behaviour and compressed air savings in direct comparison to a conventional downstream-throttled drive.

DOI
https://doi.org/10.18690/um.fs.7.2025.10

ISBN
978-961-299-049-7

Keywords:
pneumatics, pneumatic cylinder, energy efficiency, energy-saving circuit, exhaust control

University of Maribor Press

1 Introduction and state of the art

Pneumatic drives are widely utilized in industrial automation for point-to-point motions due to their simplicity, reliability, cost-effectiveness, and high power density [2]. Their operation relies on the pressure differential between the supply pressure acting on the active chamber and the back-pressure in the passive chamber. Typically, this back-pressure is regulated using downstream throttling (DT) to control the actuator's movement. However, downstream throttled systems are often considered inefficient because they consume the maximum amount of compressed air regardless of the load conditions [3].

Research on improving the efficiency of pneumatic cylinders can be divided into three categories: (1) design and parametric measures, (2) energy saving circuits (ESC), and (3) energy-saving systems [4]. The first category includes methods to optimize design and operating parameters, such as using different pressure levels for the extension and retraction stroke, reducing dead volume, and ensuring proper cylinder dimensioning. A well-known heuristic dimensioning approach by Doll et al. [5] compares a cylinder's eigenfrequency ω_0 to the required dynamics ω_f, thereby defining the *pneumatic frequency ratio* $\Omega = \omega_f/\omega_0$. An actuator is considered well-dimensioned if the pneumatic frequency ratio is between 1.1 and 1.7 [5].

ESCs enhance the efficiency by modifying the system structure for a specific load case [6]. Modifications may be upstream (e.g., early air shut-off via a 5/3 valve [7]) or downstream (e.g., storing exhaust air [8]). Recent research emphasizes combining upstream and downstream measures, such as the *combined throttling approach* [9], the *cross-flow circuit* [10] or the more complex *3-phase movement circuit* by Krytikov et al. [11] [12], which subdivides the motion into acceleration, deceleration with exhaust feedback, and fixation. The third category comprises mostly digitized energy-saving systems (e.g., a five-valve bridge circuit [13]) that offer both flexibility and efficiency for a variety of load cases [14].

Reese et al. [9] have developed a metric for evaluating the efficiency of ESCs. This metric involves comparing the consumed air mass and achieved cycle time of the ESC with the theoretical result of a well-dimensioned downstream throttled system performing the same motion task [9]. The normalized air saving $\Delta m_{\mathrm{norm},x}$ of system x is calculated by

$$\Delta m_{\mathrm{norm},x} = 1 - \left(\frac{m_{\mathrm{air},x}}{m_{\mathrm{air},DT}}\right) \cdot \left(\frac{t_{\mathrm{Cycle},x}}{t_{\mathrm{Cycle},DT}}\right)^2, \quad (1)$$

with m_{air} denoting the air mass consumption and t_{Cycle} the cycle time. Finally, the relative compressed air saving $\Delta m_{\mathrm{rel},x}$ can be expressed as a function of the relative increase in cycle time $\Delta t_{\mathrm{rel},x}$ and the normalized air saving:

$$\Delta m_{\mathrm{rel},x}\left(\Delta t_{\mathrm{rel},x}, \Delta m_{\mathrm{norm},x}\right) = \frac{m_{\mathrm{air},DT} - m_{\mathrm{air},x}}{m_{\mathrm{air},DT}} = 1 - \frac{1 - \Delta m_{\mathrm{norm},x}}{\left(\Delta t_{\mathrm{rel},x} + 1\right)^2} \quad (2)$$

Building upon the relationship between air consumption and cycle time, Reinertz et al. [1] developed a novel pneumatic-mechanical ESC to enhance the efficiency of pneumatic drives. Their approach focuses on reducing the cycle time of downstream throttled pneumatic drives, while keeping the component and commissioning expenses low [1]. By reducing the cycle time, the reciprocal quadratic relationship between air consumption and cycle time is exploited. In contrast to the conventional downstream throttled system, the novel system is extended by a switchable quick-exhaust (SQE) valve to initially increase the cylinder velocity. The SQE valve remains active during the initial and mid-part of the stroke, after which it is deactivated, allowing the exhaust air to flow solely through a downstream throttle arranged in parallel. This transition ensures that the cylinder speed is decreased by the downstream throttle, effectively preventing overloading the pneumatic end-cushion. This sequence is comparable to the movement phases of the *3-Phase Movement Circuit*. Compared to the *3-Phase Movement Circuit*, the novel system has two key differences: (1) The SQE valve is a purely pneumatic-mechanical component, which reduces the commissioning and control effort and (2) it focuses solely on the downstream, which is simpler and reduces installation space. In a preliminary feasibility study using a lumped parameter simulation, Reinertz et al. [1] showed that the cylinder can be downsized by at least one size with the novel system. However, they emphasized the necessity of experimental validation to confirm the concept's effectiveness.

This work aims to bridge this gap by providing technical implementation details and presenting experimental results of the novel system. The following sections are organized as follows: Section 2 describes the technical implementation of the proposed approach, Section 3 discusses the experimental setup and procedures, and

Section 4 presents the experimental results. Finally, Section 5 concludes this work and provides an outlook for future work.

2 Switchable quick-exhaust valve

Quick-exhaust valves provide a straightforward measure to enhance the velocity of pneumatic drives by reducing the back-pressure [15]. However, the integration of these valves must be managed carefully to prevent overloading the pneumatic end cushion. Excessive velocities or very low back-pressures can overload the end cushion, potentially causing damage to components or the load.

Rager et al. [16] investigated the energy-optimal operation of a pneumatic cylinder using a bridge circuit with an adaptive open-loop control. The findings of the study suggest that the energy-optimal trajectory is a sequence of an acceleration phase and a braking phase to reduce the cylinder velocity before it reaches the end cushion [16].

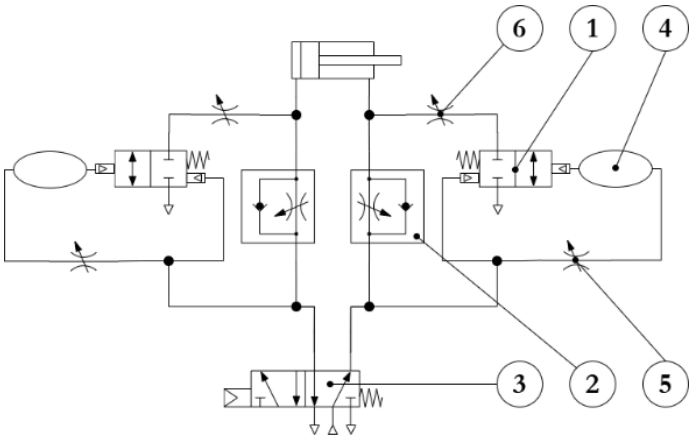

Figure 1: Schematic representation of the technical implementation of a downstream throttled actuator with a switchable quick-exhaust valve.
Source: own

This understanding of sequential acceleration and deceleration to protect the end cushion forms the foundation of a novel performance-enhancing approach involving the use of SQE valves. As described in patent DE102023104570B3 [17], this concept is realized by implementing SQE valves in parallel with the conventional

downstream throttles used for deceleration. As a result, the air in the passive cylinder chamber can be exhausted more rapidly through the low-resistance path of the open SQE valve, in contrast to the downstream throttle, thereby preventing the high back-pressure that would otherwise slow down the cylinder movement. A schematic representation of this advanced system is shown in Figure 1, and its method of operation is elaborated below.

The quick-exhaust (see Figure 1) is achieved by switching the SQE valve (1), arranged in parallel with the downstream throttle (2). The switching is based on the pressure drop in the pneumatic line that connects the downstream throttle of the cylinder to its directional control valve (3). When the direction of motion is reversed, i.e., when the active and passive chambers are switched, the pressure in this line suddenly drops. This pressure gradient is detected by comparing the line pressure with the pressure in a pneumatically damped dead volume (4). If a sufficient pressure difference arises due to a rapid pressure drop in the line, an additional cross-section is opened for venting the passive chamber. The parallel venting via the exhaust throttle and additional cross-section results in the desired quick-exhaust. The dead volume of the SQE valve is connected to the line via an adjustable throttle (5) so that the pressure in the dead volume follows the line pressure with a defined delay. The size of the dead volume, the cross-section of the damping throttle, and a minimum differential pressure specified by spring pressure for opening the SQE valve determine the duration of the quick-exhaust purely pneumatically and mechanically. To enable the utilization of the valve with varying cylinder sizes, the initial design was modified using an additional throttle (6) that defines the resistance of the quick-exhaust path compared to the downstream resistance.

Standard pneumatic components were utilized for the technical implementation of the SQE valve and the associated circuit, as illustrated in Figure 2. The circuit is connected to the cylinder via an adapter (7), which, in addition to the downstream throttle (2) and the throttle for controlling the quick-exhaust (6) (not mounted in the figure), also includes a pressure sensor (8) for measuring the chamber pressure. The actual SQE valve is designed as a low-friction, pneumatically actuated 5/2 directional control valve. One of the end caps has been replaced by a specially manufactured cap containing a spring that acts on the valve spool.

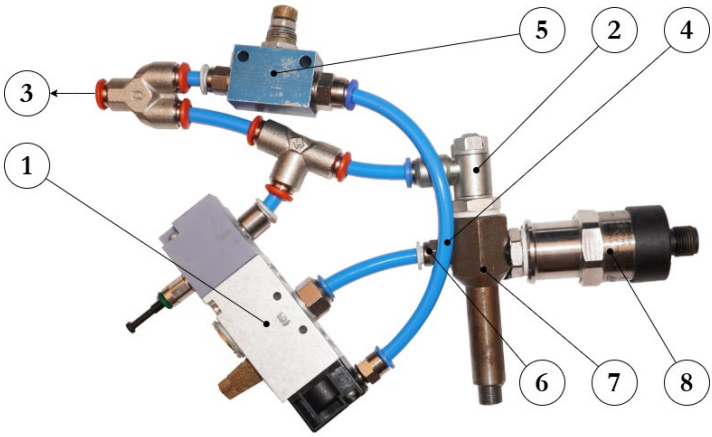

Figure 2: Technical implementation of the switchable quick-exhaust valve.
Source: own

3 Experimental setup

The novel system, described in Section 2, was experimentally investigated using a test rig for pneumatic cylinders. The test bench, which is described in detail in [9], enables the systematic study of various efficiency-enhancing concepts by measuring the cylinder dynamics under adjustable operating conditions. In addition to other measured variables, the cylinder position, the pressure in the cylinder chambers, and the air mass consumption are recorded. Using this setup, two distinct series of measurements were conducted: (1) to compare the novel system's performance with a conventionally downstream throttled system, and (2) to assess the robustness of the novel system with respect to the length of the pneumatic lines, which connect the directional control valve and the cylinder.

3.1 Measurement of the system performance

In the first series of measurements, the performance of the two systems was evaluated performing various movement tasks using different cylinder sizes. The air mass consumption of the novel system is normalized using Equation 1 to enable a direct comparison of its efficiency with the conventional system. Before data acquisition, each system is optimally adjusted to the motion task, so the cylinder has

a minimum movement time without overloading the pneumatic end cushion. Ideally, the impact velocity at the end of the stroke is zero.

To ensure accurate results, 55 cycles are recorded for each load case. The initial three cycles and the last two cycles are excluded from evaluation to ensure stable dynamic behavior. The supply pressure is set to 7 bar_{abs}, and the pneumatic line between the 5/2 directional control valve and the cylinder measures 1 m in length with an internal diameter of 4 mm. The investigated cylinders have a diameter of 20, 25, and 32 mm, a length of 0.2, 0.32, and 0.5 m, and a moving mass of 10 and 15 kg. This results in a total of 18 load cases investigated.

To contextualize these findings in existing research, a comparison is made with measurement results from a study by Boyko et al [6]. In this study, the ESCs *supply air cut-off*, *short circuit*, and *3-phase circuit* are examined for cylinders with a diameter of 32 and 50 mm and a length of 0.2 m. For comparison with the novel system, the load case of a well-dimensioned cylinder without additional external forces is utilized. The calculation of the relative cycle time $\Delta t_{\mathrm{rel},x}$ is determined by the relative moving time of the extension $\Delta t_{\mathrm{rel},e}$ and retraction strokes $\Delta t_{\mathrm{rel},r}$ and the respective pneumatic frequency ratio, as shown in Equation 3.

$$\Delta t_{\mathrm{rel},x} = 1 + \left(\Delta t_{\mathrm{rel},e} - 1\right) \cdot \frac{\Omega_e}{\Omega_e + \Omega_r} + + \left(\Delta t_{\mathrm{rel},r} - 1\right) \cdot \frac{\Omega_r}{\Omega_e + \Omega_r} \tag{3}$$

3.2 Measurement of the system robustness

In the second series of measurements, the robustness of the novel and conventional system regarding the length of the pneumatic line between the cylinder and the controlling directional control valve was investigated. To this end, both systems were optimally adjusted for pneumatic line lengths of 1 m, 4 m, and 6 m, using a cylinder with a piston diameter of 25 mm, a length of 0.5 m and a moving mass of 10 kg. Subsequently, the velocity profile of 55 cycles was recorded. In this series, we investigated how varying the line length affects the SQE valve's switching behavior by installing two additional pressure sensors on each SQE valve to measure the pressure on both sides of the valve spool.

4 Results and discussion

Figure 3 depicts the dynamic behavior of a cylinder with a piston diameter of 25 mm, a length of 0.32 m, and a moving mass of 10 kg under both SQE valve and DT configurations. The SQE valve allows faster air exhaust at the beginning of the movement followed by a deceleration through downstream throttling. As shown by the pressure curves, the back-pressure in the system equipped with SQE valves is substantially lower than in the system with DT. Correspondingly, the velocity curve indicates higher acceleration and greater maximum velocity in the novel system.

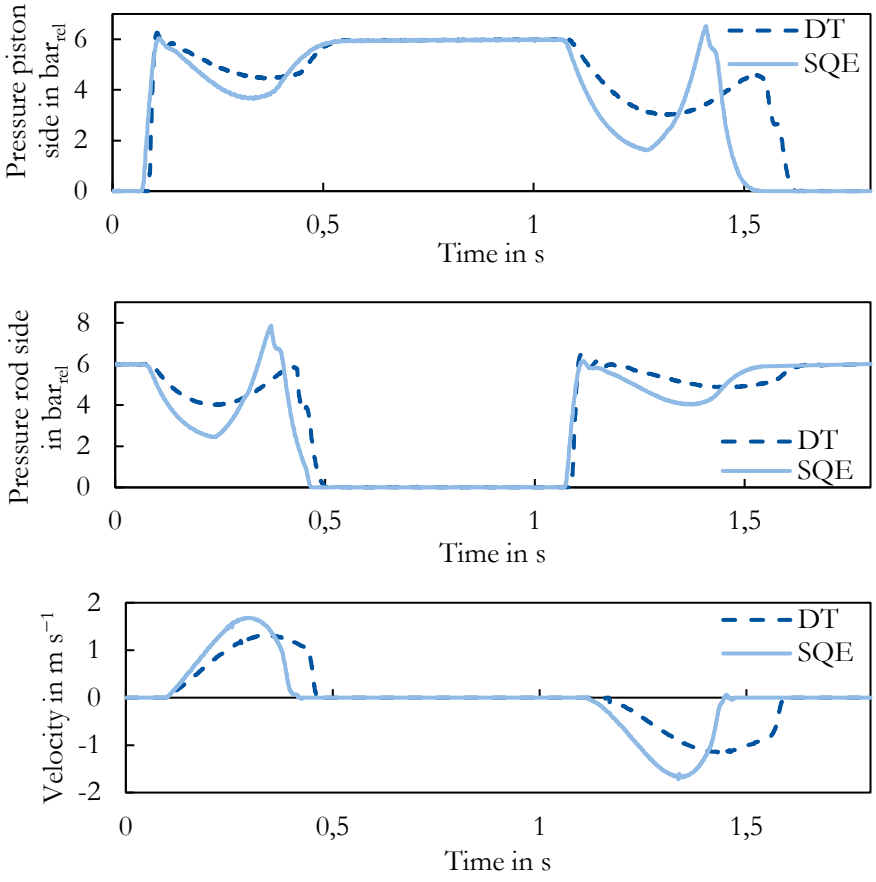

Figure 3: Experimental results of an actuator with a diameter of 25 mm, a stroke length of 0.32 m and a moving mass of 10 kg using downstream throttling (DT) and a switchable quick-exhaust (SQE).

Source: own

The switching point of the SQE valve is discernible in the pressure curve by the rising back-pressure. This increased back-pressure not only decelerates the cylinder but also enhances the capacity of the pneumatic end cushion. Consequently, even though the cylinder enters the end cushion with a higher velocity, it still decelerates sufficiently to keep the final impact velocity at a minimum level. As a result, implementing the SQE valve significantly shortens the cycle time from 0.94 to 0.78 s. Although most of the time reduction originates from the increased velocity during movement, the faster exhaust of the passive chamber also diminishes the delay time caused by the pressure adaption during retraction of a differential cylinder, as described by Reinertz et al. [3]

4.1 System performance

The measured movement times of the cylinders equipped with an SQE valve and a moving mass of 10 kg are summarized in Figure 4. In addition, the quick-exhaust duration is shown. For comparison, the movement time of the DT system is included. Two general trends apply to both systems: first, movement time typically decreases with increasing piston area, and second, the extension stroke usually finishes faster than the retraction stroke because of the smaller piston surface in the rod-side chamber. It can also be observed that movement time increases with cylinder length, as traveling a longer distance without a higher acceleration naturally prolongs the stroke.

As seen in Figure 4, all cylinders equipped with the SQE valve exhibit significantly shorter movement times than those operating with DT. This performance gap widens with the cylinder length. The effect of piston diameter on the SQE valve dynamic is more subtle. Its impact becomes clearer when focusing on how long the quick-exhaust valve remains open. In most of the cases considered, the proportion of the quick-exhaust time ranges from 40 to 60 % of the movement time. For a cylinder diameter of 32 mm, the proportion of time spent with the SQE valve open can exceed 80 % of the stroke for cylinder lengths of 0.32 m and 0.5 m. This phenomenon arises because the same SQE demonstrator was tested for every cylinder. When the SQE valve is undersized relative to a large piston area or long cylinders, the cylinder effectively experiences some additional back-pressure during the quick-exhaust phase. This back pressure decelerates the movement, allowing the valve to remain open for a longer duration without overloading the end cushion.

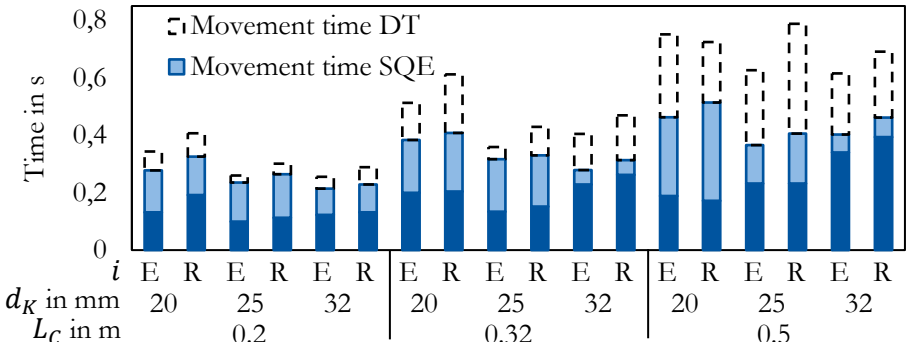

Figure 4: Movement time and quick-exhaust time of cylinders with different piston diameters d_K and cylinder lengths L_C, equipped with a switchable quick-exhaust (SQE) valve and a moving mass of 10 kg. The index i denotes the extension stroke ($i = E$) or the retraction stroke ($i = R$).

Source: own

Figure 4 shows for example, that a cylinder measuring 0.2 m in length and 32 mm in diameter can be downsized by one size yet maintain the same cycle time if SQE valves are used. For the cylinders with the lengths 0.32 and 0.5 m, the piston diameter can be reduced by at least two sizes under the same supply pressure without sacrificing performance. Smaller cylinder dimensions are advantageous because they substantially lower both acquisition costs and air consumption. Although increasing the moving mass to 15 kg prolongs the cycle time because of greater inertia, the overall difference in performance between DT and SQE configuration is similar to that observed at 10 kg.

As the cylinder length increases, the air consumption per cycle increases as well for both the DT and SQE system. However, cylinders equipped with SQE valves exhibit a slightly higher consumption due to the presence of supplementary components, which introduces additional dead volume. However, given the reduced cycle time of the novel system, there is a strong reduction in normalized air consumption. For cylinders with a length of 0.2 m, the advantage is negligible; however, as the cylinder length increases, the discrepancy in air consumption between the two systems becomes more evident. It is noteworthy that the moving mass exerts minimal influence on these efficiency gains, also comparable trends are observed for every piston diameter that was investigated.

Equation 2 is employed to calculate isolines corresponding to constant normalized air savings. These isolines, depicted in Figure 5, provide a framework for comparing the two systems. The isoline marked with zero represents no efficiency gain or loss relative to DT. Operating points to the left indicate enhanced efficiency, while those to the right reflect a decrease.

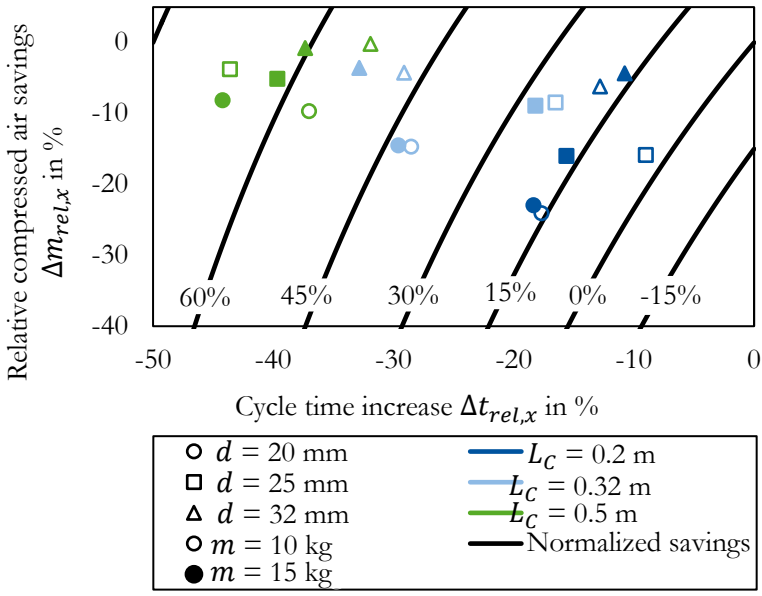

Figure 5: Efficiency map of a cylinder with a piston diameter of d, a length of L_C and a moving massof m.

Source: own

Figure 5 demonstrates that the SQE valve yields higher efficiency throughout the tested parameter space. While the normalized air savings of cylinders with a length of 0.2 m are the lowest, with values ranging from 0 to 30 %, cylinders with a length of 0.5 m demonstrate the highest normalized air savings, ranging from 45 to 75 %. The moving mass has minimal influence on these results, as nearly identical trends emerge regardless of the mass.

Also, the piston diameter does not significantly affect the improvement of energy-efficiency. Despite the fact that the SQE valve is undersized for the cylinder with a diameter of 32 mm, the efficiency gains remain comparable to those obtained with

other piston diameters investigated. Notably, for 0.32 m cylinder lengths, the energy-efficiency enhancement is even higher than that of smaller diameters, suggesting that an extended quick-exhaust phase compensates for an undersized valve.

A comparison of the normalized air savings achieved using the SQE valve with the results of other ESCs shows that the normalized air savings are in a medium range when only comparing cylinders with a length of 0.2 m. The novel system demonstrates superior efficiency in comparison to the short circuit, attaining results that are analogous to the supply air cut-off circuit within the range of 0 to 30 %. The 3-phase circuit exhibits a substantially higher degree of air savings in comparison with the novel system, at approximately 75 %. However, the novel system demonstrates comparable values when utilizing longer cylinders. Due to the absence of data concerning the other ESCs, the competitive dynamics of the circuits at extended cylinder lengths remain uncertain.

Compared to other ESCs, especially the 3-phase circuit, the novel system exhibits reduced commissioning and control effort, as well as lower component costs. These results underscore the system's viability while highlighting the need for further research to refine the SQE valve design and perform a more extensive study comparing different ESCs.

4.2 System robustness

Downstream throttled systems can be operated under various operating conditions, due to their robustness. Consequently, the second series of measurements investigated the impact of the pneumatic line length on the switching behavior of the SQE valves, thereby assessing the robustness of the novel system. Figure 6 illustrates the velocity curves of the extension stroke resulting from different pneumatic line lengths for a cylinder with a piston diameter of 25 mm, a length of 0.5 m and a moving mass of 10 kg.

As illustrated in the Figure 6, the length of the pneumatic line exerts a comparable influence on the dead time of both systems. However, a clear distinction emerges when comparing the movement time of both systems. With pneumatic lines of 1 m length, the maximum velocity of the system equipped with SQE valves is shown to be approximately double the maximum velocity of the downstream throttled system,

while maintaining a low impact velocity at the end of the stroke. The movement time decreases from approximately 0.68 s to 0.40 s by using the SQE-valves in this case. Increasing the length of the pneumatic lines results in a substantial reduction in maximum velocity of the novel system. Consequently, the movement time is prolonged to 0.57 s at a length of 4 m and 0.55 s at a length of 6 m. In contrast, the DT system's movement time changes only minimally. Because of an unstable swtiching behavior of the SQE valves at 6 m line length, no optimal cylinder setting was found. The only possible setting lead to an increased impact velocity, visible as oscillations at the stroke end.

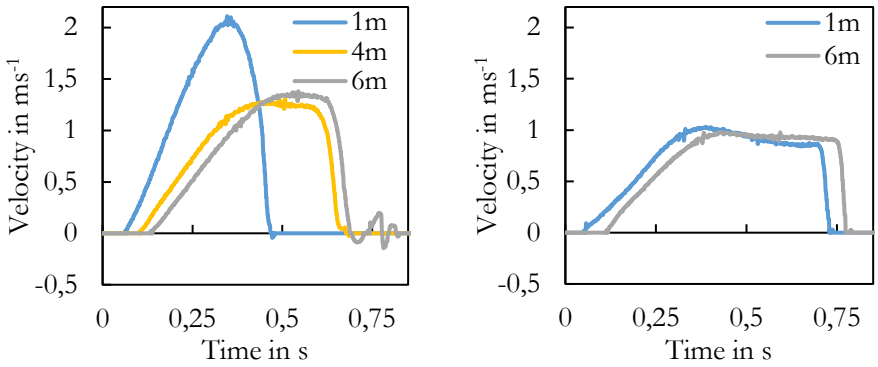

Figure 6:Cylinder velocity with varying pneumatic line lengths.
Source: own

Figure 7 illustrates the pressure difference between the two pressure signals of the SQE valve for the three investigated line lengths. Additionally, the switching point in time and the gradient of the pressure difference is shown for each curve. The figure shows the underlying rationale for the challenging adjustment with longer pneumatic lines. Longer lines result in a slower decline of the pressure in the line. To ensure an opening of the SQE valve, it is necessary to reduce the cross-section of the time controlling throttle, thereby ensuring that the pressure in the dead volume lags the pressure in the pipe. However, this results in a prolonged duration of the quick-exhaust. To avoid overloading the end cushion, the cross-section of both the downstream throttle (number 2 in Figure 2) and the quick-exhaust path (number 6 in Figure 2) must be reduced, which in turn lowers the maximum velocity.

Another negative effect of longer pneumatic lines is the lowered gradient of the pressure difference during the switching point. The greater the gradient, the more reliable the valve switches. However, given the necessity of lowering the cross-section of the time controlling throttle with extended lines, the gradient experiences a decline, as illustrated in Figure 7. This results in a more unstable switching behaviour.

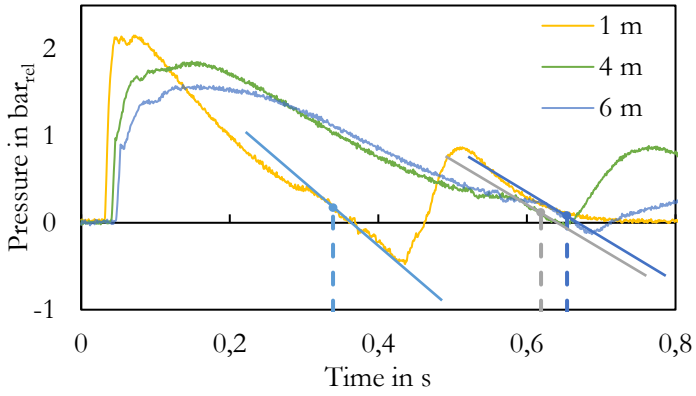

Figure 7: Pressure difference between the switching signals of the switchable quick-exhaust valve for different pneumatic line lengths.

Source: own

In summary, while performance benefits remain measurable even with extended pneumatic lines, the system's robustness is lower than that of a conventional downstream-throttled system.

5 Conclusion and Outlook

This work presents experimental results for a novel approach aimed at improving the dynamic performance of downstream-throttled pneumatic drives. By employing SQE valves as a pneumatic-mechanical solution, the system achieves lower cycle times. This reduction in cycle time is significant due to the relationship between cycle time and air consumption in pneumatic-drive sizing. Therefore, the shorter cycle times can be transferred into reduced air consumption.

The results demonstrate that downsizing a cylinder by at least one size is feasible using the SQE system. Notably, longer cylinders show even greater performance improvement when equipped with the quick-exhaust valve. Moreover, the findings indicate a substantial potential for enhancing energy efficiency in pneumatic drives, since the improvements are comparable to state-of-the-art ESCs while requiring less commissioning and control effort.

Regarding robustness, the experiments show that cylinders with an SQE valve can be operated with different pneumatic line lengths but exhibit lower robustness than conventional downstream-throttled systems. This lower robustness leads to a diminished performance increase and higher impact velocities at the end of the stroke when using longer pneumatic lines.

Despite these promising results, several challenges remain to be addressed in future research:

- Control strategies or system modifications that increase the robustness of the new system must be investigated.
- A systematic study of how the SQE valve affects cycle times is necessary to integrate it into cylinder-dimensioning procedures.
- Advancing the system beyond a laboratory demonstrator and integrating the lessons learned will enable comprehensive cost-effectiveness analysis, incorporating both manufacturing expenses and potential energy-cost savings.

Acknowledgments

The research and development project S-LEAP – Quick-Exhaust for increasing the performance and efficiency of exhaust throttled pneumatic drives - was funded by the European Union and the state of North Rhine-Westphalia. The authors would like to express their sincere thanks to all project partners, the European Regional Development Fund and the state of NRW.

References

[1] Reinertz, O., Reese, C., & Schmitz, K. (2024) Downstream throttled pneumatic drives with time-controlled pneumatic-mechanical quick-exhaust valve. *2024 Global Fluid Power Society PhD Symposium (GFPS)*, Hudiksvall, Sweden.

[2] Harris, P., Nolan, S., & O'Donnell, G. (2014). Energy optimisation of pneumatic actuator systems in manufacturing. *Journal of Cleaner Production*, 72, 35-45.

[3] Reinertz, O., & Schmitz, K. (2020). Optimized Pneumatic Drives Through Combined Downstream and Adaptive Upstream Throttling. *BATH/ASME 2020 Symposium on Fluid Power and Motion Control*. Bath, United Kingdom.

[4] Hepke, J. (2017). *Energetische Untersuchung und Verbesserung der Antriebstechnik pneumatischer Handhabungssysteme*. Aachen, Germany: Shaker Verlag.

[5] Doll, M., Neumann, R., & Sawodny, O. (2015). Dimensioning of pneumatic cylinders for motion tasks. *International Journal of Fluid Power*, 16(1), 11–24.

[6] Boyko, V., Nazarov, F., Gauchel, W., Neumann, R., Doll, M., & Weber, J. (2024). Comprehensive Application-Based Analysis of Energy-Saving Measures in Pneumatics. *International Journal of Fluid Power*, 25, 27–58.

[7] Yusop, M. Z. (2006). Energy saving for pneumatic actuation using dynamic model prediction. Retrieved from https://orca.cardiff.ac.uk/id/eprint/56066

[8] Shi, Y., Li, X., & Teng, Y. (2005). Research on pneumatic cylinder's exhausted-air reclaiming control devices. *Proceedings of the JFPS International Symposium on Fluid Power*. Tsukuba, Japan.

[9] Reese, C., Reinertz, O., & Schmitz, K. (2024). Feasibility Study and Experimental Validation of a Novel Combined Throttling Approach. *14th International Fluid Power Conference*. Dresden, Germany.

[10] Merkelbach, S. (2019). Analysis of the Economic and Ecological Properties of Pneumatic Actuator Systems with Pneumatic Transformers. Aachen, Germany. Retrieved from https://publications.rwth-aachen.de/record/781835/files/781835.pdf

[11] Krytikov, G., Strizhak, M., & Strizhak, V. (2017). The synthesis of structure and parameters of energy efficient pneumatic actuator. *Eastern-European Journal of Enterprise Technologies*, 1(7 (85)), 38–44.

[12] Krytikov, G., Stryzhak, M., & Stryzhak, V. (2018). Improving power efficiency of pneumatic logistic complex actuators through selection of a rational scheme of their control. *Eastern-European Journal of Enterprise Technologies*, 2(8 (92)), 43–49.

[13] Doll, M., Neumann, R., & Sawodny, O. (2011). Energy efficient use of compressed air in pneumatic drive systems for motion tasks. *Proceedings of 2011 International Conference on Fluid Power and Mechatronics*. Beijing, China.

[14] N., N. (2024). Motion Terminal VTEM, Festo SE \& Co. KG Datasheet. Retrieved 07.05.2025, from https://www.festo.com/media/catalog/202476_documentation.pdf

[15] Beater, P. (2007). *Pneumatic Drives: System Design, Modelling and Control*. Berlin: Springer Berlin Heidelberg.

[16] Rager, D., Neumann, R., Berner, M., & Doll, M. (2018). New programmable valve terminal enables flexible and energy-efficient pneumatics for Industry 4.0. *Fluid Power Networks: Proceedings of the 11th International Fluid Power Conference*. Aachen, Germany.

[17] Schmitz, K., & Reinertz, O. (2024). *Pneumatikantrieb, Entlüftungsventil dafür und Verfahren zum Entlüften*. DE102023104570B3.

Advanced Mechatronic Systems Featuring Pneumatic Actuation

Željko Šitum, Filip Čavić, Vid Pavlović, Lovro Zoričić, Ante Ivanković, Matija Čmelješević, Bernarda Galić, Mia Prgomet, Antonio Varović

University of Zagreb, Faculty of Mechanical Engineering and Naval Architecture, Zagreb, Croatia
zeljko.situm@fsb.unizg.hr, fc219243@student.fsb.unizg.hr, vp228634@student.fsb.unizg.hr, lz216694@student.fsb.unizg.hr, ai225599@student.fsb.unizg.hr, mc219290@student.fsb.unizg.hr, bg336707@student.fsb.unizg.hr, mp234376@student.fsb.unizg.hr, av230244@student.fsb.unizg.hr

This article presents eight innovative mechatronic systems powered by pneumatic actuators, designed as educational models for teaching pneumatic power systems and automatic control to mechanical engineering students. The first system introduced is a prototype of an autonomous vehicle that operates on compressed air and is driven by pneumatic artificial muscles. Next, four robotic systems are described, representing pneumatically actuated manipulators. These include a delta robot with a vacuum gripper, a robotic arm with a flexible gripper, a manipulator capable of avoiding obstacles on a conveyor belt, and a flexible pneumatic manipulator. The final section highlights three systems with potential industrial applications: a pneumatically powered screw mechanism, a system for automated bottle filling and capping, and an automated pneumatic machine designed to sort beans. All eight systems provide practical insights into the application of pneumatics in automation and serve as valuable tools for hands-on learning in mechatronics and control engineering.

DOI
https://doi.org/10.18690/um.fs.7.2025.11

ISBN
978-961-299-049-7

Keywords:
mechatronics, pneumatic actuators, robotic manipulators, educational models, industrial automation

University of Maribor Press

1 Introduction

Mechatronics is rapidly evolving through the integration of mechanical engineering, electronics, computer science, and intelligent control systems. Modern mechatronic systems increasingly feature flexible and adaptive components, enabling precise and autonomous execution of complex tasks [1], [2]. Among various actuation technologies, pneumatic actuation stands out for its simplicity, cost-effectiveness, and high power-to-weight ratio, making it suitable for both industrial and educational applications [3], [4]. Recent trends in robotics highlight compliant and bio-inspired actuators, such as pneumatic artificial muscles (PAMs), which offer enhanced safety in human-robot interaction and greater capability compared to rigid actuators [5], [6]. The rise of Industry 4.0 has further encouraged the development of smart, interconnected automation systems where pneumatic devices are increasingly integrated with sensors and controllers for real-time monitoring and control [7]. At the same time, there is a growing demand in engineering education for hands-on, project-based learning tools. Pneumatically powered educational models provide students with an effective way to explore core concepts such as fluid dynamics, control algorithms, sensor integration, and system optimization in a touchable and interactive manner [8]. This article presents eight innovative mechatronic systems designed to demonstrate the practical implementation of pneumatic actuation in automation and robotics.

2 Compressed-air-driven autonomous vehicle using PAMs

Autonomous mobile vehicles represent a rapidly evolving interdisciplinary field, merging mechanical, electronic, and software engineering to meet the growing global demand for efficient, safe, and sustainable transportation. These vehicles operate without human intervention, relying on advanced sensor arrays, control algorithms, and artificial intelligence to navigate complex environments. Autonomy ranges from basic driver assistance to full self-governance, with applications in logistics, transport, domestic aid, and exploration of hazardous or remote environments like underwater or extraterrestrial terrains. Despite significant advances, challenges remain, including high system costs, limited navigation reliability in novel environments, integration complexity, vulnerability to sensor or algorithm failures, and substantial energy consumption due to advanced onboard technologies. In this project, a hybrid driving system combining electric and pneumatic sources to enhance energy efficiency was used. The system employs Festo block valves and

pneumatic muscles powered by a electric compressor. Compressed air is stored in a 5-liter steel tank, with flow control according to actuators (Figure 1). Control is realized through a Controllino MAXI Power PLC (ATmega2560-based), powered by sealed lead battery (type Yuasa NP7-12, voltage 12 V, electric capacity 7 Ah) with integrated protection. Pressure sensors and a relay ensure safe compressor operation. This hybrid model offers a novel approach to propulsion systems for autonomous platforms with the integration of renewable energy sources.

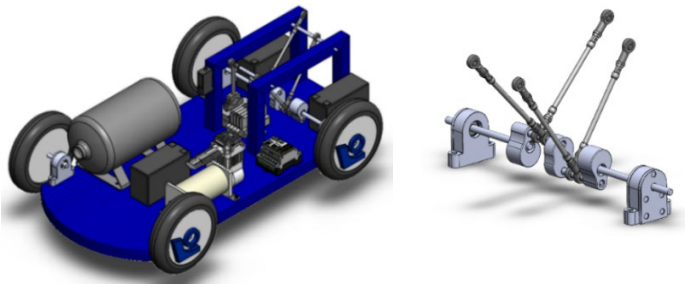

Figure 1: CAD model of the vehicle and V-configuration crankshaft.
Source: https://repozitorij.fsb.unizg.hr/islandora/object/fsb:9221 [9]

Figure 2: Autonomous vehicle actuated by PAMs.
Source: https://repozitorij.fsb.unizg.hr/islandora/object/fsb:9221 [9]

The mechanical subsystem was developed using a combination of 3D printing and traditional machining. Initial tests with a radial-drive setup (three pneumatic muscles at 120° around a crankshaft) showed limited motion due to insufficient contraction and geometric constraints. The final design adopts a V-shaped layout with four muscles (two per crank arm, turned 180°), achieving full crankshaft rotation through sequential activation. The frame is constructed from wood for ease of fabrication and reduced weight. The crankshaft includes flywheels, custom housings for

bearings, and wheel rims (all 3D-printed) along with steel half-axles, M6 threaded rods, and standard solid tires secured with regular screws. The completed vehicle is shown in Figure 2.

3 Robotic manipulators with pneumatic drive

3.1 Delta robot with a vacuum gripper

This project presents the design and implementation of a delta robot prototype optimized for high-speed pick-and-place operations (Figure 3). Utilizing a parallel kinematic structure with three independently actuated arms connected to a common end-effector, the robot achieves low inertia and high responsiveness. The kinematic model includes analytical inverse kinematics and numerically solved forward kinematics. Matlab simulations are used to evaluate the workspace by iterating actuator angles. Dynamic modelling, based on virtual work principles and Jacobian matrices, estimates actuator torques for specific trajectories. The robot is built using aluminium profiles and steel plates, with stepper motors (Nema 17HS19) driving the joints via 1.76:1 belt transmission (Figure 4). Bearings support the shafts, and adjustable motor mounts ensure proper belt tension.

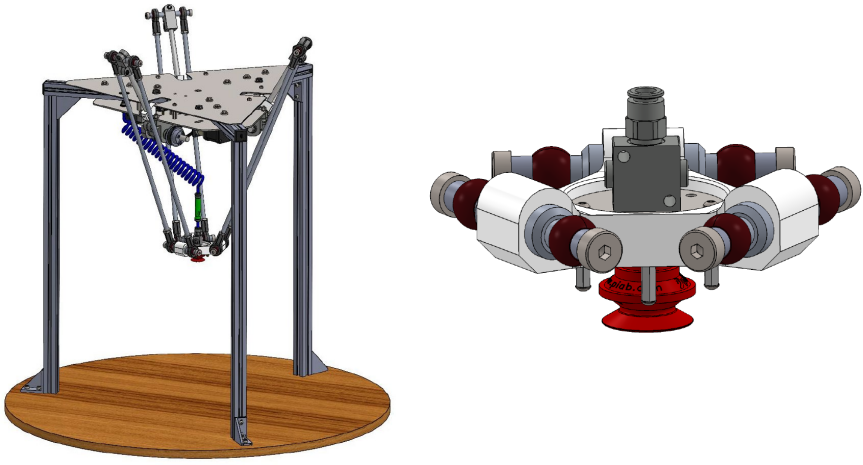

Figure 3: CAD model of the delta robot structure and robot gripper with vacuum ejector.
Source: https://repozitorij.fsb.unizg.hr/islandora/object/fsb:11268 [10]

The ESP32 microcontroller, paired with DRV8825 drivers, controls motion, while limit switches handle homing. The system supports joint-space and Cartesian motion profiles. Motion commands are received via a serial interface, with real-time joint limit and collision monitoring. A 3/2 electro-pneumatic valve, manufactured by Camozzi, controls the vacuum ejector (PIAB piINLINE MICRO Ti). The gripper is secured with alignment pins. A Python-based GUI allows .txt-based program execution. Experimental tests under a 0.56 kg load confirmed repeatable performance, with torques remaining below 0.5 Nm and consistent vacuum grip across all trajectories.

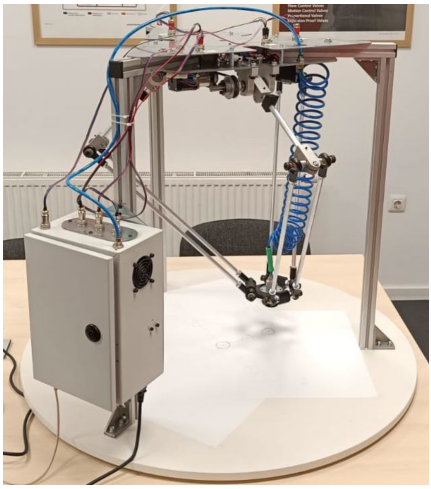

Figure 4: Assembled delta robot with frame, end-effector, and control interfaces.
Source: https://repozitorij.fsb.unizg.hr/islandora/object/fsb:11268 [10]

3.2 Pneumatic robotic manipulator with flexible gripper

This section presents the development of a pneumatic robotic manipulator with three degrees of freedom and an adaptive soft gripper, intended for repetitive handling of irregularly shaped objects. The design combines the compliance of soft robotics with the reliability of pneumatic actuation. The manipulator uses an RTT (Rotational-Translational-Translational) configuration, consisting of one rotary and two linear actuators, Figure 5. The SMC MSQB10A rotary actuator provides up to 190° of rotation via a rack-and-pinion mechanism. Translational motion is achieved with two pneumatic cylinders: a SMC CQ2Z32 for horizontal movement and a SMC CXSM20 for vertical positioning, which also supports the weight of the gripper. The

gripper operates on the granular jamming principle. A latex balloon filled with ground coffee adapts to the object's shape under compression. When a vacuum is applied inside the balloon, the particles lock together, forming a rigid structure that can securely grip the object. The vacuum is generated using a SMC ZH10B-06-06 ejector based on the Venturi effect, while a SMC ZCDUKC20-10D vacuum cylinder provides controlled actuation. To prevent contamination, a coffee filter is inserted inside the balloon. The gripper's housing, including the flange and funnel, is 3D printed for reduced weight and ease of integration. Power is supplied by a KSE 06024N AC/DC converter, delivering stabilized 24V DC to the control system. Each actuator is controlled via compact SMC VQD1121 solenoid valves in a 4/2 configuration, with flow control check valves used to regulate speed and ensure efficient airflow.

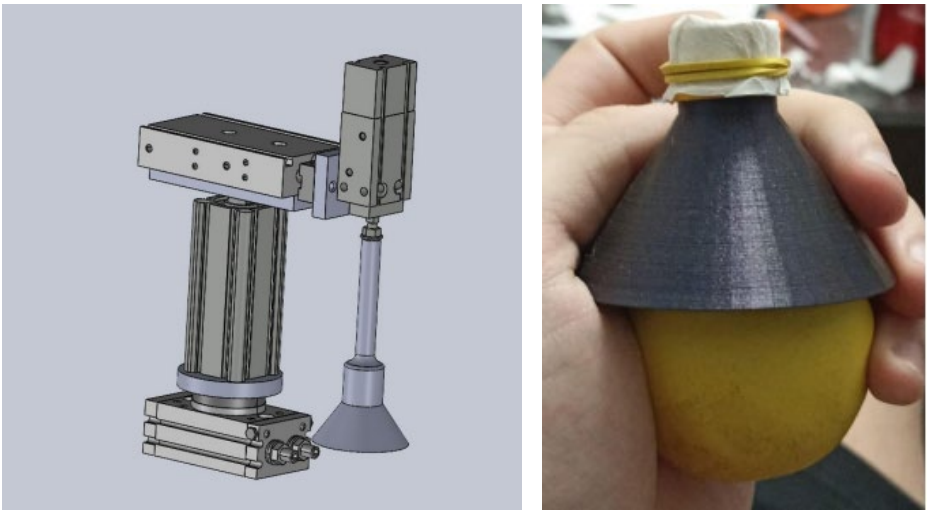

Figure 5: CAD model of the pneumatic robotic manipulator and the adaptive gripper.
Source: https://repozitorij.fsb.unizg.hr/islandora/object/fsb:9628 [11]

The system is controlled by a Controllino MINI PLC, programmed via the Arduino IDE. The PLC executes real-time logic for actuator sequencing and gripper control using digital I/O. The final prototype combines mechanical, pneumatic, and electronic elements into a compact, modular system suited for reliable manipulation and easy adaptation across applications (Figure 6).

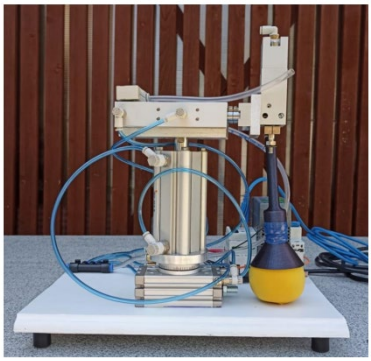

Figure 6: Final assembly of the manipulator with the flexible gripper.
Source: https://repozitorij.fsb.unizg.hr/islandora/object/fsb:9628 [11]

3.3 Pneumatic manipulator for obstacle avoidance on conveyor belt

This section presents an experimental system developed to demonstrate obstacle detection and real-time response using a pneumatic manipulator, Figure 7. Its main function is to detect user-placed obstacles on a conveyor belt and reposition a small cart using pneumatic actuation to avoid collisions. The system combines mechanical design, sensor input, and control logic, forming a compact prototype that can be used for simulations of automated obstacle avoidance on roads.

The system consists of two main components: a conveyor belt transport mechanism and a pneumatic manipulator. Objects are transported along the conveyor and detected by infrared (IR) sensors. When an obstacle is identified, the manipulator, powered by a dual-stroke pneumatic cylinder, repositions the cart to a predefined lane. The manipulator enables movement to three discrete positions (0 mm, 100 mm, and 200 mm), allowing dynamic path adjustment.

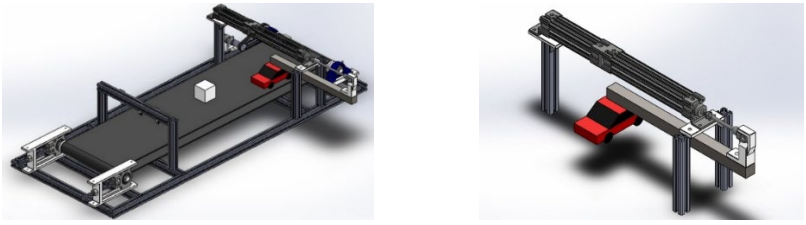

Figure 7: CAD model of the manipulator for obstacle avoidance.
Source: https://repozitorij.fsb.unizg.hr/islandora/object/fsb:9736 [12]

Mechanically, the structure is assembled using aluminum profiles. The conveyor is built from a PVC belt looped around two shafts, with custom 3D-printed parts ensuring alignment and tensioning. A DSMP320-12-0014-BF DC motor with an integrated planetary gearbox drives the system via a toothed belt and flexible coupling. The cart and actuator linkage are built from steel tubing and 3D-printed brackets, providing both strength and modularity.

The pneumatic system includes a SMC CP96SDL32-100C-XC11 dual-stroke actuator, controlled by two 5/2 solenoid valves (SMC SY3120), mounted on a valve manifold. A throttle check valve ensures smooth motion. Control is handled by a Controllino MINI PLC, which processes input from three HW-201 IR sensors. Each sensor includes an LM393 comparator and a range-adjustable potentiometer. When an object is detected, the PLC activates the appropriate valve combination to shift the cart. An electronic position sensor (D-M9BL) confirms actuator status. This prototype demonstrates a modular, sensor-driven system for automated object handling and path correction. Its structure is suitable for educational use or further expansion into more advanced sorting or robotic applications (Figure 8).

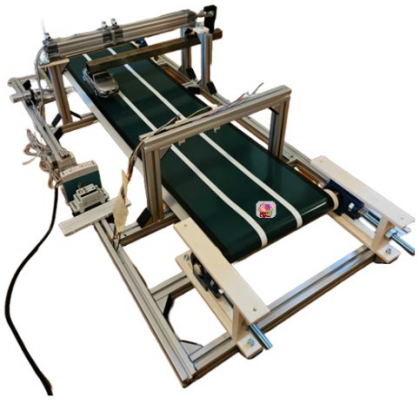

Figure 8: Pneumatic manipulator for obstacle avoidance on conveyor belt.
Source: https://repozitorij.fsb.unizg.hr/islandora/object/fsb:9736 [12]

3.4 Flexible pneumatic manipulator

This section presents the design and construction of a flexible pneumatic manipulator based on soft robotics principles, Figure 9. The system is composed of a control subsystem and an actuation subsystem, optimized for safe, adaptable, and

energy-efficient object manipulation. Inflatable actuators enable compliant motion, while a vacuum-based gripper ensures secure object handling.

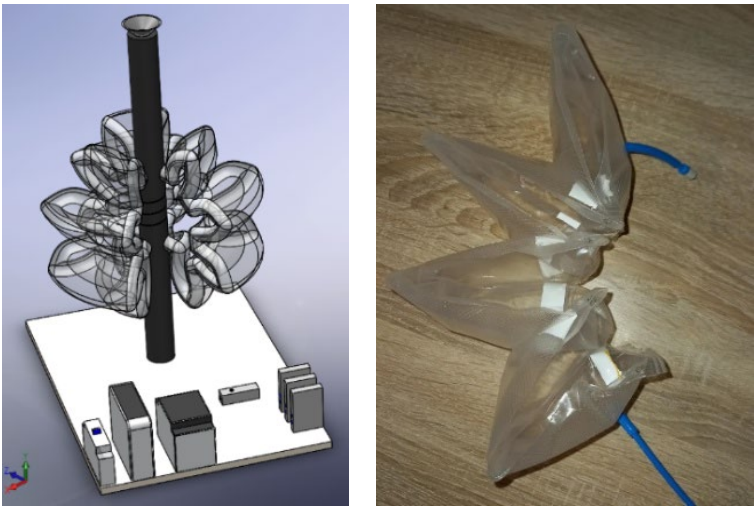

Figure 9: Conceptual design of the flexible pneumatic manipulator.
Source: https://repozitorij.fsb.unizg.hr/islandora/object/fsb:9163 [13]

The control subsystem regulates airflow using a Controllino MINI PLC, powered via a 24V DC converter protected by a single-pole safety breaker. The PLC communicates with a PC over USB and controls three Festo 3/2 solenoid valves. In their default state, the valves allow airflow to inflate the actuators. When the system is turned on, the valves send air to an ejector (SMC ZH10B-06-06), which generates a vacuum using the Venturi effect and turns on the vacuum gripper (SMC ZPT25DN-A6). The control logic minimizes power use by deactivating only one actuator at a time, while others stay inflated to provide support. Compressed air flows through a filter, safety valve, and gauge to dual-layer actuators with bellows-like folds. When inflated, they bend flexible polyethylene tubing reinforced with PVC, with radial cuts allowing directional motion. Maintaining vacuum continuity is essential during operation. The control algorithm ensures at least one actuator always remains active to avoid pressure loss and ensure the object stays gripped. The manipulator is mounted on a platform that integrates all major components: power supply, PLC, valves, actuators and vacuum gripper. This soft robotic manipulator showcases the potential of inflatable actuators for safe, adaptable, and low-power automation, Figure 10.

Figure 10: Flexible pneumatic manipulator.
Source: https://repozitorij.fsb.unizg.hr/islandora/object/fsb:9163 [13]

4 Automation systems with pneumatic drive for industrial tasks

4.1 Screw spindle mechanism with pneumatic drive

This section presents the design and operation of a pneumatic spindle mechanism based on a ball screw drive, intended for experimental linear positioning tasks (Figure 11). Unlike typical electric motor-driven systems, this setup uses a pneumatic vane motor, offering benefits such as a high power-to-weight ratio, resistance to overheating, and simple maintenance. The system is developed as a test platform to explore the potential of pneumatic control in precision mechatronic applications. The mechanical structure is built on an aluminum profile frame for stability and modularity. At its core is a 400 mm Tr8 trapezoidal leadscrew, supported at both ends by bearings.

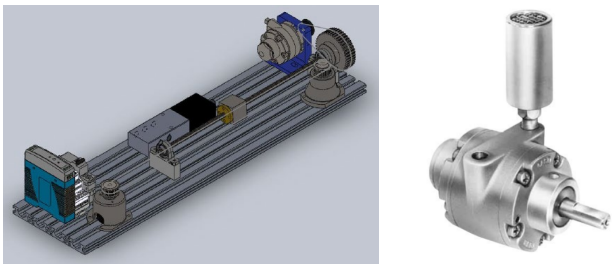

Figure 11: a) CAD model of the pneumatic spindle drive mechanism with ball screw, b) GAST pneumatic motor (model 1AM-NRV-63A).
Source: https://repozitorij.fsb.unizg.hr/islandora/object/fsb:9627 [14]

Rotary motion is provided by a GAST 1AM-NRV-63A pneumatic vane motor, coupled to the spindle via a belt and pulley system with a gear reduction ratio greater than 1, improving torque output. The motor is reversible and compact, converting compressed air into continuous rotary motion through internal rotor vanes. Linear motion is achieved by the nut traveling along the spindle as the leadscrew rotates. For accurate feedback, a rotary encoder is linked to the nut using a secondary belt drive, enabling direct position measurement. Pneumatic motor is controlled by a Festo MPYE-5-1/8-HF-010-B proportional valve, which adjusts airflow to the motor. An additional on/off valve (SMC SY7420) ensures safe engagement and shutdown of the pneumatic circuit. The realized screw spindle mechanism with pneumatic drive is shown in Figure 12.

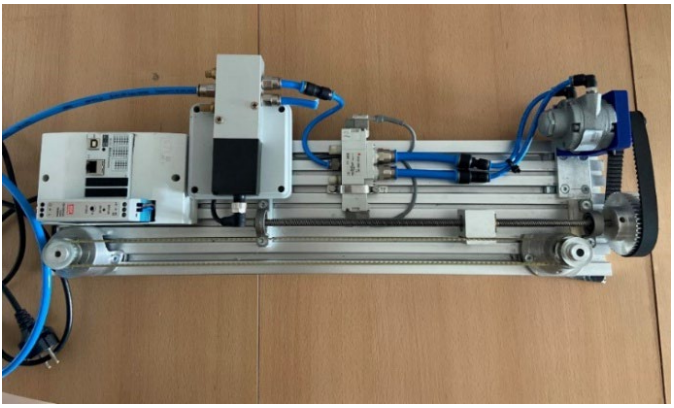

Figure 12: Screw spindle mechanism with pneumatic drive.
Source: https://repozitorij.fsb.unizg.hr/islandora/object/fsb:9627 [14]

The control system is implemented on a Controllino MAXI Automation PLC, which supports both analog output for valve control and digital input for encoder signal processing. The encoder outputs pulses corresponding to spindle nut displacement, with dual channels allowing direction detection. A PID control algorithm minimizes tracking error between the reference input and actual position, enabling real-time adjustments. Various motion profiles, including step, sinusoidal, and random inputs, were tested. The system demonstrated fast response, stable positioning, and reliable tracking performance, particularly for step and sinusoidal signals, confirming its suitability for educational and prototyping use in linear actuation and pneumatic control.

4.2 Automatic bottle filling and capping system

This section outlines the development of a compact automated system for bottle filling, closing, and capping, intended for small-scale production in pharmaceutical, food or chemical industries. The system minimizes operator involvement while ensuring consistent throughput. It consists of a conveyor with three stations: filling, closing, and capping. The conveyor features a continuous PVC belt driven by a DC motor and supported by a rigid aluminium frame (20×20 mm profiles) for mechanical stability. Bottles are manually loaded and automatically transported between stations (Figure 13).

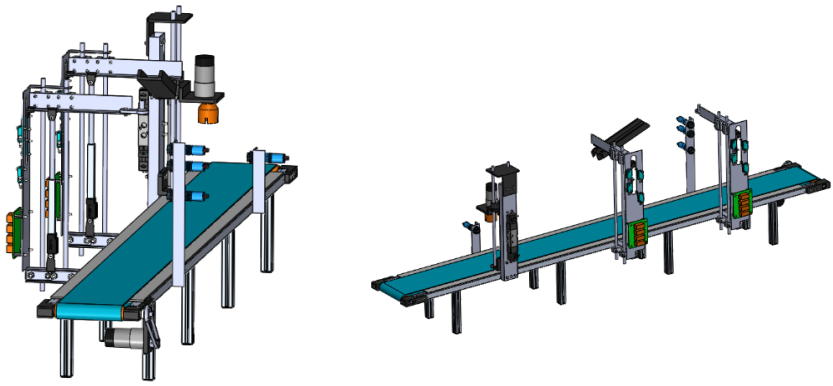

Figure 13: CAD model of the conveyor system transporting bottles.
Source: https://repozitorij.fsb.unizg.hr/islandora/object/fsb:11155 [15]

Filling and closing operations are executed by lead screw-driven linear actuators with limit switches, ensuring precise, repeatable motion. The capping station utilizes a pneumatic cylinder mounted vertically, controlled by a 5/2 solenoid valve and regulated via a throttle check valve to prevent impact forces. The system is controlled by a Controllino MAXI PLC, which receives input from PE18 photoelectric sensors detecting bottle presence and height. Based on sensor feedback, the PLC selects one of three actuator positions (low, medium, high), activating relays accordingly. Dual power supplies (12 V and 24 V) manage transport and valve operation. The complete experimental system illustrating actuator integration and capping mechanism is presented in Figure 14.

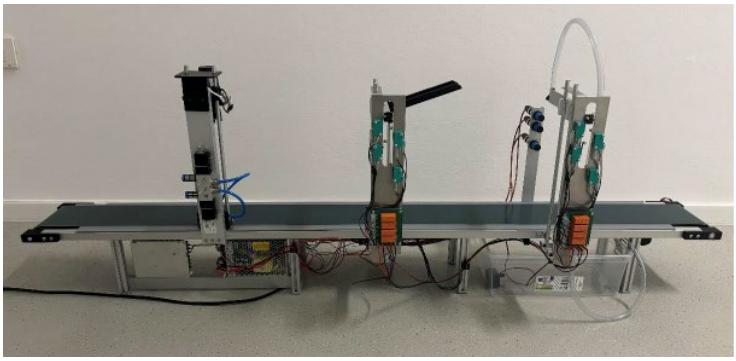

Figure 14: Final assembled automatic bottle filling and capping system.
Source: https://repozitorij.fsb.unizg.hr/islandora/object/fsb:11155 [15]

4.3 Automated pneumatic machine designed to sort beans

This section presents an automated pneumatic system for sorting and removing defective bean grains to ensure consistent product quality. The system integrates mechanical, electronic, and software components for precise classification and reliable grain ejection. At its core is a transport mechanism, developed through iterative 3D modelling, featuring 3D-printed PLA rollers driven by a DC motor and stabilized by a threaded rod, bearings, and a tensioning system (Figure 15).

Figure 15: CAD model of the sorting system and examples of defective bean grains.
Source: https://repozitorij.fsb.unizg.hr/islandora/object/fsb:10352 [16]

A wooden hopper holds up to 14 kg of beans and shields the detection chamber from ambient light. A dosing unit with four cylindrical channels, driven by a Nema 17 stepper motor, dispenses beans in pulses, forming four aligned rows on the

conveyor for inspection. An ultrasonic sensor monitors grain levels to ensure continuous flow. The sensing system includes an infrared sensor, incremental encoder (KY-040), and an Arducam CMOS AR0134 camera with a global shutter and 12-bit raw output for high-resolution imaging. Conveyor speed is managed via a toothed belt with a 2:1 reduction. System logic is controlled by a Controllino Maxi PLC programmed via Arduino IDE. Faulty grains are identified through image processing and ejected using a high-speed Matrix pneumatic valve. This modular prototype offers an efficient and adaptable solution for automated agricultural sorting (Figure 16).

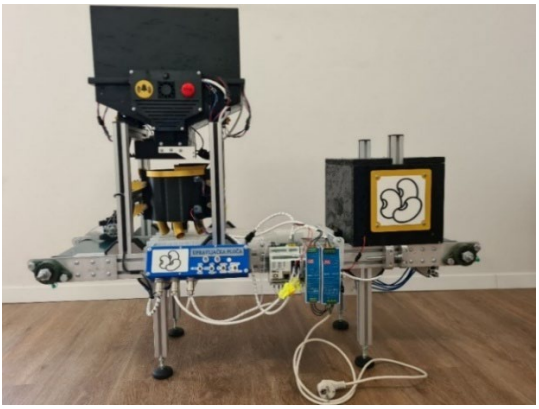

Figure 16: Final fabricated prototype of the bean grain sorting machine.
Source: https://repozitorij.fsb.unizg.hr/islandora/object/fsb:10352 [16]

5 Conclusion

This article presented eight pneumatic mechatronic systems developed as educational platforms to enhance hands-on learning in mechanical engineering. By combining mechanical design, control systems, and pneumatic technologies, the models effectively demonstrate core principles of automation, fluid dynamics, and sensor-based control. Spanning from bio-inspired robots to industrial automation prototypes, they highlight the versatility of pneumatic actuation in both teaching and real-world applications. These systems bridge theoretical knowledge and practical skills, aligning with trends in project-based learning and Industry 4.0. Overall, the work underscores the value of pneumatic systems in modern engineering education and their potential for broader industrial use.

Acknowledgments

We thank the companies Festo Croatia, SMC Croatia and BIBUS Croatia for the cooperation and sponsorship of pneumatic equipment necessary for the realization of experimental systems.
This research was funded by the University of Zagreb, through tenders for short-term annual financial support for scientific research in the period 2022–2024.

References

[1] Lee, J., Bagheri, B., & Kao, H. A. (2024). The Integration of Advanced Mechatronic Systems into Industry 4.0 for Smart Manufacturing. *Sustainability*, 16(19), 8504. https://doi.org/10.3390/su16198504.

[2] Samak, C. V., Samak, T. V., & Krovi, V. (2023). Towards mechatronics approach of system design, verification and validation for autonomous vehicles. *arXiv preprint* 2301.13425. https://doi.org/10.48550/arXiv.2301.13425.

[3] Zhao, S., Nguyen, C. C., Hoang, T. T., Do, T. N., & Phan, H.-P. (2023). Transparent pneumatic tactile sensors for soft biomedical robotics. *Sensors*, 23(12), 5671. https://doi.org/10.3390/s23125671.

[4] Sanchez, V., et al. (2023). 3D knitting for pneumatic soft robotics. *Advanced Functional Materials*, 33(26), 2370160. https://doi.org/10.1002/adfm.202370160.

[5] Wong, D. C. Y., Li, M., Kang, S., Luo, L., & Yu, H. (2023). Reconfigurable, transformable soft pneumatic actuator with tunable 3D deformations for dexterous soft robotics applications. arXiv:2311.03032. https://doi.org/10.48550/arXiv.2311. 03032.

[6] Kalita, G. R., Faruque, R. K., Saha, S., & Ghosh, S. K. (2023). A Review on the Development of Pneumatic Artificial Muscle Actuators: Force Model and Application. *Actuators*, 11(10), 288. https://doi.org/10.3390/act11100288.

[7] Even, S., Zheng, T., Lin, H., & Ozkan-Aydin, Y. (2023). Stable real-time feedback control of a pneumatic soft robot. In *Proceedings of the IEEE/RSJ International Conference on Intelligent Robots and Systems (IROS)*. https://doi.org/10.1109/IROS55552.2023.10342212.

[8] Durocher, A., & Morin, P. (2019). Project-based learning in mechatronics education using low-cost pneumatic systems. *Int. Journal of Mechanical Engineering Education*, 47(2), 126–140.

[9] Čavić, F. (2023). Mobile vehicle with pneumatic muscle engine. Undergraduate thesis (in Croatian), University of Zagreb, Fac. of Mech. Eng. and Naval Arch.

[10] Pavlović, V. (2024). Design and manufacturing of delta robot with a vacuum gripper. Master's thesis, (in Croatian), University of Zagreb, Fac. of Mech. Eng. and Naval Arch.

[11] Zoričić, L. (2023). Pneumatic robotic manipulator with flexible gripper. Undergraduate thesis (in Croatian), University of Zagreb, Fac. of Mech. Eng. and Naval Arch.

[12] Ivanković, A. (2023). Pneumatic manipulator for obstacle avoidance on conveyor belt. Undergrad. thesis (in Croatian), University of Zagreb, Fac. of Mech. Eng. and Naval Arch.

[13] Čmelješević, M. (2023). Flexible pneumatic manipulator. Undergraduate thesis (in Croatian), University of Zagreb, Fac. of Mech. Eng. and Naval Arch.

[14] Galić, B. (2023). Screw spindle with pneumatic drive. Undergraduate thesis (in Croatian), University of Zagreb, Fac. of Mech. Eng. and Naval Arch.

[15] Prgomet, M. (2024). Automatic bottle filling and capping system. Undergraduate thesis (in Croatian), University of Zagreb, Fac. of Mech. Eng. and Naval Arch.

[16] Varović, A. (2024). Machine for separating bad beans. Undergraduate thesis (in Croatian), University of Zagreb, Fac. of Mech. Eng. and Naval Arch.

Pneumatically Powered Hydraulic Rescue Shears for Firefighter Operations

Borna Matkun, Mihael Cipek, Danijel Pavković, Željko Šitum

University of Zagreb, Faculty of Mechanical Engineering and Naval Architecture, Zagreb, Croatia
bm239026@student.fsb.unizg.hr, mihael.cipek@fsb.unizg.hr, danijel.pavkovic@fsb.unizg.hr, zeljko.situm@fsb.unizg.hr

For severe traffic accidents, rapid occupant extrication is crucial. Firefighter hydraulic rescue shears, while essential for this task, are hindered by bulky hydraulic hoses which reduce maneuverability. This research investigates powering these tools with compressed air from a firefighter's self-contained breathing apparatus (SCBA) cylinder. The proposed system utilizes a compact, mobile hydraulic power unit driven by this pneumatic source. A hydraulic rescue shears and review of market solutions are reviewed, and a typical cutting loads are defined. A model of a small, mobile hydraulic power unit powered by an SCBA cylinder is proposed and its performance validated via simulation. This study aims to enhance rescue efficiency and ergonomics by potentially eliminating traditional hydraulic hose constraints.

DOI
https://doi.org/10.18690/um.fs.7.2025.12

ISBN
978-961-299-049-7

Keywords:
hydraulic shears, hydraulic power unit, pneumatic source, model, simulation

University of Maribor Press

1 Introduction

In the critical moments following a severe vehicular accident, the time to extricate a trapped occupant is a major determinant of survival and recovery outcomes. The concept of the "golden hour", the period immediately after traumatic injury during which there is the highest likelihood that prompt medical and surgical treatment will prevent death, places immense pressure on emergency responders to act with speed and precision [1]. Vehicle extrication, the process of cutting away a damaged vehicle to free a trapped person, is a foundational and often complex task for fire and rescue services. The success of these operations hinges on the effectiveness of the tools at their disposal.

For decades, hydraulic rescue tools (HRTs), often colloquially known as the "Jaws of Life," have been the standard for vehicle extrication. These tools utilize high-pressure hydraulic fluid, generated by a dedicated power unit, to actuate cutters, spreaders, and rams capable of severing the high-strength steel components of modern automobiles [2]. While undeniably powerful, the conventional design of these systems presents significant logistical and ergonomic challenges. The tools are tethered by heavy, cumbersome hydraulic hoses to a bulky, engine-driven power unit. This configuration can impede a firefighter's maneuverability, limit access to vehicles in precarious positions (e.g., down an embankment or in a narrow alley), and increase the time required to set up and deploy the equipment at the scene. These limitations can introduce delays and increase the physical strain on rescuers, potentially compromising the efficiency of the entire operation.

To address these shortcomings, this research investigates a different approach for powering hydraulic rescue shears by leveraging a piece of equipment already carried by every firefighter into a hazardous environment: the self-contained breathing apparatus (SCBA). Modern SCBA systems operate with high-pressure air cylinders, typically at pressures up to 300 bar and volumes up to 10 liters, representing a significant and readily available pneumatic energy source [3]. The proposed solution involves the development of a compact, portable hydraulic power unit that is driven by compressed air from an SCBA cylinder. This would effectively untether the rescue tool, granting the operator complete freedom of movement and drastically reducing setup time.

This paper aims to establish the feasibility of this concept. It begins with a comprehensive overview of existing firefighter hydraulic rescue shears and defines the typical cutting forces and energy requirements encountered during vehicle extrication. Subsequently, a fluid power model for a small-scale, air-powered hydraulic unit is proposed. The performance of this model is then validated through simulation to determine its capacity to meet the operational demands of rescue cutting tasks. Ultimately, this study seeks to present a viable, innovative solution that enhances the mobility, efficiency, and ergonomics of firefighter rescue operations, potentially representing the next step in the evolution of these life-saving tools.

2 Existing rescue tool technologies

The evolution of vehicle extrication tools has been driven by the concurrent evolution of automotive manufacturing. As car designers have incorporated high-strength steels (HSS) and ultra-high-strength steels (UHSS) to improve passenger safety and fuel efficiency, the demands placed on rescue tools have increased exponentially [4].

2.1 Conventional hydraulic rescue systems

The most common rescue systems in use by fire departments worldwide are traditional hydraulic tools. These systems consist of three primary components:

- **The power unit:** A gasoline or diesel engine, or an electric motor, drives a hydraulic pump. This unit is typically heavy and is placed at a safe distance from the incident vehicle.
- **The hoses:** High-pressure, non-conductive hydraulic hoses, often in coaxial or "twin-line" configurations, connect the power unit to the tool. These hoses are typically 15 to 30 meters long and operate at pressures up to 720 bar.
- **The tool:** This can be a spreader, a cutter (shears), a combination tool, or a ram. The tool contains a hydraulic cylinder that actuates the arms or blades.

The primary advantage of these systems is their immense and sustained power output, capable of handling the most demanding cutting and spreading tasks. However, as noted, the operational constraints imposed by the hoses are a significant

drawback. The setup time, potential for entanglement, and the need to move the heavy power unit to reposition for different cuts all detract from efficiency [5].

2.2 Battery-powered hydraulic rescue systems

In recent years, battery-powered (or "e-draulic") rescue tools have gained significant market share. These tools integrate the pump and a small electric motor directly into the tool's body, powered by a high-capacity rechargeable lithium-ion battery. This design eliminates the need for external power units and hoses, granting the operator complete freedom of movement.

Key advantages include rapid deployment (simply turn it on) and superior maneuverability. However, limitations exist. The power output, while sufficient for many applications, may not match the highest-end conventional systems for cutting through the most advanced UHSS. Battery life is a critical consideration; multiple batteries are required for extended operations, and their performance can degrade in extreme temperatures. Furthermore, the integrated design makes the individual tools heavier and bulkier than their hosed counterparts [6].

2.3 Pneumatic power in rescue operations

Compressed air is already a staple in rescue operations, primarily for lifting bags and powering pneumatic chisels or impact wrenches. These tools are valued for their lightweight design and simple operation [7]. However, pure pneumatic tools lack the force generation capabilities required for the heavy-duty cutting and spreading performed by hydraulic systems. The concept of using compressed air to *drive* a hydraulic system is also available on the market [8], however those systems require stable pressured air source and also requires hoses.

Therefore, the core innovation explored in this paper is a hybrid approach that seeks to combine the portability and ready availability of a pneumatic source (the SCBA cylinder) with the unparalleled force multiplication of hydraulics. To our knowledge, a comprehensive feasibility study of powering primary hydraulic extrication shears from a firefighter's SCBA cylinder has not been previously undertaken. This research aims to fill that gap by providing a foundational analysis of such a system.

3 System modeling and calculation

To assess the feasibility of an SCBA-powered hydraulic system, a theoretical model was developed and its performance parameters were calculated in this section.

3.1 System Components

Figure 1 show pneumatic and hydraulics schematic of power unit and a tool. The proposed power unit consists of a standard firefighter SCBA cylinder, a pressure regulator to step down the SCBA pressure to the motor's operating pressure, the pneumatic motor itself, a high-pressure hydraulic pump, and a compact hydraulic low and high pressure reservoirs. For this study, we proposed a common 10-liter carbon-fiber cylinder pressurized to 300 bar. This represents a finite, but readily available, energy source at any fire scene. The interface between the compressed air and the hydraulic pump is a pneumatic motor which is mechanically coupled to the hydraulic pump. The system is designed to power a standard hydraulic rescue shear, which requires a hydraulic pressure of 700 bar for maximum cutting force.

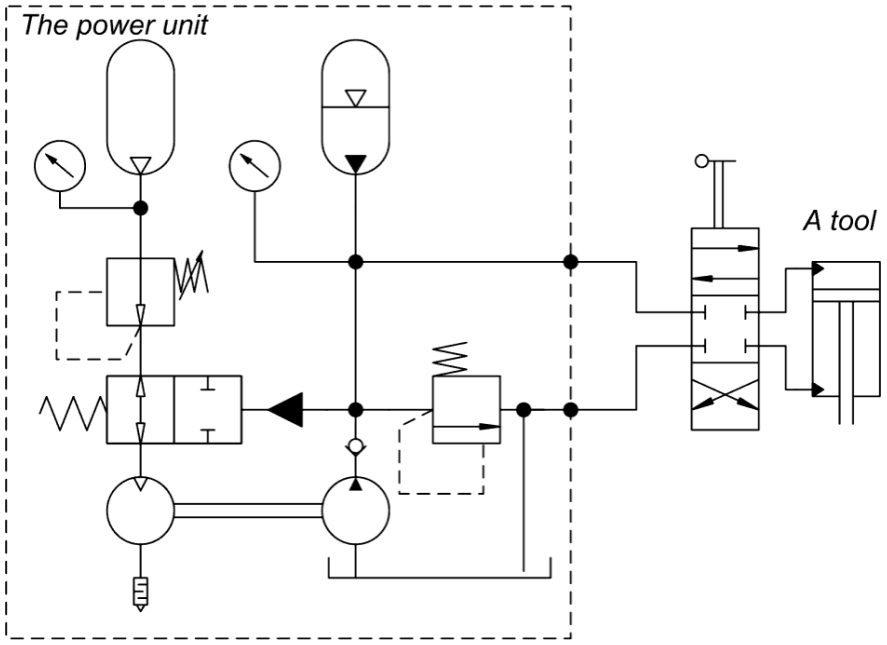

Figure 1: Schematic of the power unit and a tool.
Source: own

To save air and energy, a hydraulically controlled 2/2 pneumatic valve was added to the system. This valve interrupts the air flow if the hydraulic pressure exceeds the operating pressure, thus preventing the hydraulic safety valve from opening.

The RM 110 Piston Air Motor was selected for this study. Its operating characteristics at air pressure of 6 bar are shown in Figure 2 [9]. Figure 2a presents the motor's torque characteristic as a function of rotational speed. The motor has a starting torque of 6.8 Nm, which is slightly lower than its maximum torque of approximately 9 Nm, achieved at a speed of about 200 rpm. As the rotational speed increases, the torque decreases, reaching a value of 4.5 Nm at 2400 rpm. The air consumption, expressed in normal liters per second (NL/s), is shown in Figure 2b. It exhibits an approximately linear increase in relation to the rotational speed. Maximum air consumption is 29 NL/s at 2400 rpm.

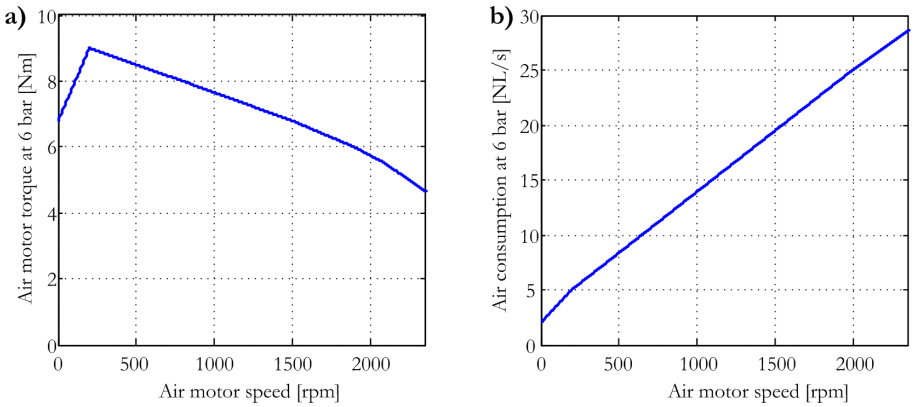

Figure 2: Air motor torque a) and air consumption b) at 6 bar pressure.
Source: derived from [9]

According to [10], the selected high-pressure pump is a radial piston pump (Type R) with a displacement of 0.43 cm³/rev and is capable of achieving a pressure of 700 bar. It has a volumetric efficiency of 98 % and a hydromechanical efficiency of 82 %. The required torque (τ) for this pump can be calculated using the following equation:

$$\tau = \frac{pD}{2\pi\eta_{hm}}, \tag{1}$$

where p is the operating pressure in Pa, D is the pump displacement, and η_{hm} is the hydromechanical efficiency. Using the specified pump parameters, the required torque to achieve 700 bar is calculated to be 5.84 Nm. The maximum torque of the air motor exceeds this value for speeds below 2000 rpm (as shown in Figure 2a). Therefore, the chosen air motor is capable of powering the proposed high-pressure pump.

3.2 Simulation model

In the model, the speed-dependent torque (shown in Figure 2a) developed by the air motor is used to both build up hydraulic pressure in the pump and accelerate the combined inertia (I_{eq}) of the motor, pump, and shaft. Therefore, the following equation can be written:

$$\tau_m(\omega) = \dot{\omega} I_{eq} + \frac{pD}{2\pi\eta_{hm}}, \tag{2}$$

where ω is angular velocity of air motor and hydraulic pump in rad/s, and combined inertia is chosen heuristically to be 0.02 kgm^2. Hydraulic flow Q is determined by the pump angular speed, its displacement and volumetric efficiency (η_{vol}) according to:

$$Q = nD\eta_{vol} = \frac{30\omega}{\pi} D\eta_{vol}\,. \tag{3}$$

The duration of the air motor's normal operation is determined by the total volume of available air (in normal state), which is calculated using the following expression:

$$V_N = \frac{p_t - p_m}{p_N}\left(\frac{T_N}{T_t}\right) V_t, \tag{4}$$

where p_m is air motor operating pressure, p_t, T_t and V_t are pressure, temperature and volume of SCBA cylinder, while p_N and T_N are pressure and temperature of air in normal state, respectively. For example, a 10 L SCBA cylinder containing air pressurized to 300 bar at a temperature of 20 °C holds a volume of 2704 normal liters (NL). This amount of air is sufficient to allow the air motor to operate for 93 seconds at its maximum speed of 2400 rpm, where the air consumption is 29 NL/s (see Figure 2b).

As shown in Figure 3, the simulation model for the power unit is built on the air motor's torque characteristic from Figure 2a, which provides the maximum torque (τ_m) as a function of rotational speed. The motor's torque is opposed by the load torque from the high-pressure hydraulic pump. The difference between these torques accelerates the pump and motor. The rotational speed is then found by integrating the angular acceleration. This new rotational speed is subsequently used to calculate the air consumption and the motor's torque for the next iteration. Furthermore, the rotational speed also dictates the oil flow rate (Q) through the pump. The simulation proceeds until the entire normal air volume (V_N) is depleted. A necessary conversion is included in the model, as the motor's characteristics are given in revolutions per minute (rpm), while the rotational speed (ω) is calculated in radians per second.

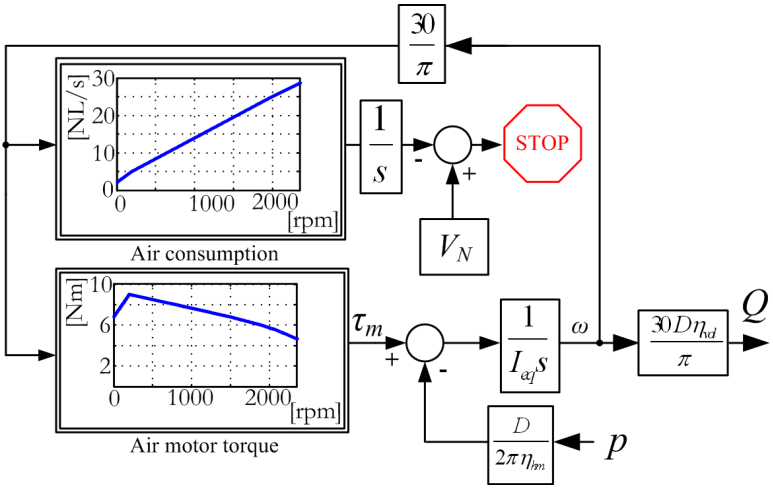

Figure 3: Simulation model.
Source: own

4 Simulation results

As shown in Figure 4a, the air motor (and the hydraulic pump) successfully accelerates despite the extremely high load torque resulting from the hydraulic system being set to its maximum operating pressure of 700 bar. After a few seconds, the motor reaches a steady-state speed of 1963 rpm. At this speed, the motor develops a torque of 6 Nm, which is precisely what is needed to maintain this steady-state condition, as seen in Figure 4b.

The motor's characteristics (Figure 2a) show that a higher torque is available at lower speeds. This allows for a faster initial acceleration, and this increase in torque is clearly visible in the first few seconds of Figure 4b. Air consumption, shown in Figure 4c, has an approximately linear relationship with the rotational speed of the air motor. The simulation runs until the motor consumes the entire available air volume, which occurs after 111 seconds.

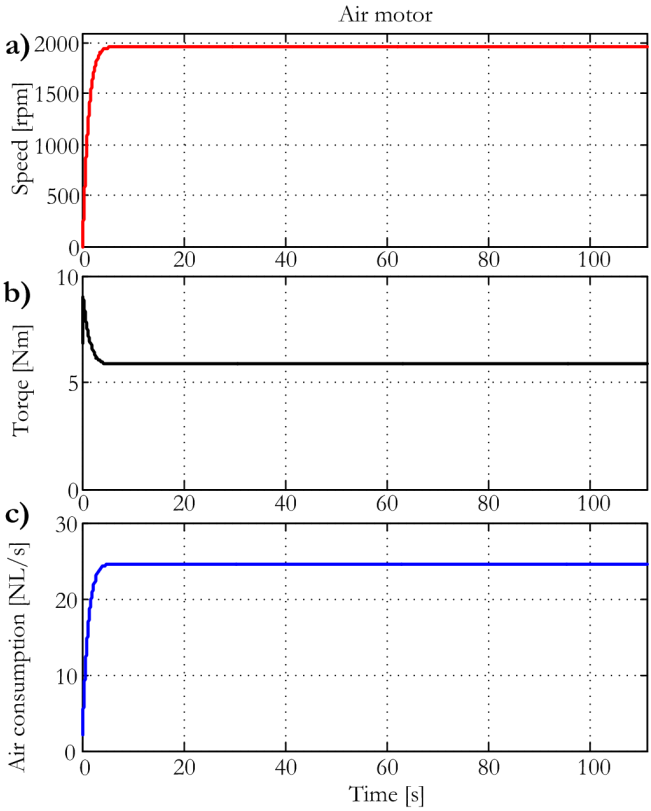

Figure 4: Simulation results of air motor speed a) torque b) and air consumption c).
Source: own

Figure 5a illustrates the oil flow rate of the pump, which is a linear function of its rotational speed (see Figure 4a). The time-based accumulation of the total volume of pressurized oil transferred by the hydraulic pump is depicted in Figure 4b. The simulation determined that this system, when powered by a 10 L compressed air tank at 300 bar, can deliver a total of 1.51 L of oil at a pressure of 700 bar.

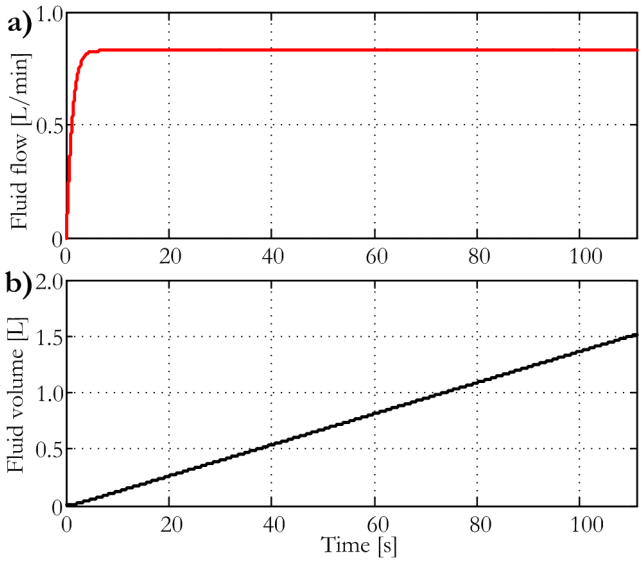

Figure 5: Simulation model.

Source: own

5 Discussion

The simulation results confirm the feasibility of a pneumatic-to-hydraulic drive system powered by a firefighter's SCBA cylinder. The model shows that the air motor can successfully accelerate and maintain a hydraulic pressure of 700 bar despite the extremely high load torque from the pump. This high pressure is essential, as it enables hydraulic shears, such as the CU 5030 CL, to achieve their maximum cutting force.

The simulation reveals that a single 10 L SCBA cylinder, pressurized to 300 bar, can maintain a maximum operating pressure for 111 seconds. During this period, the hydraulic pump transfers a total of 1.51 L of pressurized oil. Given that the CU 5030 CL shears require 0.155 L of oil per cutting cycle [11], the system is capable of performing approximately nine cuts. According to [12], this capacity is often sufficient for a single technical intervention, as a typical extrication may require between five and ten cuts. To extend the operating time and increase the number of available cuts, a two-bottle system, also called Twinpack System [13] could be implemented. This would increase the available air to 13.6 L, providing 2.06 L of pressurized oil and enabling up to 13 cuts.

The results of this study strongly suggest that powering hydraulic rescue shears from a firefighter's SCBA cylinder is not only feasible but also offers compelling advantages over traditional systems. The most significant benefit is the elimination of bulky hydraulic hoses, which untethers the firefighter and allows for unrestricted movement around a vehicle. Rescuers can more easily access components from any angle, navigate through debris, and operate in confined spaces without the risk of hose entanglement. The compact and mobile nature of the power unit means it could be carried by a single firefighter or placed on a small trolley, significantly reducing the physical strain and setup time associated with conventional gasoline-powered units.

By utilizing a power source that is already on-scene and carried by personnel, the time from arrival to the first cut can be dramatically reduced. There is no need to start a gasoline engine or run lengthy cables and hoses. In the time-critical context of vehicle extrication, saving these crucial minutes can directly impact patient outcomes. While modern battery-powered tools also offer untethered operation, the SCBA-powered system presents a different logistical paradigm. Fire departments already have a robust infrastructure for refilling SCBA cylinders on-site. An empty cylinder can be swapped for a full one in seconds, ensuring continuous operation. This contrasts with battery management, which requires charging stations, rotation schedules, and the eventual replacement of expensive batteries as they age. The performance of the SCBA system is also independent of ambient temperature, whereas extreme cold can degrade battery performance.

This study is a theoretical and simulation-based analysis and has several limitations that must be addressed through future work. The next logical step is to build a physical prototype of the compact pneumatic-to-hydraulic power unit. This prototype must be rigorously tested to validate the simulation results and assess its durability, reliability, and noise levels in a controlled environment. The final weight and dimensions of the prototype are also critical. Future work should also be focused on creating a unit that is significantly more portable than traditional power units, making it practical for a single rescuer to carry and operate. This study used a specific motor for its calculations. Future research could explore different pneumatic motors to optimize air consumption and overall system efficiency.

Ultimately, the system should be tested in realistic training scenarios with experienced firefighters to evaluate its ergonomics, usability, and effectiveness in complex extrication drills.

6 Conclusion

This study successfully demonstrates, through simulation, the feasibility of a novel pneumatic-to-hydraulic drive system for rescue shears that is powered by a firefighter's SCBA cylinder. The model confirms that the proposed system can maintain the required hydraulic pressure of 700 bar, which is essential for generating the maximum cutting force of the shears. The analysis indicates that a single 10 L SCBA cylinder provides sufficient power for approximately nine cuts, a capacity that is often adequate for a typical vehicle extrication. Furthermore, the system's operational time can be extended to support up to 13 cuts with a two-bottle configuration.

The results strongly suggest that this concept offers significant advantages over both traditional and battery-powered rescue tools. The most compelling benefit is the elimination of bulky hydraulic hoses, which grants firefighters unprecedented freedom of movement, improves access in confined spaces, and drastically reduces the risk of entanglement. By leveraging a power source that is already carried on-scene, the system also minimizes the time from arrival to the first cut, a critical factor in time-sensitive rescue operations. From a logistical standpoint, the system capitalizes on the robust SCBA refilling infrastructure already present in fire departments, offering a more dependable and low-maintenance solution compared to the complexities of battery management.

In summary, this research confirms that using an SCBA cylinder to power hydraulic shears is a viable and highly promising approach. It offers a powerful combination of portability, speed, and logistical simplicity that could revolutionize vehicle extrication. While the simulation results are compelling, the next logical step is to validate these findings through the prototyping and physical testing of a compact, real-world unit. This future work will be critical to fully assess the system's performance, ergonomics, and effectiveness in practical rescue scenarios.

Acknowledgments

This research was funded by the University of Zagreb, through tenders for short-term financial support for research in the period 2024 - 2025.

References

[1] Lerner, E. B., & Moscati, R. M. (2001). The Golden Hour: Scientific Fact or Medical "Urban Legend?". *Academic Emergency Medicine*, 8(7), 758-760. doi:10.1111/j.1553-2712.2001.tb00201.x

[2] Meteňko, J., & Marcinek, M. (2018). Hydraulic rescue equipment for firefighters. *Prace Naukowe Akademii im. Jana Długosza w Częstochowie. Technika, Informatyka, Inżynieria Bezpieczeństwa*, 6, 821 - 834. doi:10.16926/tiib.2018.06.59

[3] Composite SCBA Cylinders | SCBA Cylinder & EEBD Cylinders – 300 Bar, Available: https://breatheair.com/products/scba-cylinders/composite-scba-cylinders/, [Accessed: 11 August 2025].

[4] Galán, J., Samek, L., Verleysen, P., Verbeken, K., & Houbaert, Y. (2012). Advanced high strength steels for automotive industry. *Revista De Metalurgia*, 48(2), 118–131. doi:10.3989/revmetalm.1158

[5] Caban J, Droździel P, Vrabelj J. (2017). Overview of Selected Hydraulic Devices Supporting Road Rescue Operations. *Scientific Journal of the Military University of Land Forces*, 185(3), 81-89. doi:10.5604/01.3001.0010.5125.

[6] Battery-Powered Combination Rescue Tools for Vehicle Extraction, Market Survey Report, July 2023. Available: https://www.dhs.gov/science-and-technology/saver/st-battery-powered-rescue-tools-vehicle-extrication, [Accessed: 11 August 2025].

[7] Pneumatic Lifting Bags & Systems - WEBER RESCUE SYSTEMS. Available: https://www.weber-rescue.com/en/feuerwehr/pneumatische-rettungsgeraete/liftingbags/, [Accessed: 11 August 2025].

[8] Haskel Air Driven Pumps |High Pressure Pneumatic Pumps. Available: https://www.haskel.com/en/products/liquid-pumps/, [Accessed: 11 August 2025].

[9] RM110 Piston Air Motor - GLOBE Airmotors. Available: https://globe-airmotors.com/rm110-pistonmotor/, [Accessed: 11 August 2025].

[10] HAWE Hydraulik, Radial piston pump type R, RG, Product documentation. Available: https://productfinder.hawe.com/downloads/D6010-en.pdf, [Accessed: 11 August 2025].

[11] Holmatro Rescue Tools OBJ_BUCH-200-001.book - user-manual. Available: https://www.holmatro.com/sites/default/files/downloads/en/user-manual-cu-5030i-cu-5040i-cu-5050i-cu-5060i-en-44b5df90-f9b3-4420-9dab-f70eedf5b889-F0018435_0001.pdf, [Accessed: 11 August 2025].

[12] 8 Minute Extrication Cutting - YouTube. Available: https://www.youtube.com/watch?v=mguPr9gdse4, [Accessed: 11 August 2025].

[13] -Dräger -Compressed -Air -Breathing -Cylinders - Compressed-Air-Breathing-Cylinders-pi-100211-en-MASTER.pdf. Available: https://www.draeger.com/Content/Documents/Products/Compressed-Air-Breathing-Cylinders-pi-100211-en-MASTER.pdf, [Accessed: 11 August 2025].

Remote Control and Monitoring of a Pneumatic Workstation Using TwinCAT 3 and Beckhoff PLC

Vito Tič, Alfonz Muhič
University of Maribor, Faculty of Mechanical Engineering, Maribor, Slovenia
vito.tic@um.si, alfonz.muhic@student.um.si

For severe traffic accidents, rapid occupant extrication is crucial. Firefighter hydraulic rescue shears, while essential for this task, are hindered by bulky hydraulic hoses which reduce maneuverability. This research investigates powering these tools with compressed air from a firefighter's self-contained breathing apparatus (SCBA) cylinder. The proposed system utilizes a compact, mobile hydraulic power unit driven by this pneumatic source. A hydraulic rescue shears and review of market solutions are reviewed, and a typical cutting loads are defined. A model of a small, mobile hydraulic power unit powered by an SCBA cylinder is proposed and its performance validated via simulation. This study aims to enhance rescue efficiency and ergonomics by potentially eliminating traditional hydraulic hose constraints.

DOI
https://doi.org/10.18690/um.fs.7.2025.13

ISBN
978-961-299-049-7

Keywords:
fluid power, pneumatic workstation, remote control, Beckhoff PLC, Industry 4.0

University of Maribor Press

1 Introduction

Remote operation of industrial machinery has become increasingly important in modern manufacturing, driven by the Industry 4.0 paradigm and the need for flexible, decentralized control. Pneumatic systems are widely used in industry due to their long service life and simple maintenance. However, traditionally, direct on-site supervision is required to monitor and control such systems. Recent global events (e.g. the COVID-19 pandemic) have further underscored the value of remote access and control capabilities to maintain production with minimal on-site staffing. This paper addresses the upgrade of an existing pneumatic workstation [1] to enable remote monitoring and control over the Internet. The solution employs a Beckhoff soft-PLC [2] and TwinCAT 3 software to implement control logic and a web-based HMI [3]. With this approach, authorized users can start, stop, and adjust the pneumatic process from anywhere, and also monitor the system's status in real time. Similar approaches have been explored in prior work, but our implementation uniquely emphasizes integrated safety and live process visualization.

2 Methodology

The development of the remote-controlled pneumatic workstation involved both hardware integration and software design. Figure 1 provides an overview of the pneumatic workstation setup, while Figure 2 shows the control architecture of the system. The existing workstation's pneumatic components were leveraged and interfaced with a new Beckhoff PLC and network infrastructure. We followed an Internet of Things (IoT) approach, connecting the workstation to a networked PC controller to allow remote access in line with Industry 4.0 principles.

3 Pneumatic Workstation Design

The base of the system is a pneumatic workstation comprising multiple actuators and modules arranged on an aluminum frame. It includes two orthogonal linear axes (X and Y) and a vertical Z-axis manipulator, enabling 3-dimensional movement of a pneumatic gripper. These axes, driven by pneumatic cylinders, allow pick-and-place handling of workpieces across the workstation. Additional tools on the station include a drilling unit and a stamping unit, which can be applied to the workpieces. Various sensors are installed to ensure safe and precise operation: traditional micro

limit switches and inductive proximity sensors detect cylinder end positions, and a magnetic sensor monitors the Z-axis piston position. The station is equipped with a Festo VTUG pneumatic valve island (manifold) with multiple solenoid valves – eight 5/2 bistable valves, one 5/3 centre-closed valve, and two 3/2 monostable valves – that direct compressed air to the actuators. The use of bistable valves ensures that actuators hold position upon loss of power (each valve has a memory function), whereas monostable valves return to a default state with spring return, contributing to fail-safe behaviour. Compressed air at a regulated pressure is supplied to the station and on-board pressure gauge was added. The complete pneumatic workstation is shown in Figure 1.

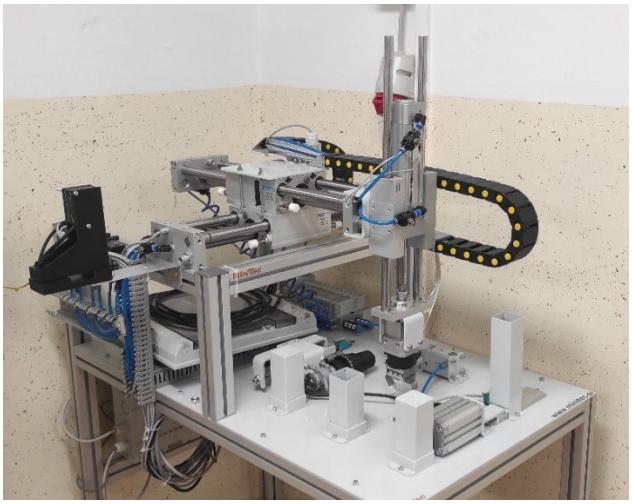

Figure 1: Pneumatic workstation with linear axes, grippers, and tooling. Sensors and valves are installed for position feedback and control.

3.1 Control System Architecture

A Beckhoff programmable logic controller system was used to control the workstation, selected for its high performance and flexibility. The PLC hardware consists of a Beckhoff embedded PC (running TwinCAT 3 in soft-PLC mode) connected to modular I/O terminals via an EtherCAT bus coupler (model EK1100). Digital input terminals (e.g. Beckhoff EL1008) interface with the limit switches and sensor signals, while analog input terminals (e.g. Beckhoff EL3214) read analog sensor values such as pressure. A special communication terminal (Beckhoff

EL6631 PROFINET interface) links the PLC to the Festo valve island, allowing direct actuation of valves via the PROFINET fieldbus. The EtherCAT coupler and I/O modules are all powered by a 24 V DC supply for safety. Figure 2 illustrates the system architecture, including the controller, I/O modules, and their connection to the pneumatic components. An emergency-stop circuit is integrated such that any critical fault will cut power to valve coils and immediately stop all motion.

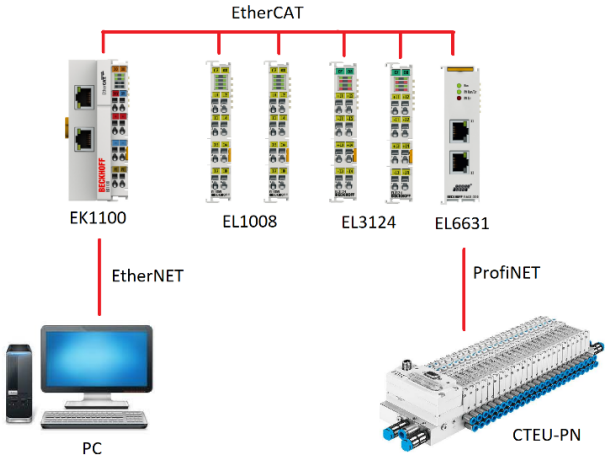

Figure 2: System architecture connecting the Beckhoff PLC (soft-PLC on embedded PC) with EtherCAT I/O modules and the pneumatic valve manifold (via PROFINET).

3.2 Control Software Design

The control logic for the workstation was implemented in the Beckhoff TwinCAT 3 environment. TwinCAT 3 supports programming in multiple IEC 61131-3 languages (Structured Text, Ladder Diagram, Sequential Function Chart, etc.). We partitioned the control program into an initialization routine and three operational modes corresponding to available processes: drilling, stamping, and a combined drill-and-stamp cycle. Upon startup, the system performs an initialization sequence that moves the robotic manipulator to a safe home position. This step prevents collisions in case the system was halted in an unknown state when last used. Operators can then select a mode via the HMI (e.g. drilling only, stamping only, or both). Depending on the selection, the PLC executes the corresponding subroutine

to handle the workpiece: retrieving a raw part from a feeder, securing it on the worktable, performing the selected process(es), and finally depositing the finished part into one of three sorting bins.

The program was structured using a combination of Structured Text (ST) and Sequential Function Chart (SFC) languages. Complex logic and data handling (such as mode selection and cycle counting) were written in ST for clarity and flexibility, while the step-by-step operational sequences were implemented as an SFC, which graphically represents states and transitions. This modular approach improved code readability and allowed real-time monitoring of both numeric variables and state transitions during runtime. Figure 3 shows a portion of the SFC implementation of one process cycle, illustrating the sequence of steps and conditions for transitions. Each step (state) triggers specific actions (e.g. move axis, activate drill) and transitions on completion conditions.

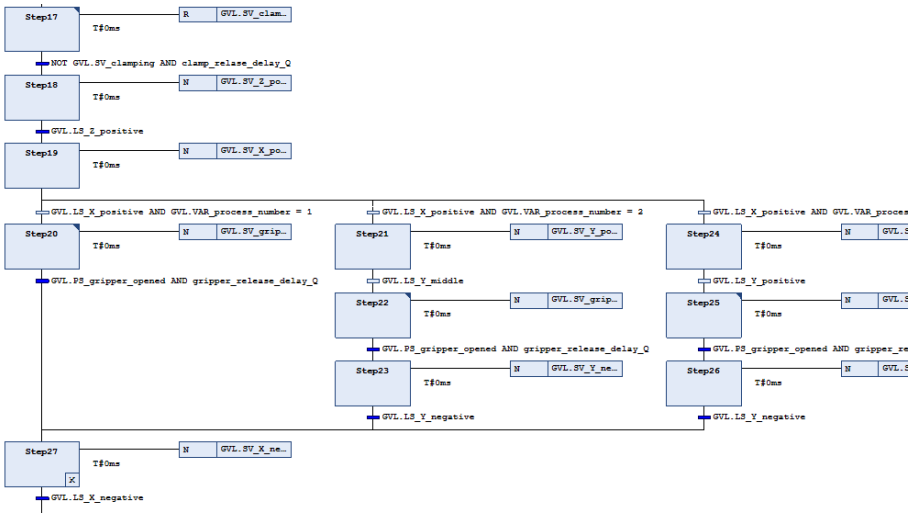

Figure 3: Excerpt of the Sequential Function Chart (SFC) program controlling one operational cycle.

3.3 HMI Development for Remote Control

A critical component of the system is the TwinCAT 3 HMI web interface, which provides remote visualization and control through a standard browser. The HMI was developed as a web application within the TwinCAT engineering environment,

using drag-and-drop widgets for buttons, indicators, and displays. We designed the interface to be intuitive and to include all necessary controls and readouts without clutter. Key controls include buttons for starting and stopping the process, selecting the operation mode (drill, stamp, or both), resetting the system, and an emergency stop (E-stop). Status indicators on the HMI show the real-time state of various subsystems (e.g. whether the manipulator is at home position, whether drilling is in progress, etc.), illuminating green when the corresponding function is active. The interface also displays counters that track how many parts have been processed out of the target quantity set by the user. In addition, a gauge widget (barometer) continuously shows the supply air pressure; colored zones on the gauge provide quick feedback if pressure moves outside the normal operating range. For easier remote monitoring of the physical process, a live video camera feed is embedded in the HMI. A normal USB webcam is connected to the controller PC and streams real-time video via an IP camera application, allowing the remote operator to visually observe the workstation during operation.

For security, the HMI requires user authentication upon accessing the page. The interface is hosted on the TwinCAT HMI server running on the controller PC, configured with secure HTTP (HTTPS) on a specified port. We set up the server with the controller's IP address and the HMI's port (3000) as an endpoint so that authorized users can reach the interface via a. The TwinCAT HMI server was configured to require an administrator username and password for login. A login screen prevents unauthorized use, addressing cybersecurity concerns – without valid credentials, no control actions can be sent to the workstation. To deploy the HMI, the project was published from TwinCAT into the runtime server environment.

4 Results

After integrating the hardware and developing the software, the remote control system was thoroughly tested. Initial tests were conducted in manual mode, verifying that each HMI button correctly triggered the corresponding action on the pneumatic station (for instance, the "Initialize" button returned the manipulator to home, and each mode selection button started the correct process sequence). Automatic mode was also tested by setting a desired count of parts and letting the system run through complete cycles; all indicators and counters on the HMI updated appropriately with the process progression. The pressure monitoring feature was validated by artificially

reducing the air supply pressure: the on-screen barometer reflected the drop and entered the warning (red) zone as expected.

To evaluate remote accessibility, the HMI was accessed from multiple devices and locations. On the local network, a second PC was used to connect to the interface and successfully start and stop the workstation. The interface was also accessed via a mobile phone over the internet from a different location. In all cases, the system responded correctly to user commands. We observed a small increase in control latency when using a mobile cellular network, but the responsiveness remained within acceptable bounds for safe operation. Throughout testing, the safety features proved effective: for example, pressing the E-stop button (either on the physical station or the HMI) immediately halted the system as intended, and the login requirement successfully barred access when incorrect credentials were entered. Overall, the system meets its design goals: it allows the pneumatic workstation to be operated remotely with real-time feedback, and it includes safeguards to prevent misuse or accidents. Figure 4 shows the final web HMI as seen by the user, with its main components annotated. The interface includes manual controls (top-left), automatic operation settings (top-right), status indicators (centre), counters (bottom-left), a pressure gauge (bottom-right), and a live video feed (bottom-centre). The E-stop and login features enhance operational safety.

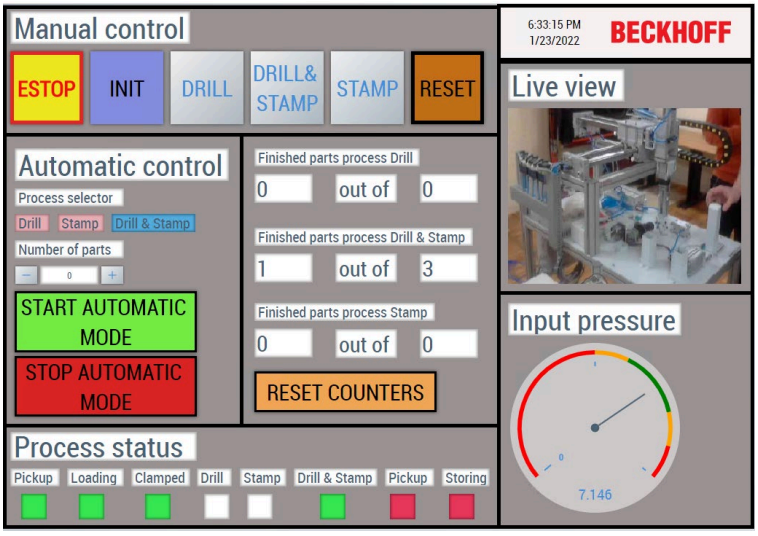

Figure 4: The TwinCAT 3 web-based HMI for the pneumatic workstation.

5 Discussion

The developed system demonstrates how an existing pneumatic workstation can be modernized for remote operation, bringing it closer to an Industry 4.0 "smart factory" cell. Using a soft-PLC running on an industrial PC (instead of a traditional standalone PLC) made it straightforward to integrate advanced features like the web HMI and camera feed. This platform leverages standard IT technologies (Ethernet networks, HTTP/HTTPS protocols) to interface with fluid power equipment, illustrating the convergence of automation and internet connectivity.

The safety measures implemented – specifically the authentication requirement and emergency stop integration – address both cybersecurity and operational hazard concerns. In practice, these measures are essential; an unsecured industrial control interface could be maliciously manipulated, potentially causing equipment damage or safety incidents. By requiring users to log in before granting control, and by designing the interface with clear E-stop functionality and real-time sensor feedback (e.g. pressure and flow sensors signalling abnormal conditions), the system ensures that remote operators have the situational awareness and control authority needed to manage the process safely. The inclusion of a live video feed further aids the operator in verifying actions and preventing potential collisions or errors, essentially serving as the remote "eyes" on the process. This combination of networked control and live monitoring significantly improves the ability to respond quickly to issues, even when off-site.

Overall, the project highlights that with appropriate hardware (modern networked PLCs) and software (web-based HMIs), even traditional pneumatic systems can be successfully integrated into a remote supervision and control framework. This opens opportunities for increased flexibility in managing manufacturing processes and enables rapid expert intervention in system issues without the need for physical presence on the factory floor.

6 Conclusion

In this work, a pneumatic workstation was successfully upgraded for remote monitoring and control. The integration of a Beckhoff PLC and TwinCAT 3 environment enabled the existing system to be controlled via a web browser

interface from anywhere with internet access. The implemented HMI provides intuitive control and continuous feedback on the process state, including safety-critical information like emergency stop status and air pressure levels. Testing confirmed that the remote operation functions as intended, with robust performance observed in both local and remote network scenarios. This development demonstrates the feasibility of retrofitting fluid power workstations with modern control technology to meet the demands of distributed and flexible manufacturing.

Future enhancements could include expanding the system with additional sensors or incorporating analytics for predictive maintenance, further aligning the workstation with smart factory principles. Nonetheless, even in its current form, the system provides a clear example of applying IoT and Industry 4.0 concepts to pneumatic automation, significantly enhancing both the usability and safety of the workstation. We believe that such remote-operated pneumatic systems can improve maintenance response times, reduce downtime, and enable new operational models (such as centralized supervision of multiple remote sites), thereby offering substantial benefits in industrial practice.

References

[1] A. Krošel, Krmiljenje pnevmatske delovne postaje z vodilom PROFINET in krmilnikom Beckhoff (Master's thesis). University of Maribor, 2019.

[2] Beckhoff Automation, TwinCAT 3 – Overview and Documentation, 2023. [Online]. Available: beckhoff.com/en-en/products/automation/twincat

[3] Beckhoff Automation, TwinCAT 3 HMI – Web-based User Interface, 2023. [Online]. Available: beckhoff.com/en-en/products/automation/twincat-3-hmi

The Importance to Consider Advanced Fluid Properties in Flow Simulation of Positive Displacement Machines

Anže Čelik
Poclain Hydraulics d.o.o., Žiri, Slovenia
anze.celik@poclain.com

Simulation of positive displacement machines requires highly skilled engineers, use of advanced simulation tools and advanced simulation approach. The paper presents recent activities and progress on simulation of positive displacement machines – in particular, the axial piston pump and the radial hydraulic motor. Despite that these machines have been designed and produced for decades, there are still (design) features and phenomena not being investigated in detail or never being simulated. The simulation advancements mainly refer to the application of complicated kinematic motion, fluid properties, physics to consider as well as mesh and numerical algorithm techniques. In this paper, the focus is on modelling of advanced fluid material properties. Numerical approach has been performed by means of CFD within the environment of Siemens Simcenter Star-CCM+. The anticipation of cavitation has been possible by implementation of existing "full cavitation model".

DOI
https://doi.org/10.18690/um.fs.7.2025.14

ISBN
978-961-299-049-7

Keywords:
positive displacement machines, cavitation model, fluid material properties, CFD simulation, Siemens Simcenter Star-CCM+

University of Maribor Press

1 Introduction

In this very first part, let's unpack the term "positive displacement machine" step by step. Positive displacement principle states that the space required to generate flow rate during a function period is geometrically reduced (compressing period) and increased again (decompressing or suction period). The pressure to be applied is determined by the resistance that the actuator (e.g. cylinder, motor) must overcome. [1], [2], [3]

Displacement machines are hydraulic machines (i.e. pumps, motors) in which hydrostatic power is transferred downstream of the positive displacement principle. In terms of the operating principle, a distinction is made between rotary type (rotating components) and reciprocating type (linear motion). In the rotary machines the transport process takes place in a circumferential direction and is characterized by the size 2π. On the other hand, reciprocating machines work with the displacement units (e.g. pistons) performing a linear movement. [1]

Figure 1: Example of reciprocating (left) and rotary machine (right).
Source: own

Typical representatives of reciprocating machines are axial piston pumps, radial piston motors, diaphragm pumps, plunger pumps etc. Typical representatives of rotary machines are gear pumps, lobe pumps, vane pumps, screw pumps etc.

1.1 Axial piston pump

An axial piston pump is a type of positive displacement machine that uses a series of pistons arranged in a circular pattern within a cylinder block (or rotor); see Figure 2. These pistons move in a direction parallel (axial) to the axis of rotation of the cylinder block. Axial piston pump exists as fixed (constant flow rate) or variable

displacement (swash plate angle can be changed, varying the stroke of the pistons and adjusting the flow rate).

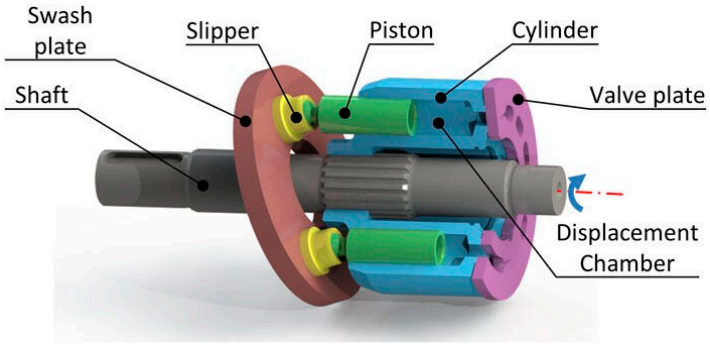

Figure 2: Rotating group of axial piston pump.
Source: [4]

1.2 Radial piston motor

Radial piston motor is a type of positive displacement machine that converts hydraulic energy (i.e. fluid pressure) into rotational mechanical energy (i.e. torque). It gets its name because the pistons are arranged radially around a central crankshaft or a cam. Two main types of radial piston motors exist: crankshaft and cam ring type (or multi-lobe cam type). The latter consists of stationary housing, rotating cylinder block, radial pistons arranged in a circle inside the rotor and multi-lobe cam ring that stays fixed (figure 3) [7].

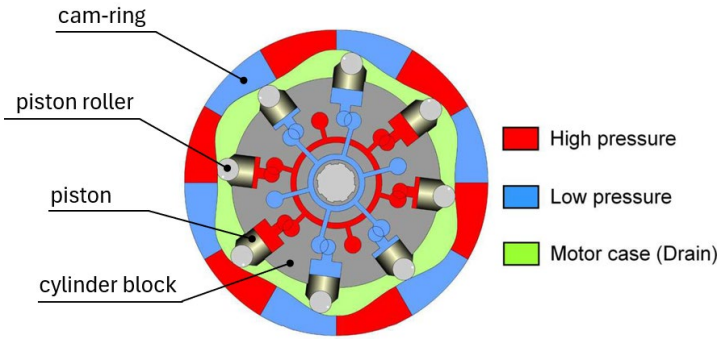

Figure 3: Typical cross-section view of radial piston motor.
Source: own

2 Physics to consider

Positive displacement machines are complex products – not just from component point of view, but also from physics point of view. Several different physical phenomena appear in such machine: starting from solid mechanics (e.g. solid stress, tribology, materials …) further to fluid mechanics (e.g. fluid properties, turbulences, cavitation …) and more.

Implementation of those phenomena into physical model(s) is of course not an easy task and knowledge from different physical domains need to be merged.
For this investigation purposes, one of the most challenging physical domains will be introduced hereafter – cavitation phenomena.

2.1 Cavitation phenomena

Cavitation is the phenomenon where vapor cavities (which are small and mostly liquid-free zones), known as bubbles or voids, are generated in a liquid due to the imbalance of the local dynamic forces. This usually occurs when a liquid is subjected to rapid changes of pressure under isothermal conditions. An example: if the pressure falls below a threshold (vapor saturation pressure), the liquid will rupture and form vaporous cavities, while the voids would implode (bubbles collapse) and generate intense shock waves when the vapor bubbles are subjected to pressure higher than the threshold pressure (Figure 4) [6].

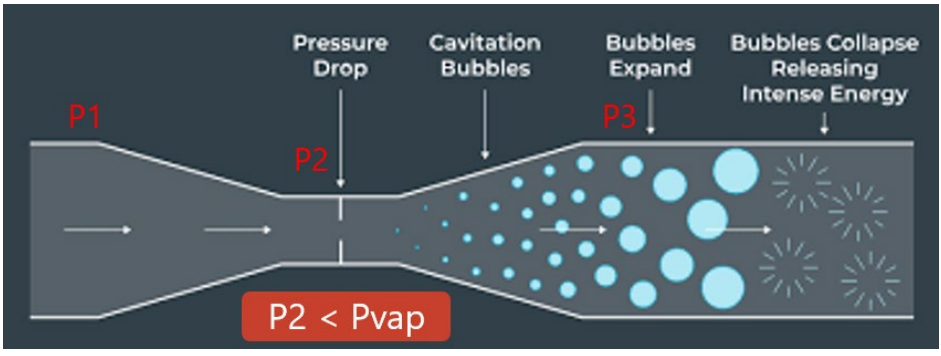

Figure 4: Cavitation resulting from a drop of pressure.
Source: [9]

Two principal types of cavitation exist: vaporous and gaseous. Vaporous cavitation is a process that takes place if the bubble grows explosively as liquid rapidly changes into vapor; this situation occurs when the pressure level goes below the vapor pressure of the liquid. Gaseous cavitation, on the other hand, is a diffusion process that occurs whenever the pressure falls below the saturation pressure of the non-condensable gas dissolved in the liquid.

Physical model for cavitation) bubble

A typical physical model for single (cavitation) bubble is shown on Figure 5.

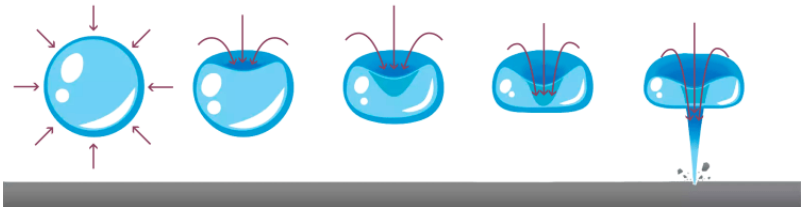

Figure 5: Collapse of single cavitation bubble.
Source: [14]

In most cases, cavitation is an undesirable phenomenon, causing significant degradation in the performance (e.g. reduces mass flow rates, lower head rise in pumps, load asymmetry, vibration, and noise). Cavitation also causes physical damage to a device due to bubble impact on surfaces (very right stage on figure 5), which can ultimately affect structural integrity.

Cavitation is a very complex phenomena and its details are still under deep investigation. Huge progress in understanding single cavitation bubble collapse has been made within the last decade (mainly thanks to deeper and sophisticated visual examination). [10], [11], [12], [13]

2.2 Difference between cavitation and boiling

Boiling is a phase change at constant pressure and variable temperature; cavitation on the other hand is a phase change at constant temperature and variable pressure (Figure 4).

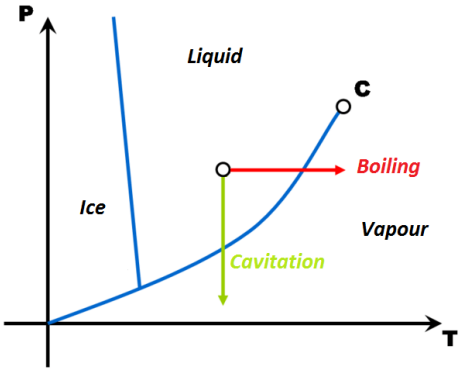

Figure 4: Boiling versus cavitation.
Source: own

Fundamentally, both cavitation and boiling are the evaporation and condensation process between liquid and vapor phases. However, the mechanisms that trigger the phase changes are different. Cavitation is predominately caused by mechanical effects which are the sharp pressure changes in fluid systems. Boiling is due to thermal effects that raise the vaporization pressure of a liquid above its local ambient pressure to cause the phase change from liquid to vapor [5].

3 Numerical techniques

Knowing and understanding appropriate physics is the very first and essential step. Then, the next challenging step is to implement physics into numerical code. Not every physical model could be efficiently coded or significant skills in programming is needed. Implemented physical model of cavitation and mesh techniques are briefly explained hereafter.

3.1 Cavitation model

For this study purposes, implementation of advanced fluid properties has been of significant importance. Numerous models are available within many scientific papers and publications. However, not many of them are suitable for 3D CFD purposes (e.g. [16]) due to the lack of numerical robustness, stability, performance etc. Hereafter, "full cavitation model" from Singhal et al. [15] has been used and implemented into CFD code within Siemens Simcenter Star-CCM+.

The basic approach consists of using the standard viscous flow (Navier-Stokes) equations for variable fluid density and a conventional turbulence model (e.g. k-ε model). The fluid density is a function of vapor mass fraction f, which is computed by solving a transport equation (1) coupled with the mass and momentum conservation.

$$\frac{\partial}{\partial t}(\rho f)+\nabla\cdot(\rho\vec{V}f)=\nabla\cdot(\Gamma\nabla f)+R_e-R_c \tag{1}$$

The source terms R_e and R_c denote vapor generation (evaporation) and condensation rates and can be functions of flow parameters (pressure, flow characteristic velocity) and fluid properties (liquid and vapor phase densities, saturation pressure, and liquid-vapor surface tension). The above formulation employs a homogenous flow approach and therefore does not consider two-phase (two-fluid) flow.

The primary focus is on proper account of bubble growth and collapse. In a flowing liquid with zero velocity slip between the fluid and bubbles, the bubble dynamics equation is derived from the generalized Rayleigh-Plesset equation.

$$\Re_B\frac{D^2\Re_B}{Dt^2}+\frac{3}{2}\left(\frac{D\Re_B}{Dt}\right)^2=\left(\frac{P_B-P}{\rho_l}\right)-\frac{4\nu_l}{\Re_B}\dot{\Re}_B-\frac{2S}{\rho_l\Re_B} \tag{2}$$

Equation (2) provides a physical approach to introduce the effects of bubble dynamics into the cavitation model. In fact, it can be considered as an equation for void propagation and, hence, mixture density.

The working fluid is assumed to be a mixture of liquid, liquid vapor and non-condensable gas (NCG). The calculation of the mixture density is defined as

$$\frac{1}{\rho}=\frac{f_v}{\rho_v}+\frac{f_g}{\rho_g}+\frac{1-f_v-f_g}{\rho_l} \tag{3}$$

where $\rho_g, \rho_v, \rho_l, f_v, f_g$ refer to the NCG density, vapor density, liquid density, mass fraction of vapor and mass fraction of NCG, respectively.

The main unknowns are p_{vap} (vapor saturation pressure) and f_g. Their variation depends on fluid type and its quality and can be significant [16]. The model has been validated on several different cases.

Besides that, this cavitation model exhibits the following characteristics:

- Can be applied to any geometric system (3D, 2D planar, or 2D axisymmetric), all grid cell types and arbitrary interfaces are supported;
- Concurrent use of the turbulence, grid deformation and/or structures solution modules are fully supported;
- Flow is assumed isothermal and fluid properties are taken as constant at a given temperature for the entire flow domain;
- NCG mass fraction (f_g) is assumed to be constant in the flow field.

3.2 Mesh morphing

Many simulations that involve motion or geometry change require moving or deforming the mesh. Different deforming mesh methods (and their naming) exist, such as overset mesh, morphing, adaptive mesh refinement, general remeshing etc. The morpher motion allows to account for the effect of moving boundaries in a transient simulation. The morpher can be used, for example, to simulate the reciprocating motion of a piston in a cylinder - where the boundaries are not changing shape, but the mesh vertices must morph to accommodate the movement [17].

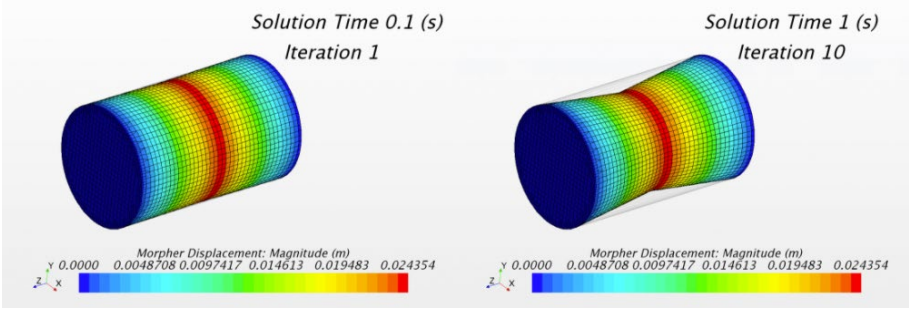

Figure 5: Cylinder with a contracting wall.
Source: [17]

The morphing motion in Siemens Simcenter Star-CCM+ redistributes mesh vertices in response to the movement of a set of control points, which can be considered as being a cloud of points overlaid onto the mesh domain. The displacement of a point can be set directly, or it can be calculated from the input of grid velocity, from which the displacement is calculated for a given time step.

3.3 Rigid body motion

Rigid body motion allows to model the motion of a rigid body in response to applied forces and moments. In a rigid body, the relative distance between internal points does not change. Therefore, it is sufficient to solve the equations of motion for the center of mass of the body (Figure 6).

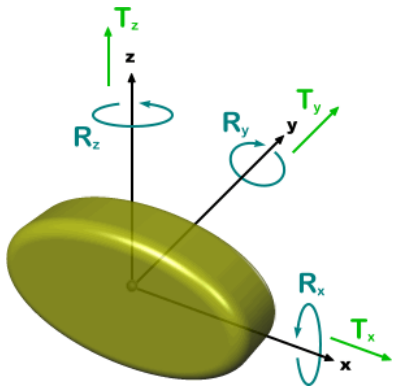

Figure 6: The motion of a 3D rigid body has 6 degrees of freedom.
Source: [17]

4 3D numerical model of the axial piston pump

The investigation refers to the flow analysis on pump PM10. The aim of this analysis is to evaluate pressure field in piston chamber for "full pump" model (i.e. all pistons are used). 3D view of the pump PM10 is depicted on Figure 7.

3D CFD model considers unsteady conditions, mesh morphing, realizable k-e turbulence model, passive scalar transport equations and user-defined equation of states (compressibility).

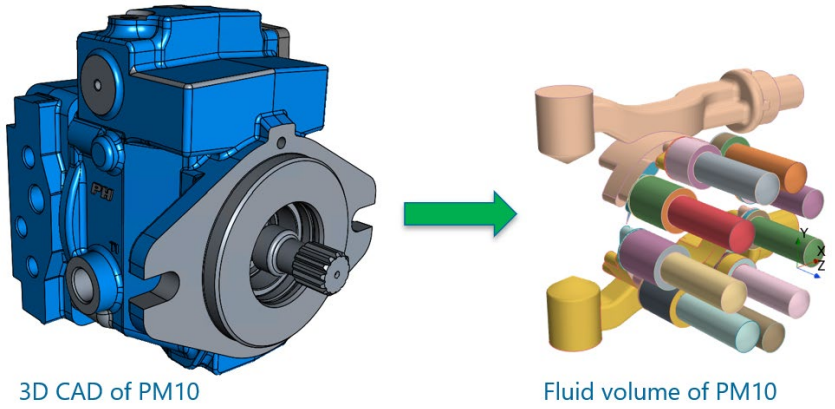

Figure 7: 3D CAD model (left) and fluid volume chambers (right).
Source: own

Flid volume has been meshed with polyhedral cells (where appropriate), hexahedral cells on areas of variable volume and with prisms next to boundaries. Contact/interface areas have been meshed with conformal mesh. Full 3D meshed fluid volume (rotating group and inlet/outlet chambers) is depicted on Figure 8.

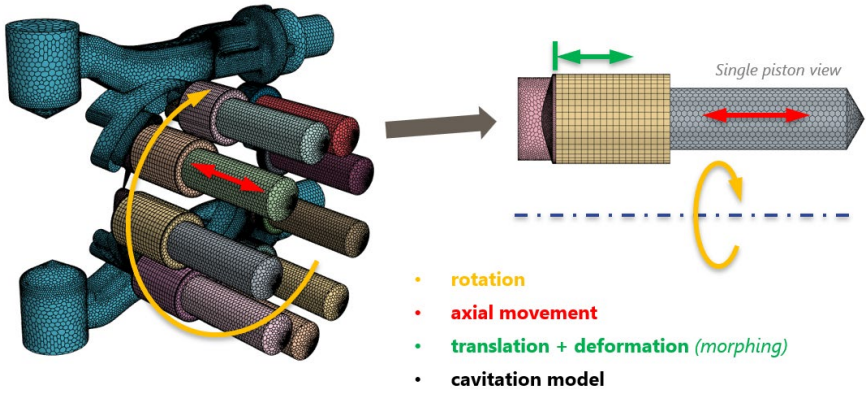

Figure 8: Mesh of fluid volume.
Source: own

Figure 9 depicts normalized piston velocities, used as boundary conditions. The curves have been obtained thanks to equation based parametric CFD model.

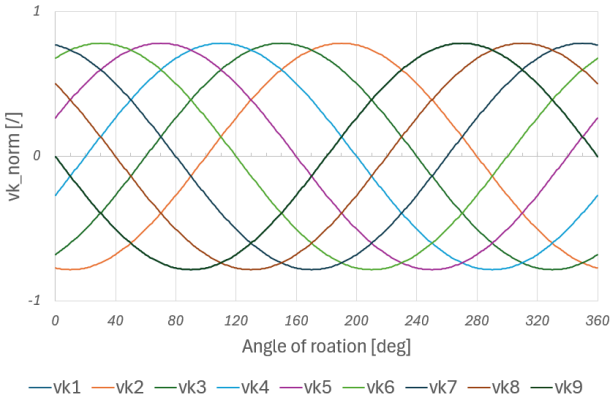

Figure 9: Imposed piston velocities.

Source: own

5 Results and discussions

Simulation has been defined for one full rotation (2π rad). During the rotation, several different physical quantities have been observed.

5.1 Piston chamber pressure

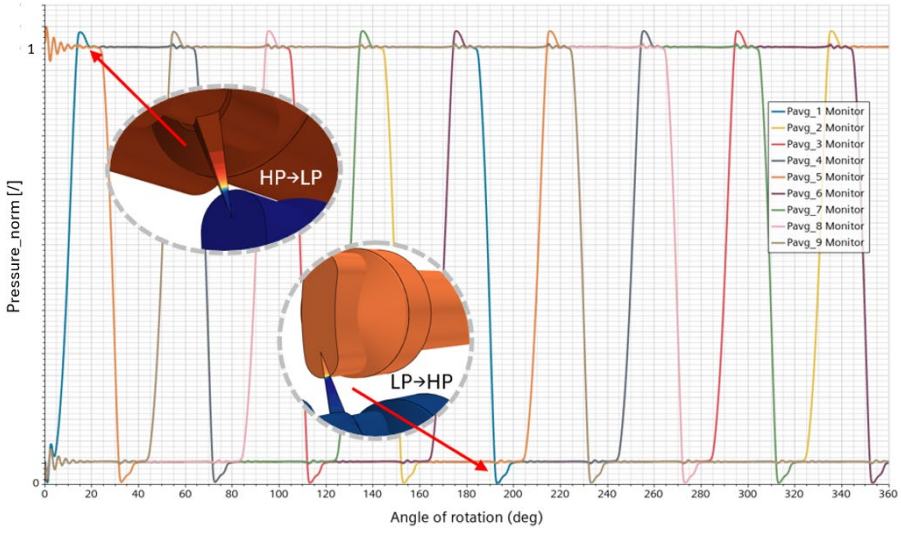

Figure 10: Normalized average piston chamber pressure.

Source: own

Piston chamber pressure (Figure 10) is a direct consequence of imposed piston velocity. A typical pressure pattern could be seen during one revolution. In the first part, there are some instabilities (i.e. oscillations) due to initialization. Then, each pressure spike (in terms of pressure under/overshoot) is a consequence of interface with high (HP) or low-pressure (LP) chambers.

Piston pressure force (in axial direction) is an integral value of pressure over the piton area. Corresponding curves have identical shape as for the pressure, so they are not shown here.

5.2 Piston tilting moment

Piston tilting moment (Mts) is depicted on Figure 11. Observing curve for piston #1, there is negative Mts in the first part of rotation. This is because piston chamber #1 is under high pressure (HP) and generated moment try to rotate in negative direction. It is opposite when the chamber is under low pressure (LP). The magenta curve depicts sum of all tilting moments (from all pistons chambers). One can sees that it is not constant and changes significantly during one revolution.

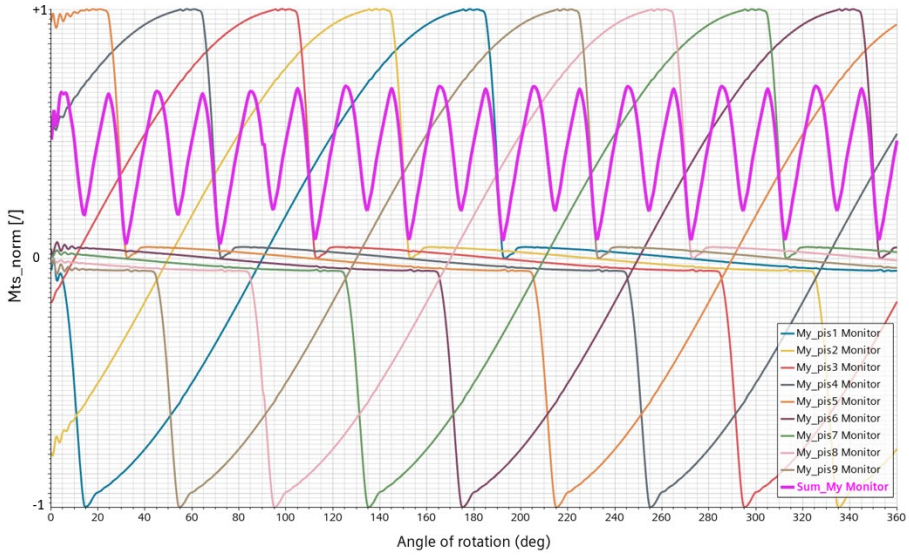

Figure 11: Normalized piston tilting moment Mts.

Source: own

5.3 Flow rate

Piston volumetric flow rate (VFR) could be seen on Figure 12. The very top and bottom curves refer to the total flow rate at the inlet and outlet ports. Total flow rates are not constant and change during the revolution. In addition, flow rate for each piston sees two local increase/decrease in flow rate (offset for π rad) due to beginning of the interface with high/low pressure zone or vice versa.

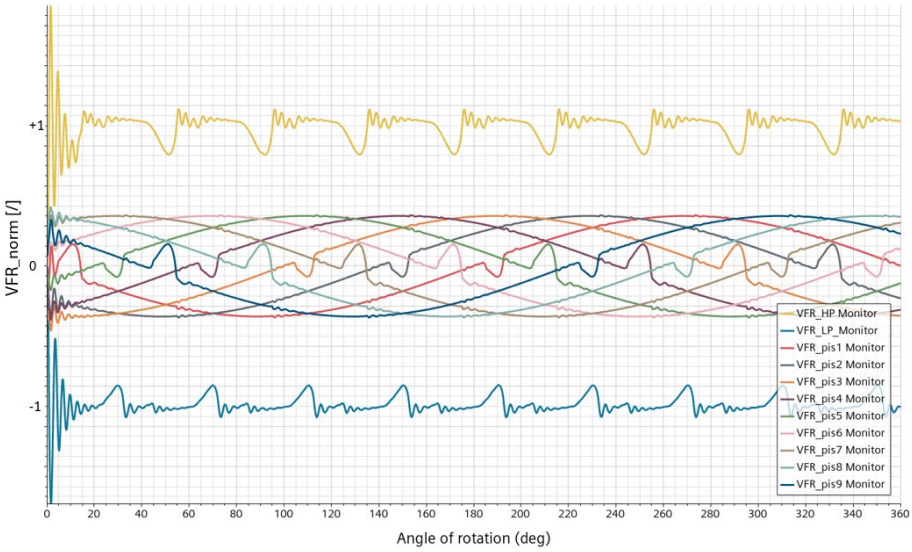

Figure 12: Normalized volumetric flow rate (VFR)
Source: own

6 Conclusion

Positive displacement machines are widely used in the engineering fields. Usually, such machines operate in a harsh environment and extreme conditions. Detailed understanding their functionalities is a key point for proper (robust) design, predicted service lifetime and finally, for customer satisfaction. Simulation-driven design can significantly decrease design cycle (lower the iteration loops), reduce experimental investigations and gain time to market. However, simulation of such machines requires advanced skills in numerical modeling. Although that these machines are presented on the market for decades, there is still lack of their detailed understanding.

In this study, numerical approach has been performed by means of computational fluid dynamic (CFD) within the environment of Siemens Simcenter Star-CCM+. The cavitation has been implemented into the CFD code in order to assess the potential cavitation areas. Results of flow analysis (e.g. piston chamber pressure, tilting moment on a swash plate etc.) enables better understanding of the key functionalities for such machines but also serve as design guidelines for engineers.The constructed numerical model opens the door for its further improvement, deeper investigation of axial piston pumps as well as its further deployment to the other type of positive displacement machine (i.e. hydraulic motor), produced by Poclain.

References

[1] https://www.hawe.com/fluid-lexicon/displacement-machine-displacement-unit/, last visited on 18.7.2025
[2] https://www.hawe.com/fluid-lexicon/positive-displacement-principle/, last visited on 18.7.2025
[3] https://www.slideshare.net/slideshow/positive-displacement-machines/54614510#1, last visited on 18.7.2025
[4] https://www.researchgate.net/figure/Typical-structure-of-axial-piston-pump_fig1_333125657, last visited on 18.7.2025
[5] https://support.ptc.com/help/creo/creo_pma/r11.0/usascii/index.html#page/simulate/cfd/Physics_5.html#, last visited on 18.7.2025
[6] https://support.ptc.com/help/creo/creo_pma/r11.0/usascii/index.html#page/simulate/cfd/Introduction_7.html#, last visited on 18.7.2025
[7] https://www.youtube.com/watch?v=G5qd-HxNuNM, last visited on 18.7.2025
[8] https://chatgpt.com/, last visited on 21.7.2025
[9] https://www.tribonet.org/wiki/cavitation/, last visited on 21.7.2025
[10] https://video.arnes.si/watch/h2ps9y5mjfh5, last visited on 21.7.2025
[11] https://www.youtube.com/watch?v=umYNj6BCszs, last visited on 21.7.2025
[12] https://www.youtube.com/watch?v=sH5uTW0sc2U, last visited on 21.7.2025
[13] https://www.youtube.com/watch?v=V9I6eV3Rs9g, last visited on 21.7.2025
[14] https://dynamox.net/en/blog/cavitation-in-industrial-pumps-understand-this-phenomenon, last visited on 21.7.2025
[15] https://asmedigitalcollection.asme.org/fluidsengineering/article-abstract/124/3/617/444321/Mathematical-Basis-and-Validation-of-the-Full, last visited on 21.7.2025
[16] https://www.tandfonline.com/doi/abs/10.1080/14399776.2010.1078099, last visited on 23.7.2025
[17] Simcenter STAR-CCM+ 2506 Help, last visited on 21.7.2025

Research Into the Influence of Critical Hydraulic Tank Parameters When Using Two Pumps Simultaneously

Franc Majdič, Matevž Kramar, Ana Trajkovski, Jan Bartolj

University of Ljubljana, Faculty of Mechanical Engineering, Ljubljana, Slovenia
franc.majdic@fs.uni-lj.si, matevz.kramar@gmail.com, ana.trajkovski@fs.uni-lj.si, jan.bartolj@fs.uni-lj.si

Simulation of positive displacement machines requires highly skilled engineers, use of advanced simulation tools and advanced simulation approach. The paper presents recent activities and progress on simulation of positive displacement machines – in particular, the axial piston pump and the radial hydraulic motor. Despite that these machines have been designed and produced for decades, there are still (design) features and phenomena not being investigated in detail or never being simulated. The simulation advancements mainly refer to the application of complicated kinematic motion, fluid properties, physics to consider as well as mesh and numerical algorithm techniques. In this paper, the focus is on modelling of advanced fluid material properties. Numerical approach has been performed by means of CFD within the environment of Siemens Simcenter Star-CCM+. The anticipation of cavitation has been possible by implementation of existing "full cavitation model".

DOI
https://doi.org/10.18690/um.fs.7.2025.15

ISBN
978-961-299-049-7

Keywords:
hydraulic tank, two pumps, interaction, uneven flow distribution, cavitation

University of Maribor Press

1 Introduction

Hydraulic devices are very common in many fields, in various industries, aviation, shipping, agriculture, construction and other fields. Hydraulic pumps are an indispensable component of hydraulic systems, as they ensure the flow of hydraulic fluid and thus perform work on the actuators side. Depending on their design and mode of operation, there are several types, the most common of which are gear pumps with external and internal gearing, vane pumps, axial piston pumps with swash plate or swash roller, radial piston pumps, etc. In closed circuits, the pumps delivered the liquid through pipes to the actuators. When the fluid has completed the circuit, it returns to the pump, from where a new circuit begins through the consumers. In open circuits, the hydraulic fluid is stored in tanks, from where it is pumped through pipes and to the consumers, and the path ends back in the tank. In this problem definition, we are focussing on an open circuit. In presented case, a hydraulic system with two gear pumps with internal gearing and two separate suction lines was considered. The larger pump has a displacement of 125 cm^3/rev, the smaller one 63 cm^3/rev. Under certain operating conditions, such a hydraulic system is likely to lead to interactions between the fluid flows at the inlet to the suction lines of the two pumps, and in extreme cases even to burning of the fluid between the pumps.

The lack of liquid or the presence of air pockets in the suction line will consequently lead to a reduced pumping capacity and an increase in the speed at the inlet to the suction line of this pump, as well as a corresponding drop in pressure due to the lack of liquid at the inlet. The air pockets are then transported with the flow into the pump, where the expansion and compression of the liquid causes cavitation and cavitation erosion of the material between the gears and the housing, which in extreme cases can also lead to pump failure.

The long-term presence of cavitation or the conditions under which cavitation occurs, lead to erosion of the surfaces exposed to the collapse of the vapour bubbles. This manifests itself as pitting on the surfaces where the bubbles have collapsed. Figure 1 shows an example of a pump with internal gearing that has failed due to cavitation erosion. The valve plate is shown, and the pitting is visible on the part of the plate where the opening for the discharge line begins. The reason for the occurrence of cavitation and the failure of the pump was too low a level in the

otherwise large-volume but too low tank [1]. This led to surface turbulence, with which the pump sucked in air, and a vacuum was created in the suction line. This created vapour bubbles, which were transported forwards by the rotation of the pump until the static pressure of the liquid rose above the vapour pressure of the bubbles again, causing them to collapse on the pressure side and erode the surface over time.

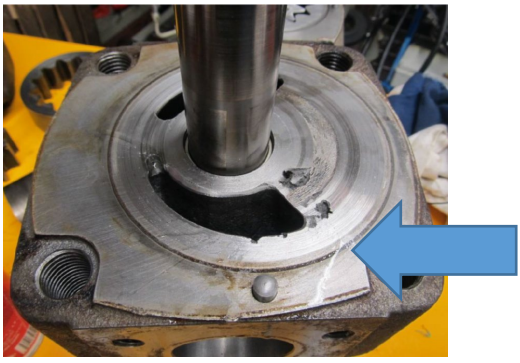

Figure 1: Internal gear pump with damaged valve plate due to cavitation erosion [1].

2 Materials and methods

In the following, the parameters of the tested hydraulic pump and the procedure with parameters for numerical calculations will be presented.

2.1 Tested internal gear type of hydraulic pumps

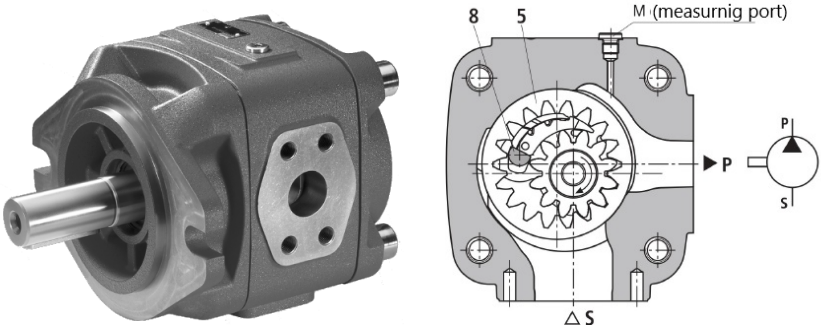

Figure 2: Tested hydraulic pump type PGH (Rexroth) [2].

Rexroth hydraulic pumps of the PGH type were used in the study (Figure 2) [2]. These are hydraulic pumps with internal gearing and constant displacement. This is 125 cm^3/rev for the larger pump and 63 cm^3/rev for the smaller pump.

2.2 Hydraulic reservoir with different suction ports for two pumps

In the experimental research we had to construct a suitable tank to investigate the influencing parameters. The model of the tank was created using the SolidWorks programme. Given the space available in the laboratory and the recommendations for the dimensions of the tank, we first established rough initial dimensions – 950 mm wide, 700 mm deep and 500 mm high – which we then used as the basis for the modelling. As we will be observing the inside of the tank, particularly the area around the suction pipes, during pump operation, the front of the tank is made of glass. The other sides and the bottom of the tank are made of sheet metal, material ST37 or S235, which is bent and then welded into sub-assemblies and into the overall assembly (Figure 3).

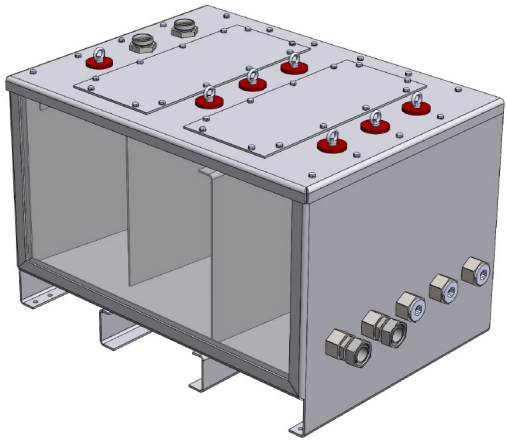

Figure 3: Special hydraulic tank for analysing the influence of the suction lines of two or more pumps (1050 mm x 750 mm x 670 mm).

2.3 Numerical calculation of the fluid dynamics of two pumps

In the following, we present the parameters of the simulations carried out in the Ansys Fluent software environment. This is a software package for computational fluid dynamics, hereinafter referred to as CFD. This is a discipline that deals with

analysing flow systems, heat transfer and associated phenomena such as chemical reactions. It uses numerical methods and algorithms (e.g. finite difference methods, finite volume methods, etc.) to search for solutions based on input parameters.

The basic (guiding) equations that describe the motion of fluids in CFD are the Navier-Stokes equations. These are a series of partial differential equations that describe the conservation of mass and momentum of the fluid.

One of the most important steps before the actual numerical calculation of the mesh is the definition of turbulence models. Most of the flows we encounter in technical practise are turbulent. Such a flow is characterised by sudden fluctuations in velocity and a disordered and rapid flow movement due to the formation of vortices. These represent an additional mechanism of energy and momentum transfer which, in contrast to molecular diffusion, occurs much faster in laminar flow, which consequently leads to higher values for friction, mass and heat transfer.

The geometric model for the simulation studies was created using the SolidWorks programme. Several models with individual differences were defined according to the simulated influencing parameters. We started from the dimensions shown in Figure 4. It is a section of a part of the suction pipes of the tank. The geometric model consists of two bodies to enable an efficient network.

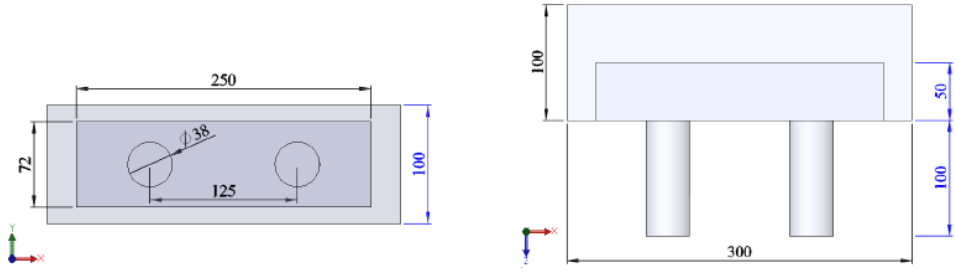

Figure 4: Dimensions of the geometric model of the simulation research (all dimensions are in mm).

The mass flow rate at the outlet surfaces of both pipes was determined (shown in red in Figure 3) as the outlet boundary condition. Here, the same volume flow was assumed as specified in the manufacturer's catalogue [2] for pumps, measured at

n = 1450 min^{-1}. Using the known volume flows of both pumps and the known density of the oil, the mass flow rate for each pump was calculated, according to the expression $\dot{m} = qV\varrho$. This amounts 2.583 kg/s for the pump with a displacement of 125 cm^3/rev, and 1.2915 kg/s for the pump with a displacement of 63 cm^3/rev. The mass flows are shown in Figure 5 as red arrows pointing out of the range.

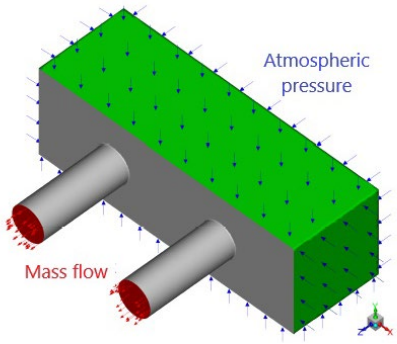

Figure 5: Boundary conditions of the simulations of two suction lines.

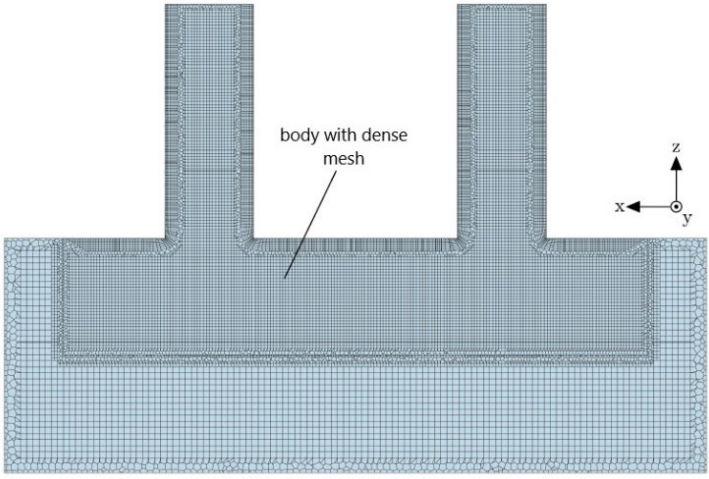

Figure 6: Meshed geometric model in the xz cross-sectional plane [9].

The geometric models were meshed with the CFD tool Fluent (With Fluent Meshing) of the Ansys software. The poly-hexcore meshing was used, which is one of the mosaic meshing technologies. It is a combination of polyhedral and

hexahedral control volumes, where polyhedral volumes fill the outer region near the wall (boundary layer) and allow the description of more complex parts of the geometry, while hexahedral volumes fill the inner region of the volume [3]. In this case, each hexahedron at each mesh density is subdivided into eight smaller control volumes called octrees (from the Greek word octo – eight and the English word tree) in a tree structure. Numerous studies and articles [4 to 8] have shown that the use of polyhexkernel meshing leads to a lower number of control volumes, higher mesh quality, shorter computation time and higher solution accuracy (Figure 6) [9].

3 Results

Here, the results of a study on the effects of different distances between two suction pipes and the influence of oil level will be presented.

3.1 Numerical results

Figure 7 shows the distribution of velocity fields for case of two suction lines at a distance of 125 mm. The left suction line belongs to a pump with a displacement of 63 cm^3/rev, the right one to a pump with a displacement of 125 cm^3/rev. It can be seen that the velocity fields of both suction lines curve or tilt in the direction of the neighbouring line. The pressure curves shown in Figure 8 show the same, whereby each is shown with its own scale due to the large differences in the pressure values of the two suction lines. The curvature or tilting of the velocity lines would mean that the velocity and pressure gradients are no longer symmetrical to the longitudinal axis (z) due to the mutual influence of the suction lines, but are greater on the side that is closer to the other suction line. This can also be seen from the velocity profiles in Figure 9.

The calculation of the difference in the absolute values of the gradients of the velocity profiles along the walls of one suction pipe and the other also proves the asymmetry.

Figure 9 shows the flow lines at the inlet of the suction lines. Due to their proximity, the interaction of the flow lines creates a "virtual liquid wall" between the delivery areas of the two pumps. This prevents liquid from being pumped through from the delivery area of the other pump.

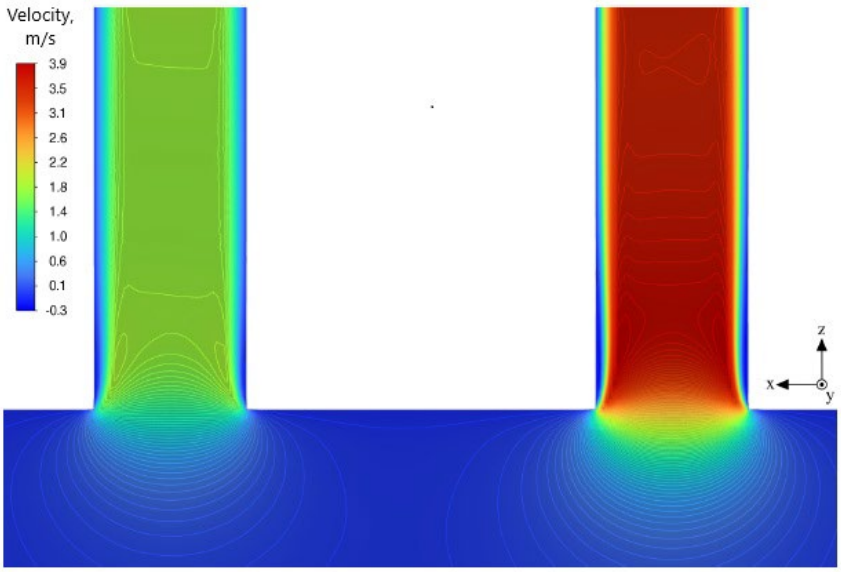

Figure 7: Velocity fields of two suction lines at a distance of 125 mm

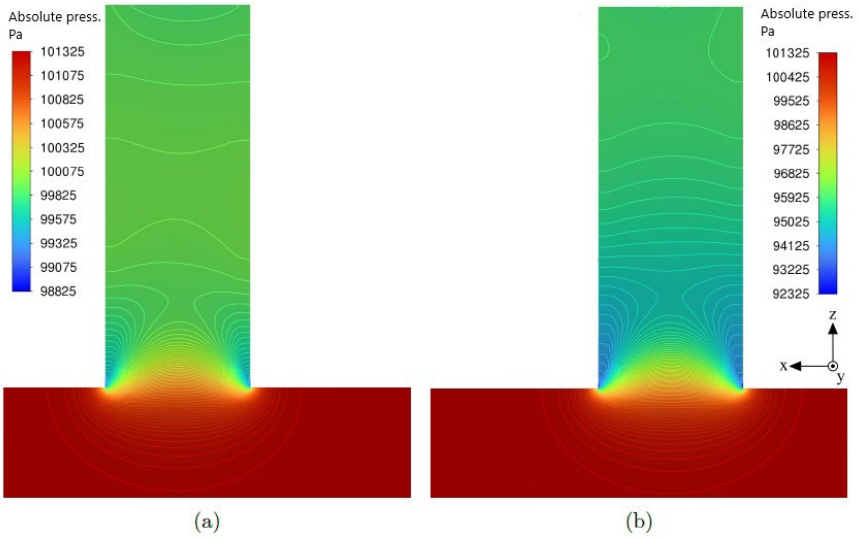

Figure 8: Absolute pressure curves of a pump with a displacement of 63 cm³/rev (a) and 125 cm³/rev (b) with suction lines at a distance of 125 mm.

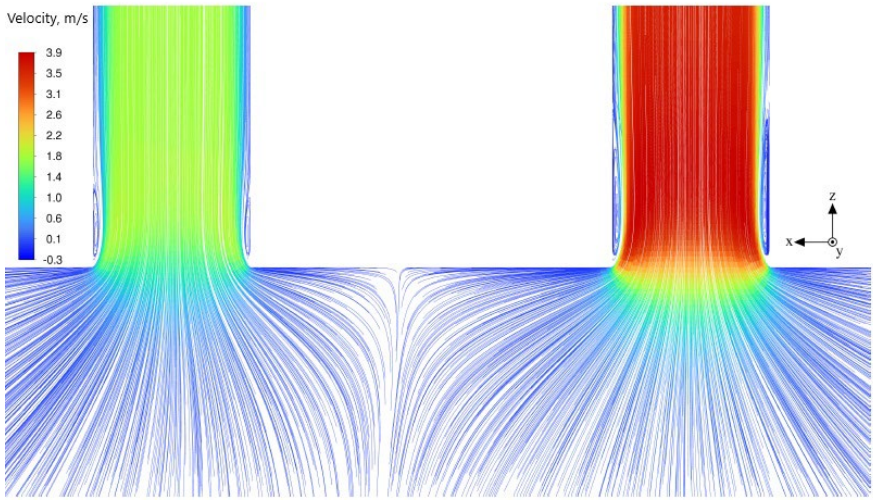

Figure 9: Streamlines at the inlet of the suction lines at a distance of 125 mm.

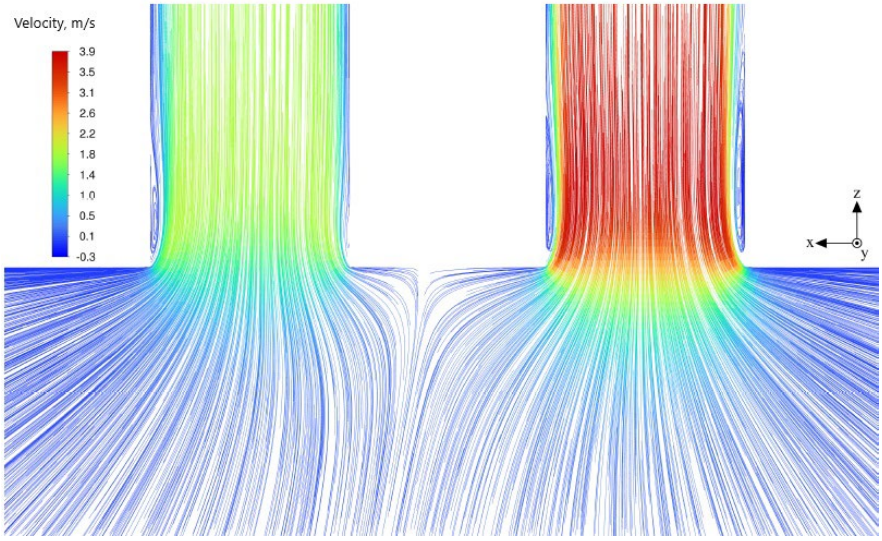

Figure 10: Streamlines at the inlet of the suction lines at a distance of 75 mm.

Due to the uneven power distribution between the suction lines, the pump with a displacement of 125 cm^3/rev has a greater influence on the liquid particles that would otherwise follow the nozzles into the suction line of the pump with a

displacement of 63 cm³/rev. The larger pump therefore interferes with the delivery area of the smaller pump and prevents a normal flow of liquid. The apparent wall of the nozzles is therefore not straight but curved in the direction of the pumping area of the smaller pump. This leads to an asymmetrical flow of liquid into the suction lines. The result is a thinning of the stagnant recirculation area along the wall, as can be seen in Figure 10 and Figure 11 - the recirculation area of the nozzles in the suction line of the smaller pump almost disappears in this part, while it starts to decrease in the case of the larger pump.

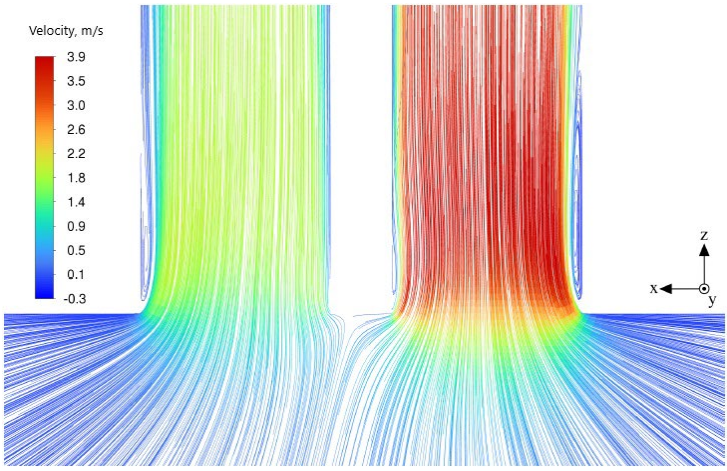

Figure 11: Streamlines at the inlet of the suction lines at a distance of 50 mm.

3.2 Experimental results

Table 1 summarises the average values of the measured absolute pressure of both sensors with the associated expanded uncertainties of type A as well as the maximum and minimum pressure values for all 4 distance measurements.

The maximum pressure drop or the lowest absolute pressure due to the change in suction conditions, as a result of the mutual influence of the suction lines is given at the smallest distance of 125 mm. Compared to the next largest distance of 250 mm, the pressure drop in the suction lines of both pumps is 800 Pa greater and the absolute pressure is correspondingly lower. The maximum absolute pressures of both pumps are also 1400 Pa lower, and the minimum absolute pressures are also

lower, namely 1300 Pa for the larger pump and 1000 Pa for the smaller pump. Above a distance of 125 mm, the pressure changes in the suction lines of both pumps are no longer uniform and begin to fluctuate around stable values. From this it can be concluded that above a distance of 125 mm the mutual influence of the suction lines is no longer present or is negligible.

Table 1: Results of the absolute pressure influence of the suction line distance and the associated type A measurement uncertainties.

	125 mm	250 mm	375 mm	500 mm
p_1, Pa	64200 ± 11	65400 ± 9	65800 ± 13	65300 ± 11
p_2, Pa	80300 ± 13	81100 ± 8	81000 ± 6	81100 ± 8
$p_{1,maks}$, Pa	65800	67200	67200	67200
$p_{1,min}$, Pa	62200	63500	63500	63500
$p_{2,maks}$, Pa	81600	83000	82500	83000
$p_{2,min}$, Pa	79300	80300	80300	80300

A reduction in the oil volume in the tank or a lowering of the level has a negative effect on the suction conditions. The already low oil volume at a given flow rate is reduced even further, resulting in turbulent oil and a turbulent level. In addition, with high flow rates and oil turbulence and a lower fill level in the tank, it often happens that the suction power of the pumps creates a localised vacuum in the oil level. This creates a vortex that is sucked into the suction line. This vortex forms and disappears within 1 to 2 seconds, as shown in Figure 12.

Figure 12: Pumping air from the surface into the suction lines – view of the tank from above.

4 Conclusions

In the present study, we determined numerically and experimentally the conditions for the interaction of two pumps mounted outside the tank with two separate suction lines and flow rates of 125 cm^3/rev and 63 cm^3/rev. During the experiments, we used a glass front to provide a real-time view of what was happening inside the tank, which contributed to more efficient and high-quality results.

The main results and findings are:

- The phenomenon of interaction of the suction lines of two hydraulic pumps was confirmed by numerical situations.
- For the experimental studies, an experimental test rig with an open circuit was designed, as well as a tank, suitable for measuring different mutual distances and other variable parameters.
- In the case of using two hydraulic pumps with internal gears and a corresponding displacement of 125 cm^3/rev and 63 cm^3/rev and two separate suction lines, we carried out pressure measurements in the suction lines at the pump inlet.
- It was found out that the mutual distance has a great influence on the flow field near the suction lines and on the non-uniform flow distribution. In our particular case, using these two pumps, the mutual distance between the suction pipes over 125 mm no longer plays a major role.
- It was experimentally confirmed, that very undesirable conditions occur when the volume is reduced and especially when the liquid level in the tank is reduced. If the volume is too low, the oil swirls strongly, and too low a level also leads to the absorption of air from the surface in the form of funnels. Air in the oil consequently leads to conditions for cavitation to occur, which can have negative consequences for efficiency and damage to pumps in the event of long-term operation without monitoring or troubleshooting.

Acknowledgments

We would like to thank the programme group P2-0231 and the agency ARIS for the financial support of the projects L2-4474, L2-2618 and L2-50083. We would also like to thank Mr Ludvik Karmuzel from the company Nord Fluid for the motivation for this work and also for the rented pumps.

References

[1] F. Majdic, M. Polajnar, Meritev podtlaka na sesalnem vodu črpalke livarskega stroja, Fakulteta za strojništvo, Ljubljana, (2020).
[2] Internal Gear Pump, Fixed Displacement: Type PGH. dostopno na: www.boschrexroth.de
[3] ANSYS Fluent Mosaic Technology Automatically Combines Disparate Meshes with Polyhedral Elements for Fast, Accurate Flow Resolution. dostopno na: https://www.ansys.com/resource-center/white-paper/ansys-fluent-mosaic-technology [ogled: 8.4.2025].
[4] ANSYS mosaic poly-hexcore mesh for high lift aircraft configuration. 21st Annual CFD Symposium, 09 2019.
[5] H. Mendis, Better meshing using ANSYS Fluent Meshing, 2018. dostopno na: https://www.linkedin.com/pulse/better-meshing-using-ansys-fluent-hashan-mendis [ogled: 8.4.2025].
[6] V. Karanović, Development of a solid particle influence model on performance of piston cylinder contacting pairs for hydraulic components, University of Novi Sad, 2015.
[7] D. Wooton, The Lubricant's Nemesis-Oxidation, Practicing Oil Analysis 5 (2007) 5–6.
[8] S. Jung-Hun, J. Kyung-Ryeol, K. Hyoung-Eui, A Study on the Effects of Contaminant Types on the Wear Degradation Characteristics in Internal Gear Pumps, Tribology and Lubricants 27 (2011) 134–139.
[9] M. Kramar, Raziskava medsebojnega vpliva sesalnih vodov dveh hidravličnih črpalk, magistrsko delo, Fakulteta za strojništvo. Univerza v Ljubljani (2025).

Upfront Simulations and (Their) Democratization – Where We Are?

Anže Čelik
Poclain Hydraulics d.o.o., Žiri, Slovenia
anze.celik@poclain.com.

Upfront simulation involves activities in the early design phase. The goal is to identify potential problems early, optimize designs, and predict performance when changes are cheaper and easier to implement. Democratization of simulation is understood as making simulation tools accessible to non-simulation experts within a company, organization, or community. This means removing barriers that limit product managers, designers, or even non-experts from running simulations and making decisions. The paper presents current status regarding upfront simulations and their democratization within company Poclain. The practical cases demonstrate the abilities brought through the upfront (or front-loading) simulations. It is also explained what activities have been made to democratize (deploy) simulation tools among the group of design engineers. The power of upfront simulations is also demonstrated on real case example, performed in real time (in-situ) at the conference. It emphasizes its ease of use, the importance of understanding the product behavior as well as the gain in time to market.

DOI
https://doi.org/10.18690/um.fs.7.2025.16

ISBN
978-961-299-049-7

Keywords:
upfront simulation, democratization, design stage, prototype, product performance

University of Maribor Press

1 Buzzy words

If one searches for the explanation or the meaning of **upfront simulation**, there are dozens of different explanations, interpretations and words used for the same (or similar) meaning ... such as upstream simulation, simulation-driven design, simulation-led design, etc. One can quickly get confused.

As with most buzzy words, upfront simulation and/or democratization are interpreted differently by different people. But all would likely agree on the broad sense of its meaning: the goal of simulation democratization is to empower more people to take advantage of simulation technology (Figure 1). On the other hand, upfront simulation means simulation activities being performed early in the design stage. ([1] to [8])

Figure 1: Simulation democratization, an example.
Source: own

1.1 To diminish the misunderstanding

The source [2] gives a meaningful example what it is meant by "democratization" – it explains the term on GPS (Global Positioning System). Deploying a GPS is not an easy task. One needs a knowledge of wireless communications, orbital mechanics, general relativity, and a whole lot more. Locating oneself with a GPS used to require just as much expertise, in the form of specialized equipment and operators who knew how to use it.

The complexity of GPS has not changed. What has changed is who can effectively make use of it: everyone. If one owns a smartphone, he has access to GPS. He does not need any knowledge of GPS to use it – he just pulls up Google Maps and tell it where he wants to go. The details are irrelevant to the end user.

The same idea lies behind the democratization of simulations.

Looking at past technological precedents, one could argue that Henry Ford saw the value of democratizing the ownership and use of motor cars a century ago by making them more consistent and affordable, and Steve Jobs created a market for smart phones a decade ago that was very different to what had gone before - allowing for the democratization of such technology. Even the worldwide web associated with the internet of the last 30 years is a form of democratization because it shares information globally. We are in an age of democratization in so many ways [8].

1.2 How did we understand those words at Poclain?

Simulation tools have been part of design process at Poclain for decades (starting much before the 21st century). In the early stage, FEA (Finite Element Analysis) has been introduced by means of dedicated "FEA expert" and later on by small team of "FEA experts". Then, 1D simulations were implemented as well. But again, they were used only by dedicated team (Figure 2). Later, CFD (Computational Fluid Dynamics) was brought into the company and was used only by single "CFD expert".

Figure 2: The early team of simulation experts.
Source: own

It needs to be mentioned that in the beginning (as well as later on), the word "simulation tool" mainly refers to the use of standalone advanced simulation tool. A lot of practice was/is necessary to be autonomous and experienced user.

Later, the number of simulation users increases year by year (Figure 3).

But still, those users mainly used simulation tools as their "main source", so daily. They were experts in this (simulation) field. By conquering new markets and new (demanding) customers, product portfolio progressively expanded along with the product complexity. Consequently, the need for deeper understanding of products behavior arises; but also, time to market was requested to be shorter and shorter. Those, along with some other reasons and needs, were the main triggers to invest more into the virtual validation (i.e. simulation) approach.

Figure 3: The extended team of simulation experts.
Source: own

As more and more people started using simulation tools, there soon raised the need to unify and standardize simulation procedures. Further, as Poclain started to acquire more companies (ex. Slovenian Kladivar, for example), there was also the need to unify simulation tools (software) as well.

The natural consequence of increasing market needs, its demands and its share, we were faced with the following fact: increase the team of experts or extend the use of simulation tools towards the design engineers (designers).

2 The path to broader leverage of simulation tools

Speaking from Poclain point of view, the leverage of simulation tools should be put in a much global aspect. Tools (any kind) are one of the main pillars of the process, called Knowledge Management (KM). This process has been put in place at Poclain since last decade. But note that KM is also one out of ten pillars of lean product and process development (LPPD). LPPD is a powerful system for developing new products and services, as well as the processes needed to produce and deliver them [9].

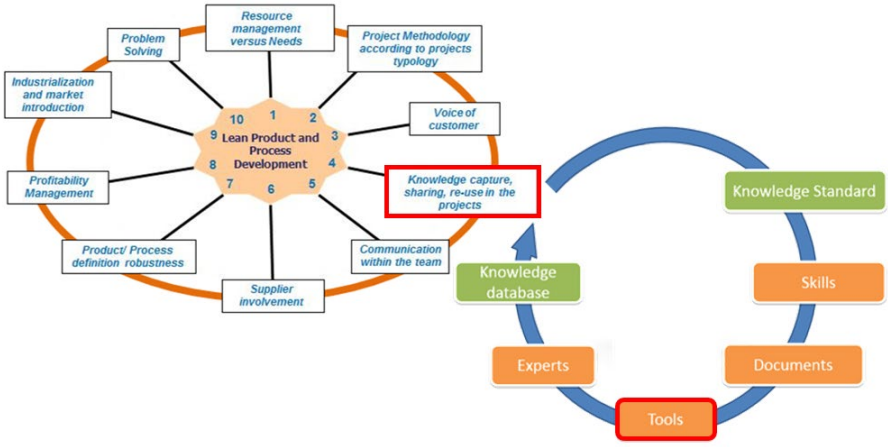

Figure 4: Tools under global aspect of LPPD.
Source: own

2.1 Democratization means changing our mindset

It may not be as easy as simply giving our design engineers simulation tools, and then waiting what will happen. Mostly nothing! Nobody will use the tools. One can go further and provide dedicated training (on-site, virtual classroom etc.). Most often, the result is also predictive – very few people will use the tools. Clearly, there's more to democratization than the simple provision of simulation tools. Similar findings are also reported by [2].

Democratization is a strategic, well-organized path. It can only be successful when an entire organization - from the managers to the analysts to the design engineers – is on board with the shift in thinking. The most difficult thing in simulation

democratization is not the technology itself – it is actually the culture, the mindset, the spirit.

And it usually takes a significant amount of time (years!) to give the right spirit to the team or to the entire enterprise. Poclain was not an exception here. Very in the beginning, project managers did not want to "book time" in a project pipeline to perform simulations because they simply did not trust the outcomes of simulations; top management did not know much about the technology and therefore investment in simulation tools has not been approved from their side; and the last but not the least, designers have seen using simulation tools just as additional (unnecessary) work. So, it has been many barriers to start with democratization.

2.2 Efforts to make democratization live

As just mentioned, changing people's mindset (starting with my own) usually takes the most resources. Here, lots of well-defined activities are incorporated, such as clear presentation (with facts!) of new approach, its added values to the stakeholders, strategic plan of deployment (trainings, workshops …), support, return of investment (for management) etc.

At Poclain, simulation tools democratization started by the group of enthusiastic who, initially, made simulations solely by themselves – mostly even before the concept stage in order to study feasibility and to build missing knowledge bricks. Along with their expertise path, simulation results became more and more aligned with test results and confidence from (project) management, design leaders and design engineers became higher. Consequently, management decided to deploy simulation approach on a design level.

And here, the main effort just started. First, standardized and validated simulation procedures have been established and official simulation tools created and codified (for those purposes, intranet portal has been established, see Figure 5). Then several training documentations have been written, demo cases prepared and training session organized. Last but not least, strong simulation (technical) support has been established in order to minimize bottleneck during design stage. All those training sessions have been integrated later into the Poclain Academy system. Each training document is accessible via intranet portal.

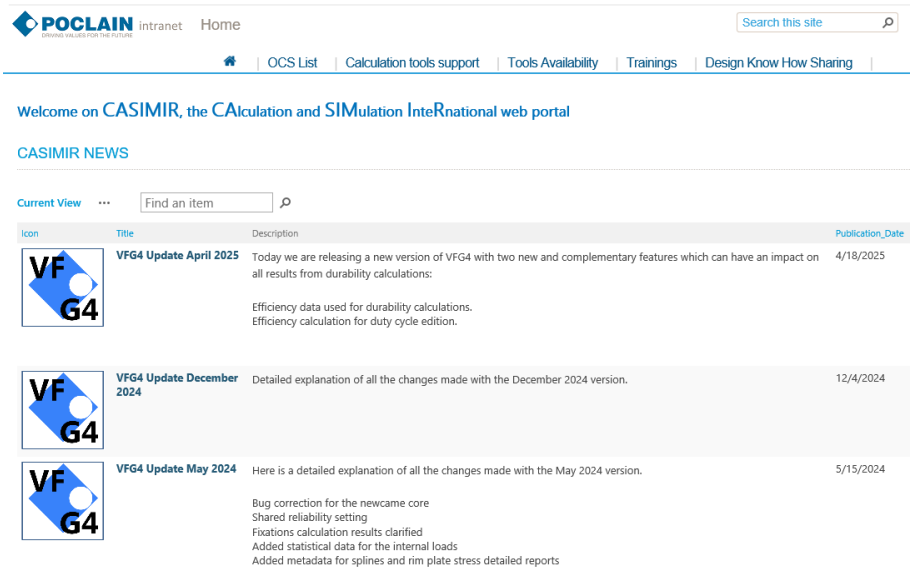

Figure 5: Intranet portal for calculation and simulation.
Source: own

2.3 Efforts to keep democratization alive

Despite numerous training sessions being organized and active support provided, there was still a lack of simulation spirit. Very few people "internalized" simulation tools as a part of their design workflow. Simulation tools with corresponding documentations, training and support were there, but not broadly used within enterprise. To (re)enforce the simulation spirit, additional steps have been introduced. Two of them are explicitly mentioned hereafter: regular workshops and yearly deployment plan (YDP).

2.3.1 Workshop

At Poclain, we found that just "pushing" people to use simulation tools is not the right approach. There is (almost) no lever to use simulation tools efficiently if their users (i.e. design engineers) do not feel "comfortable" with. There is another path we took to convinced users to "grab" the simulation tools – because they like them and because they are familiar with them. This is the path of regular practicing of

simulation tools on real demonstrative cases and showing best practices of using simulation tools. This is the path of regular workshops.

A workshop is an organized event where (limited number) participants refresh their knowledge and skills on simulation tools – simply by quick recap what they learned during the past trainings (e.g. theoretical background, Graphical User Interface GUI tool, methodologies …) and by practicing simulation tool (and methodology) on real case. Note that workshop is not a training, it is a "refreshment" of their existing knowledge and skills (Figure 6).

Figure 6: Internal workshop for the employees.
Source: own

Such a workshop is organized at least once per year for most used simulation tools (numerical or analytical). Each design engineer is invited to join the workshop.

2.3.2 Yearly deployment plan

Yearly deployment plan (YDP) is the process of creating a plan for the successful deployment of new/existing tasks, tools or systems. It involves identifying the resources, tasks and timeline needed to ensure that the deployment is successful [10].

Through the YDP, we define **where** (on which projects, topics), **who** (design engineer) and **what** (part, assembly) needs to be virtually validated by means of simulation tools. In this way, we promote people using simulation tools and project

managers to book necessary time for such analyses into project pipeline. By this way, there is no more "we do not have time" and much less design "surprises" later in a design stage.

3 Current status of simulation tools democratization at Poclain

There are numerous simulation tools currently used by design engineers and simulation experts. Some of the simulation tools are purely analytical and have been purchased (e.g. compression spring design tool) or developed internally (e.g. hydraulic motor lifetime design tool). The rest of the simulation tools are numerical, which means that they use one or more available numerical methodologies to solve governing equations (originally in partial differential form).

Whatever the nature or the origin of the simulation tools, they are all officially codified and available via intranet portal (Figure 5). Each codified tool is "equipped" with corresponding technical documentations, training sessions, associated skills and contact reference (i.e. expert for dedicated field of physics).

3.1 Upfront simulations

So far, nothing has been said about upfront simulations: what it actually is, how it is linked with simulation democratization, how it has been implemented etc. Let's focus and clarify such questions hereafter. Mechanical computer aided design (MCAD) is the center of all virtual product development processes. Embedding 3D simulation tools (e.g. FEA, CFD, topology …) inside MCAD tools is an effective way of improving user productivity and democratizing the use of such tools [8] (Figure 7).

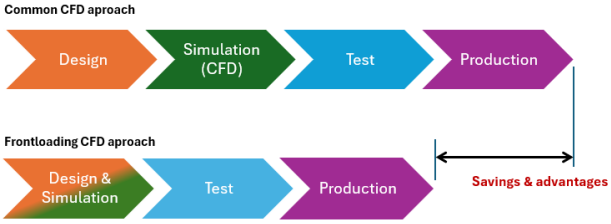

Figure 7: Classic traditional CFD design flow and its relationship to MCAD relative to a frontloading approach.

Source: own

Embedding 3D simulation tools in MCAD also allows for more simulations early in a product development design process where it has the most impact at the least cost. Such upfront or frontloaded simulations within common CAD environments and PLM workflows are done directly on the latest 3D CAD model and provide results in minutes or hours rather than days or weeks.

At Poclain, MCAD package comes from PTC and is called Creo Parametric. It has several simulation tools embedded (Figure 8), such as Simulate (FEA), Flow Analysis (CFD), Mold Analysis, Mechanism, Generative design (Topology) etc.

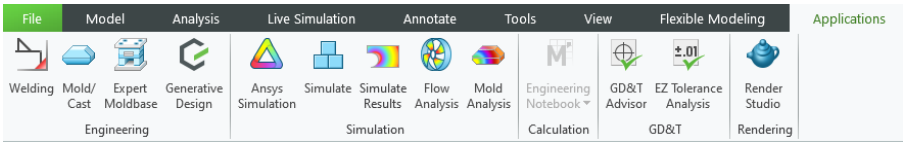

Figure 8: Embedded (simulation) tools within PTC Creo.
Source: own

3.1.1 Upfront CFD simulations

Thanks to embedded simulation tools, each MCAD user has now access to various tools. Embedding computational fluid dynamics (CFD) into native CAD software is definitely one of the biggest factors driving the democratization of CFD. Data generated by CFD is the same as any other product manufacturing information, like mass, visual appearance, kinematics, manufacturing cost, etc.

Therefore, as soon as MCAD user builds his first design idea(s), it could be evaluated by this embedded simulation tools. There is no need to switch to another CAD package or simulation software. Embedded tool also allows to keep (bi-directional) associativity with the main CAD model which significantly reduces iterative simulation loops (Figure 7).

Let's demonstrate the practical use of CFD tool on typical Poclain product: directional control valve (type KV, size 6).

1. Create/import CAD model

In this step, a CAD model is created/designed or imported in any supported format (Figure 9). It is advised to "equipped" part of interest with auxiliary elements (e.g. subplates, fittings …). This is of especially importance if simulation results need to be compared with experimental data.

2. Create new simulation project within the embedded CFD tool

Since there might be several simulation projects within the same CAD model, it makes sense to define meaningful project name (to avoid confusion or misunderstanding).

3. Follows the workflow "left to right" (in the flow analysis ribbon)

Flow Analysis Ribbon (Figure 10) guides CFD user through the complete CFD workflow of preprocessing, performing the simulation and post-processing; CFD analysis starts with fluid domain definition, fluid type (material) definition, physics to consider, definition of boundary conditions, mesh generation and (during pre- or post-processing stage) section planes, plots and monitoring points definition.

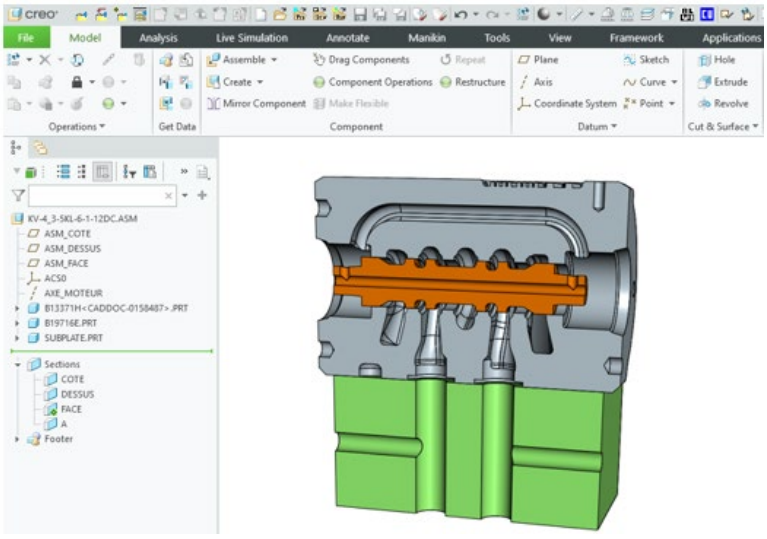

Figure 9: CAD model created within PTC Creo.

Source: own

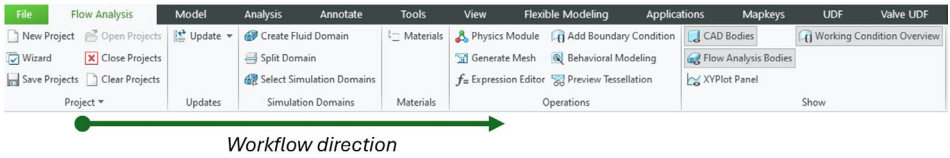

Figure 10: Workflow in embedded CFD tool.
Source: own

4. *Run simulation(s) and observe obtained results*

Once a single or multiple projects are set up, simulation run could be performed (single or batch). It needs to be emphasized that runtime is usually very fast due to efficient numerical solvers and multicore capabilities. Then, the second (and very important!) part of CFD task begins → post-processing stage is an "work of art" for CFD user. His skills and ingenuity are key factors to get most from simulation results (Figure 11).

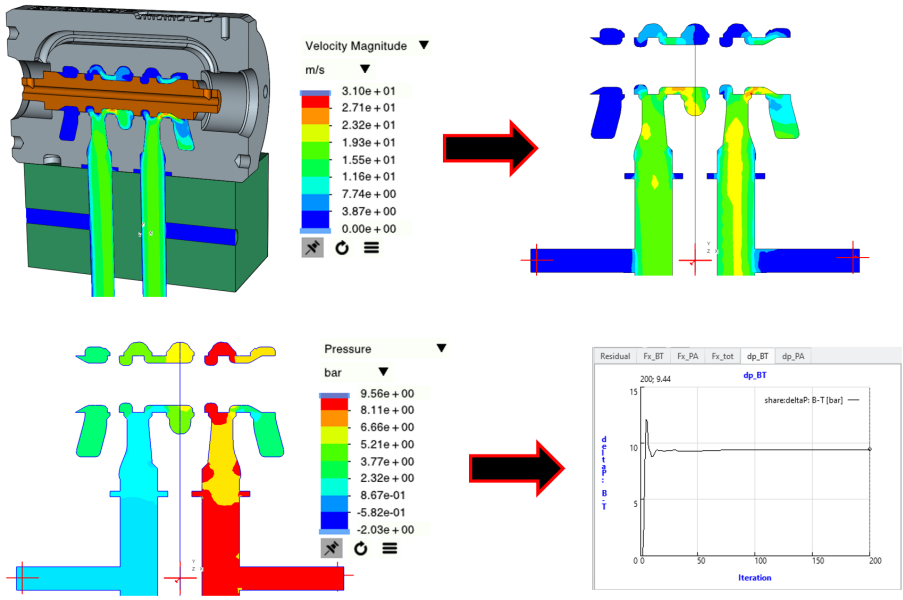

Figure 11: Post-processing activities
Source: own

4 Conclusion

The paper presents the general aim, meaning and current status regarding upfront simulations and their democratization within Poclain group. The path that explains the evolution of simulation democratization is also shown. Further, it is clearly explained that simulation democratization is all but not "just push" the simulation tools to design engineers. Otherwise, the result is well predicted – tools are not widely spread. The most difficult thing in simulation democratization is actually not the technology itself – it is the culture, the mindset, the spirit.

The ability and power of upfront simulations is also demonstrated on practical example. It emphasizes the ease of use of simulation tool, the importance of understanding the product behavior as well as the gain in time to market - due to short time from pre- to post-processing stages. Validated simulation tool can make its user more powerful, productive and can provide in-depth understanding of the product in hand. But it is user responsibility to "grab the tool from the shelf".

References

[1] https://pdsvision.com/technologies/simulation/upfront-simulation/, last visited on 24.6.2025
[2] https://www.engineering.com/the-path-to-simulation-democratization/, last visited on 24.6.2025
[3] https://www.ptc.com/en/resources/cad/white-paper/simulation-led-design, last visited on 26.7.2025
[4] hhttps://diginomica.com/ansys-democratizing-simulation-key-reducing-uncertainty, last visited on 26.7.2025
[5] https://www.digitalengineering247.com/article/the-mission-to-democratize-simulation-at-turning-point, last visited on 26.7.2025
[6] https://www.simulationhub.com/philosophy, last visited on 26.7.2025
[7] https://www.engineering.com/mentor-graphics-makes-cfd-meshing-faster/, last visited on 24.6.2025
[8] https://revolutioninsimulation.org/wp-content/uploads/2020/06/THE-DEMOCRATIZATION-OF-CFD-K-Hanna-I-Weinhold.pdf, last visited on 24.6.2025
[9] https://www.lean.org/explore-lean/product-process-development/, last visited on 26.6.2025
[10] https://www.enov8.com/blog/what-is-deployment-planning/, last visited on 26.6.2025

Presentation of a Mobile Testing Device for the Inspection of Micropiles of Rockfall Protection Nets in Alpine Terrain

Jörg Edler,[1] Matthias Rebhan,[2] Emanuel Troyer[1]

[1] Graz University of Technology, Faculty of Mechanical Engineering and Economic Sciences, Graz, Austria
joerg.edler@tugraz.at, emanuel.troyer@tugraz.at
[2] Graz University of Technology, Faculty of Civil Engineering Sciences, Graz, Austria
rebhan@tugraz.at

The protection of structural facilities in alpine regions from natural hazards--particularly rockfalls--is becoming increasingly important due to global warming. While installing protection systems such as rockfall nets is an important first step, these systems require long-term maintenance and regular inspection to ensure functionality. Although inspection of the nets themselves is often feasible in alpine terrain, inspection of the ground anchors has not been possible until now. This challenge motivated the development of a hydraulically powered, mobile testing device specifically designed to evaluate the ground anchors of rockfall nets in alpine areas. The hydraulic concept enables the required forces to be generated within a short time, while the compact design allows the device to be carried through difficult terrain by just two people.

DOI
https://doi.org/10.18690/um.fs.7.2025.17

ISBN
978-961-299-049-7

Keywords:
micropile,
testing,
testing device,
Impulse cylinder,
dynamic testing

University of Maribor Press

1 Introduction

Micropiles (ground anchors) have proven to be a reliable foundation element for protective structures, as they are able to transfer impulsive tensile loads resulting from natural hazards such as rockfall into the subsoil. In contrast to conventional foundations, where permanent loads are decisive, protective structures are primarily subjected to dynamic actions [1]. However, standardised procedures to adequately capture the dynamic behaviour of micropiles under realistic loading conditions are still limited.

Previous investigations considered different concepts for energy input, including mechanical and pneumatic approaches. These methods, however, showed considerable practical limitations, which shifted the research focus towards hydraulic solutions. By using hydropneumatic accumulators, hydraulic systems can provide the required impulse efficiently, reproducibly, and in a field-applicable manner. This makes it possible to realistically simulate the characteristic loading of micropiles in protective structures [1], [2].

The present work builds on these developments and explores the application of hydraulic testing systems for dynamic micropile loading. The objective is to highlight the potential of this approach for both research and practice and to provide a basis for the further advancement of dynamic testing methods.

2 State of the art to test micropiles

Micropiles have become a widely used foundation element for protective structures against natural hazards such as rockfall, avalanches or debris flows. In contrast to their application in conventional foundations, where mainly permanent static loads are decisive, micropiles in protective structures are predominantly subjected to short-term, impulsive tensile loads [1]. This fundamental difference requires adapted design and testing methods to ensure reliable performance under dynamic conditions.

2.1 Protective structures and micropile foundations

Protective structures (see Figure 1) are designed to reduce the consequences of natural hazards to an acceptable level, thereby safeguarding infrastructure and settlement areas and ensuring economic sustainability. While earth embankments dissipate impact energy through their mass and internal load transfer, flexible systems such as rockfall protection nets rely on a combination of interception structures, superstructures and cables to redirect forces into the foundation [1]. Micropiles act as key anchorage elements in these systems, transferring high tensile forces into the ground.

Figure 1: Typical projective structures.
Source: [1]

2.2 Characteristics and installation challenges

According to EN 14199 (2016), micropiles are versatile elements used to reduce settlements and transfer compressive or tensile loads. In protective structures, however, their function differs from classical geotechnical applications: tensile loading is often eccentric, and additional deflections arise due to cable extensions and system flexibility [1]. Installation in steep or inaccessible terrain poses further challenges, as lightweight drilling rigs are required and the use of fully cased or double corrosion-protected elements is often restricted. Current developments therefore investigate self-drilling micropiles with double corrosion protection (DCP-SBZ) as a potential solution [2]. Different tendon diameters (DN22–DN40) are

commonly used depending on the load level and boundary conditions of the protective structure.

Conventional testing procedures

As with anchors (EN 1537:2015) or soil nails (EN 14490:2010), micropiles must be tested to validate design assumptions and ensure functionality. Investigation, suitability and acceptance tests are defined depending on the project stage [1]. In Austria, acceptance criteria include the creep rate ($k_s \leq 5$ mm, ONR 24810:2020) as well as conditions regarding constant load maintenance and maximum load decrease.

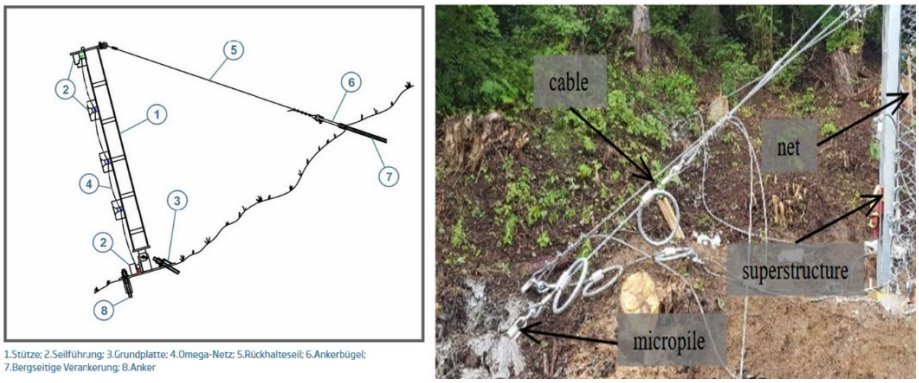

Figure 2: Micropile installation.
Source: Trumer Schutzbauten and [1]

For protective structures, however, the creep-rate criterion appears only of limited relevance, as the actual loading case is defined by short-term impacts. Static testing procedures therefore provide insufficient insight into the real behaviour of micropiles under dynamic conditions [1].

2.3 Approaches to dynamic testing

Dynamic testing methods have so far been mainly applied to large-diameter piles, where wave propagation techniques (e.g. ASTM D5882-16) are used to evaluate production quality and structural integrity. While useful in that context, such methods provide little information on the tensile bearing capacity of micropiles [1], [3]. Drop-weight systems and other commercial testing devices (e.g. Allnamics)

demonstrate the general feasibility of dynamic loading, but their application to small-diameter micropiles in tension remains restricted [1]. Against this background, research efforts have focused on developing dedicated test concepts capable of reproducing the impulsive loading scenarios relevant for protective structures. Pendulum-based approaches, inspired by Charpy impact tests, represent one line of investigation and mark an important step towards the establishment of suitable dynamic test procedures for micropiles [1].

3 Requirements for a new dynamic testing device

The development of a dynamic micropile testing device aims to meet the objectives outlined in the preceding chapters. To achieve this, specific technical and practical requirements must be fulfilled. Table 1 summarises the main criteria, which represent an initial consolidation of conceptual considerations and can be refined in the course of further development.

Table 1: Requirements for a dynamic micropile testing device

Requirement	Description
Dynamic loading	Application of an impulsive load up to 250 kN
Load rise time	The target force must be applied within a maximum of 5 ms to reproduce impact-like loading [1]
Adjustable load level	Impulse should be adjustable on-site between 100 kN and 250 kN
Simple handling	Device should only need to be mounted and pre-tensioned on site
Reaction system	Ideally, no external abutment required; optional integration for higher loads or research purposes
Weight	Device should be portable by two persons, even in rough terrain
Compatibility	Interchangeable adapters to connect to different tendon diameters (DN22 to DN40)

source: own source

4 Construction and function of the dynamic testing device

4.1 General design

The dynamic micropile testing device is based on a hydraulic impulse cylinder, developed at the Institute of Production Engineering, TU Graz. Its design enables the rapid application of tensile impulses up to 250 kN within ≤ 5 ms, fulfilling the

requirements defined in Chapter 3. A CAD model with the main components is shown in Figure 3.

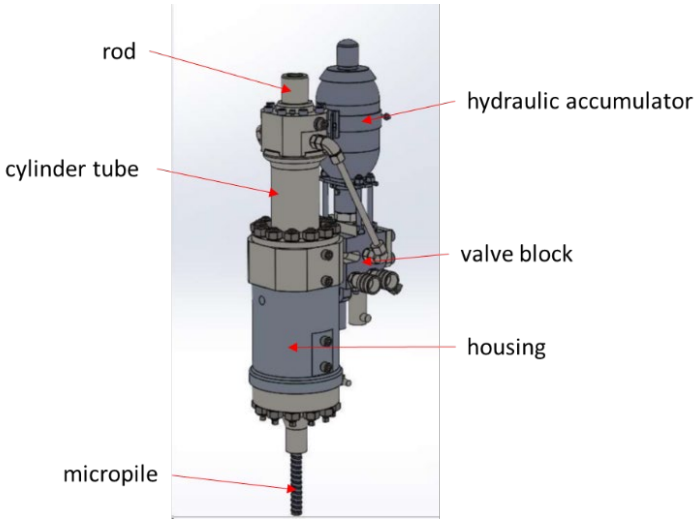

Figure 3: Impulse cylinder.
Source: own source.

4.2 Accumulator system

A bladder-type accumulator is integrated. It separates hydraulic oil and nitrogen by an elastomer bladder; pre-charging stores hydraulic energy that is released when the valve opens, covering peak flow demand and allowing millisecond-scale piston acceleration. The current design allows maximum accumulator charging pressures up to 450 bar, providing sufficient energy for impulsive load levels typical of protective structures [1], [2]. Unlike conventional systems, there is no separate safety shut-off valve on the accumulator; instead, a dedicated hydraulic circuit ensures pressure control and safe energy release.

4.3 Cylinder–piston unit

The piston–cylinder assembly is optimised for very high acceleration. No piston seal is used; sealing to the environment is achieved solely by rod seals. This reduces moving mass and internal friction, enabling the required stroke velocity. The rod

seals face high dynamic loads because sliding speeds reach up to 15 m/s in this application. Under such conditions, frictional heating, lubrication breakdown, and extrusion must be considered. Design guidance from hydraulic fundamentals and sealing handbooks recommends pressure- and temperature-stable materials, optimised lubrication, and anti-extrusion back-up elements; high-performance PU or PTFE composite rod seals are commonly used for piston velocities above ~10 m/s to 15 m/s [10], [11].

4.4 Valve technology

A 2/2 seat-type directional valve is used (rather than a spool valve) for tight shut-off, lower contamination sensitivity, and short actuation travel. In the rest position, a spring keeps the valve closed; when pilot pressure is applied, the valve opens and the accumulator discharges into the cylinder chamber, producing rapid piston acceleration (see Figure 4) [10].

4.5 Impulse generation

When the valve opens, hydraulic fluid acts on the piston surface, accelerating it until it strikes the impact plate at the cylinder head. The resulting momentum transfer generates the impulsive tensile load that is transmitted to the micropile. The stroke is ~130 mm; after impact, oil returns to tank via the return lines, and the piston retracts for the next cycle.

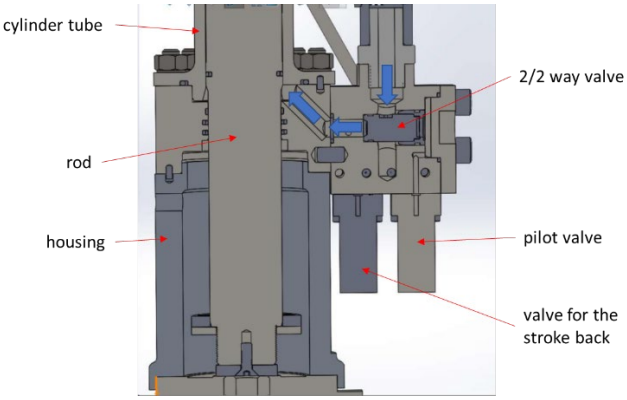

Figure 4: Valve block and oil flow.
Source: own source.

4.6 Hydraulic supply

Lab tests used a compressed-air driven hydraulic pump (up to ~700 bar). For field use, a battery-driven pump unit is foreseen to ensure mobility in alpine terrain.

4.7 Control of impulse intensity

The impulse $\mathbf{p}$ depends on piston mass and velocity:

$$\mathbf{p} = m\,\mathbf{v}, \quad \mathbf{v} = \frac{Q}{A} \tag{1}$$

with Q the flow rate through the valve and A the piston area. Thus, system pressure and valve geometry govern piston velocity and the resulting impulse [4], [10]. This allows on-site adjustment of test loads between 100 kN to 250 kN as specified in Chapter 3 [1].

4.8 End-of-stroke cushioning

At the extremely high rod speeds in this device (up to 25 m/s), uncontrolled end-of-stroke impact would produce harmful pressure spikes, rebound, and structural stress. End-of-stroke cushioning ("cushions") decelerates the piston/rod assembly near the stroke limit by restricting the outflow from the cushioning chamber or by introducing energy-absorbing elements. This converts the kinetic energy $E_k = \frac{1}{2} m_{eq} v^2$ into fluid or material work over a defined cushion travel ΔL, limiting peak force and pressure [12] to [16].

In this application, cushioning not only protects components but also enables the targeted impulse transfer: by braking the piston rod in a controlled manner, the impulse change Δp is shaped so that the required reaction force within ≤ 5 ms is achieved. Thus, the cushioning is directly linked to the fulfilment of the functional requirement defined in Chapter 3.

As a first approach, an elastomeric buffer was implemented. The specially shaped rubber cushion acts as a deformable damping element at the end of the piston stroke. Its geometry was optimized using finite element (FEM) simulations, allowing the

energy absorption characteristics and stiffness profile to be tailored to the impulse requirement. Compared to fluid-based cushions, this solution offers a compact design and robust behaviour under the very short impulse durations considered here. Literature describes various approaches, including plunger/bushing tapers, grooved pistons, and progressive multi-stage metering to control fluid discharge [12] to [15]. For high-energy systems, a combination of material-based buffers (e.g., elastomer pads) with fluid cushioning can provide additional robustness.

5 Calculation of the elastomeric buffer for end-of-stroke cushioning

In order to realise the required end-of-stroke cushioning within ≤5 ms, an elastomeric buffer was designed and analysed. The buffer is intended to absorb the residual kinetic energy of the piston rod after impulse transfer, thereby shaping the impulse change and generating the defined reaction force. Three different buffer geometries were evaluated using finite element method (FEM) simulations, each aiming to achieve a favourable stress distribution, controllable deformation, and reproducible damping behaviour.

Because elastomeric materials exhibit a strongly nonlinear stress–strain relationship even within the elastic regime, all calculations were performed using nonlinear FEM. This approach accounts for large deformations, geometric nonlinearity, and the nonlinear constitutive behaviour of rubber-like materials, ensuring that stiffness and damping effects are represented realistically.

5.1 Variant A – Solid elastomer disc (Shore 40)

The baseline design consisted of a solid rubber disc with a uniform thickness. The material selected was a standard elastomer with Shore A 40, representing a comparatively soft and energy-absorbing configuration. This variant was used as reference to evaluate the achievable stiffness and deformation without additional geometric modifications.

5.2 Variant B – Chamfered disc (Shore 40)

To reduce stress peaks and to create a softer transition during compression, the second variant introduced a chamfer on the inner edge of the same Shore 40 disc. The chamfer modifies the local stiffness and allows the buffer to engage progressively, distributing stresses more evenly across the contact surface. Nonlinear FEM results indicate that the chamfer geometry can delay the onset of maximum stresses and provide a smoother force–displacement response.

5.3 Variant C – Structured disc with cavities (3D-printed, Shore 50)

As a third concept, a 3D-printed elastomer disc with integrated cavities was investigated. The structured geometry was designed to guide deformation into specific zones, reducing stiffness in selected areas while retaining higher strength elsewhere. Due to the limitations of additive manufacturing materials, the available elastomer had a higher hardness (Shore A 50) compared to the previous variants. Despite the higher base stiffness, nonlinear FEM analyses showed that the targeted cavities effectively reduced the effective modulus and enabled controlled energy dissipation.

5.4 Model setup and simulation outputs

Symmetry of the cylinder–buffer assembly was exploited to reduce the computational cost and, in our case, to allocate the freed degrees of freedom to a finer mesh in the region of interest.

The optimized geometry resulting from the nonlinear analysis is a rubber disc with internal holes (see Figure 5). The perforations are designed to guide and localize deformation, thereby tailoring the effective stiffness and energy absorption of the elastomer.

Figure 6 presents the computed force–time response. The initial condition for the simulation is a cylinder-rod velocity of $v_0 = 5$ m/s. The contact force rises rapidly to a peak and then exhibits a damped oscillation. This oscillatory decay is attributed to the combined effects of material/structural damping and contact interaction,

while the rod continues to bear against the hard stop, maintaining a compressive preload during the rebound phase.

Figure 5: 3D printed elastic buffer.
Source: own source.

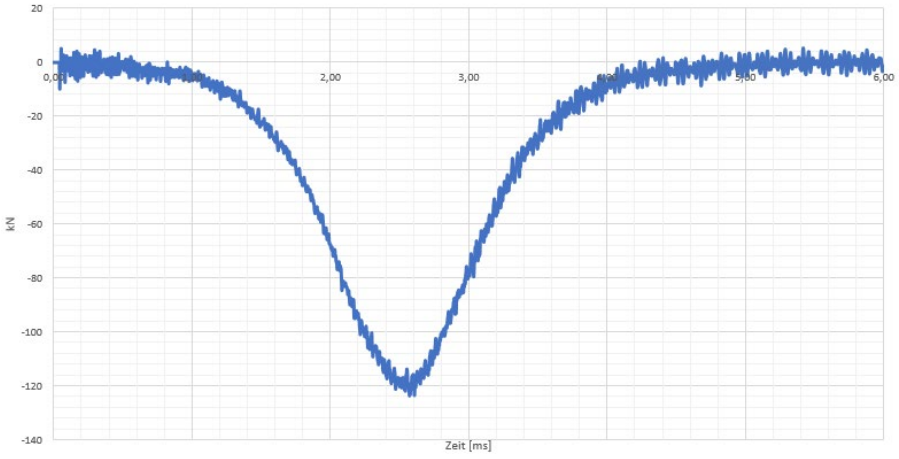

Figure 6: Simulated impact of the cylinder rod into the buffer variant C with 5 m/s.
Source: own source.

6 Test and results

Many different tests were made to determine the response of the impuls cylinder on the structure of an micropile. At the beginning all test were made in a laboratory and to field test were made. To measure the reaction force on the micropile was one of the most challenges. Different methods were investigated:

- High speed camera to determine the speed of the cylinder rod.
- Laser vibrometer to determine the reaction velocity on the housing of the cylinder.
- Load cell to measure the reaction force directly.

The best results came out from the solid joint, which can be seen in Figure 7 left, as data recording system a system from National Instruments was used.

The whole system was mounted on a steel construction with a weight of about 5000 kg (see Figure 7 right). The connection between the structure and the micropile was made as a welding construction, because it has been seen that a screw solution can not be fixed. The connection between the micropile and the impulse cylinder is the original screw of the micropile which must be fixed after each test, resulted by the pitch of the screw on the micropile.

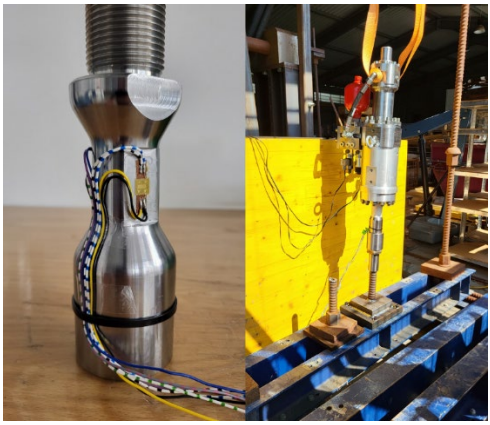

Figure 7: DMS measuring system (left) and mounted impulse cylinder on the test rig (right).
Source: own source.

The tests were made with different pressures in the hydraulic accumulator. The pre pressure of the accumulator is 70 bar so the tests were started with 100 bar up to 250 bar. It was not a hydraulic accumulator with a maximum pressure of 450 bar uses, for the first test a accumulator with a maximum pressure of 300 bar was used.

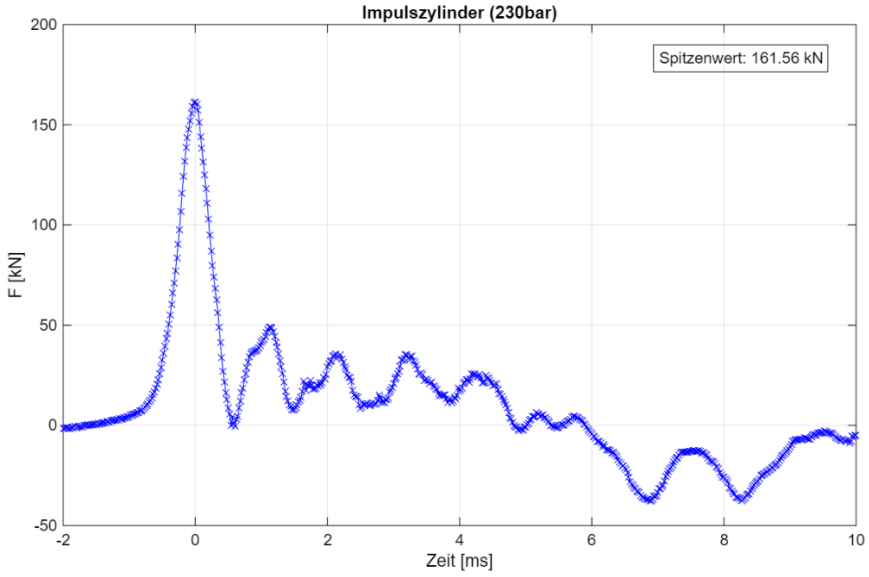

Figure 8: Test of the Impulse Cylinder with 230 bar supply pressure.
Source: own source.

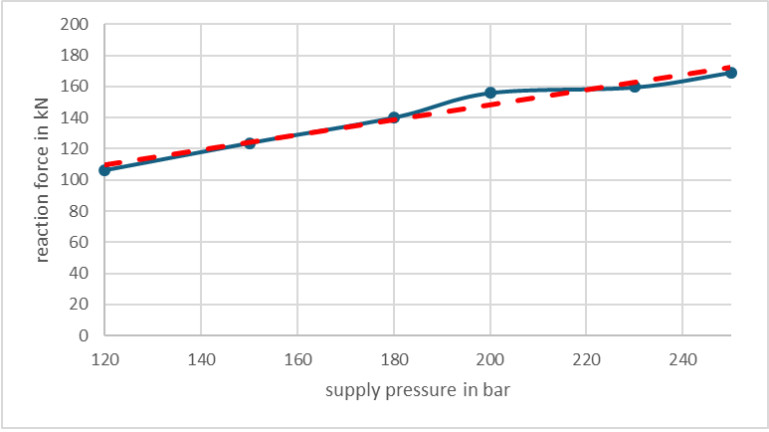

Figure 9: Test series over the supply pressure.
Source: own source.

Figure 8 shows the result of the test with 230 bar. It can be seen that the force rises up in 0.5 ms to a maximum of 161 kN and decrease in 0.5 ms back to zero. Then oscillation can be seen. These oscillation results out of the damping system and of the whole structure of the test rig.

Figure 9 shows all test, a linear dependency between 120 bar and 250 bar of supply pressure can be seen. Pressures under 100 bar cannot be tested resulted by the pre pressure of the hydraulic accumulator.

7 Conclusion

Protective structures in alpine regions increasingly rely on micropiles (ground anchors) to safely transfer impulsive tensile loads from rockfall events into the subsoil. Existing static test procedures do not capture this dynamic loading regime, motivating the development of a mobile, hydraulic impulse device for in-situ verification of micropile performance. Building on state-of-the-art concepts, the device applies adjustable tensile impulses up to 250 kN with a load rise time ≤ 5 ms, while remaining field-portable (two-person carry) and compatible with common tendon sizes (DN22 to DN40). The design features a bladder accumulator (final concept up to 450 bar), a 2/2 seat-type valve for rapid discharge, and a piston–cylinder unit without a piston seal (external tightness via high-speed rod seals).

To shape the impulse and avoid rebound/overloads at high rod speeds (up to 15 m/s), an end-of-stroke cushioning concept was implemented using an elastomeric buffer. Three geometries were assessed via nonlinear FEM: (A) solid Shore-40 disc, (B) Shore-40 disc with inner chamfer for smoother engagement, and (C) structured, additively manufactured disc (Shore-50) with internal cavities for guided deformation. The elastomer behaviour was modelled with a Mooney–Rivlin formulation to reflect geometric and material nonlinearity.

Laboratory and initial field tests investigated multiple measurement strategies (high-speed camera, laser vibrometer, load cell, and a strain-gauged solid joint). The solid-joint approach delivered the most reliable reaction-force data. With a pre-charge of 70 bar and supply pressures from 100 bar to 250 bar (300 bar accumulator used in the first campaign), the device produced fast impulses; e.g., at 230 bar the force increased to ≈ 161 kN in ~0.5 ms and decayed within another ~0.5 ms, with a largely

linear pressure–force trend between ~120 bar and 250 bar. These results demonstrate the technical feasibility of compact, hydraulic dynamic testing for micropiles and provide a validated basis for further optimisation of the cushioning geometry, the measurement chain, and on-site procedures.

References

[1] Rebhan, M., Marte, R., Kainz, F., & Edler, J. (2024, October 2–4). Dynamic testing of micropiles subjected to tensile loads. In *Proceedings of the 5th European Conference on Physical Modelling in Geotechnics (ECPMG 2024)*, Delft, Netherlands: ISSMGE.

[2] Rebhan, M., König, U., Kogelnig, A., & Schuch, M. (2021). Developments and findings in the area of micropiles used for the foundation of protective structures. Journal of Torrent, Avalanche, Landslide and Rock Fall Engineering, 85(187).

[3] Steurer, A., & Adam, D. (2012). Dynamic pile testing in Austria – experiences and results. Geotechnik, 35(1), 38–48.

[4] Wittel, H., Muhs, D., Jannasch, D., & Vossiek, J. (2009). Roloff/Matek Maschinenelemente (20th ed.). Springer, Berlin. https://doi.org/10.1007/978-3-540-70988-5.

[5] EN 14199 (2016). *Execution of geotechnical works – Micropiles.* Austrian Standards International (ASI), Vienna.

[6] EN 1537 (2015). *Execution of geotechnical works – Ground anchors.* Austrian Standards International (ASI), Vienna.

[7] EN 14490 (2010). *Execution of geotechnical works – Soil nailing.* Austrian Standards International (ASI), Vienna.

[8] ONR 24810 (2020). *Technical protection against rockfall – Terms and definitions, effects of actions, design, monitoring and maintenance.* Austrian Standards International (ASI), Vienna.

[9] ASTM International (2016). *Standard Test Method for Low Strain Impact Integrity Testing of Deep Foundations (ASTM D5882-16).* ASTM, West Conshohocken, PA.

[10] Murrenhoff, H. (2011). *Grundlagen der Fluidtechnik – Teil 1: Hydraulik*. Shaker Verlag, Aachen.

[11] Freudenberg Sealing Technologies (2015). *Hydraulic Sealing Guide.* Technical Manual, Weinheim.

[12] Algar, A., Codina, E., Freire, J., & Castilla, R. (2021). Simulation of hydraulic cylinder cushioning using bond-graph and CFD approaches. *Sustainability, 13*(2).

[13] Lai, Q., Liang, L., Li, J., Wu, S., & Liu, J. (2016). Modeling and analysis on cushion characteristics of fast and high-flow-rate hydraulic cylinder. *Mathematical Problems in Engineering*, 2016.

[14] Schwartz, C., De Negri, V. J., & Climaco, J. V. (2005). Modeling and analysis of an auto-adjustable stroke end cushioning device for hydraulic cylinders. *Journal of the Brazilian Society of Mechanical Sciences and Engineering.*

[15] Chen, X., Chen, F., Zhou, J., Li, L., & Zhang, Y. (2015). Cushioning structure optimization of an excavator arm cylinder. *Automation in Construction.*

[16] Hänchen GmbH. (2020). *Endlagendämpfung – Auslegung von Hydraulikzylindern.* Retrieved from https://www.haenchen-hydraulik.de.

Contribution to the Research and Failure Analysis of the Geroler Hydraulic Motor

Almir Osmanović,[1] Darko Lovrec,[2]
Jasmin Halilović,[1] Salko Ćosić[1]

[1] University of Tuzla, Faculty of Mechanical Engineering Tuzla, Tuzla, Bosnia and Herzegovina
almir.osmanovic@untz.ba, jasmin.halilovic@untz.ba, salko.cosic@untz.ba
[2] University of Maribor, Faculty of Mechanical Engineering, Maribor, Slovenia
darko.lovrec@um.si

This paper analyses the key aspects of the operation of geroler hydraulic motors, widely used rotary hydraulic motors. The focus is on understanding their performance, efficiency and durability in different working conditions. The work includes a theoretical analysis of the principles of work, supported by modelling. Furthermore, experimental tests conducted to characterize the motors in terms of torque, speed, flow and efficiency are considered. Special attention is paid to the analysis of factors that influence the wear of internal components. The results of the analysis provide deeper insight into the behaviour of geroler hydraulic motors, identify areas for potential improvements in design and application and for optimizing their operation and extending their service life in various industrial and mobile applications. In conclusion, the work contributes to a better understanding of hydraulic motors, which is crucial for engineers and technicians involved in the design, application and maintenance of hydraulic systems.

DOI
https://doi.org/10.18690/um.fs.7.2025.18

ISBN
978-961-299-049-7

Keywords:
hydraulic motors, orbital motor, geroler, fault analysis,. reconstruction

University of Maribor Press

1 Introduction

Hydraulic components that are used to convert energy are motors and pumps. Hydraulic pumps convert mechanical energy into hydraulic energy, while hydraulic motors convert hydraulic energy into mechanical energy. Hydraulic motors falling into the group of executive elements. The conversion of hydraulic energy into mechanical energy is achieved by the action of the fluid pressure force on the working element of the motor.

The mechanical energy obtained by the operation of hydraulic motors is manifested in the form of rotary or linear (translational) motion [1]. The principle of operation of motors is achieved by increasing and decreasing the volumes filled with fluid, which in the case of motors is associated with high pressure on the suction side and lower pressure on the discharge side. For this reason, these devices are called positive displacement motors, or pumps.

2 Rotary hydraulic motors

Rotary hydraulic motors are motors whose output element moves in a rotary manner, without any limitation of angle or speed. According to the speed of rotation, they can be divided into slow-speed (up to 1000 rpm) and high-speed (over 1000 rpm) motors [2]. Since the power of the motor is equal to the product of the torque and the speed of rotation:

$$P_M = M \cdot \omega \tag{1}$$

for the same hydraulic motor power, the torque must be increased with a decrease in speed or vice versa. That's why slow motors often have a high torque.

Hydraulic motors can be variable and fixed displacement. According to the design and the possibility of the direction of rotation, the motors can be represents as motor that always rotates in the same direction, or aa motor that has the ability to rotate in both directions (reversible), which is achieved by exchanging the sides of the fluid inlet and outlet [3]. Examples of symbols for the configuration of rotary motors are given in Figure 1. The flow of the working fluid through the hydraulic motor is equal to:

$$Q = \eta_V \cdot n \cdot V \tag{2}$$

where:

n - number of revolutions per unit of time,
V - theoretical working volume,
η_V - volumetric efficiency of a hydraulic motor.

The power of the hydraulic motor is:

$$P_M = \eta_M \cdot n \cdot V \cdot \Delta p = \eta_M \cdot Q \cdot \Delta p \tag{3}$$

where:

Δp - pressure drop in the hydraulic motor,
η_M - total efficiency of a hydraulic motor, product of volumetric η_V and mechanical η_m efficiency ($\eta_M = \eta_V \cdot \eta_m$).

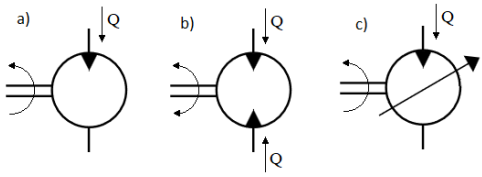

Figure 1: Hydraulic motors configuration symbols.

3 Orbital hydraulic motor

The orbital hydraulic motor developed from studies on rotary piston machines, which are volume displacement machines with chambers between rotor and stator (also known as "star" and "ring"). The epitrochoidal profile is used for the star's profile, while the ring's profile is the envelope, using the same design architecture as the Wankel engine. The previously mentioned design, when applied to hydrostatic machines, leads to increased power density and smaller dimensions of hydraulic motors. The forms of the star and ring are continually changing, allowing trochoidal and hypotrochoidal profiles for the star and encompassing curves for the ring. The

key advantage of this design is that it uses fewer components and sealed elements than a traditional gear pump and motors.

Orbital hydraulic motors or in practice known as gerotor motors with a gear ring are mainly used as slow-speed motors with high torque. Compared to other motors with the same torque, they are significantly smaller in size and weight. The advantages of these motors are: simple and compact construction, favourable speed and torque ratios, precise fluid flow distribution, simple change of direction of rotation, relatively low noise production, easy starting under load, high radial and axial load capacity, resistance to external influences, and high mechanical strength and long service life under high pressures [4], [5]. Due to their good working capabilities, orbital motors find their application in industry, mostly in construction with heavy machinery and agriculture with various attached machines.

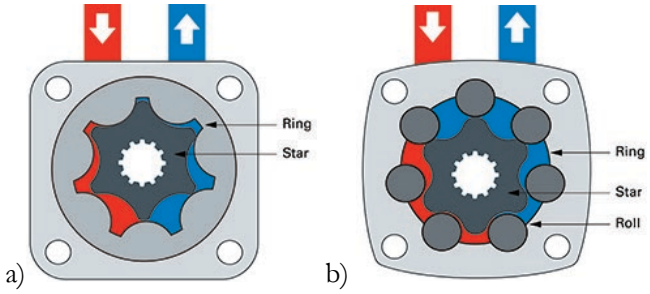

Figure 2: Working principle and basic parts of gerotor (a) and geroler (b) hydraulic motor.

The construction of orbital motors is very simple, the main working element is a star-shaped gear pair composed of one gear with internal teeth that represents the stator and one gear with external teeth that rotates, where the rotor gear always has one tooth less than the stator gear. A decade after the appearance of the first orbital motor, a new concept of the orbital motors was formed and its characteristics were significantly improved. There are two types of orbital hydraulic motors: original orbital hydraulic motor – gerotor type and an improved model of the original - a roller gerotor type (geroler) hydraulic motor. Both variants are shown in Figure 2.

Within this type of motor design, the rotor assembly consists of a stationary ring called the stator and a moving, planetary gear, the rotor. The stator is machined into a star shape within a metal motor housing that houses the rotor, the star-shaped

gear, and its walls are used to form fluid chambers to propel the motor. As oil enters the stator-rotor assembly, passing through zones of high to low pressure, it causes the rotor to rotate within the stator and convert the fluid force into torque. Each cavity between adjacent teeth of the moving gear, enclosed by the inner surface between the teeth of the stationary gear, represents a fluid chamber. During operation, these fluid chambers change shape and volume. If these chambers are properly connected to the inlet and outlet ports, during the dynamic change in the volume of the chambers, fluid will gradually be transferred from the inlet to the outlet, while at the same time transmitting torque and power to the shaft [6]. In order to ensure the correct operation of such a hydraulic motor, the openings on the distributor must be correctly positioned in relation to the fluid chambers, otherwise the may malfunction. The distributor can be in the form of a spool or in the form of a disc.

Although the gerotor design can meet the needs of various applications and is an economical option, it has larger clearance tolerances. These clearances allow more oil to pass from high to low pressure than necessary, resulting in greater slip and less torque conversion. The rotor and stator moving relative to each other within a gerotor design can cause them to wear over time, which is why for medium to heavy duty applications at high pressures that require a more robust option, that is a roller gerotor design.

The roller gerotor (geroler) version of the orbital motor functions in the same way as a gerotor motor, i.e. the way the fluid drives the rotor inside the stator, converting hydraulic power into torque [7]. The stator of a geroler motor is constructed slightly differently and instead of using the entire stator wall to form the pressure chambers, roller inserts are also used. It is these roller inserts that eliminate the gaps found in the gerotor design, which leads to a smaller clearance tolerances between the stator and rotor, allowing less oil flow and therefore more torque. These rollers also act as a roller bearing, reducing friction when the rotor rotates, increasing mechanical efficiency and reducing wear in hydraulic systems using low-viscosity fluids.

Motors with this design are more robust and perform better, especially at low speeds, however, there is an additional cost associated with these benefits. Depending on the position of the stator and rotating elements, several types of geroler hydraulic motors have been developed as shown in the Figure 3.

Figure 3: Types of geroler hydraulic motors.

3.1 Geometry of orbit hydraulic motor

In the gerotor design process, two types of curves are used: epicycloids and hypocycloids. These forms of tooting are commonly used due to their excellent meshing properties, endurance to shock load, low noise, etc. Figure 4 illustrates uncorrected and corrected gear profiles [8].

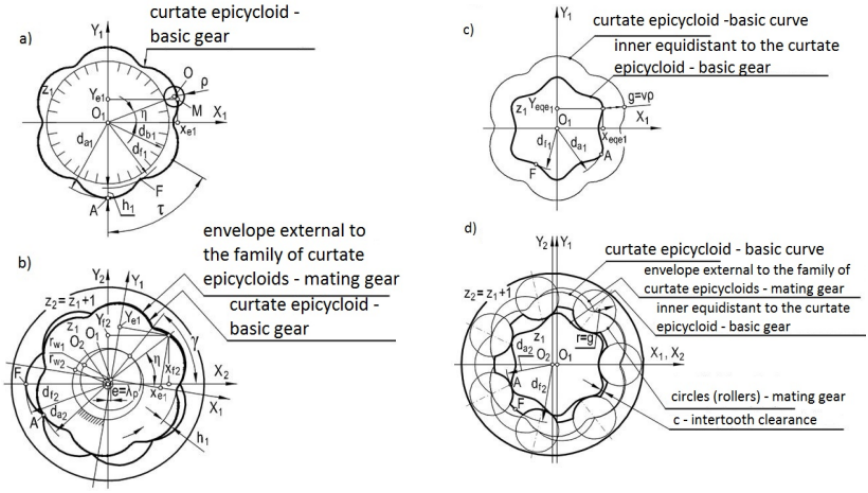

Figure 4: Designing epicycloid gears: a), b) uncorrected gears: internal and external; c), d) corrected gears: external and internal [8].

Figures 4a and 4b present the principles of designing a system of uncorrected epicycloid gears. In Figure 4 the following parameters are shown: z_1 - number of teeth identical to the number of the epicycloid's or hypocycloid's arcs present in the entire closed cycloidal curve, m - a module which in accordance with the principle of constructing cycloidal curves is equal to the diameter of the moving wheel $m = 2\rho$, λ - tooth depth factor ($\lambda = OM/\rho$), η- the angle of the cycloidal curve, v - correction coefficient of the cycloidal profile, g - shift of the profile ($g = v\rho$), b - tooth width.

Using these variables, the geometry and kinematics of cycloidal gears may be characterized, as well as machine hydraulic parameters such as delivery and delivery pulsation. It shows the adaptability of the selected parameter system and its utility throughout the design process. The parametric equations describing the family of wheels with an epicycloid outline have the following form:

$$x_{f2} = \frac{m}{2}\left[\lambda cos\gamma + (z_1 + 1)cos\frac{z_1\eta - \gamma}{z_1} - \lambda cos\frac{(z_1+1)z_1\eta - \gamma}{z_1}\right] \tag{4}$$

$$y_{f2} = \frac{m}{2}\left[\lambda sin\gamma + (z_1 + 1)sin\frac{z_1\eta - \gamma}{z_1} - \lambda sin\frac{(z_1+1)z_1\eta - \gamma}{z_1}\right] \tag{5}$$

Equations (1) should be supplemented with a condition of the envelope which connects angle of rotation γ of the basic wheel relative to the collaborating wheel with angle of the epicycloid η:

$$d_{a2} = 2(z_1\rho + \rho - \lambda\rho + \lambda\rho) = m(z_1 + 1) \tag{6}$$

$$d_{f2} = 2(z_1\rho + \rho + \lambda\rho + \lambda\rho) = m(z_1 + 1 + 2\lambda) \tag{7}$$

Figure 4b shows that formulas for finding the contour of internal gears are difficult to apply directly. The teeth of both gears have incorrect proportions between the head and foot, resulting in excessive contact pressures. Additionally, creating an internal gear with a complex design is difficult and costly. In such a situation, the gears and gear systems are corrected [9]. First, basic external gear is corrected.

Figure 4c illustrates that the correction involves forming an internal equidistant relative to the curate epicycloid and shifting it by $g = v\,\rho$. The parametric equations that describe the equidistant have the following form:

$$x_{eqe1} = \frac{m}{2}\left[(z_1+1)cos\eta - \lambda cos(z_1+1)\eta - v\frac{cos\eta - \lambda cos(z_1+1)\eta}{\sqrt{1-2\lambda cosz_1\eta+\lambda^2}}\right] \quad (8)$$

$$y_{eqe1} = \frac{m}{2}\left[(z_1+1)sin\eta - \lambda sin(z_1+1)\eta - v\frac{sin\eta - \lambda sin(z_1+1)\eta}{\sqrt{1-2\lambda sinz_1\eta+\lambda^2}}\right] \quad (9)$$

The formulas for calculating the outside diameter and the root diameter in the corrected gear are:

$$d_{a1} = 2(z_1\rho + \rho + \lambda\rho - g) = m(z_1 + 1 + \lambda - v) \quad (10)$$

$$d_{f1} = 2(z_1\rho + \rho - \lambda\rho - g) = m(z_1 + 1 - \lambda - v) \quad (11)$$

Next, the collaborating internal gear is corrected. As shown in Figure 4d, circles of a radius equal to the equidistant shift of $r = g$ are drawn from the vertices of the envelope, and then those circles are connected to each other by arcs of the r_{f2} radius circle, which rotates from the centre of the collaborating gear O_2. The characteristic diameters of the collaborating gear after correction are derived from the formulas:

$$d_{a2} = 2(z_1\rho + \rho - \lambda\rho - g + \lambda\rho) = m(z_1 + 1 - v) \quad (12)$$

$$d_{f2} = 2(z_1\rho + \rho + \lambda\rho - g + \lambda\rho) = m(z_1 + 1 + 2\lambda - v) \quad (13)$$

It can be following defined:

- the formulas for calculating the gear outlines are simple and easy to use in the design process,
- the teeth and gears are proportional,
- manufacturing of the gears is much simpler and cheaper compared to the uncorrected gears, particularly in the case of the collaborating internal gear.

3.2 Hydraulics motor delivery and pulsation

Using the characteristic parameters of the teeth and the mesh, it is possible to make formulas for calculating of the hydraulic parameters of the machines.

The delivery of gerotor machines is determined by the formula:

$$\frac{q_{st}}{\pi bm} = \frac{1}{4}\left[(z_1 + 1 + \lambda - \nu)^2 - \frac{z_1}{z_1+1}(z_1 + 1 - \nu)^2 + z_1\lambda^2\right] \tag{14}$$

and the pulsation of delivery from the formula: $\delta = f(z, \lambda, \nu)$.

In the case of orbital machines, which, by principle, work only as motors, the delivery is determined by the formula:

$$q_{or} = z_2 q_{st} \tag{15}$$

4 Model and analysis of geroler hydraulic motor

Geroler hydraulic motors come in many types and versions. In order to be able to show all the elements, CAD model of the geroler hydraulic motor is created. For the analysis is used is used hydraulic motor installed in the excavator JCB mini backhoe (Figure 5), where in the assembly with the valve block and the planetary gear it served as the rotation drive of the upper part of the hydraulic excavator. Hydraulic motor has newt characteristics: volume: 51.5 cm^3, maximum speed: 775 rpm, maximum torque: 100 Nm to 130 Nm, maximum power: 8.2 kW to 9.7 kW, maximum flow: 80 l/min, maximum oil pressure: 140 bar to 175 bar.

Figure 5 shows a CAD model of a hydraulic motor housing. On a hydraulic motor, inside the oil inlet and outlet openings there is a thread whose type and size also determines the type of coupling. Inside the housing walls there are openings and channels through which oil is supplied and discharged under pressure to the orbital part of the motor. Housings are generally symmetrical in structure and made of hard steel resistant to many external influences. Between all parts of the housing (body and covers) there are seals that enable complete sealing and prevent fluid flow at very high pressures.

Figure 6. shows a model of the stator: before inserting the rollers and with the rollers. This parts, together with the rotor, forms the orbital part of the motor. The inner part of the stator is made to a size and shape that depend on the dimensions and shape of the rotor. Like the interior of the stator, the rollers are made by fine machining so that the friction between the stator and the rotor is completely eliminated or reduced to a minimum.

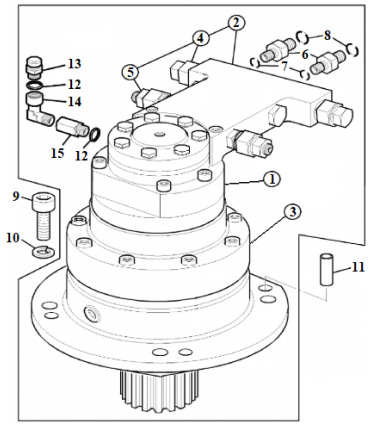

(1) Geroler hydraulic motor
(2) Valve block
(3) Planetary transmission
(4) Flow valve
(5) Safety valve
(6) Hose fittings
(7) (8) O-ring seal
(9) (10) Screw
(11) Wedge
(12) Sealing
(13) Breather
(15) (16) Pipe connections

Figure 5: Geroler hydraulic motor with planetary reducer [12].

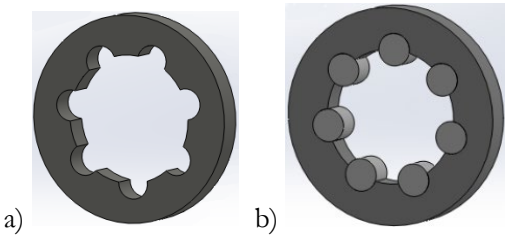

Figure 6: Stator model of geroler hydrauli motor without and with roller elements.

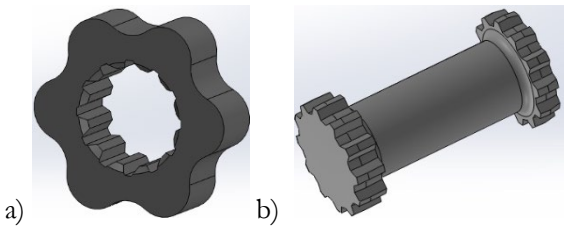

Figure 7: Rotor (star gear) and shaft model.

In Figure 7a, model of the drive gear in the form of an epitrochoid star is shown. This gear represents the rotor of the motor, which, together with the inner shape of the stator, forms fluid chambers. The rotor is made of hardened steel and subjected to thermal and chemical finishing treatments such as hardening and cementation. In Figure 7b, a model of a toothed/splined shaft is presented, which is used to transmit movement and torque from the rotor to the output shaft. The toothed part of this shaft is bevelled at a certain angle because one side of the shaft that is connected to the rotor performs both rotary and planetary motion, while the side that is connected to the spool valve performs only rotary motion.

5 Analysis of geroler hydraulic motor

During work and before the hydraulic motors stopped working completely, it was noticed that the motor was running rough, the rotation speed was reduced. The overhaul was done after the motor stopped working completely and upon removing the upper motor cover, a defect was found. In Figure 8. the rotor of the hydraulic motor is shown, where one can notice an almost uniform way of cracking and damage on the individual segments of the rotor and severe wear of the internal teeth through which the rotational movement is transmitted to the toothed shaft. A visual inspection concluded that the motor stator and the rollers inside the stator were not damaged.

a)  b) 

Figure 8: Motor rotor condition: a) damage; b) signs of wear on the internal teeth.

Furthermore, damage was observed to the teeth of the toothed shaft that enter the assembly with the motor rotor. The condition of the teeth on the shaft is shown in Figure 9.

In order to restore the hydraulic motor to working condition, it is necessary to manufacture a new rotor and shaft. Manufacturing the new shaft was not very demanding because most of the dimensions could be determined based on the current condition and considering that the teeth on both sides of the shaft are identical. While the reconstruction of the rotor was quite demanding due to the decomposed condition of the rotor. Based on precise measurements of all rotor segments, the inner stator ring and the rollers on which the rotor moves, a rotor model was manufactured. According to model and designed model in CAD software, a new rotor was manufactured by machining (Figure 10a).

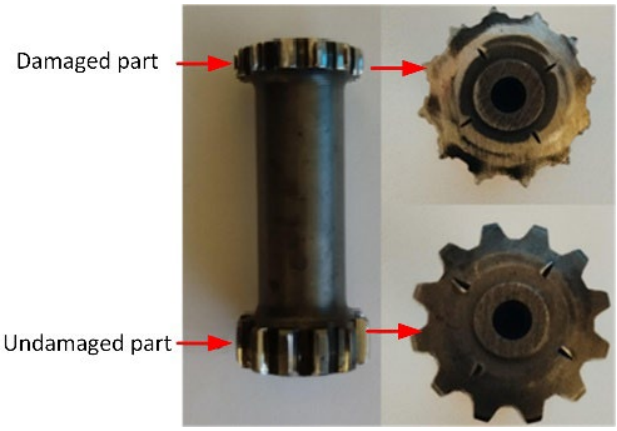

Figure 9: The condition of the teeth on the shaft.

The hydraulic motor was then assembled and put into operation. During the operation of the motor, a major error was found, namely, the motor did not rotate properly. When the motor gave rotational motion in the counterclockwise direction, i.e. when the turret of the excavator turned to the left, the rotation torque was too great, and the rotation happened too fast.

After the analysis, it was concluded that there was an error during the manufacturing of the rotor. The inner teeth of the rotor on which the shaft was supported were not correctly arranged in relation to the outer shape of the rotor. Due to that, a new rotor was made. In order for the hydraulic motor to work properly, Φ must be equal to 0, i.e. the axis of the inner tooth must coincide with the axis of the star arm of the rotor.

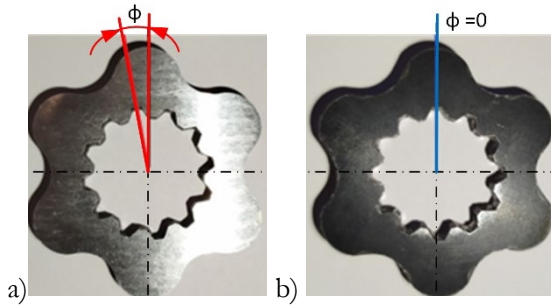

Figure 10: Comparison new rotors: a) rotor with error, b) rotor without fault.

After replacing the faulty rotor with a new rotor, the hydraulic motor was put into trial operation to check for any errors. During the trial operation, the hydraulic motor performed all its functions correctly, rotated at normal operating speed and provided the required torque equally on both sides.

However, the grinding sound during rotation of the turret was still present, i.e. the cause that led to the motor failure had not been eliminated. Further analysis of the entire upper part drive assembly concluded that it was necessary to replace the tapered bearings (Figure 11.) located in the planetary gear. At first glance, the bearings were not particularly damaged, but during operation under load, the high torque caused a small instability in the bearings to lead to large vibrations inside the orbital hydraulic motor. It was precisely this constant exposure of the hydraulic motor to these vibrations that led to the complete failure of the rotor and the cessation of operation of the hydraulic motor.

Figure 11: Tapered roller bearing.

6 Conclusion

The aim of this paper was to analyse the hydraulic motor used in hydraulic systems. It should be emphasized that hydraulic motors in hydraulics play a very important role in converting energy. Choosing the right type of hydraulic motor is a very important factor for hydraulic systems. With the correct choice and installation of the hydraulic motor, the output torque and the number of revolutions can be properly controlled on the external actuators, which as such are used for lifting and lowering loads or for moving large masses. If the hydraulic system needs to perform mechanical work in the form of large torques at low rotation speeds, then orbital hydraulic motors are used. The orbital hydraulic motor of the geroler type represents an improved version of the original orbital motors. The created CAD model in work of the orbital hydraulic motor shows its components and assembly, the connection between individual components, and as such the model was used as a basis for reengineering and subsequent production of the damaged parts of the hydraulic motor. The aim of the paper was to analyse an orbital motor during its work to show the great importance of synchronizing all working elements of the motor. Given that if synchronization is not performed according to, it can lead to damage and permanent deformation of individual parts of the hydraulic motor.

Particular attention must be paid to their mutual compatibility during manufacture and assembly, because even very small deviations can lead to improper operation of the motor. Geroler hydraulic motors are ideal for applications that require high torque and low speed. It should be emphasized that their reliability, compactness and efficiency make them indispensable in a wide range of industrial and mobile applications.

References

[1] Dieter W., Norbert G., (2008). Hydraulik – Grundlagen, Komponenten, Schaltungen. Springer Verein Deutscher Ingenieure, Berlin. doi: 10.1007/978-3-540-79535-3
[2] A. Osmanović, E. Trakić (2021). Hidraulika. ISBN 978-9958-894-83-1. Tuzla: Off-set.
[3] A. Osmanović, B. šarić, E. Trakić (2015). Mechatronic approach to the analysis of hydraulic system of mobile machine. International Conference Fluid power (2015), 17-18.09.2015. Maribor, Slovenia ppt. 189-201.
[4] Gamez-Montero, P. & Codina, Esteban & Castilla, Robert. (2019). A Review of Gerotor Technology in Hydraulic Machines. Energies. 12. 2423. doi:10.3390/en12122423.

[5] Sang, X.; Zhou, X.; Liu, X (2015). Numerical simulation of an inner engaging gerotor based on the optimization of inlet and outlet cavities. 5th International Conference on Advanced Design and Manufacturing Engineering (ICADME 2015).

[6] Hsieh, C.-F., Hwang, Yii-Wen. (2007). Geometric Design for a Gerotor Pump with High Area Efficiency. Journal of Mechanical Design, ppt. 1269-1277. doi: 10.1115/1.2779887

[7] G. Gregov (2022). Modeling and predictive analysis of the hydraulic geroler motor based on artificial neural network. Engineering review, Vol. 42 No. 2, 2022. doi:10.30765/er.1813

[8] J Stryczek, S Bednarczyk, E Codina, P J Gamez-Montero, L Ivanovic and Mmatejic (2019). Gears or rotors – three approaches to design of working units of hydraulic machines. IRMES 2019 IOP Conf. Series: Materials Science and Engineering. doi:10.1088/1757-899X/659/1/012006.

[9] Nang A and Maiti R (2012). Unification of epitrochoid origin profile design approaches for external lobed star member used in hydrostatic and gear units. Journal Mechanical Science 227(2) 299-310. doi: 10.1177/0954406212448365

THE LAST 30 YEARS OF HYDROPOWER IN THE WORLD AND SLOVENIA

ANDREJ PREDIN,[1] MITJA KASTREVC,[2] GORAZD HREN[1]

[1] University of Maribor, Faculty of Energy Technology, Krško, Slovenia
andrej.predin@um.si, gorazd.hren@um.si
[2] University of Maribor, Faculty of Mechanical Engineering, Maribor, Slovenia
mitja.kastrevc@um.si

Over the past three decades, the hydropower sector has seen major technological advancements, driven by rising global electricity demand, increasing energy prices, and growing awareness of the environmental impacts of conventional power generation. These factors have strengthened the role of renewable energy sources-particularly hydropower-in building sustainable energy systems with lower ecological footprints. Current research focuses on retrofitting and digitalizing existing hydropower infrastructure, developing next-generation hydro and aero-hydrodynamic technologies, and deploying hybrid systems integrated with advanced energy storage solutions. Given the inherent variability of renewable sources, high-capacity storage technologies are essential for enhancing grid stability, frequency regulation, and overall resilience. Furthermore, the development of advanced smart grid architectures is crucial to enable distributed, multi-nodal power generation, improve demand–supply balancing algorithms, and support the seamless integration of small and medium-scale energy producers. Together, these innovations aim to optimize energy efficiency, support decarbonization goals, and ensure a reliable and flexible power supply in the face of evolving energy needs and climate challenges.

DOI
https://doi.org/10.18690/um.fs.7.2025.19

ISBN
978-961-299-049-7

Keywords:
hydro power plants, renovation, improved characteristics, improved efficiency, alternative turbines

University of Maribor Press

1 Introduction

The electrical production by source "Our world in data, 2025 "[1] shows that in 2025 the hydropower was the third most powerful source of electricity production after coal and gas, and before nuclear and oil. In 2024, the ratio is similar, only the production is higher by about 50 %

Over the past three decades of energy production development, the developed world has steadily moved toward:

a) The development of smart power grids, towards bilateral operation and protection, distributed energy production, and its optimization according to the energy demand in the network.
b) The combination of different energy systems, in the field of renewable energy sources, mainly the combination of wind and hydropower (reversible hydroelectric power plant).
c) The modernization and upgrading of existing hydropower systems, such as the replacement of Kaplan Turbine and Francis Turbine with the Deriaz turbine, of course, in the mixed field, where both types of classic hydraulic turbines (Kaplan and FT) have been used so far, by placing the powerhouse at an increased pressure in it (high-pressure Pelton systems).
d) The installation or revival of older forms of hydraulic turbines, especially modernized water wheels, improved designs (Steff turbine), screw designs, matrix arrangement of turbines in the watercourse (MATRIX, HydroMatrix), tube designs and derivatives (Saxo, Darrieus designs, ...).
e) Installation of alternative forms of hydraulic turbines (Vortex), mainly in the field of medium and small hydroelectric power plants.

2 Smart networks

The need for smart grids has been established with the increased share of energy obtained from renewable sources. It is known that renewable sources are "volatile" in terms of forecasting production and, of course, subsequent distribution into the grid system [2]. Therefore, the need for two-way communication and automation (regulation + optimization) of the grid has become evident, which will enable monitoring of the amount of energy in the grid in real time (use of sensors, smart

meters, control systems that analyse or process data based on which quick decision-making will be enabled (in the future also with the use of artificial intelligence).

Optimization of such a grid system operation will enable automatic switching of energy flows according to current needs, better integration of dispersed energy production (especially from renewable sources), better and balanced supply and demand for energy, and rapid detection of errors and their elimination [3].

Thus, connected users will be able to control their consumption, storage in storage tanks (e.g., batteries), and return energy to the grid (e.g., from a solar power plant) during times of domestic production surpluses.

By using smart grids, we will therefore achieve:

- greater reliability of electricity operation (supply)
- better grid efficiency (higher efficiency and lower losses),
- more straightforward and better integration of "capricious" energy sources,
- greater influence of users (producers and consumers) regarding grid operation and
- greater influence on the price and, above all, on the dynamic determination of electricity prices.

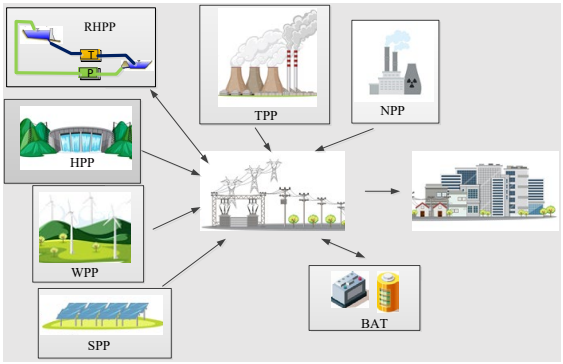

Figure 1: Smart networks.

Europe is at the forefront of renewable energy development, having achieved 24.5 % of its energy supply from renewables in 2023, with a goal of at least 42.5 % by 2030, as specified in European Directive 2009/28/EC.

2.1 Smart grids in Slovenia

In Slovenia, we are significantly lagging behind Europe, as the development of Slovenia's electricity distribution network has only recently begun in terms of greater investment in modernization through the introduction of innovative (smart) grid components [4]. Elektro Primorska, Ljubljana, Gorenjska, Celje, and Maribor promise to invest 150 million euros in upgrading the network by the end of 2026. Approximately 71 million euros should be invested by the national recovery plan, and the aforementioned dispatching companies should invest the rest.

A **smart transformer station** with a power of 15 MW and a capacity of 30 MWh has been installed in Kidričevo since 2021, which is still the only storage station in the Slovenian electricity grid. Near Maribor (in Pekre) and around Ljubljana, two storage stations with a power of 5 MW and a capacity of 25 MWh have been installed.

In total, in Slovenia, in the last 30 years. We have 25 MW of installed power with a capacity of 80 MWh, which is significantly too little for any severe accumulation. However, increases in power and capacity and new installations are planned [5].

3 Combination of Energy Systems

The combination of different energy systems provides a solution for stabilizing the electricity grid when multiple renewable energy producers are integrated. In such cases, significant fluctuations in grid power can occur due to variable wind speeds. The first practical combination involved integrating wind farms (WPP) with reversible hydropower plants (RHE).

The basic principle of parallel operation between a wind farm and reversible hydropower systems is known as the short-circuit operation mode. In this mode, the RHE operates in parallel in the pumped-turbine mode. This means wind energy is used to drive pumps that lift water into a higher reservoir while turbines simultaneously generate electricity from the stored water. Although this operation introduces additional system losses, it greatly enhances the operational reliability of the energy supply during potential power shortfalls from wind farms. In practice, any loss of wind turbine production is nearly simultaneously compensated by the

RHE operating in turbine mode. This results in improved grid stability, making the system less sensitive to fluctuations from renewable energy sources. At the same time, RHE continues to fulfill its primary role of storing excess energy during periods of surplus generation.

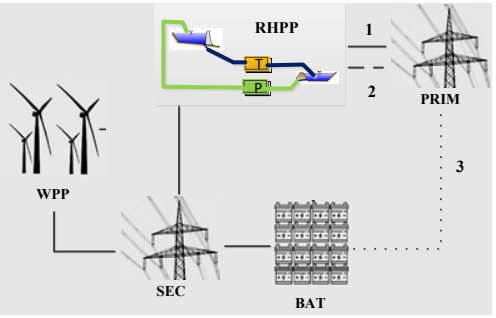

Figure 2: The combination of RHE with WPP.

The integration of RHE with wind systems is organized so that all wind farms within a wind field are first connected to the secondary network (SEC), which is linked to the RHE network. From the RHE, electricity enters the primary (national) grid (PRIM). The RHE maintains a dual connection: directly to the primary grid and indirectly via the secondary network of wind fields. This configuration allows the RHE to operate independently, even when wind production is absent, either as an energy storage system or, if needed, as a direct electricity producer for the primary grid.

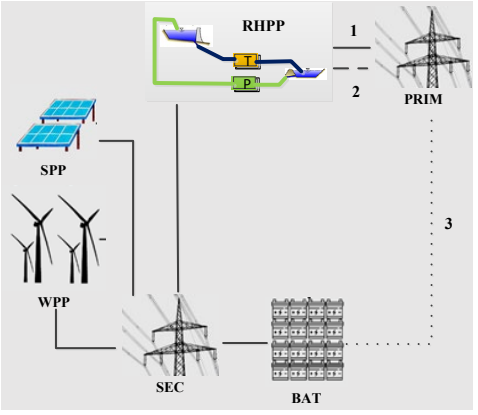

Figure 3: The combination of RHE with WPP and SPP.

In extended combined systems, solar power plants (SPP) are also integrated with RHE. This addition allows the system to balance daily surpluses of solar energy, which would otherwise need to be curtailed to prevent excessive load on the electricity grid.

3.1 Combination of energy systems in Slovenia

In Slovenia, there is currently only one operational reversible hydroelectric power plant: RHE Avče, located on the Soča River, with an installed capacity of 185 MW. This plant is not directly connected to any wind farm or solar power plant in the country. Theoretically, RHE Avče could serve as a compensatory source for the NEK Krško Nuclear Power Plant (NPP); however, this would only apply to the Slovenian portion of the power supply. If Slovenia had followed global or European development trends, this RHE should have been constructed alongside NEK, which began operations 42 years ago.

Several additional RHE projects are planned in Slovenia, with the closest being RHE Kozjak, which is expected to have an installed capacity of 2 × 220 MW. Construction of this project is scheduled to begin in 2027. Currently, Slovenia does not have any operational wind farms, so it is not possible to combine wind power with the existing RHE Avče.

Slovenia does, however, have several solar power plants (SPPs) installed in conjunction with hydroelectric power plants (HPPs). These include installations near HPP Brežice on the Sava River, as well as HPPs at Dravograd, Maribor, Zlatoličje, and Formin. Among these, the largest solar-hydro combination is at HPP Brežice, with the SPP providing an installed capacity of 6 MW. Notably, the solar plant is connected to the 110 kV transmission network as the fourth unit of HPP Brežice, making it the largest solar power installation in Slovenia.

On the Drava River, next to the hydroelectric power plants, we have installed HPPs:

- HPP Dravograd, SPP with an installed capacity of 40 kW,
- HPP Mariborski otok, SPP with installed capacity of 25.5 kW,

- HPP Zlatoličje, SPP with an installed capacity of 777 kW,
- HPP Zlatoličje – segment 5, SPP with installed capacity of 2.5 MW,
- HPP Formin, SPP with an installed capacity of 112 kW.

4 Upgrades and modernizations

As the first direction of upgrades, or modernization in the world, especially in Europe, the direction of upgrades and modernization of hydropower systems is also moving towards replacing the turbine type, e.g., Francis and Kaplan with Deriaz. In the mixed operating range, between Francis and Kaplan, the basic form is successfully replaced by Deriaz. This replacement achieves a higher "yield" of production, because the efficiency of Deriaz is higher at partial loads (when operating outside the maximum efficiency point). The higher yield of Deriaz is possible due to the possibility of operating at a higher available head compared to Kaplan, and the better efficiency of Deriaz compared to Francis, due to better regulation compared to Francis. Deriaz has dual regulation, just like Kaplan.

In terms of efficiency, Deriaz is even better in the partial load range (between 20 % and 50 % of full load) than both compared forms (Francis and Kaplan).

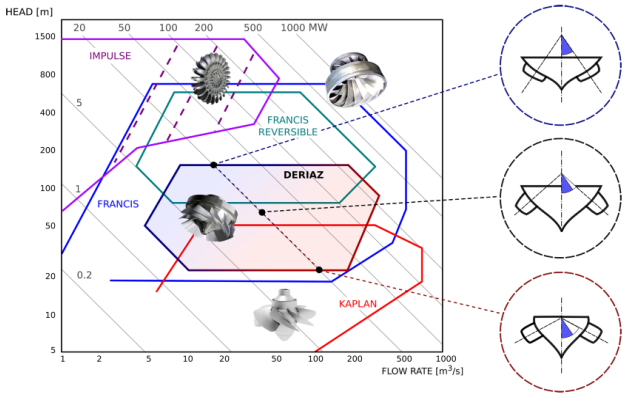

Figure 4: Deriaz pump-turbine.
Source: [8]

By replacing worn-out hydraulic turbines operating in a mixed range between Francis and Kaplan, significantly better production can be expected, especially in smaller, sub-optimal flows. Hence, during times of low water, energy yield is significantly better.

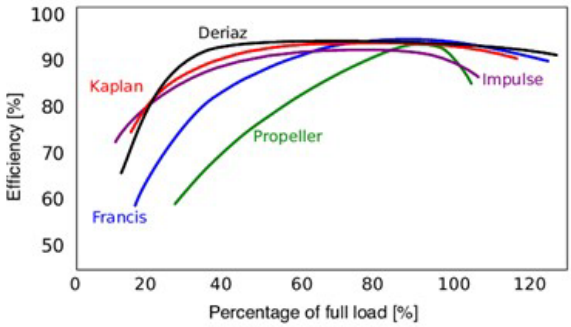

Figure 5: Efficiency comparison.
Source: [8]

Another direction of upgrades is taking place in impulse types of hydraulic turbines Pelton, whereby placing the engine room at a lower level and with increased air pressure in the engine room, production (yield) can be increased, mainly due to the increased head. The engine room is usually placed approximately. 10 m lower, and the ambient pressure (pressure in the engine room) is increased to 2 bar absolutes. That means that we have to maintain the increased air pressure in the engine room with an air compressor system that maintains a constant increased air pressure in the engine room. That is, of course, necessary to place the outlet water angle approximately. 10 m lower, thus ensuring that the Pelton still flows into the air, as the impulse type of turbine requires.

In one such project (KOPS II) [8], we collaborated with the Technical University of Graz, where we tested the impact of increased pressure in the engine room of a Pelton turbine in a laboratory environment. Measurements on the model demonstrated a positive energy yield achieved by increasing the Pelton head, even though a portion of the compressed air in the engine room casing, approximately 3 % to 5 %, was lost through the outflow of the lower water. The increase in power due to the greater head was significantly greater than the energy losses of the compressed head.

The third direction of upgrades or modernization is classic modernization, which replaces older hydraulic turbines of all types with new, more modern ones of the same type and dimensions. Due to better design and better materials, these achieve better efficiency and thus enable greater production than older designs.

4.1 New construction, upgrades, and modernization in Slovenia

Unfortunately, we do not have rivers on which Deriazs and larger Peltons could be installed in Slovenia. Following the example from the neighbourhoods, the upgrade could be installed. Mainly, the upgrade or replacement of older forms of hydraulic turbines with newer ones, with a minimal increase in efficiency, was done.

In the last 30 years, Slovenia has upgraded or modernized six major hydroelectric power plants, namely:

- HPP Boštanj, new construction, built in 2006, as part of the chain of hydroelectric power plants on the lower Sava, average annual production 115 GWh
- HPP Blanca, new construction, built in 2008, as part of the chain of hydroelectric power plants on the lower Sava, average annual production 144 GWh
- RHE Avče, new construction, built in 2009, nominal capacity 180 MW, with an efficiency of 77 %
- HPP Krško, new construction, built in 2012, as part of the chain of hydroelectric power plants on the lower Sava, average annual production 144 GWh
- HPP Brežice, new construction, built in 2017, as part of the chain of hydroelectric power plants on the lower Sava, average annual production 161 GWh;
- HPP Zlatoličje underwent modernization and expansion, including the small hydroelectric power plant Melje. Between 2007 and 2013, a comprehensive renovation of the Zlatoličje HPP, upgrades to the Melje

Dam, and construction of the Melje SHPP were completed. After these improvements, it produces approximately 600 GWh annually, almost 5 % of Slovenia's total electricity production.

5 Renaissance of older forms of hydraulic turbines

Classical water wheel layouts:

a) Undershot Water Wheel Design
b) Overshot Water Wheel Design
c) Pitchback Water Wheel Design
d) Breastshot Water Wheel Design

Add a)

The Undershot Water Wheel Design, also known as a "stream wheel," was the most used waterwheel type and the simplest, cheapest, and easiest type of wheel to construct.

In this type of waterwheel design, the wheel is placed directly into a fast-flowing river and supported from above. The motion of the water flow below creates a pushing action against the submerged paddles on the lower part of the wheel, allowing it to rotate in only one direction relative to the flow of the water.

Add b)

The Overshot Water Wheel Design is the most common type of design. The overshot waterwheel is more complicated in its construction and design than the previous undershot waterwheel, as it uses buckets or small compartments to catch and hold the water.

These buckets fill with water flowing onto the wheel through a penstock design above. The gravitational weight of the falling water in the full buckets causes the wheel to rotate around its central axis as the empty buckets on the other side of the wheel become lighter.

Add c)

The Pitchback Water Wheel Design is a variation on the previous overshot water wheel, as it also uses the gravitational weight of the water to help rotate the wheel. However, it also uses the wastewater flow below it to give an extra push. This type of waterwheel design uses a low head infeed system that provides water near the top of the wheel from an open penstock trough above.

Unlike the overshot waterwheel, which channelled the water directly over the wheel, causing it to rotate in the direction of the flow of the water, the pitchback waterwheel feeds the water vertically downwards through a funnel and into the bucket below, causing the wheel to rotate in the opposite direction to the flow of the water above.

Add d)

The Breastshot Water Wheel Design is another vertically mounted waterwheel design where the water enters the buckets about halfway up at axle height, or just above it. Then it flows out at the bottom toward the wheel's rotation. Generally, the breastshot waterwheel is used when the head of water is insufficient to power an overshot or pitchback waterwheel design from above.

The disadvantage here is that the gravitational weight of the water is only used for about one quarter of the rotation, unlike previously, which was for half the rotation. To overcome this low head height, the waterwheels' buckets are made wider to extract the required amount of potential energy from the water.

5.1 Modern water wheels

Modern water wheels have changed in the last 30 years mainly in two directions:

1) with better hydrodynamically designed blades

   From 2004 to 2009, the hydrodynamics of water wheel blades were improved, mainly by using CFD. In this way, the total efficiency increased by approximately 3 %.

2) by solving the problem of low water wheel speeds

Modern water wheels eliminate the disadvantage of transmitting torque from the wheel to the generator shaft with a new generator design directly integrated into the water wheel itself. Permanent magnets are installed on the larger radius of the wheel so that the passing speed increases even at low wheel speeds. The stator windings, with a larger number of pole pairs, are also installed on this larger radius, which achieves good generator efficiency even at low speeds. As mentioned, the electric generator is integrated into the water wheel itself, so the transmissions required due to the higher speed of classically designed generators are also eliminated. The solution was patented in 2003, DE 102 18 443, which presents a modular solution of a segmentally placed generator, which enables direct drive with the water wheel.

Steff turbine

The subsequent "modernization" of the water wheel is in the form of the Steff turbine, a turbine developed by the company Walter Reist Holding AG (WRH) from Switzerland. The first physical (concrete) installation was done in 2011. It works on the principle of an "extended path of pulleys", which are attached to a rubber elevation belt on an additional wheel on the other side. The water is fed to the lower part of the belt, which means the water flow is used as in a water wheel with a bottom inlet.

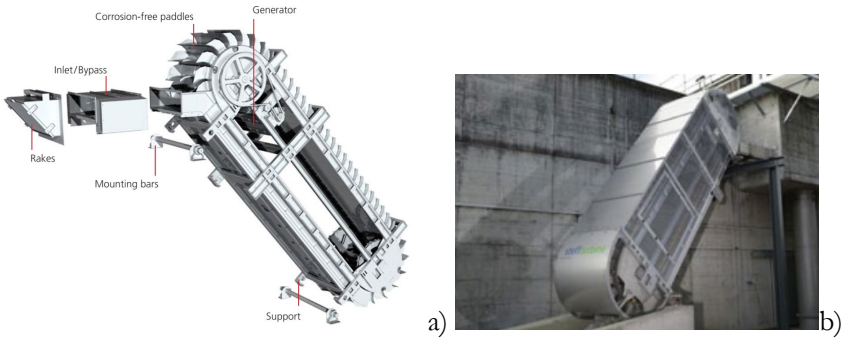

Figure 6: Implemented Steff turbine.
Source: [10]

The application range of the Steff turbine ranges from about 2 to 5 m head and at flow rates between 0.2 and 0.6 m^3/s, up to about 12 kW of power (Figure 7a).

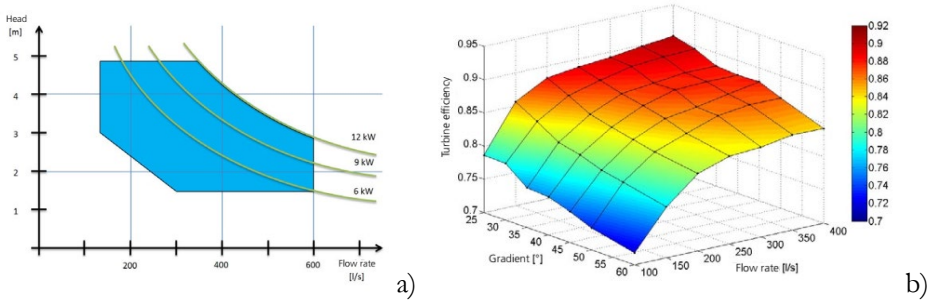

Figure 7a: a) Field of use; b) efficiency.
Source: [10]

The efficiency achieved by the Steff turbine reaches somewhere up to 0.9, which is a good efficiency for such a design (Figure 7b). It is also interesting because of its low maintenance and relatively simple installation work. It is also distinguished by its low operating noise level and possible operation even at low ambient temperatures.

Screw turbines

Screw turbines for harnessing the energy of overflow, equalization, or wastewater have emerged in the last 30 years as a cheap and reliable system for harnessing small or small hydro potentials. They can utilize falls from 1.5 m onwards. They are fish-friendly, as the fish survive the passage through the screw rotor. They are relatively undemanding to maintain, even in the case of dirty water. Since they are open, they can be easily cleaned.

5.2 The renaissance of older forms of hydraulic turbines in Slovenia

Is, secondly, only slightly present. As far as the authors know, very few such systems have been implemented in Slovenia, the most famous being the Mill on the Mura River, which was renovated in 2024.

6 Alternative designs and layouts of hydraulic turbines

Vortex turbine

Iis a commercially viable implementation of an alternative hydroelectric power plant. It is intended for small falls and flows and is ideal for implementing small and/or simple hydropower systems (sHPS). Due to its simple design, its use is interesting for smaller watercourses. Flood protection is also well solved, as it can be easily separated from the watercourse flow by closing the inlet gate.

Other alternative forms are mostly still in the development phase, so we do not include them in the comparison.

6.1 Alternative designs and layouts of hydraulic turbines in Slovenia

To the best of the authors' knowledge, no Vortex turbines have been installed in Slovenia. Small hydroelectric power plants employing serial water pumps operating in turbine mode represent the closest alternative. Several such installations exist in Slovenia, particularly in the hilly regions of Gorenjska and Koroška.

7 Conclusions

A comparative analysis with Slovenia's western neighbours, Austria, Germany, and Switzerland, reveals marked disparities in the share of electricity generated from renewable energy sources (RES) (Table 1). Austria leads with over 75 % of its electricity produced from RES, followed by Switzerland (65 %), Germany (55 %), and Slovenia (35 %). When nuclear energy from the Krško Nuclear Power Plant (NEK) is counted as a low-carbon source alongside RES, Slovenia's share rises modestly to around 40 %. Although the figures in Table 1 are drawn from unverified online sources, they nonetheless illustrate a meaningful and indicative trend.

A key structural weakness of Slovenia's power system is its dependence on a single pumped-storage hydroelectric facility, the Avče Plant, commissioned in 2010, with an installed capacity of 185 MW and a round-trip efficiency of 77%. While several pumped-storage projects have been proposed, their development remains stalled. The primary reason is the diversion of financial and institutional resources into

economically unsound and environmentally detrimental projects, most notably the Šoštanj Thermal Power Plant Unit 6 (TEŠ 6) and the Ljubljana District Heating Plant. These misallocated investments have significantly reduced the capacity to finance technologically advanced, low-carbon alternatives, limiting progress in expanding flexible generation infrastructure.

The modernization of Slovenia's energy sector has therefore fallen short of the benchmarks set by international environmental agreements, most notably the Kyoto Protocol and the Paris Agreement. The disproportionate allocation of resources to failed or inefficient projects, epitomized by TEŠ 6, has severely hampered systemic progress. This mismanagement has led to the suspension of hydropower development along the lower and middle Sava River and effectively stalled the rollout of new pumped-storage facilities. The RHE Kozjak project stands as the sole partial exception, having advanced only marginally through initial stages of documentation, permitting, and regulatory review.

No major investments have been made in the alternative sector, and unfortunately, none are planned in the near future.

Table 1: Overview of the state of the main (national) grid system.

Year: 2024	Germany	Austria	Swiss	Slovenia
Ratio RES	~55%	>75%	~65%	35% (from NEK 40%)
Main resources RES	Wind, Sone	HPP	HPP	HPP
Storage	Battery + HPP	RHPP	RHPP	Minimal (Avče)
Weaknesses	Medium	High	Very high	Medium+
Excesses	Market, export, shutdown	RHPP modulation	HPP + import	Export + regulation
Flexibility	Medium	High	High	Low

source: various online data for 2024

References

[1] https://ourworldindata.org/grapher/hydropower-consumption
[2] Agencija za energijo Slovenije: Report on Energy sector in Slovenia*;* https://www.agen-rs.si/documents/54870/68629/AzE_PorociloEnergetika2020ANG.pdf
[3] https://energy.ec.europa.eu/topics/markets-and-consumers/smart-grids-and-meters_en
[4] statista*, Smart Cities – Slovenia,* https://www.statista.com/outlook/tmo/internet-of-things/smart-cities/slovenia
[5] Stritih, U., Ristić, A., Mlakar, U. (2023): Energy storage country report, https://iea-es.org/wp-content/uploads/public/Slovenia-Country-Report-2023.pdf

[6] Čuš, I. (2006): Črpalna hidroelektrarna na Dravi in daljnovodna povezava ČHE-RTP Maribor, Hidroenergetska raba vode v Sloveniji, Mišičev vodovodarski dan, 2006
[7] Al-Mansour, F., Sucic, B., Pusnik, M.(2014): *Challenges and prospects of electricity production from renewable energy sources in Slovenia*, Energy, Volume 77, Pages 73-81
[8] Wannenmacher, H.(2006): Kops II Pressure Tunnel, Felsbau Magazin.
[9] Morabito, A., de Oliveira e Silva, G. Hendrick, P. (2019): Deriaz pump-turbine for pumped hydro energy storage and micro applications. *Journal of Energy Storage,* https://doi.org/10.1016/j.est.2019.100788
[10] www.steffturbine: *From materials handling to hydropower, steff turbine, Linear Power*, WHR Walter Reist Holding AG, CH-8340 Hinwill/Schweiz

WATER TURBINE HYDRAULIC REGULATING SYSTEM AND MODIFICATIONS TO MEET GRID STABILITY REQUIREMENTS

MARKO HROVAT
Hainzl Motion & Drives d.o.o., Ljubljana, Slovenia
M.Hrovat@hainzl.si

DOI
https://doi.org/10.18690/um.fs.7.2025.20

ISBN
978-961-299-049-7

Keywords:
water turbine, hydraulic power unit, design and operation, design modifications, grid stability

Over the past three decades, the hydropower sector has seen major technological advancements, driven by rising global electricity demand, increasing energy prices, and growing awareness of the environmental impacts of conventional power generation. These factors have strengthened the role of renewable energy sources-particularly hydropower-in building sustainable energy systems with lower ecological footprints. Current research focuses on retrofitting and digitalizing existing hydropower infrastructure, developing next-generation hydro and aero-hydrodynamic technologies, and deploying hybrid systems integrated with advanced energy storage solutions. Given the inherent variability of renewable sources, high-capacity storage technologies are essential for enhancing grid stability, frequency regulation, and overall resilience. Furthermore, the development of advanced smart grid architectures is crucial to enable distributed, multi-nodal power generation, improve demand–supply balancing algorithms, and support the seamless integration of small and medium-scale energy producers. Together, these innovations aim to optimize energy efficiency, support decarbonization goals, and ensure a reliable and flexible power supply in the face of evolving energy needs and climate challenges.

University of Maribor Press

1 Introduction

The beginning of utilization of hydro power for electricity production dates back almost 150 years. In this time, many types of water turbines in a very wide range of sizes were developed. Hydro power generating unit consist of water turbine, which converts energy of the water into rotation and generator, which converts rotation into electricity. Main parts of water turbine are runner (rotated by the flow of water), shaft (connecting the runner to generator) and distributor (carefully regulates the flow of water on to the runner from closed position to maximum discharge). These assemblies include all components necessary to run the units – load bearing structures, bearings, seals, mechanisms for power transmission, etc.

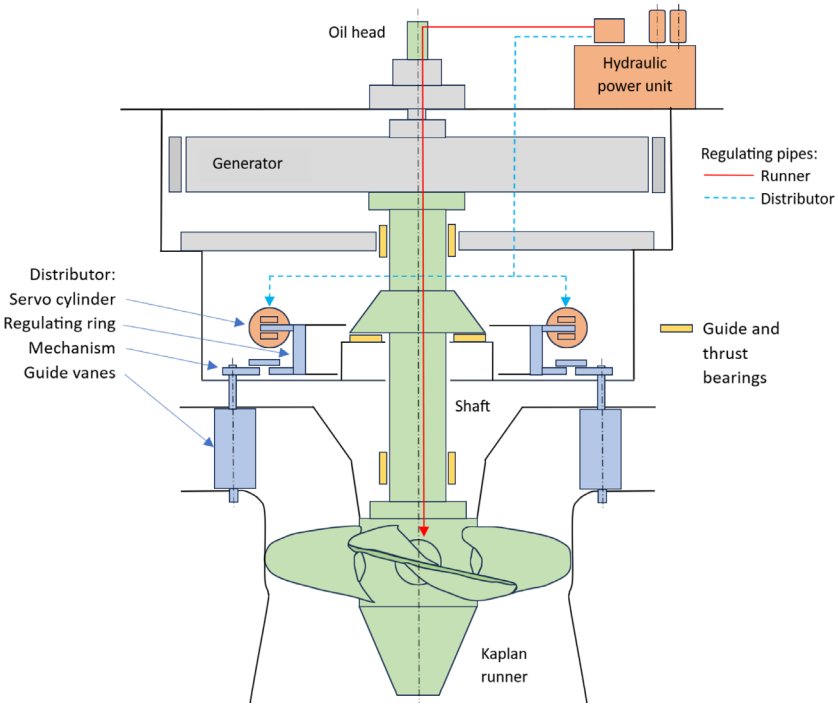

Figure 1: Typical Kaplan generating unit.
Source: own

Water turbines can achieve impressive efficiency. Up to 96 % of water energy can be converted into rotation of the unit (various mechanical and electrical losses decrease effacing of the whole unit). To reach such values, each water turbine and

generator must be carefully adopted to specific hydraulic conditions. Available head and flow of the river are the most contributing factors.

Main classification of hydraulic units is based on the type of runner installed:

- Kaplan runner is designed to be regulated together with distributor which is suitable for low head and large discharge hydropower plants (HPP). Double regulation allows high efficiency in a wider operation range which is necessary to utilize all water level fluctuations at low head.
- Francis runner is designed with fixed blades, compete regulation is performed only with distributor. These units can cover the largest range of heads and discharges. Such runners are less expansive to manufacture and do not need a regulating system. Narrower operating range is acceptable due to lesser influence of the head fluctuation.
- Pelton type of water turbine is fundamentally different to Kaplan and Francis in mechanical design and physical principles that govern energy transformation. Open water jet is used to power the runner (impulse turbine). Such units are suitable for the highest heads and small discharges. In comparison, Kaplan and Francis are a reaction type turbines, where runner is encased into sealed water passage connecting upstream and downstream water level. Pressure, kinetic and potential energy of the water are being transformed inside the passage to achieve optimal conditions to power the runner.

Figure 2: Kaplan, Francis and Pelton runners.
Source: own

Main design variations of the units, in addition to runner selection, include vertical or horizontal main shaft, main shaft bearing arrangement (1 thrust and typically 2 or 3 guide bearings with different locations in relation to generator), distributor type

(cylindrical or spherical), water passage design (steel liner or concrete, bulb, open pit, etc.). Design influencing factors are natural conditions of HPP location, quality vs. cost, maintenance requirements, limitation of transportation to HPP locations, etc.

Generating units are equipped with auxiliary systems which enable their operation and typically include hydraulic regulation, lubrication, cooling and drainage systems.

2 Turbine regulating system

Turbine regulating system has a function of starting, regulating and stopping the unit. It also performs a safety function (shut down or "speed no load" operation) in case of turbine and generator faults. Kaplan and Francis turbine regulating systems have similar basic design. Major difference is that a complete section for runner regulation is not necessary for Francis turbine. Regulating system is divided into mechanical assemblies (distributor and runner) and hydraulic power unit which are discussed in the next chapters and various electrical control systems.

HPP are, in addition to the generating units, equipped with other systems which are also typically operated by hydraulic power units (HPU) such as turbine inlet valves, water passage gate mechanisms, trash rack cleaning machines, etc.

2.1 Distributor

Main parts of distributor are hydraulically shaped guide vanes arranged in circumference around the runner (typically 16, 20 or 24 pieces). Their purposes are:

- Close the water passage, stop the flow of water on to the runner and stop the unit (normal stop or emergency)
- Regulate and assure optimal water flow to the runner while unit is operating

Each guide vane is connected through a linkage mechanism to a common regulating ring which is rotated by hydraulic servo cylinders. Depending on the size and type of units 1 or 2 cylinders are installed. Varus layouts are possible (parallel on each side of the unit, rotated by 180°, located on inner or outer diameter of regulating ring) which influence the oil requirement for movement, regulating force and dimensions.

Distributor is equipped with locks for closed position (automatic) and open position (typically mechanical) for safety and maintenance reasons. Locks can also be installed to servo cylinders which can simplify regulating ring design.

For specific units with horizontal shaft a closing weight can be installed to assure closing in case of HPU failure (larger size turbines with no possibility of safety turbine inlet valve). Most units have vertical shaft where weight cannot be installed (direction of gravitational force is perpendicular to regulating ring movement).

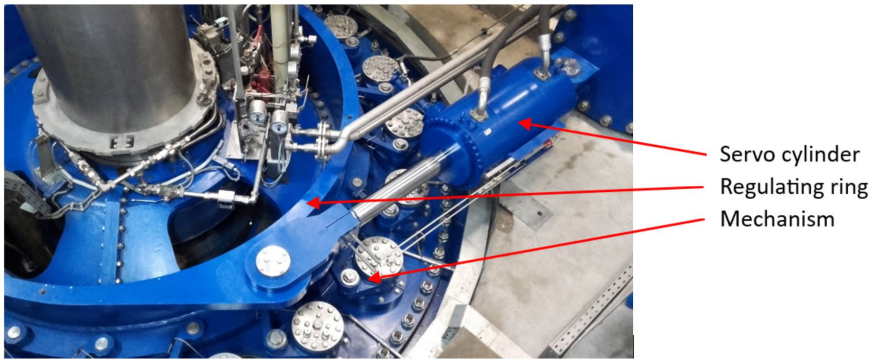

Figure 3: Distributor.
Source: own

2.2 Kaplan runner, oil head and pipes in shaft

Kaplan runner blades are regulated by servo cylinder integrated into the runner hub. Cylinder and blades are connected through a linkage mechanism. Complete assembly is carefully designed to fit inside a narrow hub where access and maintenance possibilities are very limited and operate in harsh conditions completely submerged into water passage. Operational life is typically minimum 40 years.

Regulation of blades is arranged with hydraulic power unit located in the powerhouse (15+ meters above runner), through oil head (special assembly connecting stationary pipes and rotating shaft) and special pipes in shaft (connecting oil head and runner).

Oil head is located on the top of the generator and unit main shaft. It has many design challenges:

- It must maintain high regulating pressure with minimum leakage losses;
- It must sustain constant blade position for a long operating periods where oil flow is very low (only compensation of losses) and handle large flows in case of emergency where fast movement are required;
- Sealing between stationary and rotating parts is contact free. Minimum clearances are achieved by fitting one part to another which prevents repairs. Complete assembly must be replaced in case of damage.
- It must handle vibrations.

Pipes in shaft are specially designed section of hydraulic piping. Two pipes are installed, one into another, and both together inside a central hole of unit main shaft. Diameter of shaft hole varies depending on the size of the unit and is typically between 160 mm and 250 mm. Due to length of main shaft and site assembly limitation both pipes must be splitted into sections (up to 6 m long) with flange or thread connections. These connections are very critical:

- They must conform to tight space inside main shaft hole;
- Bolted flange connections cannot block the flow of oil (especially in emergency – large flows);
- Assembly is performed under difficult condition;
- They must maintain good sealing properties during the operational life time.

Inner pipe is connected to the moving part of the servo cylinder inside the runner (depending on design a piston or cylinder housing can move). Complete piping assembly must be straight over the complete length and allow free movement which enables runner blade position feedback. Position is monitored at the oil head.

Shaft hole and two pipes form three channels. Two are used for runner regulation, third one is used to fill (or drain) the runner hub with oil or water (ECO runners). Top of the rotating shaft is designed to allow drainage of fluid away from the shaft and generator.

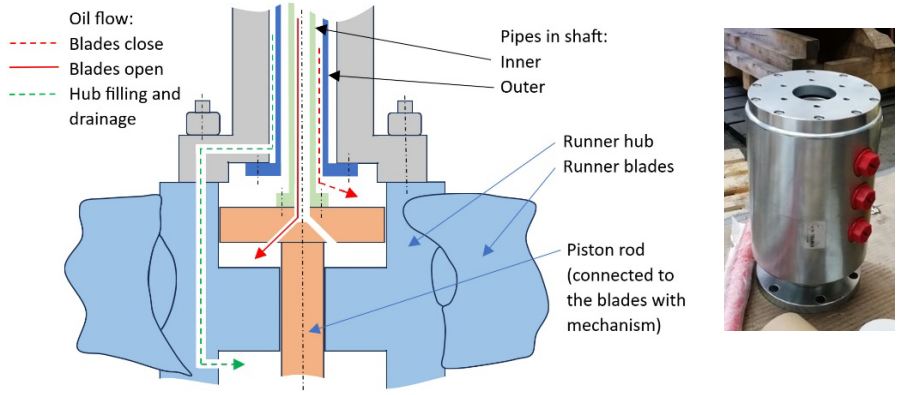

Figure 4: Kaplan runner with integrated servo cylinder and pipes in shaft, oil head (right).
Source: own

Runner, oil head and pipes in shaft have in recent decades undergone significant design changes driven by increasing oil regulating pressure. Level was slowly raised from 20 bar to 40 bar and 60 bar and recently quickly to 130 bar and even 160 bar which has downsized the equipment, allowed for cylinder placement change inside runner hub (from top to bottom), influenced oil head leakage, etc.

2.3 Hydraulic power unit (HPU)

Hydraulic power unit has a function of suppling pressurized oil for turbine regulation. All operational regimes, especially safety functions, must be considered in design (they are presented in the next section). Basic design and operational requirements are always similar but final solution can be significantly adjusted for each Customer. Main driving factors are price, working pressure level and safety requirements.

HPU is a complex assembly. Typical main pars are:

- Oil sump tank
- Variable displacement piston pump with electric motor – 2x
  - Main pumps for pressurizing accumulator station, which then supplies the oil for regulation.

  - Primary pump is working permanently, second is stand by, priority changed periodically for reliability and equal wear.
  - Pumps are activated in predetermined sequence to compensate consumed oil (at first low pressure point main pump is regulated to increase discharge, at second low point stand by pump is activated).
- Accumulator station
  - Source of pressurized oil for the system.
  - Size determined based on safety requirements – number of cylinders strokes in case of system fail (typically 3 strokes before minimum pressure is reached).
  - Typical arrangement with piston and nitrogen bottles or bladder type.
- Main regulation valves used during normal turbine operation
  - Servo proportional directional valve – 2x
  - One valve for runner, second for distributor regulation
  - Pilot operated for larger units
- Emergency shut down valve system
  - Fault signal triggers a sequence which isolates both main proportional valves and opens cartage valves which allow higher oil flow to distributor and quick stopping of the unit
  - Solenoid directional control valves activated by fault signal – 2x
  - Hydraulically actuated cartridge valves for isolation of both main proportional valves – 2+2x
  - Hydraulically actuated cartridge valves for oil supply during emergency shut down – high flow – 2x
  - During emergency shut down distributor is closed and runner remains in the current position
- Manual control for maintenance purposes
  - Guide vane and runner blade position is manually set to required opening and blocked to prevent unvented movement during maintenance works
  - Main proportional valves are isolated with cartage valves (the same as used for emergency stop)
  - Solenoid directional control valves, separate for distributor and runner – 2x
  - Manual isolation valves with lock – 2+2x

- Filtration loop unit – continues operation
- Cooling loop unit
- Oil head minimum pressure requirement
  - Modern oil head solutions suitable for high pressures are designed with minimal clearances between rotating and stationary parts. Constant minimal pressure (typically 5 bar) is mandatory to prevent seizure.
  - Pressure regulating valve with check valves for each flow direction
  - Isolation valve for unit standstill

HPU is equipped with all necessary parts for safe operation inside designed parameters, continues system monitoring and alarm or emergency shut down signaling (safety valves – for each pump and accumulator station section, temperature, pressure, flow and level transmitters and switches, shut off valves for maintenance, additional high pressure filters after each main pump, oil heater arrangement, etc.).

HPU is designed to be operated automatically. Electrical signals for valve actuation are received from digital turbine regulator. Runner and distributor opening feedback signals are continually monitored by independent linear transmitters and compared to the input signals to assure correct position.

Figure 5: Hydraulic power unit.
Source: own

3 Hydro generating unit operating regimes

Hydro generating unit has three basic operating regimes – normal operation, emergency shut down and load rejection.

3.1 Normal operation (start up, power regulation and shut down)

Starting procedure can begin when turbine, generator and all auxiliary systems are ready which is confirmed by a number of signals (pumps on; oil, pressure, temperature levels OK, filters not clogged, safety element OK, distributor lock OFF, hydrostatic bearing lubrication ON, water passage gates removed, etc.).

HPU begins opening of runner and distributor proportional valves which releases water flow on to runner blades at which point the unit starts rotating. At approx. 15 % opening "speed no load" point is reached and unit is ready for synchronization with the electrical grid. This is the most critical sequence during which the unit must quickly increase the power output to desired value inside the operational limits while all the time maintaining nominal speed and grid frequency. Maximum output can typically be reached in approx. 15 sek.

During normal operation the unit power output can be regulated. These actions are also performed by actuation of both proportional valves. Runner and distributor positions are carefully matched across the entire opening range to assure optimal hydraulic conditions at any point. This is referred as on-CAM operation.

Normal shut down procedure is as well carried out by proportional valves. During this sequence the distributor will close and stop the water flow and power generation. Runner typically remains submerged in the trapped standing water inside the water passage (depending on the height difference between runner centerline and level of the water at the HPP outlet – tail water level). Due to high weight and inertia of rotating parts the runner is moved into open position where turbulent mixing of trapped water creates braking effect which significantly reduces the time until unit reaches stand still.

Distributor servo cylinder is designed to dampen the last ~20% of the stroke to prevent water hammer effect in the power plant water passage. Fast initial closing time is approx. 4 sek, complete closing time is approx. 15 sek.

3.2 Emergency shut down

Emergency shut down can be triggered by a number of different faults on the unit, its systems or even inside complete HPP and results in the unit being stopped. Main proportional valves are immediately isolated which leaves the runner in its current position while pressurized oil for distributor closing is supplied trough two separate high flow cartridge valves.

3.3 Load rejection

Load rejection is triggered by a sudden loss of generator load and results in unit rotating at nominal speed with no load (speed no load). Runner and distributor are both closed trough main proportional valves until they reach "speed no load" point. If no other faults are signalled the unit can be quickly restarted. Load rejection can occur during start up (unsuccessful synchronization with grid) or during normal operation.

4 Electric grid regulation requirements

Hydro generating units are typically connected to country's electric grid to which it must strictly conform during operation. The main challenge of ensuring stable grid is to continually and very accurately balance the power demand with production from various sources with very different characteristics while all the time maintaining grid frequency inside a narrow tolerance.

Demand for electricity is constantly changing but the general daily trends are predictable. Traditional power generation sources are also very predictable and provide good balance between stable base production (nuclear, coal) and required flexibility (hydro, gas). All these power plants have an additional advantage of large inertia which provides resistance against rapid power balance changes and aids in grid stability efforts.

Solar and wind power plants are in comparison unpredictable both in time and amount of electricity generation. In addition, the inertia of these systems is extremely low. As a result, these power plants are causing disturbances in the grid and make them more unstable. With very fast implementation of such projects and decommissioning of nuclear and coal plants their share in energy mix is increasing and so are the challenges.

Hydro power plants positively address many of these topics. Electricity produced is green without emissions and renewable, operation can be regulated and they have good inertia. Their impact on the installed location is however large which has in recent times stopped or delayed many new projects. Despite some of the impacts, like flood prevention, being very positive. In more developed countries majority of the river potential is already utilized and the focus is on the modernization of existing equipment which is between 40 and 60 years old.

Since hydro equipment is built for long service life the requirements for more flexible operation first started affecting existing units which were not designed for such load cycles. As a result, equipment started failing. New and newly modernized existing turbines are designed considering new load cases, but due to the nature of equipment which can only be tested when fully assembled at site, and many new additional design upgrades (self-lubricating bearings in mechanism linkages, oil free ECO Kaplan runners, etc.) the development path exposed new unexpected technical challenges.

5 Turbine design considerations to meet grid stability requirements

Due to large verity of turbine types and sizes and locations of installation with specific local needs the operation was always diverse. But typical low head Kaplan double regulating units were operated in a steady regime with few starts and stops and small number of adjustments to power output. It was common to set it to current river flow conditions and operate in best efficiency point for longer durations. During such operation the hydraulic loads are uniform and changes are gradual with small impact.

5.1 Load cycles

Higher flexibility requirements significantly increased the number of start-stop cycles and power adjustments necessary to respond to larger power fluctuations and even more importantly, highly increased the number of micro adjustments for maintaining grid stability (commonly referred as primary frequency control – PFC).

Older units which were first subjected to such loads without any modifications started experiencing mechanical failures. This was due to not being designed for such cases, lower quality materials (general purpose castings), not developed non-destructive testing (NDT) methods to check material quality and looser tolerances. The most common fault was braking of the linkage parts of runner blade mechanism where design compromises must be made due to tight space.

In modern turbines all these areas were already improved due to natural engineering and manufacturing advances. The biggest challenge remained due to micro position adjustments – how to determine and evaluate their actual load cycles and effect on bearings and seals. Finite element method (FEM) analysis has greatly improved, moving from individual parts to full assembly evaluation with more accurate loads and boundary conditions specification and including prediction of equipment lifetime.

Runner hub sizes have also reduced allowing higher water discharges and increased power outputs. This has additionally compacted and complicated mechanism design.

5.2 Bearings

Bearing (and partly seal) behaviour was significantly impacted by new strict environmental regulations. Runner hubs with complete mechanism were traditionally filled with oil which ensured optimal lubrication. Since this creates risk for river water pollution (protected only by one set of seals which are very difficult to maintain and replace) a modern oil free ECO runner was developed. Hub is in this case empty (dry) or water filled, which has a negative effect on the friction during mechanism movement.

In ECO runners, traditional bronze bearings were replaced by self-lubricating bearings (solid lubricant forms part of the base material) of different designs – sintered bronze with graphite of PTFE (approx. 10 %) or complete composite design (filament wound of casted). For some designs it was determined only after the turbine was put in operation that bearings are not suitable and need to be redesigned and replaced which created extreme costs and long unit shut down periods. The most critical example are PTFE bearings where it was established that damp environment significantly raises the friction, in many cases beyond the capacity of regulating system.

Despite great improvements and some clear advantages (example: reduced edge pressure) the self-lubricating bearings result in higher friction compared to oil filled runner design. For PFC regulation it was established that micro movements suffer from stick slip effect since solid embedded lubricant need certain minimum movement lengths to be fully effective.

Interestingly some Customers have recently started switching back to bronze bearings lubricated by oil for the new runners. This is another example of diversification of the hydro industry and that individual Customer experiences and good practices are the main driver for their decisions.

5.3 Deadband

Deadband represents the length of servo cylinder stroke before movement is observed on runner blade or guide vane when direction of travel is changed. Because of the requirements for precise positioning and frequent micro movements for adjustment the deadband must be minimized. Typical target specified in recent technical specifications is 0.1 % of servo cylinder stroke which amounts to 0.6 mm at average stroke of 600 mm.

This value is low considering the number of parts and bearings in runner and especially distributor mechanism. Distributor with 24 guide vanes is equipped with 120 bearings (3x for each guide vane and 2x for each link connection) ranging from 50 mm to 220 mm with fit tolerance H8/f7, where individual clearances can reach up to 0.1 mm. Regulating ring radial bearing diameter typically ranges between 3 m and 6 m and has a clearance between 0.3 mm and 1 mm.

When complete assembly is evened out the dead band value typical slightly exceeds the new requirements. The issue is also that standard bearing tolerances in worst case allow for higher unacceptable deviation and that the actual value can only be confirmed once the unit is assembled on site. Modifications at that point are extremely difficult, costly and will result in long project delays.

Since the requirement for lower deadband is relatively new the modifications are not yet matured and are not part of the standard design principles. It is however certain that the target will not be achieved without bigger changes.

One known and proven solution used in hydro industry is to replace the standard fit tolerance with final machining of one part, based on exact measured diameter of counterpart. Diameter of bearing counterpart would be determined based on minimum technically allowed clearance. This process is used occasionally and for smaller parts which are easy to handle. Due to the high number and large size of the parts and the difficulty of positioning them on the machines to perform additional final step, such technological procedure will significantly raise project costs and extend the timelines.

6 Conclusions

Ensuring grid stability will continue to be a challenge. Modern electric control systems are capable of processing large amount of information and quickly respond with adjustment signals. Hydraulic power units and especially main servo proportional valves have also developed and offer high frequency response.

The main issue remains to be runner and especial distributor assemblies. Big number of large and heavy parts crate deadband regardless of very tight machining tolerances (example: 1 ton guide vane bearing surfaces run-out is inside 0.02 mm). Further reduction of bearing clearances is technically possible but in practice difficult and expensive to achieve. Additional consideration is the negative effect of new load cycles on the turbine equipment and especially bearings.

Therefore, it is worth reviewing if water turbines should be utilized for primary frequency control operation or at least limit the required micro adjustments to the technically acceptable level. Rapidly developing battery storage systems offer an elegant solution which could solve the issue electronically instead of mechanically.

Factors Affecting the Accuracy of Operation of the Electrohydraulic Actuation Position System With Throttling Control

Dragan Nauparac, Nemanja Višnjić
PPT-Engineering, Belgrade, Serbia
dragan.nauparac@ppt-inzenjering.rs, nemanja.visnjic@ppt-inzenjering.rs

The paper analyses most of the factors that influence the positioning error in the stationary mode of the electrohydraulic positional actuation systems and several ways to calculate the positioning accuracy in relation to the considered factors that influence the accuracy. Criteria are defined so that it is possible to check whether the desired accuracy of positioning can be achieved in the early design phase, but also the repeatability of accuracy over the full range of positioning. This is important to know, i.e. to define in the early design phase in relation to the basic limit performance of the actuation system, above all in relation to the bandwidth of the actuation system and to see if there are possibilities for algorithmic and/or structural correction of the positioning accuracy of the actuation system in the later stages of design. It starts from the basic 3-order linearized model, but in the analysis, factors of unmodeled dynamics are added in the 3-order linear model.

DOI
https://doi.org/10.18690/um.fs.7.2025.21

ISBN
978-961-299-049-7

Keywords:
hydroelectric power plant, ship lock, hydraulic actuating system, positioning error, accuracy

University of Maribor Press

1 Introduction

One of the important tasks at hydroelectric power plants is to ensure the synchronous motion of two cylinders that operate the flat plate valve of the upper head of the ship lock system. The issue concerns the hydroelectric power plant Djerdap 1.

The electrohydraulic actuation system with throttling control is speed-driven in nature, i. e. the control distributor controls the direction of fluid movement, flow intensity and rate of flow change. Depending on which type of feedback loop we close, we get a positional, speed, force- and acceleration-controlled actuation system. The requirements for a positional actuation system are accuracy with repeatability, speed of response and stability. Accuracy is the difference between the set and desired position, the positioning error, and if we can maintain that value after repeated positioning with a certain precision and speed, then the repeatability feature is ensured. That speed must be such that it provides a sufficient reserve of stability, that is, the gain in the actuation system that ensures the speed of response during positioning is chosen in such a way that it does not impair the stability of the actuation system.

When designing an electrohydraulic actuation system, it is useful to know already in the first stages of designing whether the desired positioning accuracy can be ensured. Basically, every linear actuator (executive hydraulic cylinder) as a positional electrohydraulic system can be loaded inertially, positionally and with friction, individually or in combination with these three types of loads. The character of the load primarily affects the project solutions in order to ensure the required positioning accuracy.

2 Factors affecting positioning accuracy

In addition to the character of the load, the configuration of the electrohydraulic actuation system and the algorithmic solution for position control are the three basic groups of factors that affect positioning accuracy. When it comes to load, inertial and positional are dictated by the character of the drive mechanism whose drive member is the hydraulic cylinder as the executive organ of the electrohydraulic actuation system. Friction exists internally in the hydraulic cylinder and externally in

the loading mechanism. Friction as a type of load is the most difficult to compensate with the control algorithm. There are some solutions with sliding surface mode variable structure algorithms, the application of which is limited. In terms of reduced impact on positioning accuracy for friction compensation, emphasis is placed on the quality of the hydraulic cylinder and on ensuring minimal friction in the external elements of the drive mechanism.

The configuration of the electrohydraulic actuation system, as another factor, is important in terms of the correct dimensioning of the hydraulic cylinder and the choice of the distributor with the required dynamic properties, which will be considered separately in the next chapter. The correct choice of the initial control algorithm is particularly important because it directly affects the shortest path to the optimal algorithmic solution for positioning accuracy, i.e. to compensate for the influence of the load and certain phenomena of the non-linear nature of the configuration of the electrohydraulic system, the consideration of which also follows. Within the nonlinear nature of the configuration of the electrohydraulic system, gap-type nonlinearity (hysteresis-type memory nonlinearity) must also be considered, which includes the influence of mechanical clearances and partial friction on the positioning accuracy of the electrohydraulic system and is most often the cause of the oscillatory behaviour of the positional response. The speed of the computer as well as the level of discretization also affects the positioning accuracy, which is also analysed by simulation.

3 Selection of distributor and hydraulic cylinder dimensions

The bandwidth of the actuation system is the best representation of the accuracy of the electrohydraulic actuation system in the initial stages of design, while respecting the compromise for the stability of the actuation system. There are two important elements for the performance of the actuation system that need to be reconciled in terms of achieving a sufficiently large bandwidth. It is the maximum speed of the hydraulic cylinder, dictated by the dynamics of the drive mechanism and the dimensions of the hydraulic cylinder dictated by the speed, but also the working pressure, which defines the elements that determine the bandwidth of the cylinder with the load that should be modeled as precisely as possible. In order to choose the distributor properly, we need to define the bandwidth of the actuation system. In this way, one component of accuracy is defined. The basic principle is that the

dynamics of the actuation system must not affect the object where the actuator is the driving element of some mechanism of the object. There are experimentally verified recommendations for most facilities. Then we can simply arrive at the necessary dynamics of the distributor valve, through whose performance we can further consider the correctness of its selection and the impact on positioning accuracy, primarily through flow amplification and according to static stiffness conditions. It should be emphasized that the computationally-simulated bandwidths in practice are lower by about 27 % than actually possible [1].

In addition, here we have an open question whether to choose a distributor with a linear flow change or with a gap, which is again related to static hydraulic stiffness and its influence on positioning accuracy. Here also remains the dilemma of whether to "consume" a larger part of the algorithmic amplification through the amplification by the flow of the distributor. Both amplifications are contained in the amplification of the open circuit of the actuation system, Figure 1. This then leaves us with fewer opportunities to compensate for some elements of nonlinear phenomena of electrohydraulic positioning systems through greater algorithmic amplification.

With that in mind, there is also the application of a distributor with two amplifications, Figure 2, one for example for +/- 30 % of the displacement of the piston, the other, larger for the remaining part of the range, in order to have more opportunities for algorithmic amplification in case of smaller displacements for positioning, in order to have more accurate positioning.

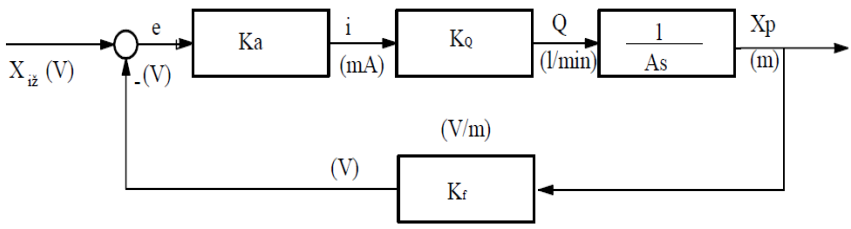

Figure 1: Basic structure diagram of electrohydraulic actuation position system.

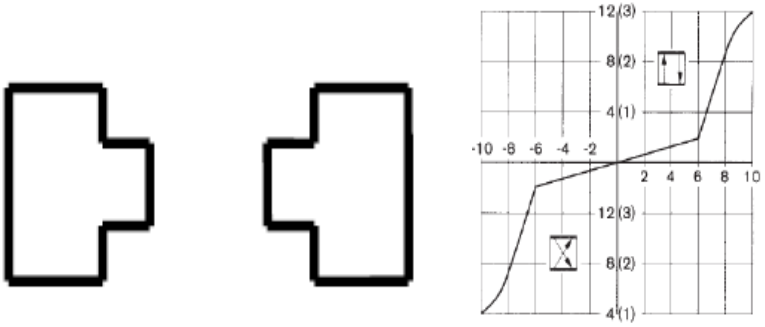

Figure 2: Two gain static characteristic of distributor.

$$K_{open} = \frac{K_a K_q K_f}{A}(1/s) \tag{1}$$

$$K_a = \frac{AK_{open}}{K_q K_f}(amp/volt) \tag{2}$$

Based on equation (1) and on the recommendations that exist in practice it follows:

$$K_{open1} = 0.1\omega_{cil\_opt\_nat\_freq} \tag{2.1}$$

$$K_{open2} = 0.4\omega_{servorazvodnik\_nat\_freq} \tag{2.2}$$

As can be seen from the above, the idea is to determine the algorithmic gain *K*a. Simple transformations lead to basic expressions for analysis:

$$\frac{X_i(s)}{X_{iz}(s)} = \frac{G(s)}{1+G(s)H(s)} \tag{3}$$

$$G(s) = \frac{K_a K_q}{As} \qquad H(s) = K_f \tag{4}$$

$$\frac{X_i(s)}{X_{iž}(s)} = \frac{\frac{1}{K_f}}{\frac{A}{K_a K_q K_f}s+1} = \frac{\frac{1}{K_f}}{\frac{1}{K_{open}}s+1} = \frac{\frac{1}{K_f}}{Ts+1} \tag{5}$$

$$T = \frac{1}{K_{open}}\sec \tag{6}$$

$$\frac{X_i(s)}{X_{iž}(s)} = \frac{1}{Ts+1} \tag{7}$$

$$X_i = \frac{1}{K_f}X_{iž} \tag{8}$$

Previous equation represents the simplest mathematical model of the actuation system, which only allows us to check the maximum gain, ignoring the cylinder load. Based on the block diagram, Figure 1, we can write:

$$I = K_a K_f x_{err} \tag{9}$$

$$X_{iž} = 0 \tag{10}$$

$$\boldsymbol{I = K_a K_f x_{doz}} \tag{11}$$

$$x_{doz\_\max} = \frac{0.05 I_N}{K_a K_f} \tag{12}$$

Based on the previous expression (12), we get an estimate of the positioning error by assuming that 5 % of the control signal is the minimum value sufficient to compensate for the asymmetry of the distributor and the negative impact of friction during positioning, i.e. that 5 % is the maximum hysteresis of the distributor, based on the previously calculated algorithmic gain.

In the following approach to positioning error estimation, we start from the assumption that we have external force data. Here we have taken 2 % as the control signal because for most servo and proportional distributors this is the gain value per pressure. This means that the position error caused by an external force can be compensated for by changing the pressure.

$$I_{ser\_raz} = 0.02 * I_N * \frac{F_{opter.}}{A * P_N} \tag{13}$$

$$x_{doz\_\max\_opter.} = \frac{I_{ser\_raz}}{K_a K_f} \tag{14}$$

$$x_{doz\_\max\_opter.} = 0.02 * \left[\frac{I_N}{K_a K_f}\right] * \left[\frac{F_{opter.}}{A * P_N}\right] \tag{15}$$

As can be seen from expression (15), already after 2 % of the control signal, the position error becomes a function of the external load. Figure 3 shows the experimental diagram of the pressure gain of the proportional-servo manifold, MOOG 671, which shows the asymmetry of the distributor when it comes to the pressure gain.

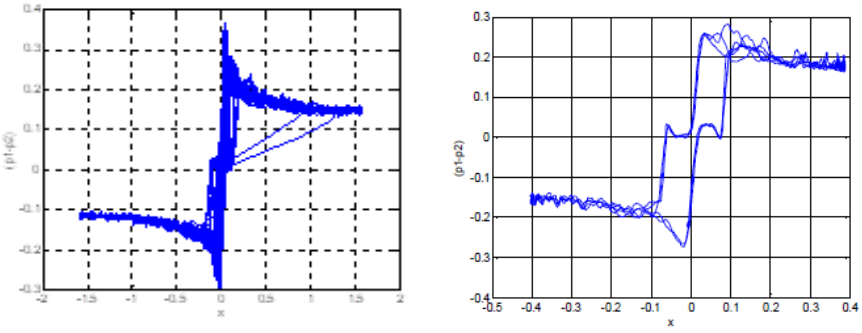

Figure 3: Experimental diagram for pressure gain asymmetry for MOOG 671 distributor.

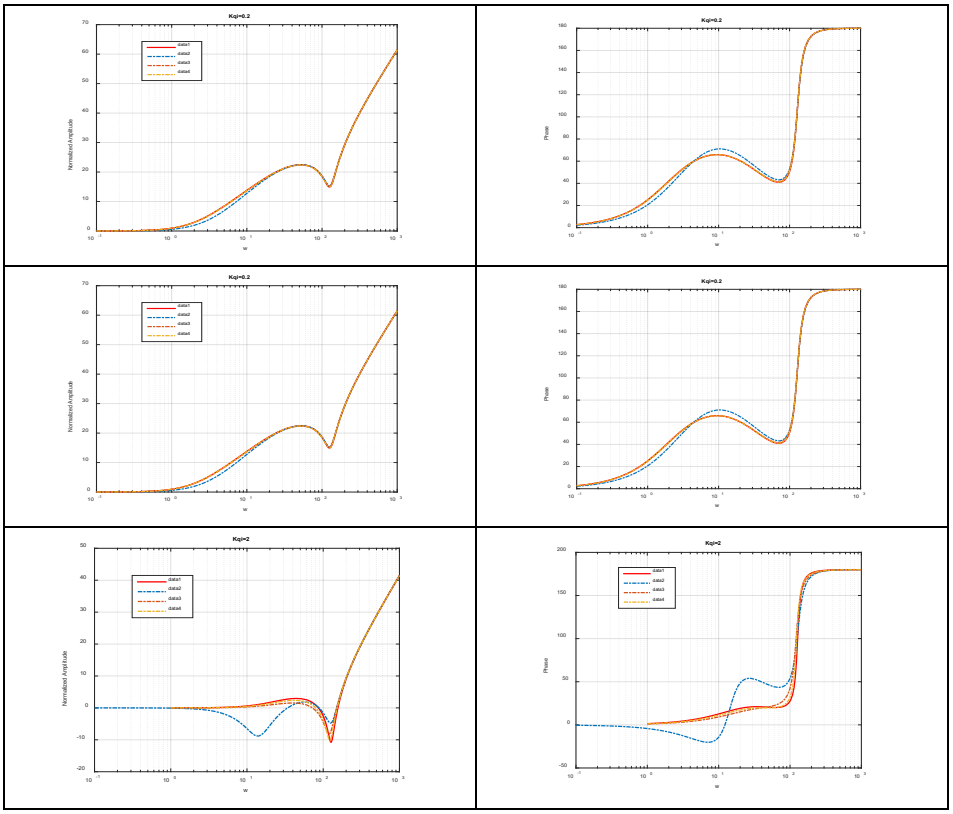

Figure 4: Results of simulation for static stiffness of distributor.

The static stiffness of the distributor was analysed by considering its dynamics. At this point we do not consider the influence of the overlap of the distributor. For the dead zone type nonlinearity, there are hardware and software solutions to compensate. The simulation check was done for three values of gain per flow and three values of the distributor bandwidth, as well as for the variant when the distributor bandwidth is not considered. The results are presented through frequency analysis. It can be seen from Figure 4 that high bandwidths and high gains per flow are critical.

Data 1: the distributor dynamics is neglected

Data 2: $\omega_v = 10$,data 3: $\omega_v = 130$, data 4: $\omega_v = 300$

4 Acceleration and deceleration time of the cylinder - influence on the accuracy of reaching the set position

The time of acceleration and deceleration also affects the positioning accuracy. There are several approaches to define this time. One is approximate, based on well-known relations:

$$\omega_n = \sqrt{\frac{40 \times E \times A_1}{h \times m}} \times \frac{1+\sqrt{\frac{A_2}{A_1}}}{2} \tag{16}$$

$$t_{\min} = \frac{35}{\omega_n} \tag{17}$$

Basically, this time is also a criterion to determine the maximum bandwidth of the actuation system. Since this criterion is not unique, the values 18 or 35 are adopted, it is much more useful to take the following approach. Ramp time is based on [2]:

$$x = v_0\left[1-\frac{t}{t_r}\right], t \le t_r \tag{18}$$

$$y = C_0 + C_1 t + C_2 t^2 - C_0 e^{-\alpha t}\left[\cos(\beta t) + \frac{\alpha}{\beta}\sin(\beta t)\right] \tag{19}$$

$$e = \left|x_{t=t_r} - y_{t=t_r}\right| = \frac{v_0}{\omega_n^2 t_r}\left\{1 - e^{-\alpha t_r}\left[\cos(\beta t_r) + \frac{\alpha}{\beta}\sin(\beta t_r)\right]\right\} \tag{20}$$

$$e_{rel} = \frac{e}{x_{t=t_r}} = \frac{2}{\omega_n^2 t^2{}_r}\left\{1 - e^{-\alpha t_r}\left[\cos(\beta t_r) + \frac{\alpha}{\beta}\sin(\beta t_r)\right]\right\} \tag{21}$$

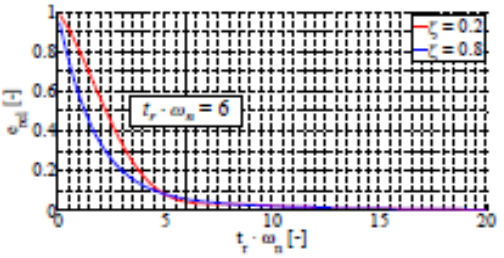

Figure 5: Graphic representation of the error for two limiting degrees of damping [2].

The point of intersection of these two curves defines the minimum time of deceleration:

$$t_r \geq \frac{6}{\omega_n} \quad . \tag{22}$$

Expression (17) is a very loose approximation. Expression (22) was obtained based on the previous settings for two dampings in the electrohydraulic actuation system. Although the two constants 35 and 18 are widely used, (22) is a more accurate limiting value.

In any case, the acceleration limits are important for the overall quality when designing an electrohydraulic actuation system. It should also be considered that in reality, the natural frequencies are lower than those obtained by calculation

5 Simulation verification of positioning accuracy

Simulation verification of positioning accuracy is suitable for certain fixed parameters (gains) to check the impact on positioning accuracy of the basic features of computer control, selection time and discretization resolution. This is done through the models shown in Figure 6, and the results are shown in Figure 7. In this case, only the computer component of the control and its influence on the positioning accuracy is checked.

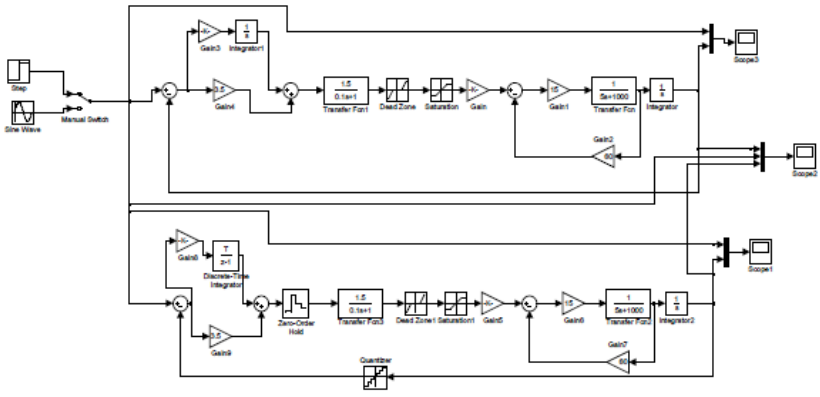

Figure 6: Basic MatLab simulation model.

The model shown in Figure 6 allows for the variation of a large number of simulation parameters, which are used to check the accuracy, sampling time, resolution of the discretization, gains, proportional and integral, the bandwidth of the directional valve as well as its gains. In addition, it is easy to switch from the constant reference option to the variable sinusoidal one.

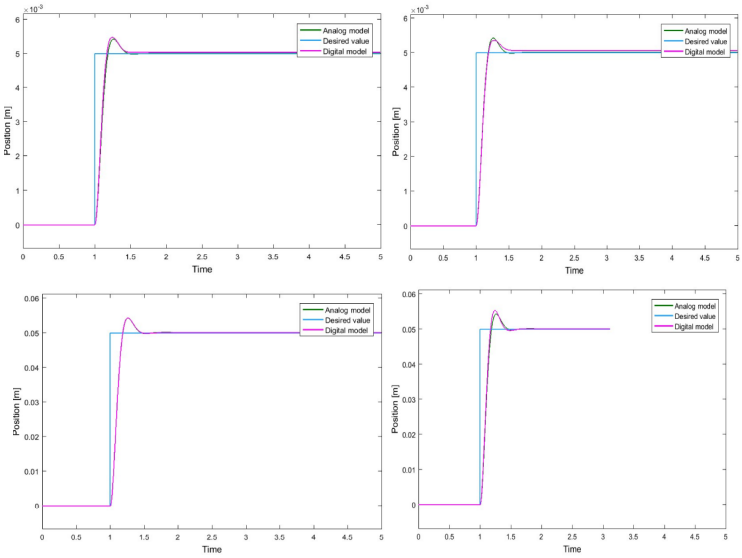

Figure 7a: Simulation results

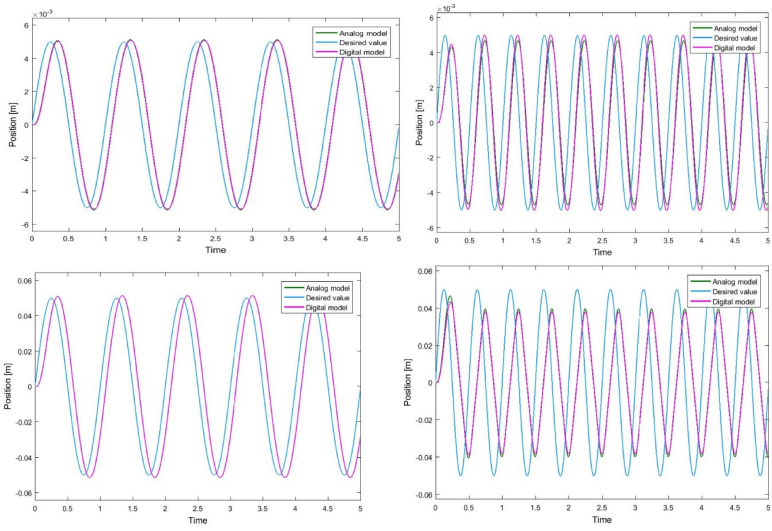

Figure 7b: Simulation results.

Simulation results depicted in Figures 7a and 7b, show the changes when varying the desired position value, 0.005 to 0.05 m (set point and amplitude). In the case of a sinusoidal change, we have two frequencies, 1 Hz and 2 Hz, (2 Hz need different gain). At steps in Figure 7a we have an average gain of 8.5 to 9.5. We see that for the selected computer parameters, the sampling time of 0.001 s (1 Hz) and the discretization of 0.0005 we have almost a coincidence of the „analog" and „digital" curves, small deviations are only at the desired value of 0.005 m there is a small difference and at 0.05 m we have no difference.

6 The initial optimal structure of the actuation system

The Figure 8 shows the structure that is shown in the literature [3] as optimal for the performance of the electrohydraulic actuation system, and thus for the issue of accuracy. Regarding the application of different control algorithms, there are many works that compare two or at most three algorithmic solutions, but there are few works that compare multiple algorithmic solutions with full experimental verification. One of these is [4], which graphically shows, Figure 9, the quality of algorithmic solutions through statistics for position control.

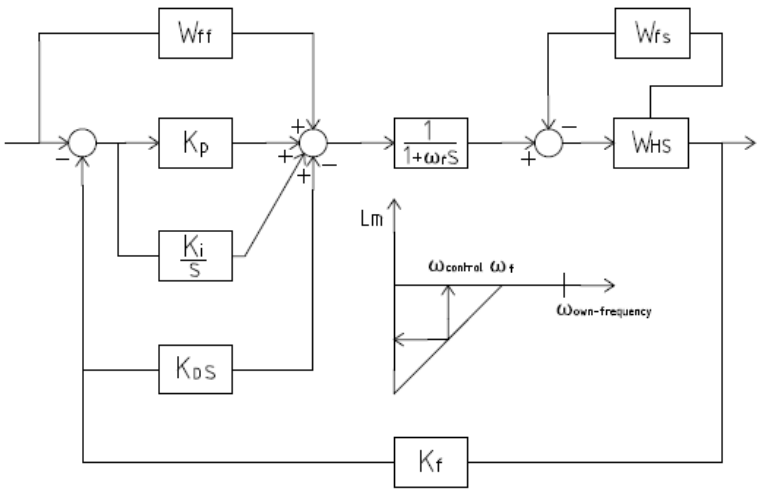

Figure 8: „Ideal" structural diagram of electrohydraulic actuation system.

In the Figure 8, we clearly see that the structural PID algorithm is "broken", by putting the differential action in the feedback loop in order to avoid the negative influence of the differential action when we have the desired value of the set point

type, when there is an impulse component in the response that generally generates an oscillatory positional response. In addition, the differential gain increases with frequency, so that certain components of the signal caused by disturbances can be severely amplified, so a filter block is necessary. Stabilizing feedback block shows that it is useful to use the resources of computer control and available sensors, in order to improve the response of the control system, increase the damping, by adding feedbacks primarily by pressure. A block with feed forward gains is necessary to reduce the effect of control change on positioning error. In addition to this structural solution, to improve the algorithmic solutions, it is useful to apply a cascade configuration for the actuation structure, so that we have an inner loop for control by force and an outer loop for control by position.

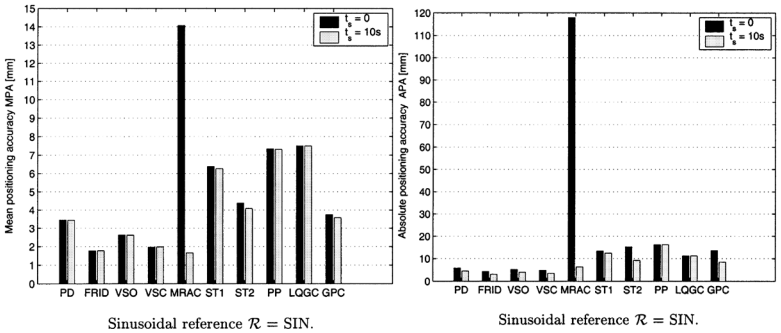

Figure 9: Mean positioning accuracy MPA of various controllers, for nominal plant P = NOM [4].

Designations of the considered control algorithms on the diagrams: proportional derivative (PD), acceleration feedback using an experimentally identified friction model (FRID), acceleration feedback using a variable structure friction observer (VSO),variable structure with sliding mode (VSC), model reference adaptive control (MRAC), self-tuning using a recursive least square parameter estimator (ST1), self-tuning using a Kalman filter for parameter estimation (ST2), pole placement (PP), linear quadratic Gaussian control (LQGC), self-tuning generalized predictive control (GPC). The diagrams (Figure 9) show the tracking error according to the criterion being defined. The MPA of a controller is defined as the root mean squared position error obtained for a reference signal, a plant condition, and averaged over a defined time interval. The APA of a controller is defined as the maximum absolute position error obtained for a reference signal, a plant condition, over a defined time interval. The time interval for tracking positioning error is 10 seconds.

7 Friction and mechanical backlash, influence on positioning accuracy

Friction as a mechanical phenomenon and the non-linear nature of friction have the greatest impact on positioning accuracy. The main problem is that friction cannot be measured directly, but only certain algorithmic compensations are possible, but with limited possibilities. Friction is a function of speed and is greatest at low speeds and when changing direction. That is why one of the tasks is to design the actuator system in such a way that the positioning speeds are as high as possible. Figure 10 shows an experimental recording for two frequencies, 02 Hz and 4 Hz, (friction force, red colour, blue colour position) for a hydraulic cylinder of size Ø200/125x650, where the difference in the effect of friction for two movement speeds of the hydraulic cylinder, for a time-varying position, is clearly visible. The basic question is what can be done in the initial design stages. The literature, [5] suggests that it is useful to test the model of the actuation system with some of the description of the friction nonlinearity with the PD control algorithm, and if we get satisfactory results, then we can expect better results with the variable structure algorithm or the observer with the friction model at a later stage.

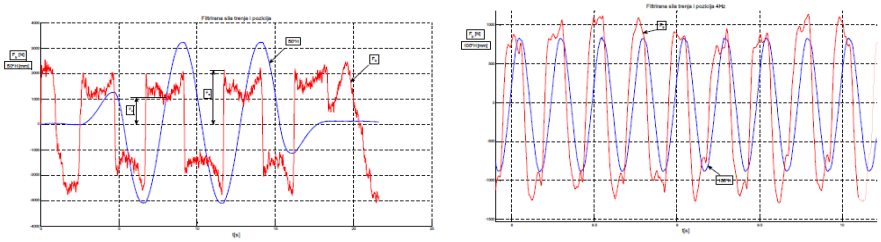

Figure 10: Experimental result for cylinder friction for two frequencies [6].

Backlash (gap) control, the clearance between the cylinder connecting rod and the drive mechanism, the positional electrohydraulic actuation system and the effect on the positioning accuracy is the least investigated in the large number of works that consider electrohydraulic actuation systems. There is no simple methodology that can be applied in the initial stages of designing electrohydraulic actuation systems for this analysis. There is experience that generally requires one to try the inverse nonlinearity at the level of simple linearized models and then add the nonlinearity to compensate for the gap nonlinearity in the control algorithm. It means a simulation check is required, while there are no general computational approaches. One of the main advantages of an electromechanical actuation system over an electrohydraulic

one is that it is possible to generate a torque several times higher than the nominal torque for a short period of time, which compensates for the effect of friction. [7]

8 Error of synchronous motion of two hydraulic cylinders in relation to position accuracy – the example of slide gate of the upper head of the HPP "Djerdap 1" ship lock

The position accuracy affects another control function of electric hydraulic drives – the accuracy of synchronous motion of two cylinders. Here, the accuracy of synchronous motion of two cylinders for a slide gate will be analysed as a specific practical example. Slide gate is the most common steel construction within hydromechanical equipment of every hydroelectric power plant, be it a pre-turbine gate, a spillway gate or a ship lock gate. Only the initial error of synchronous motion is analysed which sometimes happens to be the maximum error, because the greatest disbalance of load is at the beginning of manipulation (one cylinder starts moving before the other, so a significant error is accumulated in the acceleration phase, Figure 11).

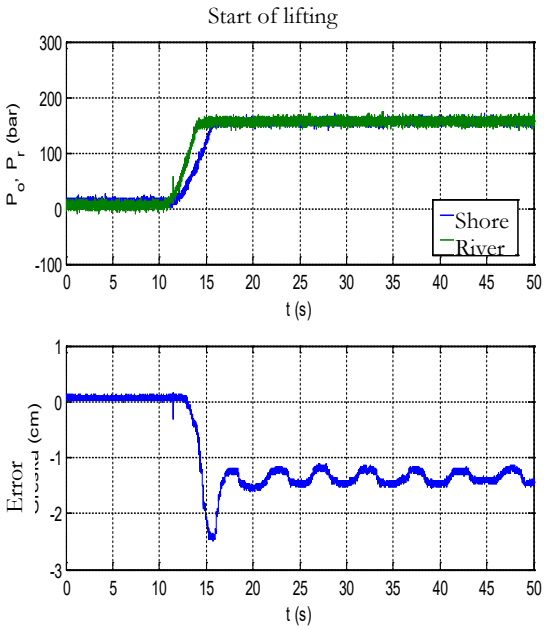

Figure 11: Pressure and synchronous motion error - slide gate of the upper head of HPP „Djerdap 1" ship lock.

It is important to be able to estimate the error in the initial phase of design of an electric hydraulic actuation drive using a mathematical model whose outline is given below [8]. The idea is to determine the necessary acceleration time for slide gate lifting based on initial error of synchronous motion, since it is important for the definition of basic parameters of electric hydraulic drive.

Cylinder motion time:

$$t = \frac{\Delta V}{Q} \tag{23}$$

Cylinder motion time delay (the difference between the beginning of motion of two cylinders due to the difference in load each of them is subjected to):

$$\Delta t = \frac{\Delta V_1}{Q_1} - \frac{\Delta V_2}{Q_2} \tag{24}$$

$$\Delta t = \frac{V\beta\left(p_1 - p_2\right)}{Q} \tag{25}$$

Force equation is given as follows

$$A_1 p_1 - A_2 p_2 = M_{red}\frac{d^2x}{dt^2} + f_{v\_fr}\frac{dx}{dt} + F_{fr} + F \tag{26}$$

Where:

$$p_2 = 81,6\frac{lv\rho A_2}{d^4}\frac{dx}{dt} \tag{27}$$

Flow equation discarding leakage is:

$$K_q X_v = A_1\frac{dx}{dt} + V_0\beta\frac{dp_1}{dt} \tag{28}$$

Combining equations (26), (27) and (28) and solving the equation using Laplace transformation yields the following:

$$x = \frac{K_q X_v}{A_1} - \frac{2K_q X_v M_{red} V_0 \beta}{A_1^3 T} + \frac{2K_q X_v M_{red} V_0 \beta}{A_1^3 T} e^{-\frac{t}{T}} \cos \omega t - \\ - \frac{K_q X_v \sqrt{M_{red} V_0 \beta}}{A_1^2} e^{-\frac{t}{T}} \sin \omega t \tag{29}$$

where

$$T = \frac{2M_{red}}{f_{fr} + 81,6 \frac{l v \rho A_2^2}{d^4}} \tag{30}$$

$$\omega = \frac{A_1 \sqrt{M_{red} V_0 \beta}}{M_{red} V_0 \beta} \tag{31}$$

or

$$x = \frac{K_q X_v}{A_1} - \frac{2K_q X_v M_{red} V_0 \beta}{A_1^3 T} - \frac{K_q X_v \sqrt{M_{red} V_0 \beta}}{A_1^2} e^{-\frac{t}{T}} \sin(\omega t - \varphi) \tag{32}$$

where:

$$\varphi = arctg \frac{2\sqrt{M_{red} V_0 \beta}}{A_1 T} \tag{33}$$

Substituting t with Δt (cylinder motion delay time for the cylinder subjected to greater load) in (32) yields the initial position error – distance already covered by the cylinder subjected to lesser load before the motion of the one subjected to greater load starts

$$\delta_{x_{init}} = \frac{K_q X_v}{A_1}\Delta t - \frac{2K_q X_v M_{red} V_0 \beta}{A_1^3 T} - \frac{K_q X_v \sqrt{M_{red} V_0 \beta}}{A_1^2} e^{-\frac{\Delta t}{T}} \sin\left(\omega \Delta t - \varphi\right) \tag{34}$$

Differentiating (29) and discarding the higher order terms, the piston velocity is defined as follows

$$v = \frac{K_q X_v}{A_1}\left(1 - e^{-\frac{t}{T}} \cos \omega t\right) \tag{35}$$

From (31) and (35) and assuming $t = 3T$ and $v \approx v_{\max}$, piston acceleration time to nominal velocity is defined as follows:

$$t_{acc} \approx \frac{6M_{red}}{f_{fr} + 81,6\frac{l\nu\rho A_2^2}{d^4}} \tag{36}$$

9 Conclusion

The design of an electro-hydraulic actuation position system, including the synthesis of the control algorithm, is a complex process and consists of several phases. In order to verify certain phases, it is necessary to check the basic parameters of the actuation system. One of the main basic parameters for an actuation positioning system is positioning accuracy. Here are several ways of checking the accuracy of positioning in the first phase of designing an electrohydraulic positioning system, in order to define the actuation system as precisely as possible at the beginning of the design, which in any case is an important condition for the rational and efficient design of an electrohydraulic actuation positioning system. The question of precisely defining the actuation system is also connected with the choice of the initial structure of the electrohydraulic actuation system.

References

[1] M.Tang, L.Chen, The system bandwidth analysis in electro-hydraulic servo system with PDF control, Conference Control, 5th Asian, 2004

[2] M. K. Bak, Model Based Design of Electro-Hydraulic Motion Control Systems for Offshore Pipe Handling Equipment, Ph. D dissertation, University of Agder, Faculty of Engineering and Science, 2014

[3] K-E Rydberg Hydraulic Servo Systems – Dynamic Properties and Control, Department of Management and Engineering Linköping University, November , 2014

[4] A.Bonchis, P. Corke, and D. Rye, Experimental Evaluation of Position Control Methods for Hydraulic Systems, IEEE TRANSACTIONS ON CONTROL SYSTEMS TECHNOLOGY, VOL. 10, NO. 6, NOVEMBER 2002

[5] R. Ghazali, Y. M. Sam, M. F. Rahmat, A. W. I. M. Hashim and Zulfatman, Sliding Mode Control with PID Sliding Surface of an Electro-hydraulic Servo System for Position Tracking Control, Australian Journal of Basic and Applied Sciences, 4(10): 4749-4759, 2010

[6] D.Nauparac, Z.Ribar, Project of an electrohydraulic system for a vibration platform for earthquake testing, Faculty for Civil Engineering, Split, 2012.

[7] S. Vukosavljevic, Digitalno upravljanje električnim pogonima, Akademska Misao, Beograd, 2003. (Serbian language)

[8] Гидропривод и гидропневмоавтоматика 4, Республиканский межведомственный научно-технический сборник, издательство «Техника», Киев, 1968. (Russian language)

Experimental Study on Performance of Centrifugal Pump

Beena Baloni, Maitrik Shah,
Salim Abbasbhai Channiwala

Sardar Vallabhbhai National Institute of Technology-Surat, Department of Mechanical Engineering, Gujarat, India
pbr@med.svnit.ac.in, maitrikshah2006@gmail.com, sac@med.svnit.ac.in

A centrifugal pump is designed to enhance the fluid pressure head through energy transfer. Fluid enters the impeller axially, which increases the fluid velocity and pressure by converting mechanical energy. The present work aims to conduct an experimental performance analysis of a centrifugal pump. The experimental test setup as per ISO 9906 (grade 1) is developed for better accuracy and minimum uncertainty. The experimental analysis is carried out, for the 7.5 hp end suction pump, at various speeds and valve opening positions. After conducting a repeatability test, the performance curves are obtained at various operating conditions. The performance curves identified the best efficiency region by varying valve positions in the interval of 1% in the optimum region. At BEP, the head coefficient ranges from 0.90 to 0.82, the flow coefficient from 0.16 to 0.13, and the pump efficiency from 66 % to 63 %, depending on the pump speed.

DOI
https://doi.org/10.18690/um.fs.7.2025.22

ISBN
978-961-299-049-7

Keywords:
centrifugal pump, performance curves, experimental analysis, power consuming turbomachine

University of Maribor Press

1 Introduction

A centrifugal pump is a device that transfers fluids (liquids or gases), or slurries, by dynamic action. There is a conversion of electrical and mechanical energy into fluid energy. The amount of electrical energy used by the pumps in an average industrial facility will vary by plant type. A typical pulp and paper mill will use 30 % of their energy usage to drive pumps. A chemical plant may use 27 % and a petroleum refinery may use 60 %. Over a short time, the cost of the energy to drive the pump will exceed the initial purchasing and installation costs. The reduction in energy consumption and efficiency (η) enhancement can be achieved by proper design, assembly with auxiliary parts, and regular services of centrifugal pumps. The actual performance of a centrifugal pump can be judge by experimental readings. The precise and accurate readings should build the confidence to accept reading among researchers, manufacturers, and consumers. Also, the precision class (grade 1 category) experiment setup of the centrifugal pump gives better repeatability and the ability to address minor variations in the pump efficiency due to design changes.

The Indian standards, IS 13538 [1], and the international standards, ISO 9906 [2], are described with the precision class of centrifugal pump hydraulic performance acceptance test and followed globally. Also, the American National Standard Institute/Hydraulic Institute (ANSI/HI) 1.6 [3] standards for centrifugal pump test detailed procedures on the setup and conduct of hydrostatic and performance tests are globally accepted by industries. D. F. de Souza et al. [4] discussed guidelines for an energy assessment of water pumping systems in multifamily buildings. The pump with an efficiency of 40% was rated as very low-VL for all motor efficiency classes (IE1 to IE5). Whereas the pump with 60 % efficiency was rated as average and gradually increased to very high-VH as the energy consumption in the pumps decreased and the motors' energy efficiency classes increased. The impeller draws and throws a large scale of fluid during its rotation, and that results in the generation of axial and radial force in the impeller. These may result in imbalance, noise creation, and reduce the life of the centrifugal pump. V. Godbole et al. [5] concluded that the axial thrust reduces the pump efficiency by 3.5 %. The fluid dynamic excitation at the impeller blade passing frequency mainly depends on the radial cavity space between the impeller and the volute tongue [6]. R. Barrio et al. [7] studied fluid-dynamic load induced in a centrifugal pump with a specific volute with four different impellers outer diameter (OD) by progressive trimming of preliminary

geometry of impeller. The researcher suggested 5 % to 10 % of the radial gap with respect to the impeller radius for a volute pump. G. Wegener et al. [8] suggested that the effects of hysteresis, reproducibility, surrounding environment properties, etc., should be considered while calculating the uncertainty. Using more accurate instruments, frequently calibrating them, improving the physical conditions for experiments, and enhancing the metrological process are a few recommendations for reducing these effects. S. Lorefice et al. [9] have described the traceability of calibration and uncertainty analysis for volume measurement instruments. D. W. Braudaway et al. [10] claimed that the data acquisition system had an uncertainty associated with it. The reasons for these uncertainties could be the internal resistance of the system, electrical or magnetic interferences, improper calibration, system environment, etc. Hence, a simple method to account for these uncertainties was described by the authors [10].

The objective of the present work is to carry out experiments on a centrifugal pump with ISO 9906 (grade 1) standard setup and analyze the obtained performance curves based on experimental readings. The developed test setup is used for measuring the flow rate (Q), net head (H), torque (T), speed (N), and net positive suction head (NPSHr) of the centrifugal pump. The outline of this paper is as follows. At first, the experimental set-up and instrumentation are described, followed by results and discussion based on the obtained performance curves of the selected centrifugal pump.

2 Experimental setup and instrumentation

The grade one accuracy experimental test setup of measuring capacity up to 15hp power input, 100 m^3/hr of flow, and 50 meters of the head with net positive suction head measurement is developed at the institute laboratory as shown in Figure 1. The selection of instruments, preparation of layout, and structure are as per standard [2].

The selection of design inputs of centrifugal pump data is decided based on a survey of the most widely used pumps for different applications. As a result, the 38-meter head, 50 m^3/hr flow rate, and 2980 rpm speed pump design data (7.5 hp) are chosen.

Figure 1: Centrifugal pump test setup.
Source: own, RGD lab, Department of Mechanical Engineering, S.V.N.I.T.- Surat.

Table 1: Design parameters of centrifugal pump

Parameter	Value
Impeller suction eye diameter, D_1 (mm)	80
Impeller outlet diameter, D_2 (mm)	172
Impeller outlet width, b_2 (mm)	19
Impeller blade inlet angle, β_1 (°)	24
Impeller blade outlet angle, β_2 (°)	36
Impeller blade wrap angle, φ (°)	127
Impeller blade number, Z (nos.)	6
Impeller blade thickness, δ (mm)	4
Volute base diameter, D_3 (mm)	189
Volute inlet width, b_3 (mm)	24
Volute tongue angle, φ_o (°)	24
Volute outlet diameter, D_d (mm)	65

Source: own

A radial flow single-stage impeller pump is the best suited for this range. One-dimensional design methodology is used for the initial selection of design data. The impeller and volute of the centrifugal pump are designed based on meridional plane velocity and constant velocity methods, respectively. The main geometric parameters of the impeller and volute are shown in Table 1. The geometrical model of the single-stage radial flow centrifugal pump follows ISO 2858:1975 [11].

The developed test setup is used for measuring the flow rate, net head, torque, speed, and NPSHr of the centrifugal pump. As per the literature, a centrifugal pump test setup having instruments of a high degree of accuracy with a control and data acquisition system would lead to minimum uncertainty in the results. The test setup is equipped with a variable frequency drive (VFD), Programmable Logic Controller (PLC) supported by SCADA software for automatic control, and a Data Acquisition system (DAQ) with RS 485 interface for data logging. A computer system will be connected for data storage and result plot of centrifugal pump performance. ABB makes an induction electric motor of 22 kW of capacity with 2900 rpm which is used for pump shaft prime mover. FUJI makes 30 hp capacity of variable frequency drive (VFD), which is used for maintaining constant speed or centrifugal pump. The speed of the test pump can be varied using PLC, which takes corrective action through proportional-integral (PI) control and generates a proportional 4-20 mA current signal as command output. Onyx makes metal bellow coupling which is used to transmit torque from drive end to driven end. The bellow coupling with zero-backlash and tight design tolerance allows transmitting torque with zero slip. The coupling can allow radial, axial, and angular misalignments up to 200 microns, 500 microns, and 1.5 degree, respectively. Test bed frame is made from c section channel and fitted on a concrete structure with the help of a U-shaped foundation bolt. Accurate taping hole is provided on the test frame for inline assembly of the pump, torque transducer, and electric motor. Honeywell VBA type flanged mounted tow-way ball valves are used for modulating control of flowing fluid in suction and discharge pipelines. They are regulated by 0-10 mV analog signals through a programmable logic controller (PLC). The modulating control is used for the percentage-wise opening and closing of the valve. The frictional loss of a flowing fluid is proportional to the flow area. As a result, one commercial size larger is chosen for suction and discharge lines, i.e., 6-inch and 4-inch, resulting in lower frictional losses. The effective lengths of the suction and discharge pipes are 12 and 18 meters, respectively. A Hollow mesh structure type pipe is used for the discharge flow line in the sump, affecting in reducing the swirl effect of water flow and minimizing water recirculation in the sump. The pumping fluid is contained in RCC made sump size of 8×4×3 cube meter and separated by a thin separation wall for suction and discharge fluid. The distance between the suction pipe and the discharge pipe submerged in two tanks is 5 meters to minimize fluid flow disturbances passing from the discharge to the suction tank. PLC will centrally control the centrifugal

pump testing. User interference for the operation and control of the pump test is provided by SCADA software installed on a computer.

The Adept MagFlow 6410 type electromagnetic flowmeter with a measuring range of 0.2 m/s to 12 m/s is installed through a flanged end connection joint in the discharge line. It has an output signal of 4 mA to 20 mA with a response time of less than 100 mSec, and accuracy is ± 0.3 % of the measuring value. The upstream and downstream distance from the flowmeter is kept at ten times and fifteen times of internal pipe diameter for the stability of fluid flow in the horizontally mounted piping system. The FKP and FKH type vacuum and pressure transducers, manufactured by Fuji, are installed at the suction and discharge flow lines, respectively, and have a span range of -1 bar to 1.3 bar and 0.3125 bar to 5 bar. The transducers have low response time, high accuracy ±0.1 % for FKP, and ±0.2 % for FKH for all calibrated span, stability, and performance over the operating range of pressure and temperature. The span is adjusted with calibration of the output signal in 4-20 mA. the Magtrol makes TMB 310; an inline torque transducer worked on the strain gauge principle is used. It measured the torque by non-contact differential transformer torque measuring technology. It has an accuracy of < ±0.1 % and less response time. This instrument has (0 to 50 N. m) measuring span for torque, and rpm is up to 4000. The integrated electronic circuit, supplied by a single DC voltage (VDC), provides torque and speed signals without any additional amplifier. The conditioning electronic circuit incorporated in the transducer converts the voltage to a nominal torque signal of 0 to ± 5 VDC and sends it to PLC as an analogue input signal. The level transmitter and RTD are mounted on the sump. The contact type capacitance level transmitter is used for sump water height level measurement during the testing of the pump. It has an accuracy of ± 0.5 % of full scale with 5 mm of resolution.

A single stage 7.5 hp centrifugal pump is designed, developed, and tested with an experiment test rig. The methodology to carry out performance test of centrifugal pump is represented by flow chart as shown in Figure 2. By throttling the discharge valve of the pump discharge line, the volumetric flow rate can be controlled. A fully open valve has maximum flow, whereas a reduction in flow is achieved with a partially closed valve. Whereas speed variation is done with VFD.

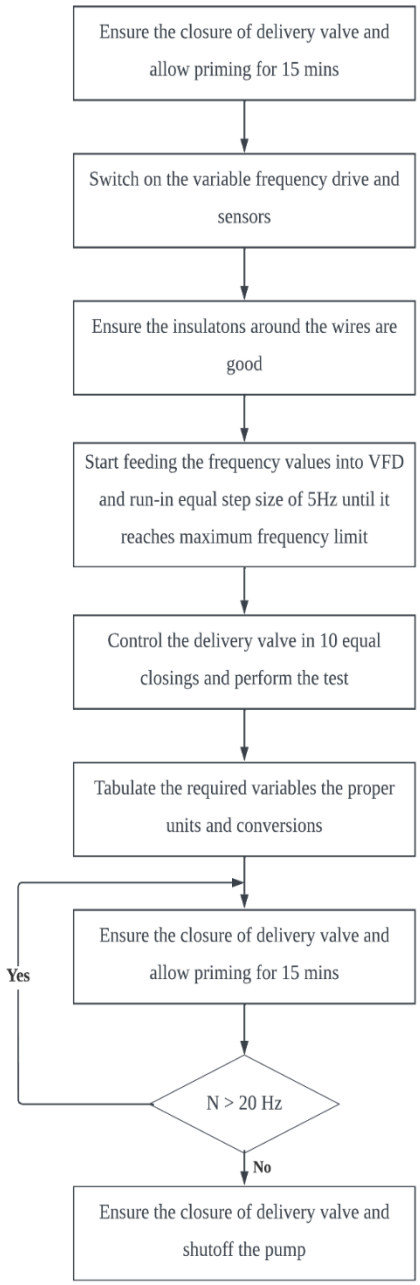

Figure 2: Testing methodology for experimental analysis of centrifugal pump.
Source: own

3 Results and discussion

For experiment analysis developed grade 1 pump setup is used. Initially, the experiment is carried out at a rated speed of the pump for a minimum to maximum mass flow rate conditions, i.e., shutoff to full open condition of discharge valve. After satisfactory results and analysis, the same procedure is applied for the other speed range, i.e., from 45 Hz to 25 Hz in the interval of 5 Hz. The repeatability of the experimental setup is also checked. The non-dimensional performance curves are plotted based on obtained readings at different speed for different mass flowrate.

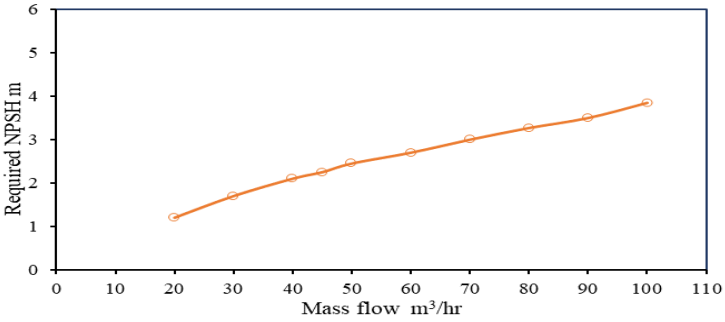

Figure 3: NPSH curve for 50 HZ speed.
Source: own

First, the NPSHr test is performed to determine whether cavitation is possible. The testing method of the 3 % drop in the head is followed to measure the NPSH-R for the tested centrifugal pump. Figure 3 depicts the NPSHr test results for 50 Hz speed. NPSHr tests have been performed for the flow of 20 m^3/hr to 100 m^3/hr. By maintaining these flow rates at a constant level, the suction valve is throttled till there is a pressure head drop of 3 %. The NPSHr is recorded as 2.25 m, 2.70 m, and 3.50 m for the flow rate of 45 m^3/hr, 59 m^3/hr, and 92 m^3/hr, respectively. Comparatively, both the values are below the NPSH available, and this pump is less prone to cavitation. Friction loss calculation suggests the effective total head loss at maximum flow, duty point flow, and lowest possible flow are 2.80 m, 1.11 m, and 0.16 m, respectively for the present test setup. The overall uncertainty in measured pump efficiency is ± 0.63 %, ±0.72 %, and ±1.54% for duty flow, highest flow, and lowest flow measuring data, respectively. Whereas; relative uncertainty in efficiency is in the range of ±0.010 % (Duty point), which is quite lower. The lower value of

absolute and relative uncertainties in the measurement of efficiency, torque, flow, and total head parameters will satisfy the requirements of the grade 1 setup as per standards.

The performance characteristics curves are plotted in a non-dimensional form as shown in Figure 4 and Figure 5. The variations of head coefficient (ψ) for different speeds ranging from 50 Hz to 25 Hz are plotted for different flow coefficients (ϕ) as shown in Figure 4. The obtained nature of ψ – ϕ curves agreed well with the theoretical performance curve. One can observe the maximum head coefficient at (discharge valve) shut-off conditions, which decreases with the opening of a discharge valve, i.e., an increase in flow coefficient. Figure 4 also reveals that for a constant value of flow coefficient, the head coefficient increases as we increase the speed of the pump by varying frequency from 25 Hz to 50 Hz up to the 0.225 flow coefficient. For flow coefficient values greater than 0.225, head coefficients are high at the low speed of the pump. This is due to the significant fluid frictional losses within the pump at high speed and higher mass flow rate due to unaccounted secondary eddies and turbulence. The operational range of the current pump is anticipated up to the flow coefficient value of 0.225.

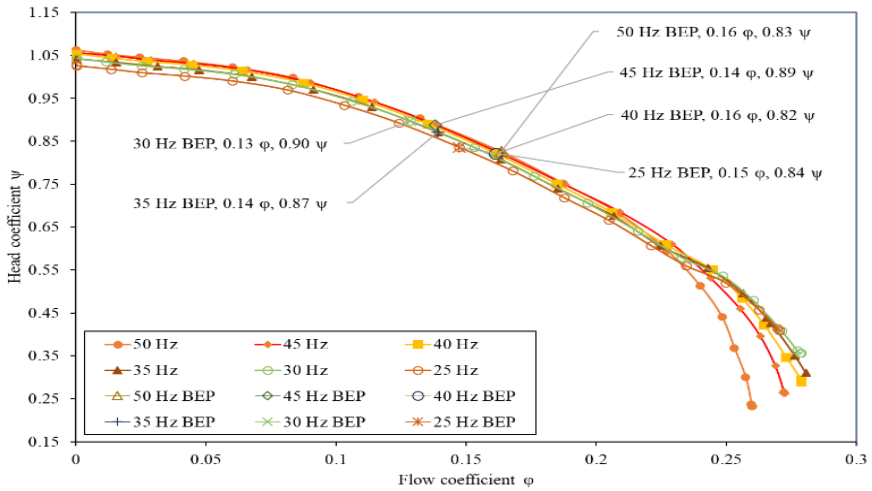

Figure 4: Variations in head coefficient for different flow coefficient.

Source: own

Figure 5 represents the graph of pump efficiency (η) vs. flow coefficient (ϕ) for the full range of experiments. It also reveals good agreement with the available theory of the centrifugal pump performance curve. The best efficiency points (BEP) are identified at various speeds of the pump based on the highest efficiency of a curve, and the value of the flow coefficient as well as the head coefficient is calculated at this point. Table 2 reveals the details of ψ, ϕ, and η at BEP for different speeds of the centrifugal pump. The head coefficient at BEP varies from 0.90 to 0.82, and the flow coefficient from 0.13 to 0.16. The greatest efficiency is obtained at 50 Hz and declines progressively with decreasing speed. Pump efficiency at the BEP ranges from roughly 66 % to 63 %, depending on pump operating speed.

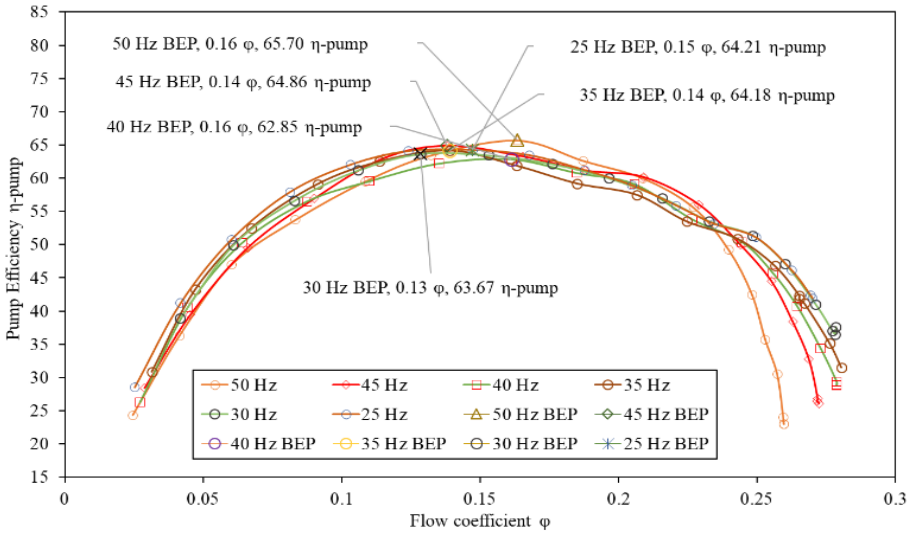

Figure 5: Variations in efficiency for different flow coefficient

Source: own

Table 2: Experimental head coefficient, flow coefficient, and pump efficiency at BEP

Speed, Hz	Head coefficient, ψ	Flow coefficient, ϕ	Pump efficiency, %
50	0.83	0.16	65.70
45	0.89	0.14	64.86
40	0.82	0.16	62.85
35	0.87	0.14	64.18
30	0.90	0.13	63.67
25	0.84	0.15	64.21

Source: own

4 Conclusions

In this work, the experimental analysis of a single-stage centrifugal pump with a power input capacity of 7.5 horsepower, a head of 38 meters, a flow rate of 50 cubic meters per hour, and a speed of 2980 rpm is carried out. The following conclusions are derived from the results.

1. The ISO 9906 grade 1 established centrifugal pump test configuration yields uncertainty observed values within allowable limits of ± 2.9%.
2. For the chosen centrifugal pump, the experimental BEP head coefficient, flow coefficient, and efficiency range from 0.82 to 0.90, 0.13 to 0.16, and 66% to 63%, respectively.

References

[1] Bureau of Indian Standards (1993), IS 13538, Centrifugal, Mixed Flow and Axial Pumps-Code for Hydraulic Performance Tests-Precision Class

[2] ISO 9906: (2012), Rotodynamic pumps - Hydraulic performance acceptance tests - Grades 1, 2 and 3. United Kingdom: British standard, ttps://www.iso.org/standard/41202.html

[3] ANSI-HI-1.6 (2000), Centrifugal Pump Test

[4] de Souza D. F., E. L. A. da Guarda, Sauer, I. L. and Tatizawa H. (2021), Energy Efficiency Indicators for Water Pumping Systems in Multifamily Buildings, Energies (Basel), 14 (21), pp. 1-13, doi:10.3390/en14217152

[5] Godbole V., Patil R., and Gavade S. S. (2012), Axial Thrust in Centrifugal Pumps - Experimental Analysis, 15th International Conference on Experimental Mechanics, vol. 1, p. 14

[6] Barrio R., Blanco E., Parrondo J., Gonzalez J. and Fernandez J. (2008), The Effect of Impeller Cutback on the Fluid-Dynamic Pulsations and Load at the Blade-Passing, Journal of Fluids Engineering, vol. 130, pp. 1–11, doi:10.1115/1.2969273

[7] Spence R. and Amaral-Teixeira J. (2008), Investigation into Pressure Pulsations in a Centrifugal Pump Using Numerical Methods supported by Industrial Tests, Computers & Fluids, 37 (6), pp. 690–704, doi:10.1016/j.compfluid.2007.10.001

[8] Wegener G. and Andrae J. (2007), Measurement Uncertainty of Torque Measurements with Rotating Torque Transducers in Power Test Stands, Measurement, 40 (7–8), pp. 803–810, doi:10.1016/J.MEASUREMENT.2006.08.001

[9] Lorefice S. (2009), Traceability and Uncertainty Analysis in Volume Measurements, Measurement: Journal of the International Measurement Confederation, 42 (10), pp. 1510–1515, doi:10.1016/J.MEASUREMENT.2009.07.016

[10] Braudaway D. W. (2006), Uncertainty Specification for Data Acquisition (DAQ) Devices, IEEE Transactions on Instrumentation and Measurement, 55 (1), pp. 74–78, doi:10.1109/TIM.2005.862014

[11] ISO 2858:1975 (2017) - End-suction centrifugal pumps (rating 16 bar) — Designation, nominal duty point and dimensions, Switzerland: International Organization for Standardization, https://www.iso.org/standard/7862.html

Experimental Investigation of Ultrasonic Cavitation Erosion: Implications for Water Turbines and Hydraulic Machinery

Luka Kevorkijan, Tilen Jernejc, Luka Lešnik, Ignacijo Biluš

University of Maribor, Faculty of Mechanical Engineering, Maribor, Slovenia
luka.kevorkijan@um.si, tilen.jernejc@um.si, luka.lesnik@um.si, ignacijo.bilus@um.si

Cavitation erosion is a major concern in water turbines and hydraulic machinery, where bubble collapse near solid surfaces leads to material degradation and reduced efficiency. In this study, ultrasonic cavitation tests were conducted using a Sonics VCX-750 ultrasonic vibratory apparatus operating at 20 kHz to investigate erosion behaviour of aluminium and steel specimens under identical conditions. The sonotrode tip was submerged 30 mm below the water surface, with amplitude of 30 μm and fluid temperature maintained at 17 °C. High-speed imaging at 100,000 frames per second captured bubble dynamics. After 3 hours of exposure, surface photographs revealed significantly more extensive erosion on aluminium compared to steel, demonstrating higher resistance of the latter to cavitation. The results highlight the importance of material selection in hydraulic applications and provide insights into cavitation mechanisms relevant to the durability and performance of water turbines.

DOI
https://doi.org/10.18690/um.fs.7.2025.23

ISBN
978-961-299-049-7

Keywords:
cavitation erosion, hydraulic machinery, ultrasonic cavitation, water turbines, material selection

University of Maribor Press

1 Introduction

Cavitation is a critical phenomenon in hydraulic machinery such as water turbines, pumps, valves and marine propellers, where rapid pressure fluctuations cause the formation and violent collapse of vapor bubbles. The implosion of these bubbles near solid surfaces generates intense micro-jets and shock waves, leading to material damage known as cavitation erosion. This degradation not only shortens the service life of components but also reduces efficiency and reliability, resulting in significant operational and maintenance costs. Understanding cavitation erosion mechanisms is therefore essential for improving the durability and performance of hydraulic systems.

Experimental studies of cavitation in full-scale water turbines are challenging due to the complexity of flow conditions, high costs, and limited accessibility for in-situ observations. Consequently, laboratory-scale methods are widely employed to simulate cavitation and to evaluate material resistance under controlled conditions. Among these, ultrasonic vibratory cavitation testing using a sonotrode has become a standardized and effective approach for accelerated erosion assessment. The ultrasonic method creates highly localized cavitation zones, enabling systematic analysis of bubble dynamics, erosion mechanisms, and comparative material performance. In addition to erosion quantification, the visualization of cavitation plays an important role in linking laboratory experiments to real hydraulic applications. High-speed imaging provides insight into the formation, collapse, and spatial distribution of cavitation bubbles, which closely resemble the microscale processes occurring inside hydraulic machinery, for example turbine blades or valve gates under cavitating flow.

Numerous studies have sought to understand cavitation erosion in hydraulic machinery through both field observations and laboratory investigations. Field measurements on turbines and pumps have provided valuable evidence of erosion patterns, typically concentrated near runner blades, guide vanes, and draft tubes where pressure fluctuations and vortex structures are most intense [1], [2], and [3]. However, the complexity of large-scale flows has limited the ability to directly correlate bubble dynamics with erosion mechanisms. To overcome these challenges, researchers have turned to model testing and accelerated laboratory techniques.

Recently computational approaches to predict erosion from CFD simulations have emerged as complementary approach to experimental approaches.

Ultrasonic vibratory cavitation testing has been widely adopted as a standardized method (ASTM G32) for laboratory scale material erosion assessment [4]. This technique enables the generation of stable cavitation zones, allowing systematic evaluation of erosion rates and material degradation. Previous works have focused on identifying material parameters which influence material response to cavitation – cavitation erosion. Franc [5] proposed a model which describes cavitation erosion of work-hardening materials. Cavitation aggressiveness in ultrasonic cavitation was studied by Du and Chen [6] by combining experimental approaches with CFD simulations, showing that microstructural features such as hardness, grain size, and phase distribution strongly influence erosion. In a more material focused experimental study, Ye et al. [7], observed the material response, particularly change in Vickers hardness. High-speed visualization studies have further revealed the role of transient bubble collapses and micro-jets in initiating and propagating surface damage [8]. Despite these advances, most studies focus on quantitative erosion rates, with fewer works linking observed bubble dynamics to material-specific erosion mechanisms in a way that directly connects laboratory testing to hydraulic machinery.

The present study investigates cavitation erosion using an ultrasonic sonotrode under controlled laboratory conditions. High-speed imaging was employed to capture cavitation dynamics. Erosion was observed on aluminium and steel samples to examine and differentiate material-specific erosion patterns. The experimental findings are discussed in the context of hydraulic machinery.

2 Methods

Cavitation erosion experiments were conducted using an ultrasonic vibratory apparatus (Sonics VCX-750) operating at the standard frequency of 20 kHz. The sonotrode tip was positioned 30 mm below the free surface of tap water in a transparent test tank. The vibration amplitude was set to 25 % of the maximum rated amplitude of the device, which resulted in approximate amplitude of 30 μm. The water temperature was maintained at 17 °C using an additional closed-loop cooling system to ensure consistent operating conditions throughout the test.

Experimental setup for investigation of ultrasonic cavitation erosion at the Turbomachinery Laboratory of the Faculty of Mechanical Engineering, University of Maribor is shown in Figure 1.

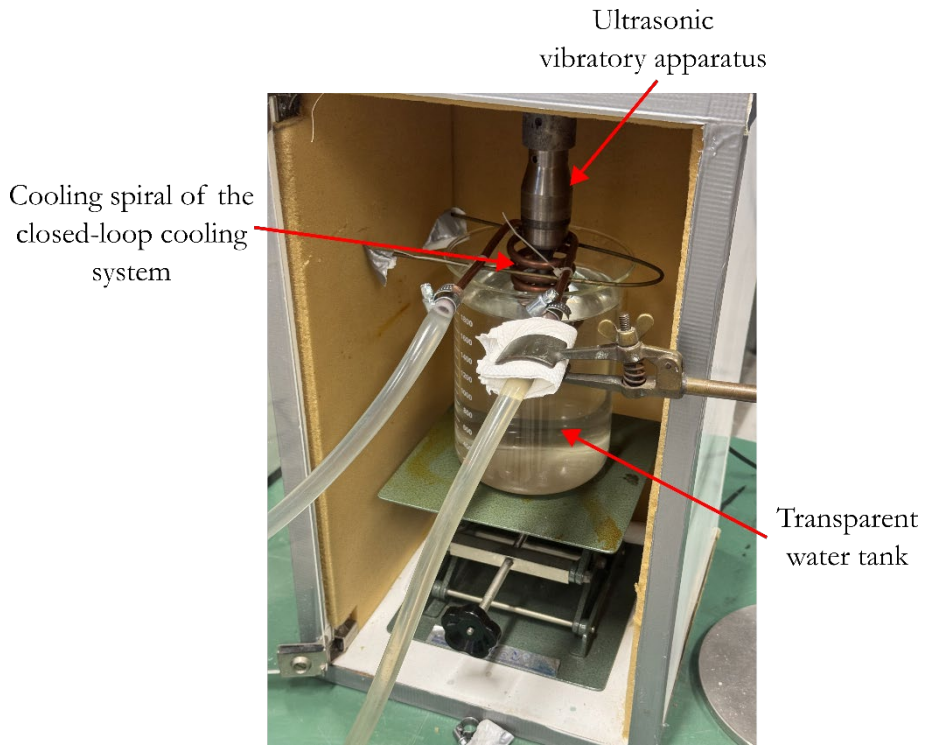

Figure 1: Experimental setup for investigation of ultrasonic cavitation erosion.

Two metallic materials, aluminium and steel, were selected as test specimens. Test specimens were produced as replicable threaded tips for the sonotrode with 13 mm in diameter, shown in Figure 2. Both materials were subjected to identical cavitation conditions. Each test was run for a total duration of 3 hours, after which the specimens were removed for surface examination. The identical test conditions allowed a direct comparison of erosion behaviour between the two materials.

High-speed imaging was employed to observe cavitation activity in the vicinity of the sonotrode with the setup shown in Figure 3.

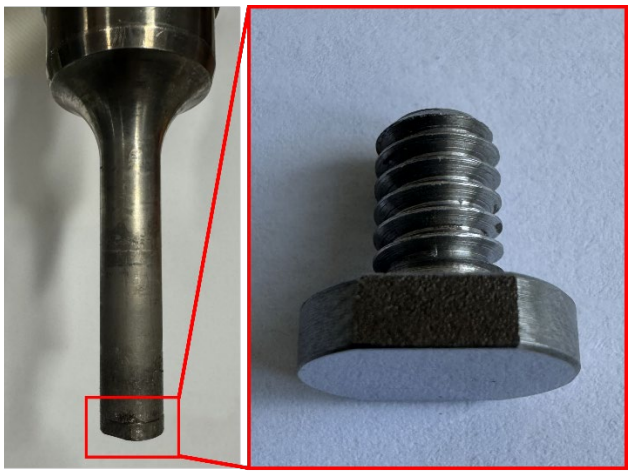

Figure 2: Ultrasonic vibratory apparatus tip: a) view of the full vibrating apparatus with replaceable tip, b) replaceable threaded tip used as sample to study cavitation erosion, displayed is steel tip.

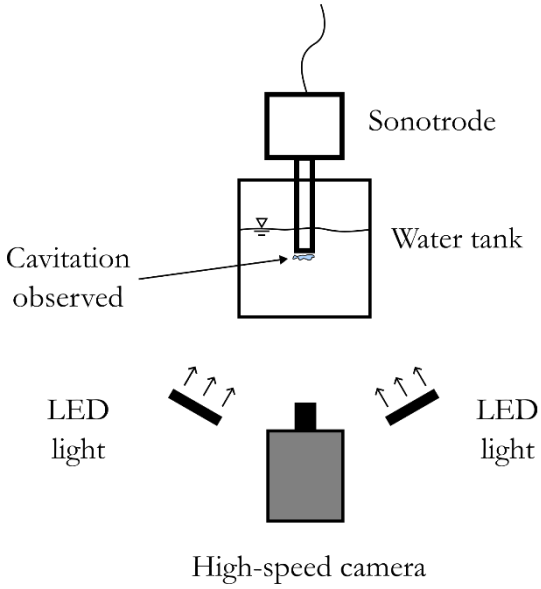

Figure 3: Schematic view of experimental setup for high-speed filming.

A Photron Fastcam SA-Z high-speed camera was used, recording at 100,000 frames per second. Illumination was provided by GSVITEC Multiled LED lights (GSV_G8_KIT) with a correlated color temperature of 6500 K and a luminous flux of 12,000 lumens, ensuring sufficient lighting.

After testing, the eroded surfaces of the aluminum and steel specimens were documented by photography. These images provide a qualitative assessment of erosion patterns and damage characteristics, which are then related to the cavitation dynamics observed in the high-speed recordings.

The chosen materials are directly relevant to hydraulic machinery: steel is traditionally used for turbine runners and hydraulic components due to its strength and durability, while aluminium alloys are increasingly considered as alternatives in certain applications because of their low weight and manufacturability. Comparing their cavitation erosion response under identical laboratory conditions therefore offers insights into material selection and long-term performance in water turbines and other hydraulic systems.

3 Results

First, we present the results of high-speed filming of acoustic cavitation phenomenon in Figure 4 where pictures covering one full cycle are shown (peak-to-peak movement of the sonotrode tip). High-speed recordings revealed the formation of dense cavitation clouds at the sonotrode tip. The bubble dynamics were characterized by rapid growth and collapse cycles, consistent with the periodic pressure oscillations at 20 kHz. Bubble collapses were frequently observed close to the specimen surfaces (see Figure 4 e and f for example), producing localized high-intensity events. We can see two distinct cavitation zones. The first zone features larger cavitation structures (macroscopic bubbles) attached to the sample surface in a band near the circular edge of the sample (pointed out on Figure 4 a) outline drawn with red dotted line). The second zone features a narrow column of microscopic bubbles extending radially from the axis of tip movement and bellow the tip towards the bulk liquid (pointed out in Figure 4 b).

The zone of attached larger cavitation structures corresponds well to the area of maximum erosion observed on the samples as shown in Figure 5. These observations are consistent with previously reported mechanisms of micro-jet and shock wave formation during bubble implosion which are most erosive when cavitation is in proximity with the solid surface and recognized as primary causes of cavitation erosion in hydraulic machinery.

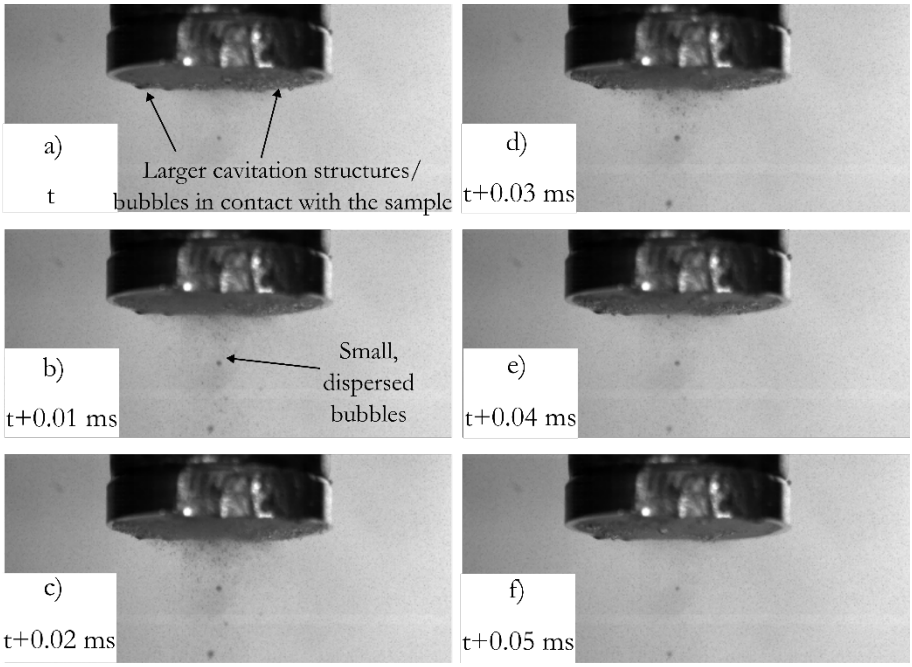

Figure 4: Results of filming with high-speed camera. From a) through f) a full cycle (peak-to-peak amplitude) of sonotrode tip movement is shown with cavitation structures pointed out.

However, some differences can be observed between aluminium and steel samples, particularly when looking at the state of the surface at intermediate time (60 minutes of exposure). In the case of aluminium, pronounced surface damage was visible already after 60 minutes, characterized by extensive pitting and roughening of the surface, particularly larger pits can be seen in Figure 5 c). Then at final time of 180 minutes, the material exhibited a relatively large eroded area, suggesting lower resistance to cavitation.

In contrast, the steel specimen showed only small pits after 60 minutes of exposure. After 180 minutes more localized damage, with distinct larger pits can be seen. In comparison to aluminium sample after same duration of exposure, less overall surface degradation is visible. These differences indicate that steel exhibits a higher intrinsic resistance to cavitation erosion under the tested conditions.

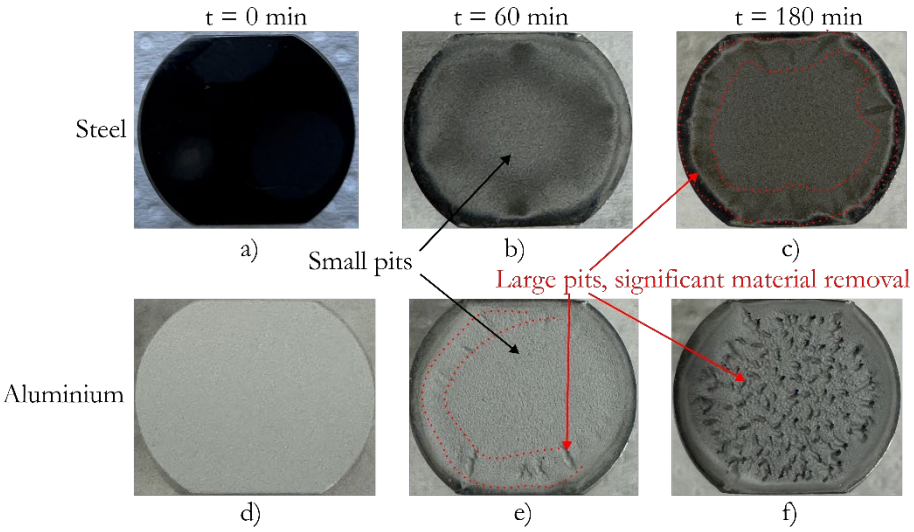

Figure 5: Steel and aluminium samples shown at various times: a) and d) before exposure to cavitation, b) and e) after 60 minutes exposure to cavitation and c) and f) after 180 minutes exposure to cavitation.

The results highlight the critical role of material selection in mitigating cavitation erosion in water turbines and other hydraulic components. While steel remains the conventional choice for turbine runners and guide vanes due to its durability, aluminium alloys are being considered for certain applications where reduced weight and ease of manufacturing offer advantages. However, the present findings indicate that aluminium is significantly more susceptible to cavitation damage under identical operating conditions, which may limit its applicability in erosion-prone regions of hydraulic machinery. High-speed visualization provided further insight by linking the bubble collapse dynamics to observed surface damage, thus bridging laboratory-scale testing with real cavitation erosion mechanisms in turbines.

4 Conclusion

Overall, the combined use of ultrasonic cavitation testing, high-speed imaging, and post-test surface inspection provided a comprehensive picture of cavitation erosion processes. The study reinforces the importance of material resistance in prolonging the service life of hydraulic machinery and underscores the value of laboratory testing for predicting field performance.

Acknowledgments

The authors acknowledge the financial support from the Slovenian Research Agency (research core funding No. P2-0196).

References

[1] Brennen, C. E. (1995). *Cavitation and Bubble Dynamics*. Oxford University Press.
[2] Franc, J. P., and Michel, J. M. (2004). *Fundamentals of Cavitation*. Kluwer Academic Publishers, Dordrecht.
[3] Avellan, F. (2004). Introduction to Cavitation in Hydraulic Machinery. Presented at the 6th International Conference on Hydraulic Machinery and Hydrodynamics, Timisoara, Romania, October 21-22, 2004.
[4] ASTM G32-16. "Standard Test Method for Cavitation Erosion Using Vibratory Apparatus." ASTM International, West Conshohocken, PA, 2016.
[5] Franc, J. P. (2009). Incubation Time and Cavitation Erosion Rate of Work-Hardening Materials. *Journal of Fluids Engineering*, 131, 021303. doi: 10.1115/1.3063646
[6] Du, J., and Chen, F. (2021). Cavitation dynamics and flow aggressiveness in ultrasonic cavitation erosion. *International Journal of Mechanical Sciences*, 204, 106545. doi: 10.1016/j.ijmecsci.2021.106545
[7] Ye, L., Zhu, X., Wei, X., and Wu, S. (2020). Damage characteristics and surface description of near-wall materials subjected to ultrasonic cavitation. *Ultrasonics – Sonochemistry*, 67, 105175. doi: 10.1016/j.ultsonch.2020.105175
[8] Reuter, F., Deiter, C., and Ohl, C.-D. (2022). Cavitation erosion by shockwave self-focusing of a single bubble. *Ultrasonics Sonochemistry*, 90, 106131, doi: 10.1016/j.ultsonch.2022.106131

Improving Energy Efficiency Through Using Modern Hydraulic Oil

Aleš Hrobat,[1] Jošt Mohorko,[1] Vito Tič,[2]
Milan Kambič[1]

[1] Olma d.o.o., Ljubljana, Slovenia
ales.hrobat@olma.si, jost.mohorko@olma.si, milan.kambic@olma.si
[2] University of Maribor, Faculty of Mechanical Engineering, Maribor, Slovenia
vito.tic@um.si

The service life of hydraulic oil is significantly influenced by operating conditions as well as by its composition. Manufacturers have access to different groups of base oils for the production of hydraulic fluids. Due to the varying properties of these groups, the service life of the final product also varies. This article discusses hydraulic oils according to different groups of base oils, their basic characteristics, and the differences between them. Furthermore, it introduces the new series of Energolubric hydraulic oils, focusing on extended service life compared to conventional mineral-based hydraulic oils. Results of comparative testing on oxidation stability of various oils will be presented. The article will also address the aspect of energy efficiency in hydraulic system operation, which is also influenced by the choice of hydraulic oil.

DOI
https://doi.org/10.18690/um.fs.7.2025.24

ISBN
978-961-299-049-7

Keywords:
hydraulic oil,
base oils,
oxidation stability,
energy efficiency

University of Maribor Press

1 Introduction

Base oils are the fundamental component of lubricants and hydraulic fluids and are classified into five major groups according to production method and physicochemical properties:

- Group I: Mineral base oils obtained through conventional refining techniques such as solvent extraction and distillation. They exhibit lower oxidation stability and higher levels of impurities compared to higher groups.
- Group II: More refined mineral oils produced by hydrocracking, offering improved properties such as greater oxidation resistance and longer service life.
- Group III: Highly refined mineral oils processed via hydrocracking and isomerization, which closely approach the performance of synthetic oils.
- Group IV: Synthetic oils based on polyalphaolefins (PAOs), characterized by excellent oxidation stability, low volatility, and a wide temperature operating range.
- Group V: All other base oils not included in Groups I–IV (e.g., esters), typically used in specialized applications due to exceptional lubricity and thermal stability.

Each base oil group has its own advantages and limitations, which directly affect the performance characteristics of the final hydraulic fluid. Choosing the appropriate base oil is essential for achieving optimal performance and extended service life in hydraulic systems [1] to [4].

The extension of service life for mineral-based hydraulic oils is closely related to their oxidation stability. Oxidation leads to the formation of acids, varnish, and other degradation products that can negatively affect system performance. The use of highly refined mineral oils or synthetic alternatives with advanced antioxidant formulations can significantly slow down this process, resulting in longer oil change intervals and reduced maintenance costs [2], [4].

In addition, hydraulic oil plays a crucial role in the energy efficiency of hydraulic systems. Its formulation and viscosity influence frictional losses, energy dissipation, and system temperature. Fluids with lower viscosity at low temperatures and stable viscosity-temperature characteristics at high operating temperatures contribute to reduced energy consumption and improved system efficiency.

Consequently, the industry is increasingly adopting hydraulic oils based on higher-group base oils and containing advanced additive technologies that enhance oxidation stability and energy efficiency. A relevant application example is the plastic injection moulding industry.

Plastic injection moulding machines are energy-intensive, requiring heating of the material, operation of hydraulic drives, and cooling. Monitoring energy consumption allows [5]:

- Real-time consumption tracking – identifying peak energy use during start-up, operation, standby, or shutdown phases.
- Injection cycle analysis – comparing consumption across different moulds or products to assess process efficiency.
- Cost-per-part evaluation – calculating energy use per production cycle to support cost analysis and pricing strategies.
- Detection of anomalies – sudden increases in energy consumption may indicate mechanical failures, inadequate maintenance, or operational changes.
- Optimization opportunities – for example, identifying high idle-time consumption may justify implementing automatic energy-saving modes or reducing system pressure during standby.

2 Oxidation stability – a key performance parameter for long-life hydraulic oils

Oxidation stability is a critical property of hydraulic fluids, especially in demanding industrial applications where long service life, system reliability, and cost-efficiency are of paramount importance. Oxidation refers to the chemical reaction between the oil and atmospheric oxygen, which is accelerated at elevated temperatures, in the presence of catalytic metal contaminants (e.g., copper, iron), or in systems where moisture ingress occurs.

This degradation leads to the formation of a variety of harmful by-products, including organic acids, sludge, varnish, and insoluble compounds. These products can cause filter plugging, valve sticking, increased wear, and changes in oil viscosity–ultimately reducing the efficiency and reliability of the hydraulic system. In

severe cases, oxidation-induced deposits may result in unplanned downtime, expensive repairs, and reduced equipment life.

The oxidation stability of a hydraulic oil is strongly influenced by the type and quality of the base oil used, as well as by the formulation and performance of the antioxidant additive system. Oils formulated with highly refined Group II or Group III base stocks–or with fully synthetic Group IV (PAO) base oils–exhibit superior oxidation resistance due to their low content of unsaturated hydrocarbons and impurities. Synthetic base oils also provide enhanced thermal stability and volatility characteristics.

To further inhibit the oxidation process, carefully selected antioxidants are incorporated into the formulation. Over time, however, antioxidant levels deplete, which is why oxidation stability is also a key indicator of oil life. These improvements extend service intervals, reduce oil change frequency and waste oil generation, and lower maintenance and filter replacement costs. At the same time, system reliability increases and the risk of unplanned downtime decreases. In summary, proper oil selection and an understanding of oxidation stability have a direct impact on the efficiency, safety, and cost-effectiveness of hydraulic system operation.

The oxidation stability of various ISO VG 46 hydraulic oils was evaluated using the RapidOxy 100 instrument (Figure 1).

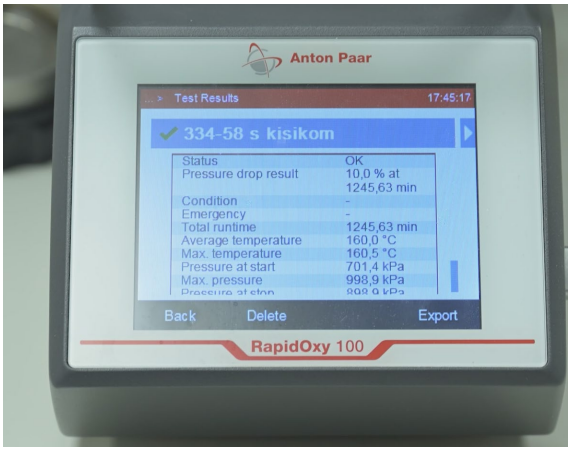

Figure 1: RapidOxy 100 instrument for measuring oxidation stability of oils.
Source: own

RapidOxy 100 is a modern laboratory instrument designed for fast and reproducible determination of the oxidation stability of lubricants, fuels, and other organic materials. It is based on the accelerated aging method under elevated pressure and temperature, in which the pressure drop of oxygen (or synthetic air) in a sealed chamber containing the sample is continuously monitored.

Compliant with ASTM D8206 and DIN 51466 standards, the instrument measures the oxidation induction time (OIT)—defined as the time it takes for the pressure in the chamber to drop by a defined percentage (typically 10 %) from its initial value. This parameter is a reliable indicator of oxidation resistance and, by extension, the expected service life of the oil. The measurement procedure includes the following steps:

- A small sample (approximately 5 mL) is carefully measured and placed into the steel pressure chamber of the instrument.
- The chamber is sealed and pressurized with pure oxygen or synthetic air to about 700 kPa.
- The sample is heated to a defined temperature (most commonly 140 °C), while the instrument continuously monitors the pressure drop.
- The test ends when the pressure has decreased by 10%; the elapsed time is recorded as the test result (OIT in minutes).

Advantages of the RapidOxy method include:

- Speed: the complete test is significantly faster than traditional methods (e.g., RPVOT, TFOUT), typically requiring only 1 hour to 3 hours.
- Low sample volume: suitable for R&D and high-value products where sample availability may be limited.
- Versatility: applicable to various types of oils (hydraulic, engine, compressor) and additive formulations.
- Excellent reproducibility and sensitivity: allows for reliable comparison of different formulations or production batches.

Due to its efficiency and robustness, RapidOxy 100 has become an essential tool in the development and quality control of high-performance lubricants intended for demanding industrial applications, where extended service intervals and high oxidation resistance are critical performance requirements.

The measurement results are presented in Table 1. It is evident that the oxidation stability of the Energolubric oils is significantly higher than that of all other tested oils. In some cases, the stability is more than twice as high. Given this, it is not surprising that these oils demonstrate substantially longer service life under comparable operating conditions.

Table 1: Oxidation stability of different oils

Oil name	Method	Value [min]
Energolubric 3046 ZF	ASTM D8206	1310
Energolubric 2046 ZF	ASTM D8206	1300
Energolubric 4046 ZF	ASTM D8206	1220
Energolubric 2046	ASTM D8206	1067
Hydrolubric VG 46	ASTM D8206	664
Hydrolubric HD 46	ASTM D8206	570
Hydrolubric HLP 46	ASTM D8206	529
Hydrolubric VGS 46	ASTM D8206	672
Hydrolubric HVLP 46	ASTM D8206	787
Hydrolubric VG 46 D	ASTM D8206	536

Source: www.olma.si

This improved performance directly translates into lower overall operational costs, despite the slightly higher purchase price of these oils. Extended oil change intervals, reduced maintenance frequency, and less waste oil generation all contribute to improved cost-efficiency and system reliability.

3 The impact of hydraulic oil on energy efficiency

We conducted energy consumption measurements on several plastic injection moulding machines: Krauss Maffei 1100 MX, Krauss Maffei 1150 MX, and Krauss Maffei KM 1000. On the first machine, the initial test was carried out using standard hydraulic oil (Hydrolubric VG 46), which was later replaced with the high-performance, energy-efficient oil Energolubric 2046 for a repeated test. Similarly, on the second machine, measurements were made first with Hydrolubric VG 46 HC and then with Energolubric 2046.

In both cases, energy consumption was recorded at the main power supply input to the machine, which includes all major electrical loads — most notably the hydraulic pump motor and the plasticizing heaters.

Data acquisition was conducted using Beckhoff hardware and software (Figure 2), employing the EL3443 power measurement module in combination with SCT6421 – 500 A current transformers (accuracy class 0.5). This system enables high-frequency recording (every 20 ms) of key electrical parameters, such as voltage, current, active power, and energy.

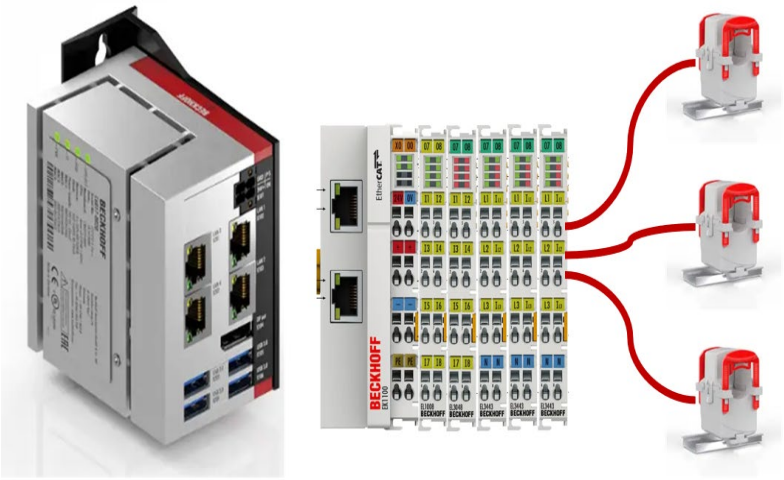

Figure 2: Beckhoff data acquisition system.

To verify consistency and ensure reliability, three separate test runs were performed for each oil type on each machine. However, analysis of the results revealed a significant limitation: measuring at the main power inlet was not the most effective or meaningful approach. The repeatability of machine operation from cycle to cycle proved to be very difficult to maintain due to several internal control loops — such as those regulating plastic temperature — where heating elements switch on and off at varying times and intensities.

This limitation is clearly illustrated in Figure 3 which shows the active energy consumption of the KM 1100 MX machine using Energolubric 2046 over three consecutive cycles, each lasting 63.0 seconds. As shown, the energy usage varies considerably from one cycle to the next. This variation makes it nearly impossible to achieve reliable, repeatable measurements with this method alone.

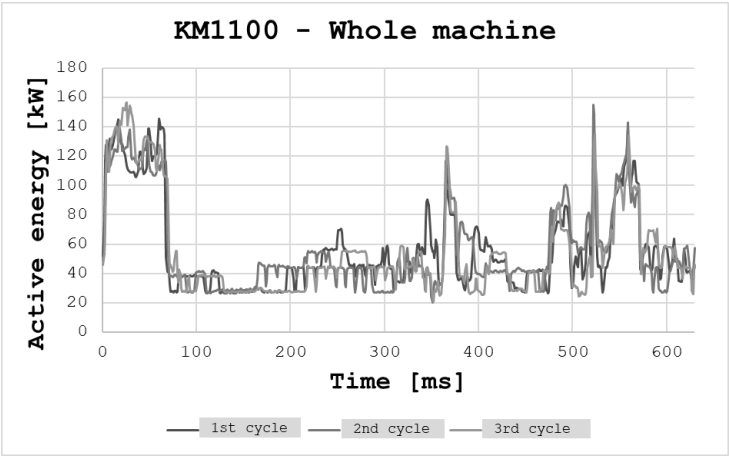

Figure 3: Comparison of three consecutive cycles measured at the main power input.

Although a detailed analysis of the active energy in individual cycles, when measuring on the main power supply, shows a strong non-repeatability of the heaters switching on, we nevertheless performed a numerical analysis of the average active electrical energy in the half-hour interval of the machine's operation. In this case, the influence of the heaters' operation is to some extent removed, since such a measurement contains their average consumption in the aforementioned half-hour interval. Table 2 shows the average active energy during operation of the KM 1100 MX machine in a 30-minute interval when using the classic hydraulic oil Hydrolubric VG 46 and the energy-saving hydraulic oil Energolubric 2046.

Although we are aware that such a measurement of consumption on the main power supply to the machine itself is not completely authoritative, the first analyses of the electricity consumption when using the energy-saving hydraulic oil Energolubric 2046 indicate certain savings of 4.3 %.

Table 2: Comparison of average active energy

KM MX 1100 (30 min interval)	Average active energy [kW]	
Hydrolubric VG 46 – 1st measurement	53.3	53.35
Hydrolubric VG 46 – 2nd measurement	53.4	
Energolubric 2046 – 1st measurement	50.7	51.05
Energolubric 2046 – 2nd measurement	51.4	

Since the measurements performed on the first two machines show promising results, we are now continuing with measurements on the hydraulic pump's drive electric motor itself, which will eliminate the effects of other energy consumers, such as heaters and others. These measurements are performed on the third KM 1000 machine, where it is planned to replace the currently used classic hydraulic oil Hydrolubric VG 46 with the energy-saving oil Energolubric 2046. The measurements are not yet complete. However, we can present the first analysis of the measurements with Hydrolubric VG 46, which confirm that the measurement results of three consecutive cycles are now much more repeatable and comparable, as shown in Figure 4.

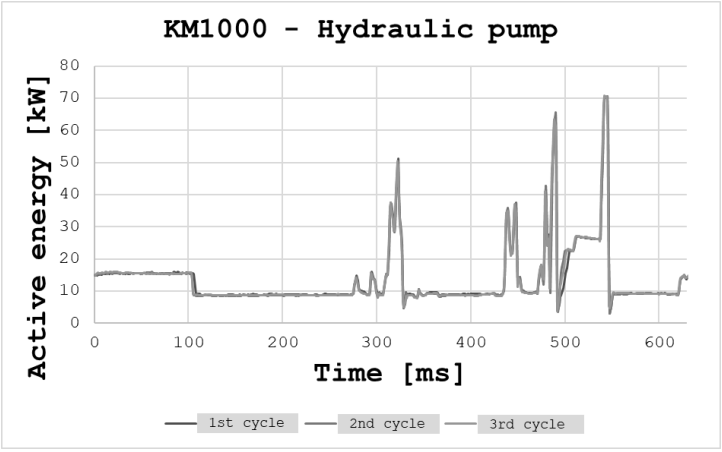

Figure 4: Comparison of three consecutive cycles measured on the drive electric motor.

We decided to perform 6 readings of electricity consumption within each measurement, namely in two consecutive cycles at the beginning of the measurement, in two consecutive cycles after 30 minutes and in two consecutive cycles after 60 minutes. The second measurement on the same machine and during the production of the same product was performed in the afternoon shift, and the third the next day in the morning shift, to determine repeatability or possible deviations between individual measurements. After the machine was used to produce another product in the following days, the fourth and fifth measurements were taken on this machine again a week later on the same product as the week before. The fourth measurement was performed in the morning shift and the fifth in the afternoon shift. The results of the first set of measurements are shown in

Table 3 and Figure 5. We can see that the differences in active power between two consecutive cycles and over a period of 30 minutes or 60 minutes are not large.

Table 3: Comparison of active energy readings of first measurement

Cycles	Avgerage active Power [kW]	Difference to previous cycle [%]	Difference to before 30 min [%]
Start_1	27.865		
Start_2	28.004	0.50	
Middle_1	27.800		
Middle_2	28.143	1.23	0.13
End_1	28.085		
End_2	28.060	-0.09	0.36
1-hour run average	**27.890**		

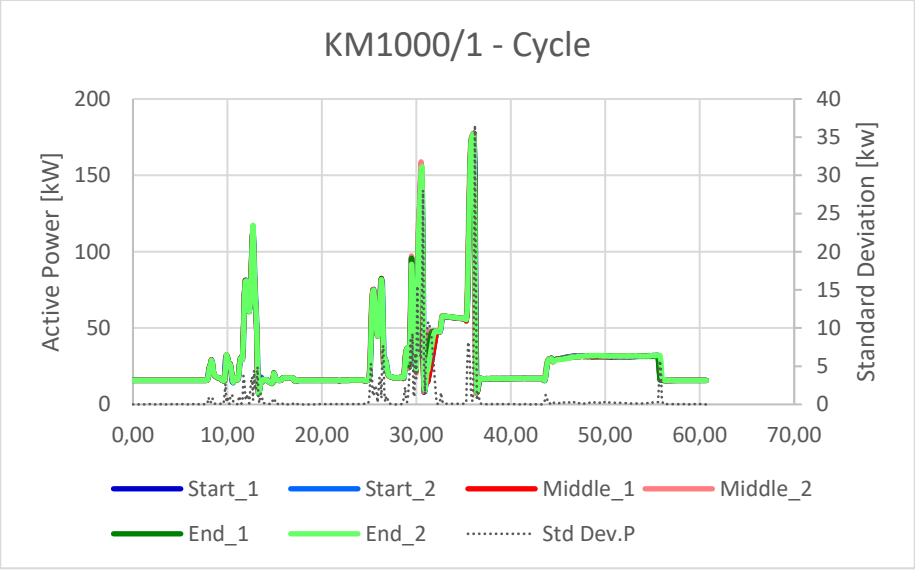

Figure 5: Comparison of active energy consumption during first measurement.

We were able to find a similar result in measurements two, three, four and five. The average active power consumption [kW] in two adjacent cycles and in cycles over a period of 30 min and 60 min is accurate or repeatable to approximately ± 1 %.

A comparison of the average active power consumption [kW] in a 1-hour interval (Table 4) demonstrates that the average active power consumption [kW] in a 1-hour interval is accurate or repeatable to approximately ± 0.4 %, i.e. under 1 % in total.

This will allow us to realistically assess whether the new oil will actually bring savings and what kind.

Table 4: Comparison of average active energy consumption of all five measurements

	1-hour run Average Active Power [kW]	Difference to average [%]
Measurement 1	27.890	-0.52
Measurement 2	28.112	0,28
Measurement 3	27.976	-0.21
Measurement 4	28.064	0.10
Measurement 5	28.134	0.35
Average (1-hour run)	**28.035**	

4 Summary

This paper explores the impact of modern hydraulic oils on the operational efficiency and energy consumption of hydraulic systems. It begins by examining the role of different base oil groups in determining oil performance and service life. The study emphasizes the significance of oxidation stability as a key property influencing oil degradation and system reliability. A new line of Energolubric hydraulic oils was introduced, demonstrating superior oxidation resistance compared to conventional mineral oils.

Oxidation stability tests using the RapidOxy 100 instrument confirmed that Energolubric oils significantly outperform traditional oils, resulting in extended service intervals and lower maintenance costs. Furthermore, energy consumption measurements conducted on plastic injection moulding machines revealed measurable energy savings, up to 4.3 %, when using energy-efficient hydraulic oils. Subsequent, more targeted tests on the hydraulic pump motor confirmed improved measurement repeatability and consistency, with deviations in average power consumption remaining within ±1 %. These measurements were performed using conventional hydraulic oil Hydrolubric VG. The next step will be to repeat the measurements using the modern energy-saving oil Energolubric 2046. These measurements should confirm that this oil actually saves energy and also allow for an accurate assessment of these savings.

The findings suggest that selecting high-quality, oxidation-resistant hydraulic oils can contribute not only to extended oil life and enhanced system reliability but also to measurable improvements in energy efficiency and overall cost-effectiveness.

References

[1] Kambič, M.: Mala šola mazanja, Profidtp, Škofljica, 2022.
[2] Kambič, M: Razvoj in praktična uporaba vrhunskega hidravličnega mineralnega olja, Ventil 28(2022)4, str. 268–275.
[3] Kambič, M.: Mineralna bazna olja, IRT3000 16(2021)6, str. 128-130
[4] Kambič, M.: Premium quality hydraulic oils, Fluidna tehnika 2021, str. 231-241
[5] O. AI, »Open AI« 2025 (https://openai.com.)

Wear Particles in the Hydraulic System and Their Impact on the Gear Pump Efficiency

Nejc Novak, Ana Trajkovski, Jan Bartolj, Mitjan Kalin, Franc Majdič

University of Ljubljana, Faculty of Mechanical Engineering, Ljubljana, Slovenia
nejc.novak@fs.uni-lj.si, ana.trajkovski@fs.uni-lj.si, jan.bartolj@fs.uni-lj.si, mitjan.kalin@fs.uni-lj.si, franc.majdic@fs.uni-lj.si

Wear particles in hydraulics accelerate the wear of elements in a gear pump. The contact between the gear and the pump housing is particularly exposed to wear. With an increase in the amount of particles in the oil, the volumetric efficiency of the pump deteriorates rapidly in the aforementioned contact and the useful life of the pump is thus reduced. The paper shows the calculation of the concentration of wear particles in the oil according to the ISO 4406 standard using the example of 20/19/18. Adding wear particles and sustainable testing at different concentrations affect the rate of decrease in the volumetric efficiency of gear pumps when increasing the concentration of particles in the oil.

DOI
https://doi.org/10.18690/um.fs.7.2025.25

ISBN
978-961-299-049-7

Keywords:
wear particles, gear pumps, calculation of concentration, test procedure, volumetric efficiency

University of Maribor Press

1 Introduction

Particles in hydraulic fluid are causing up to 70 % of failures of hydraulic component therefore cleanliness of oil is an important parameter [1]. Esteves et al. [2] described general influence of particle size distribution regarding wear mechanism factors.

The degradation of the pump is reflected in the increase of micro-particles in the liquid, leading to a decrease in the quality of the liquid, which is a class that does not meet prescribed standards. Solid particles bring specific wear mechanisms to the contact surfaces (abrasion, erosion, material fatigue, etc.) [3], [4]. Karanovič et al. [3] describe the influence of solid particle impurities in the radial gap between the control piston and the housing of the valve: due to three-body abrasion, they wear away material and increase the gap. As the gap increases, so does the flow through the gap (internal leakage), which causes even more particles to travel through the gap. This further increases friction and accelerates the wear process. Pressure losses in the gaps and the friction of particles cause local heating. To reduce wear intensity, optimal cleanliness is required. Jung-Hun et al. [5] studied the influence of particle composition and quantity. Three different types of particles in oil were used and gear pumps were tested with an output of 14.5 cm^3/rev. at a pressure of 1.6 MPa, rotational speed of 7000 rpm, and temperature of 120 °C. Type 2 particles contain over 97 % of SiO_2 with an average particle size of 27 µm to 31 µm. Type 7 particles contain 34 % to 40 % particles of the same size of SiO_2. A comparison of the achieved flow rates of the pumps before and after the addition of 25 g of powder particles at different shaft rotational speeds shows that particles with a higher content of SiO_2 wear down the elements more. The researchers imply that adding of particles reduce the performance of gear pumps.

The analysis of particle size distribution is an established procedure and clearly presented in standard ISO 4406 [6]. But there is also volume- and mass-based distribution that are in practical use and described in literature [7] according to standard ISO 9276.

The purpose of this paper is to present the transformation of cleanliness ISO 4406 code to adding appropriate mass for achieving the desired cleanliness in hydraulic oil, demonstrate the degree of decrease in volumetric efficiency in gear pumps and to predict the failure of the gear pump due to oil cleanliness.

2 Materials and methods

2.1 Adding particle mass to achieve appropriate concentrations

The mass of particle addition to achieve the appropriate fluid cleanliness classes was estimated based on the calculation of particle volume and particle density. It was assumed that the particles were in the form of a ball with a nominal diameter, made of two materials, namely steel with a density of 7874 kg/m^3 and quartz sand (SiO_2) with a density of 2650 kg/m^3.

The calculation of the mass of steel particles is presented using the example of two cleanliness classes. Transition from cleanliness 16/15/14 to cleanliness 20/19/18 according to ISO 4406 in a system with 13 L of hydraulic fluid. Initially, it is necessary to determine how many particles need to be added to move from class 16 to class 20. ISO 4406 shows that in class 16 there are 480 particles (mean particle number) larger than 4 µm, while in class 20 there are 7500 particles larger than 4 µm in 1 mL of liquid. Therefore, it is necessary to determine the difference in particle number for the move from class 16 to class 20 using equation (1).

$$\Delta x_{4\ \mu m} = x_{H\ 4\ \mu m} - x_{L\ 4\ \mu m} = 7500\,\frac{\text{particles}}{\text{mL}} - 480\,\frac{\text{particles}}{\text{mL}} = \\ = 7020\,\frac{\text{particles}}{\text{mL}} \tag{1}$$

Where:

- $\Delta x_{4\mu m}$ [/]… the difference between the number of particles between two classes greater than 4 µm,
- $x_{H\ 4\mu m}$ [/]… the number of particles in the higher class (in this case 20. class),
- $x_{L\ 4\mu m}$ [/]… the number of particles in the lower class (in this case 16. class).

The procedure is repeated for the next two classes (particles larger than 6 µm and 14 µm). The volume of the sphere is given by the particle diameter and the average particle volume between the two particle diameters can be calculated. Equation (2) gives the mean value of the volume of the spheres between 4 µm and 6 µm.

$$V_{\text{avg 4 µm−6 µm}} = \frac{V_{4\ \mu\text{m}} + V_{6\ \mu\text{m}}}{2} = \frac{\left(\frac{4 \cdot \pi \cdot r_{4\ \mu\text{m}}^3}{3} + \frac{4 \cdot \pi \cdot r_{6\ \mu\text{m}}^3}{3}\right)}{2} = \tag{2}$$

$$= 7.33 \cdot 10^{-17}\ \text{m}^3$$

Where:

- $V_{\text{avg 4 µm−6 µm}}$ [m^3]…the mean value of the volume of the balls between 4 µm and 6 µm,
- $V_{4\ \mu\text{m}}$ [m^3]… volume of a sphere with radius 4 µm,
- $V_{6\ \mu\text{m}}$ [m^3]… volume of a sphere with radius 6 µm,
- $r_{4\ \mu\text{m}}$ [m]… radius 4 µm particle (2x10^{-6} m),
- $r_{6\ \mu\text{m}}$ [m]… radius 6 µm particle (3x10^{-6} m).

For each particle class, it is necessary to determine the mean volume value. For example, between 4 µm and 6 µm, the volume value of the spheres is 7.33x10^{-17} m^3, and the weight is expressed by considering the density of the material, in our case steel. If we additionally multiply the mean weight of the spheres by the number of calculated particles, we obtain the concentration of particles (c) occurring in the size range from 4 µm to 6 µm (Equation (3)).

$$c_{\text{particles 4 µm−6 µm}} = V_{\text{avg 4 µm−6 µm}} \cdot \rho_{\text{Fe}} \cdot \Delta x_{4\ \mu\text{m}} = 0.026\ \frac{\text{g}}{\text{L}} \tag{3}$$

If we assume an exponential distribution and divide the particles into groups from 4 µm to 6 µm, from 6 µm to 14 µm, from 14 µm to 21 µm, from 21 µm to 26 µm, and so on up to 100 µm, and add the values and divide by the volume of the liquid in which the particles are located, we obtain the mass of particles that needs to be added to the system to ensure adequate cleanliness (equation (4)).

$$m_{\text{particels}} = \frac{c_{\text{particles 4µm–6 µm}} + c_{\text{particles 6 µm–14 µm}} + \cdots + c_{particles\ 91\ \text{µm–100 µm}}}{V_{\text{fluid}}} = \frac{c_{\text{particles 4µm–100 µm}}}{V_{\text{fluid}}} = \frac{0{,}146\,\frac{\text{g}}{\text{L}}}{13\ \text{L}} = 1.89\ \text{g} \quad (4)$$

We determined that 1.89 g of particles were required to be added to a 13 L hydraulic fluid system to go from a fluid cleanliness of 16/15/14 to a fluid cleanliness of 20/19/18. We assumed that the particles were steel and that the size distribution of the added particles matched the calculated differences in the particles to be added.

2.2 Testing procedure and test rig for gear pumps

The durability testing of gear pumps was done with the control adding of wear particles to the hydraulic system. Table 1 shows concentration of wear particles in 13 L of hydraulic oil ISO VG 46, used to carry out the tests.

Table 1: Concentration of wear particles in oil used for durability tests of gear pumps.

	Test 1	Test 2	Test 3	Test 4	Equivalent to cleanliness 20/19/18
Added mass of wear particles [g]	8.00	5.04	3.51	2.08	1.89
Wear particles concentration [g/L]	0.615	0.387	0.270	0.160	0.146

The rig (Figure 1) for testing gear pumps is consisting of conical reservoir. The design of reservoir is restricting particles to settle and therefore even distribution of particles in the fluid is present in the oil. Gear pump (the specimen) sucks the oil from reservoir and pushes it to 4/3 directional valve with solenoids and hydraulic aluminium block. Valve redirects flow to two pressure relief valves that are loading the pump at 22 MPa. The flow goes onwards to priority valve where oil has two paths. It can return directly back to reservoir, or it goes through the filter back to reservoir. This priority valve is there to remain cleanliness at desired level.

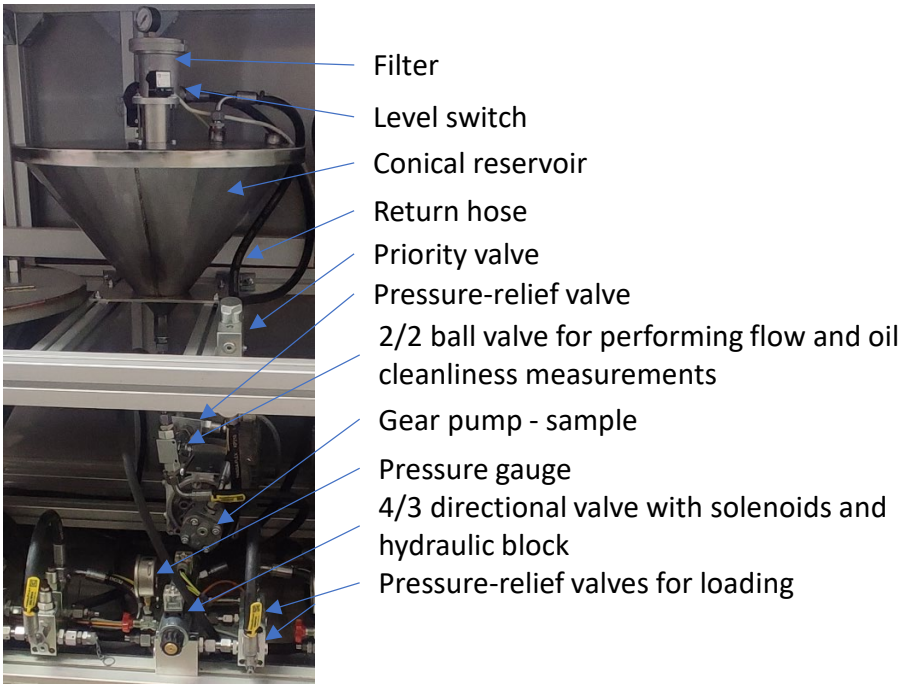

Figure 1: Test rig for durability testing of hydraulic gear pumps with wear particles.

3 Results

The pump tested at a concentration of 0.387 g/L (Figure 2) experienced the first major drop in volumetric efficiency at 50 h of operation, when at 0 MPa pressure the pump achieved an efficiency of 0.97, at 5 MPa it achieved an efficiency of 0.90, at 10 MPa it achieved an efficiency of 0.81, at 15 MPa it achieved an efficiency of 0.77, at 20 MPa it achieved an efficiency of 0.71 and at 25 MPa the efficiency dropped to 0.48. After 429 h of operation the efficiency dropped to 0 at 25 MPa pressure, while the efficiencies at lower pressures did not change significantly. After 546 h of operation the efficiencies dropped to 0 also at 150 MPa and 200 MPa. The oil temperature in the tank during the test was 60 ±4 °C.

Figure 3 compares volumetric efficiencies at different concentrations of wear particles in the oil at different pressures. It is important to note that the pump service lives and thus the operating times are different. Figure 3 shows that with increasing pressure, the efficiency decreases at the same pressure.

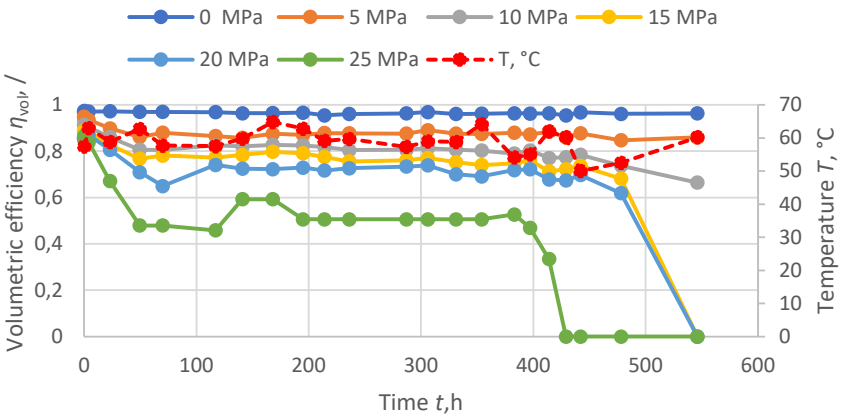

Figure 2: Measured volumetric efficiency of a pump tested with wear particles at a concentration of 0.387 g/L at a durability test site.

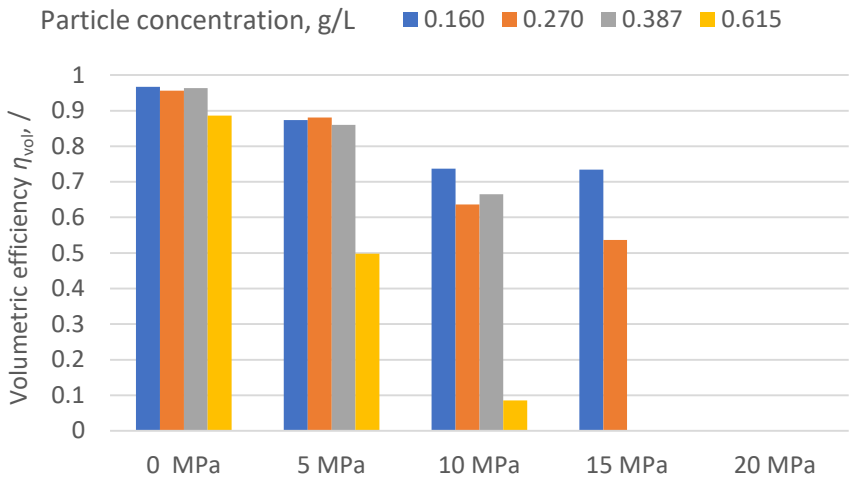

Figure 3: Measured volumetric efficiency of pumps tested with wear particles at the end of the test at different concentrations on a durability test rig.

The cleanliness of the oil according to ISO 4406 was monitored during each pump test with wear particles. A deterioration in cleanliness means that more particles have entered the oil and therefore, according to ISO 4406, the particle counter shows higher classes according to which cleanliness is defined. In the case of an

improvement in cleanliness, this means that there are fewer particles in the oil (and consequently lower classes) than at the beginning of the test due to appropriate filtration of the hydraulic oil in the system. The clean oil measurements taken before each pump test were 16/15/12 and 15/14/12, respectively (Figure 4). The oil cleanliness classes after 20 minutes of testing the pump with wear particles at a concentration of 0.387 g/L increase sharply from the initial values of 16/15/12 to the value of 22/22/21. After 70 hours of pump operation, the second class, which records the number of particles larger than 6 µm, and the third class, which records the number of particles larger than 14 µm, are reduced by one class so that the cleanliness stabilizes at 22/21/20. At the end of the test, the cleanliness is 22/21/19 after 546 hours of operation.

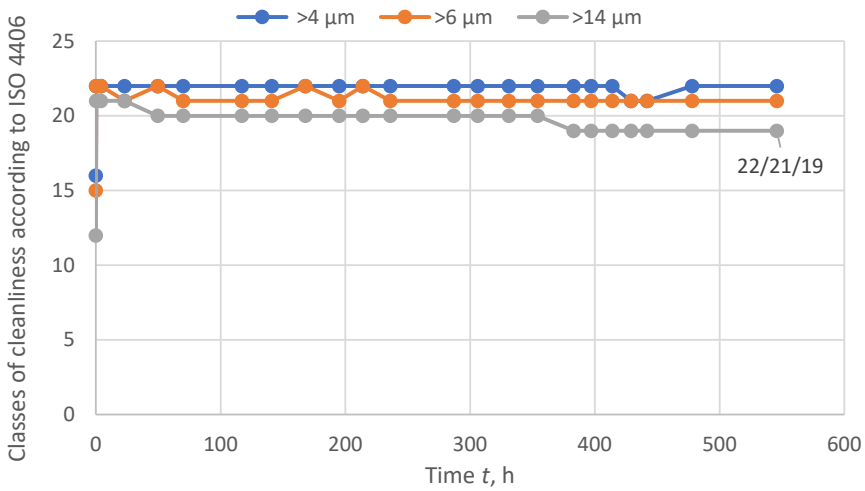

Figure 4: Measured oil cleanliness of a pump tested with wear particles at a concentration of 0.387 g/L.

4 The effect of particles on reducing volumetric efficiency

The consequence of the gradual decrease in the volumetric efficiency of the pump is a gradual increase in internal leakage due to wear. By adding particles to the system, we accelerate the wear processes in the pump. This was proven by durability tests that were carried out without adding particles at constant filtration, with the addition of wear particles.

In the durability test without adding particles and with constant filtration, the pump operated flawlessly for 7079 h, which is 295 days at 24-hour continuous operation. After the test, the volumetric efficiency was 0.84 at a pressure of 20 MPa.

All volumetric efficiencies of durability tests of pumps with wear particles were presented, and for an easier and more constructive understanding. A comparison of regression lines was made, which describe the trend of decreasing volumetric efficiency with operating time at different concentrations of wear particles. An example of such lines in tests with wear particles is shown in Figure 5. At a pressure of 20 MPa, the slope of the curve for wear particles with a concentration of 0.270 g/L is much smaller than for a particle concentration of 0.615 g/L, indicating a faster decrease in volumetric efficiency at a higher concentration of wear particles in the oil. For comparison, Figure 5 also shows a measurement without the addition of particles (WITHOUT).

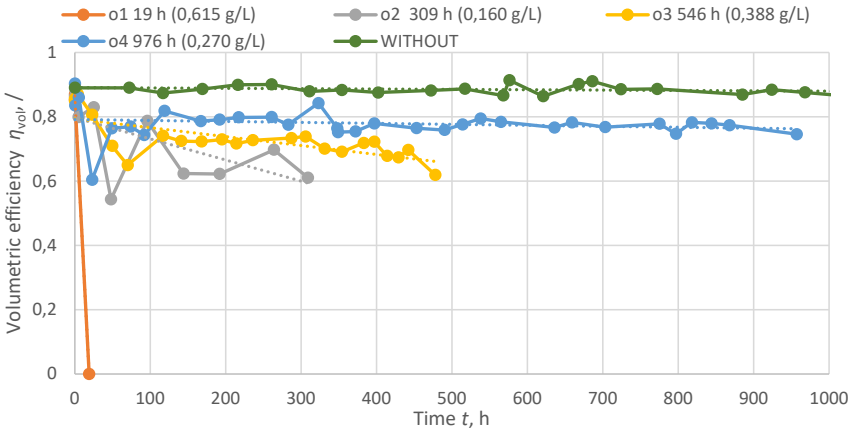

Figure 5: Results of volumetric efficiency measurements for pumps at 20 MPa pressure tested with wear particles at different concentrations and comparison without adding particles (WITHOUT).

Figure 6 shows the slope of the regression lines in pump tests with different concentrations of wear particles. The slope of the lines varies at 0.045 1/h at a concentration of 0.615 g/L, 0.0003 1/h at a concentration of 0.388 g/L, 0.00003 1/h at a concentration of 0.270 g/L and 0.0007 1/h at a concentration of 0.160 g/L. We find that at lower concentrations of wear particles, the volumetric efficiency does not decrease as rapidly, as the particles deform and have a smaller impact on the

efficiency and do not significantly affect the pump, and it turns out that they do not have a significant impact on the remaining hydraulic components either. When a sufficient amount of wear particles appears in the system, the volumetric efficiency of the pump begins to decrease more rapidly, as can be seen in Figure 6.

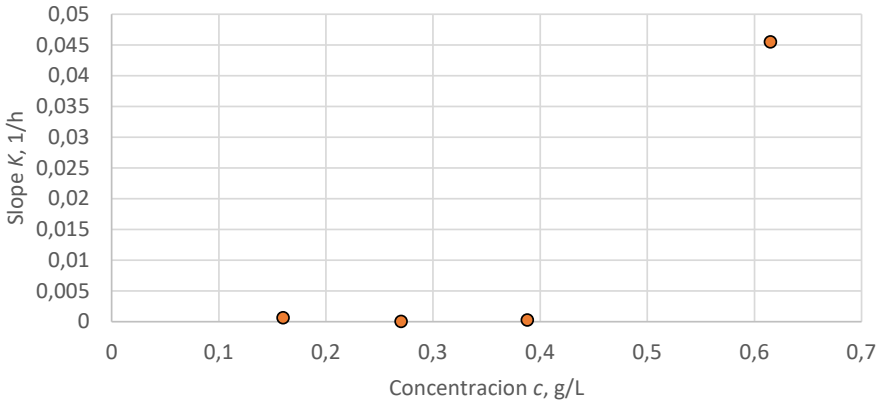

Figure 6: Slope of the lines at a pressure of 20 MPa for pumps tested with wear particles at different concentrations.

5 Conclusion

The calculation of mass of added particles to reach desired cleanliness of ISO code 20/19/18 and thus the concentration was represented. The concentration of particles was 0,146 g/L and the amount of mass added was 1,89 g in 13 L of oil. Research shows that the volumetric efficiency of a gear pump decreases slowly, with a more pronounced acceleration at higher concentrations. The slope of the regression lines describing the decrease in volumetric efficiency varies depending on the particle concentration. A higher concentration of wear particles causes a faster decrease in efficiency, which is consistent with the expected accelerated effect of wear. The results of the research allow the determination of an acceleration factor based on the measured service life of pumps tested at different particle concentrations. The acceleration factor for tests at typical oil cleanliness in the industry is also described.

Acknowledgments

We would like to thank the program group P2-0231 and the ARIS agency for financial support of projects L2-4474, L2-2618 and L2-50083.

References

[1] Y. Cao, Y. Deng, Y. Wang, Evaluation on Influential Factors of Hydraulic Gear Pumps Wear Life Using FAHP, in: ICME 2015, 2015.

[2] P.J. Esteves, V. Seriacopi, M.C.S. de Macêdo, R.M. Souza, C. Scandian, Combined effect of abrasive particle size distribution and ball material on the wear coefficient in micro-scale abrasive wear tests, Wear 476 (2021) 203639. https://doi.org/https://doi.org/10.1016/j.wear.2021.203639.

[3] V. Karanović, Development of a solid particle influence model on performance of piston cylinder contacting pairs for hydraulic components, University of Novi Sad, 2015.

[4] D. Wooton, The Lubricant's Nemesis-Oxidation, Practicing Oil Analysis 5 (2007) 5–6.

[5] S. Jung-Hun, J. Kyung-Ryeol, K. Hyoung-Eui, A Study on the Effects of Contaminant Types on the Wear Degradation Characteristics in Internal Gear Pumps, Tribology and Lubricants 27 (2011) 134–139.

[6] ISO 4406:2017 Hydrulic fluid power-Fluids-Method for coding the level of contamination by solid particles, 2017.

[7] https://www.microtrac.com/knowledge/particle-size-distribution/, 2025 (n.d.).

FTIR Changes of Differently Degraded Mineral and Turbine Oils

Milan Kambič,[1] Jošt Mohorko,[1] Aleš Hrobat,[1]
Karin Pivec,[1] Darko Lovrec[2]

[1] Olma d.o.o., Ljubljana, Slovenia
milan.kambic@olma.si, jost.mohorko@olma.si, ales.hrobat@olma.si, karin.pivec@olma.si
[2] University of Maribor, Faculty of Mechanical Engineering, Maribor, Slovenia
darko.lovrec@um.si

This paper investigates the oxidative degradation of mineral-based hydraulic and turbine oils using Fourier Transform Infrared (FTIR) spectrometry and RapidOxy 100 testing. A hydraulic mineral oil and two turbine oils of the same viscosity grade were studied under accelerated thermal and oxidative stress. FTIR analysis monitored additive depletion, base oil degradation (oxidation, nitration, sulfation), and contaminant accumulation (water, soot, fuel, glycol), while RapidOxy 100 tests provided oxidation induction times as a measure of resistance to degradation. Accelerated laboratory aging confirmed a consistent trend of decreasing oxidation stability and increasing oxidation/nitration products across all oils, with hydraulic mineral oil showing the fastest degradation. Results highlight the importance of base oil composition, additive system, and moisture control in determining oxidation stability and service life of lubricants in demanding industrial applications.

DOI
https://doi.org/10.18690/um.fs.7.2025.26

ISBN
978-961-299-049-7

Keywords:
hydraulic mineral oil,
turbine oil,
oxidation,
oxidation stability,
FTIR

University of Maribor Press

1 Introduction

In general, oils suitable for use in hydraulic systems come from two different sources, biological or non-biological, which offer a large number of hydrocarbon compounds. These usually occur as complex mixtures and can be used for many purposes other than lubrication (i.e. controlling wear and friction). The required properties of lubricants in modern industry are on the one hand greater, and on the other hand increasingly diverse. Therefore, the selection and "design" of an appropriate mixture of hydrocarbons for lubrication is a professional and complex process. Most natural oils contain substances that can hinder the lubricating properties, but at the same time they also contain compounds that are essential for the lubrication process. Lubricants derived from natural or mineral oils are partly refined and partly impure. The balance between the impure and refined parts is crucial for the oxidation stability of the oil and is important for the area of application of the lubricant. So, it is necessary to deliberately add additives to the oils in order to improve their properties and to make them more suitable for a certain use under certain operating conditions. These can radically change the properties of the lubricants and are essential for its overall effectiveness. In addition, additives determine the specific properties of the lubricant, such as oxidation stability, protection against wear and friction, corrosion tendency, foaming, hardening, and other properties.

A typical mineral oil consists of 95 % base and 5 % additive. The physicochemical properties of the oil depend on both the additives and the base oil itself. Base oils can be classified into three basic categories: biological, mineral and synthetic, with mineral oils being the most commonly used lubricants in industry.

For long service life under harsher operating conditions, the oxidation stability of a hydraulic fluid is important. The oxidation stability of three different mineral oils will be discussed below, a hydraulic mineral oil and two turbine oils. All three oils are of the same viscosity grade.

2 Oxidation stability – a key performance parameter for long-life of hydraulic and turbine oils

Oxidation stability is a critical property of hydraulic fluids, especially in demanding industrial applications where long service life, system reliability, and cost-efficiency are of paramount importance. Oxidation refers to the chemical reaction between the oil and atmospheric oxygen, which is accelerated at elevated temperatures, in the presence of catalytic metal contaminants (e.g., copper, iron), or in systems where moisture ingress occurs.

This degradation leads to the formation of a variety of harmful by-products, including organic acids, sludge, varnish, and insoluble compounds. These products can cause filter plugging, valve sticking, increased wear, and changes in oil viscosity - ultimately reducing the efficiency and reliability of the turbine or hydraulic system. In severe cases, oxidation-induced deposits may result in unplanned downtime, expensive repairs, and reduced equipment life [1].

The oxidation stability of the oil is strongly influenced by the type and quality of the base oil used, as well as by the formulation and performance of the antioxidant additive system. Carefully selected antioxidants are incorporated into the formulation. Over time, however, antioxidant levels deplete, which is why oxidation stability is also a key indicator of oil life. These improvements extend service intervals, reduce oil change frequency and waste oil generation, and lower maintenance and filter replacement costs. At the same time, system reliability increases and the risk of unplanned downtime decreases. In summary, proper oil selection and an understanding of oxidation stability have a direct impact on the efficiency, safety, and cost-effectiveness of system operation.

2.1 ASTM E2412 method

ASTM E2412 test method [2] is commonly used to monitor the condition of used lubricants using trend analysis based on Fourier Transform Infrared (FTIR) spectrometry. It covers the use of FTIR to monitor additive depletion, contaminant accumulation, and base component degradation in machine lubricants, hydraulic fluids, and other fluids used in normal machine operation.

Oxidation stability indicates the resistance of a substance to chemical degradation in the presence of oxygen. It is crucial for fuels, oils and foodstuffs, as oxidation can cause rancidity of fats and oils, the formation of resins and deposits in fuels and shorten the service life of lubricants. Factors affecting the stability of a medium include the presence of air, light, heat, and especially moisture and metal ions, while antioxidants are used to slow down the degradation process.

Oxidation according to ASTM Standard (American Society for Testing and Materials), is used to measure and monitor the oxidation of materials, most commonly lubricants, fuels and other hydrocarbon-based products. These tests evaluate the resistance of a material to oxidation as well as identify and determine oxidation products using techniques such as Fourier Transform Infrared Spectrometry (FTIR) or by monitoring exothermic reactions. Key ASTM Standard include D943 for steam turbine oil oxidation, D2274 for diesel fuel stability and D7414 for monitoring oxidation in lubricants during their use.

In our case, the purpose of ASTM E2412 oxidation tests is to assess the oxidative stability of hydraulic oils. In other words, to determine how well the oil resists degradation when exposed to oxygen and heat, especially in applications where the oil is exposed to more demanding operating conditions such as those typical of hydraulic systems.

The ASTM E2412 test is based on the use of FTIR to track molecular changes in the spectrum of the oil, which can indicate the following three groups of changes that occur:

- Additive depletion: As additives are consumed, their characteristic absorption peaks in the spectrum decrease.
- Base stock degradation, which includes:
    - Oxidation: Formation of new carboxylic acids due to heat and oxygen exposure, a common form of oil degradation.
    - Nitration: Reactions that form nitrous oxides, particularly in high-temperature engines, which can lead to increased oil acidity and viscosity.
    - Sulfation: Formation of sulfuric acid from sulphur compounds and heat, leading to increased acidity and sludge.

In addition, the test also provides the occurrence of the formation and accumulation of the following contaminants:

- Water: A key contaminant and degradation accelerator.
- Soot: As products of incomplete combustion, which can be present in the oil.
- Ethylene glycol: A commonly present coolant that can also contaminate lubricants.
- Fuel: The presence of fuel can be detected by characteristic spectral changes.

Oxidation, nitration and contamination of hydraulic oil (test label H) and two different turbine oil (test labels M and C) were measured by Spectrum Two spectrophotometer with automatic sampler (Figure 1).

Figure 1: Spectrum Two spectrophotometer with automatic sampler.
Source: own

The spectrophotometer measures the transmittance and absorbance of IR light in the spectrum from 7,800 to 370 cm^{-1}. The IR light source sends rays with the full spectrum through the sample on a ZnSe prism or between two KBr plates. The remaining light on the other side is detected by a sensor, which records the intensity of each wavelength and converts it into a graph. In this way, the presence of various additives, molecules, contaminants, oxidation, soot etc. can be determined [3].

2.2 Determining the oxidation stability of hydraulic oils

The oxidation stability of hydraulic oil (test label H) and two different turbine oil (test labels M and C) was evaluated using the RapidOxy 100 instrument (Figure 2).

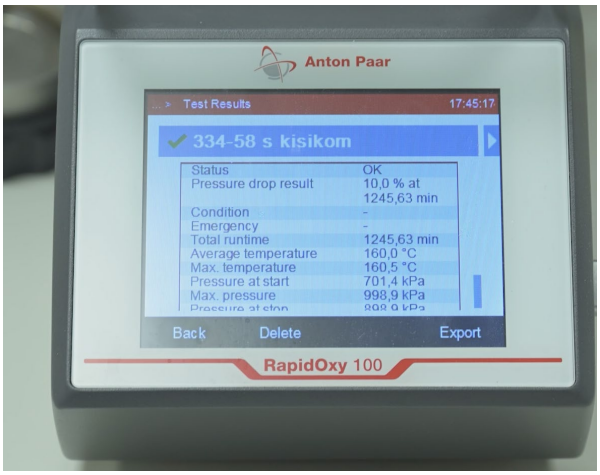

Figure 2: RapidOxy 100 instrument for measuring oxidation stability of oils.
Source: own

RapidOxy 100 is a modern laboratory instrument designed for fast and reproducible determination of the oxidation stability of lubricants, fuels, and other organic materials. It is based on the accelerated aging method under elevated pressure and temperature, in which the pressure drop of oxygen (or synthetic air) in a sealed chamber containing the sample is continuously monitored.

Compliant with ASTM D8206 and DIN 51466 Standards, the instrument measures the oxidation induction time (OIT) - defined as the time it takes for the pressure in the chamber to drop by a defined percentage (typically 10 %) from its initial value. This parameter is a reliable indicator of oxidation resistance and, by extension, the expected service life of the oil. The measurement procedure includes the following steps:

– A small sample (approximately 5 mL) is carefully measured and placed into the steel pressure chamber of the instrument.

- The chamber is sealed and pressurized with pure oxygen or synthetic air to about 700 kPa.
- The sample is heated to a defined temperature (most commonly 140 °C), while the instrument continuously monitors the pressure drop.
- The test ends when the pressure has decreased by 10 %; the elapsed time is recorded as the test result (OIT in minutes).

Advantages of the RapidOxy method include [4]:

- Speed: the complete test is significantly faster than traditional methods (e.g., RPVOT, TFOUT), typically requiring only 1 to 3 hours.
- Low sample volume: suitable for R&D and high-value products where sample availability may be limited.
- Versatility: applicable to various types of oils (turbine, hydraulic, engine, compressor) and additive formulations.
- Excellent reproducibility and sensitivity: allows for reliable comparison of different formulations or production batches.

Due to its efficiency and robustness, RapidOxy 100 has become an essential tool in the development and quality control of high-performance lubricants intended for demanding industrial applications, where extended service intervals and high oxidation resistance are critical performance requirements.

3 Initial condition of the tested oils

When monitoring the condition of hydraulic oils, it is important not only to know the current condition of the oil, but also to know the initial values of the observed parameters, i.e. the baseline values of the material properties of the oil. Knowing the baseline values is crucial for all further analyses and for monitoring the trend of changes in individual parameters. Table 1 gives the baseline values for the fresh oils under consideration.

The oxidation properties of hydraulic mineral oil HL type (test label H) and two different turbine oil (test labels M and C) is discussed. Turbine oil with the M designation, is a medium-high performance circulating lubricant specifically designed for steam and water turbine systems and other industrial applications. In

case of turbine oil labelled with C, is a turbine oil formulated with highly refined mineral base stocks (Group II base oils) and a complex additive package, including rust and oxidation inhibitors. It has no anti-wear additives and is designed for the lubrication of steam and industrial gas turbines, especially those with high local temperatures, due to its excellent resistance to foaming, air release and water separation properties.

Table 1 gives the experimental values obtained according to ASTM E2412 Standard. In our case study, oxidation stability and oxidation are in the foreground, as well as moisture (water) content and the content of AW additives. The other parameters listed are less important for our discussion. For example, it is immediately clear that turbine oil C has a very high oxidation stability, especially compared to mineral hydraulic oil H, and the lowest oxidation tendency value. The moisture content and the already mentioned AW additives present (typical for C) are also low.

Table 1: Baseline values of monitored parameters for three types of oils

Parameter \ Label	H0	M0	C0
Oxidation stability (OS) (160 °C, 700 kPa, 10 % O_2) [min]	378.1	907.3	1353.6
Water (ASTM E2412)	6.9470	4.3432	3.7144
Soot (ASTM E2412)	3.2736	3.222	3.2467
Oxidation (ASTM E2412)	4.6453	2.7543	1.8388
Nitration (ASTM E2412)	3.0719	1.9743	1.5966
AW additive (ASTM E2412)	13.039	10.525	9.6119
Gasoline (ASTM E2412)	-0.0190	0.0117	0.01944
Diesel fuel (ASTM E2412)	261.36	207.997	200.157
Sulphates (ASTM E2412)	14.6555	11.5042	11.2905
Ethylene glycol (ASTM E2412)	0.4110	0.3059	0.4681

Oxidation stability (OS) is a substance's resistance to chemical breakdown and degradation caused by exposure to oxygen over time, which is measured by the duration it remains stable before undergoing undesirable changes. Data on oxidation, nitration and sulfation by-products indicate the degree of fluid degradation. Oxidation testing performed by FTIR measures the breakdown of a lubricant due to age and operating conditions and is reported in abs/cm (absorbance units per centimetre). By observing specific absorption, FTIR testing detects the presence of carbonyl groups (C=O), such as ketones, esters, and carboxylic acids, that result from oxidation in the oil. Nitration testing is also performed using FTIR (ASTM E2412 method), which indicates the presence of nitric acid, which speeds

up oxidation. Nitrates exhibit peaks in the infrared spectrum, allowing FTIR to identify their presence in the oil.

An OS value expressed (in minutes), indicates how long a substance, such as oil, can resist degradation from oxygen. A higher OS value signifies greater resistance to oxidation, meaning the product will have a longer useful life and perform better under stress before producing undesirable gums, sediments, or rancid odours. A lower value indicates a substance is more prone to oxidation and has a shorter shelf life.

An oil oxidation value indicates the extent of chemical aging and degradation in an oil due to exposure to heat, oxygen, water, and metals. A low value generally signifies good oil quality and longevity, while a high value signals that the oil is breaking down, forming sludge and varnish, and needs to be changed to prevent equipment damage. For mineral oils, an oxidation value above 30 or 40 may indicate the end of the oil's life.

The table clearly shows that both turbine oils have much better oxidation resistance than mineral hydraulic oil. This is especially true for turbine oil with the C designation.

4 Accelerated degradation process of hydraulic oils samples

For the purposes of accelerated oil aging, a self-developed laboratory dry thermal test was used, with which accelerated oil aging can be performed on a larger sample volume (1500 mL), which enables a wide range of laboratory analyses to be performed. It basically consists of two glass beakers, placed one inside the other, so that the smaller 3-liter one is placed inside the larger 5-liter one.

The larger one contains rapeseed oil as a heating (tempering) fluid, which, with constant stirring, ensures constant temperature conditions of the tested fluid. A copper wire with a cross section of 1.5 mm^2, a length of 15 ±0.1 m, twisted into a spiral with a diameter of 10 mm, is inserted into the smaller beaker, which serves as a catalyst (accelerating the degradation of the tested fluid). Oxygen is known to be a further accelerator of oil aging. Therefore, compressed ambient air with a flow rate of 3 ±0.1 L/min is blown into the test oil, which is previously dehumidified using a ready-made group for pneumatic systems. The test is carried out at atmospheric

pressure in a closed test chamber. The temperature of the tested oil is maintained during the test, in our case 160 ±0.5 °C. The test setup is shown in Figure 3.

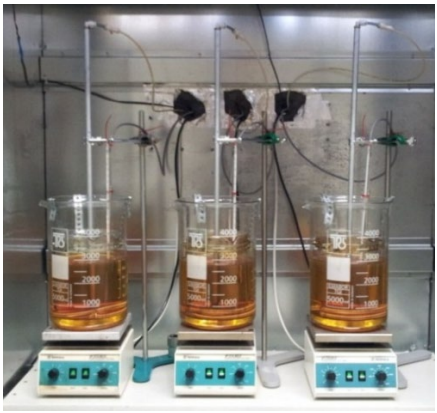

Figure 3: Accelerated aging test of hydraulic oil – baseline condition.
source: own

5 Results

As an example, Figure 4 shows the change in colour of a sample of C turbine oil over the course of thermal loading, briefly described in the previous chapter (more on this can be found in [5], [6] and [7]). For example, the C60 designation means that it is a C oil sample after 60 hours of thermal stress at 160 °C. The image clearly shows the colour changes in the sample and also the occurrence of varnishing and sludge formation. The colour change is more or less similar for the other two samples, another turbine oil (sample M) and a conventional hydraulic oil (sample H).

Figure 4: Colour changes as a result of thermal stress in case of sample C.
source: own

The measurement results for aged turbine oil sample C are presented in Table 2. All values refer to the mentioned ASTM E2412 Standard and oxidation stability measurements with RapidOxy 100. Values are rounded to two decimal places.

RapidOxy 100 and FTIR are two completely different methods for measuring the same phenomenon; namely, oil degradation as a result of chemical reactions, primarily oxidation and nitration. Both techniques have also already been standardized through various (mainly) ASTM standards. It is impossible to claim that one method is the "correct" one and the other is not. These are complex processes that are not easy to monitor and are essentially detected indirectly.

In our case, the RapidOxy 100 device was used to expose the sample to an accelerated oxidation process. The results of the two methods are not directly comparable, but it is possible to meaningfully track trends in the results obtained by both methods. The tables 2, 3 and 4 clearly show that the trend of the results is similar and meaningful.

Table 2: Results for aged turbine oil C over testing time

Label / Parameter	C0	C60	C75	C90	C105	C150
Oxidation stability [min]	1353.6	1280.7	1191.7	39.0	37.7	61.0
Water	3.71	3.69	3.70	10.04	30.95	60.49
Soot	3.25	3.22	3.21	3.57	4.62	6.11
Oxidation	1.84	2.20	2.26	23.61	79.68	151.85
Nitration	1.59	1.48	1.47	3.10	8.68	16.91
AW additive	9.61	9.54	9.54	13.28	21.44	30.76
Gasoline	0.02	0.02	0.02	0.02	0.02	0.02
Diesel fuel	200.16	200.40	200.50	199.63	198.78	198.54
Sulphates	11.29	10.82	10.79	17.05	32.70	52.15
Ethylene glycol	0.47	0.64	0.64	0.849	0.883	0.39

The data show that the oxidation stability value gradually decreases from the beginning of the test until 75 hours of testing under the same conditions, while the oxidation value increases. However, at longer times of thermal stress under the test conditions, i.e. at 90, 105 and 150 hours, both values change significantly. At these testing times, a large drop in the OS value is visible, because these samples were exposed to moisture after testing. Thus, the interdependence of the moisture present on the OS is clearly given.

Similarly, Table 3 shows values for turbine oil (M), and Table 4 shows values for hydraulic oil (H).

Table 3: Results for aged turbine oil labelled with M.

Parameter \ Label	M0	M60	M90	M120
Oxidation stability [min]	907.3	1030.2	726.6	146.3
Water	4.34	4.08	4.06	12.94
Soot	3.22	3.23	3.24	3.73
Oxidation	2.75	2.65	3.60	29.59
Nitration	1.97	1.70	1.72	4.11
AW additive	10.53	10.40	10.46	14.00
Gasoline	0.01	0.01	0.01	0.01
Diesel fuel	207.99	207.00	205.76	203.01
Sulphates	11.50	10.85	11.04	18.30
Ethylene glycol	0.31	0.36	0.41	0.31

Table 4: Results for aged hydraulic oil labelled with H.

Parameter \ Label	H0	H60	H90	H110
Oxidation stability [min]	378.1	273.9	129.1	98.4
Water	6.95	6.50	10.35	12.91
Soot	3.27	3.34	3.77	4.07
Oxidation	4.65	6.11	14.16	19.39
Nitration	3.07	3.32	4.41	5.22
AW additive	13.04	12.62	14.55	15.63
Gasoline	-0.02	-0.03	-0.03	-0.03
Diesel fuel	261.36	259.01	254.49	252.30
Sulphates	14.65	14.35	16.76	18.10
Ethylene glycol	0.41	0.86	1.06	0.84

In all three cases it is evident that the oxidation stability decreases with aging. On the other hand, with oil aging, nitration and oxidation increase.

6 Summary

The study focused on understanding oxidation stability as a key performance parameter for long-life lubricants, especially of turbine oils. Oxidation is a primary cause of oil degradation, leading to sludge, varnish, viscosity changes, and reduced system reliability. Three mineral oils were evaluated: hydraulic oil H, turbine oil M, and turbine oil C.

- Baseline analysis: Turbine oil C had the highest oxidation stability (1353.6 min), followed by M (907.3 min) and H (378.1 min). FTIR revealed lower oxidation and nitration tendencies in turbine oils compared to hydraulic oil.
- Aging experiments: A self-developed accelerated aging test exposed oils to high temperature, oxygen, and catalytic copper. Results showed that with aging, all oils exhibited reduced oxidation stability and increased oxidation/nitration by-products. Moisture significantly accelerated degradation.
- Comparative results: Turbine oils, particularly oil C, demonstrated superior resistance to oxidation compared to hydraulic oil. RapidOxy and FTIR produced consistent trends, proving reliable for monitoring degradation though values are not directly comparable.

Overall, the findings confirm that turbine oils with higher-quality base stocks and antioxidant systems significantly outperform hydraulic mineral oils in oxidative stability. Moisture ingress and additive depletion are critical factors reducing oil lifetime. Proper lubricant selection and monitoring by FTIR and RapidOxy 100 are essential for extending service intervals, minimizing maintenance, and improving system reliability.

References

[1] Hrobat A., Mohorko J., Tič V. (2025). Podaljšanje uporabne dobe hidravličnega olja in vpliv na energetsko učinkovitost. *16. Industrijski forum IRT Portorož*, 189-192

[2] ASTM E2412-23a, Standard Practice for Condition Monitoring of In-Service Lubricants by Trend Analysis Using Fourier Transform Infrared (FT-IR) Spectrometry

[3] Internal material KP 13.3

[4] O. AI. "Open AI" 2025 (htpps://openai

[5] Tič V., Lovrec D. (2017) *On-line condition monitoring and evaluation of remaining useful lifetimes for mineral hydraulic and turbine oils*. 1st ed. Maribor: University of Maribor Press, pp. 174. ISBN 978-961-286-130-8. http://press.um.si/index.php/ump/catalog/book/309, DOI: 10.18690/978-961-286-130-8.R

[6] Tič V., Tašner T., Lovrec D. (2014) Enhanced lubricant management to reduce costs and minimise environmental impact. Energy. 1 Dec. 2014, vol. 77, pp. 108-116. ISSN 0360-5442, http://www.sciencedirect.com/science/article/pii/S0360544214005799#, DOI: 10.1016/j.energy.2014.05.030

[7] Lovrec D. (2015) Determining different turbine oils' estimated lifetime. V: ISOPP, Jutta (ur.), DANKL, Andreas (ur.). *Jahrbuch Instandhaltungstage 2015*. [S. l.]: Dankl+partner consulting GmbH [etc.], [2015]. Str. 57-62. ISBN 978-3-7011-7969-5.

Automated Detection of Compressed Air Leakage in Pneumatic Stations

Vito Tič, Andrej Baligač
University of Maribor, Faculty of Mechanical Engineering, Maribor, Slovenia
vito.tic@um.si, andrej.baligac@student.um.si

Effective detection of compressed air leaks is crucial for improving energy efficiency in pneumatic systems. In this paper, we present an automated leak detection approach for a pneumatic workstation using integrated pressure and flow sensors. The system monitors the baseline operating cycle and identifies anomalies such as excess air consumption or pressure drops that indicate leakage. A Beckhoff PLC with TwinCAT 3 was used to collect real-time data, and a parallel simulation model was developed in Automation Studio to validate the approach. Experimental results from both simulation and a physical pneumatic station demonstrate that flow-based measurements are far more sensitive to small leaks than pressure-based methods. Even a 1 mm diameter leak orifice produced a significant increase in airflow consumption with minimal detectable pressure change. The comparison between simulated and real-world leak scenarios confirms the viability of continuous sensor-based monitoring for early leak detection in pneumatic systems.

DOI
https://doi.org/10.18690/um.fs.7.2025.27

ISBN
978-961-299-049-7

Keywords:
pneumatic manipulator, leak detection, self-diagnosis, Beckhoff,. TwinCAT 3

University of Maribor Press

1 Introduction

Compressed air is a widely used energy source in industrial automation. However, a substantial portion of generated compressed air is wasted through system leaks, leading to higher operating costs and reduced efficiency. The U.S. Department of Energy has estimated that industrial compressed air systems typically lose about 25% of their air to leaks (and in some cases up to 80%). Other studies indicate that on average as much as one-third of the compressed air in a facility is wasted due to leakage. These losses translate directly into increased energy consumption and expense. For example, a single small leak (1.6 mm orifice) can cost on the order of $1000 per year. Beyond energy cost, leaks can impair system performance by causing pressure drops that hamper the operation of pneumatic equipment and even lead to unscheduled downtime. It is therefore imperative for manufacturers to implement effective leak detection and remediation programs to maintain both energy efficiency and system reliability. [1]

Conventional methods for detecting compressed air leaks include manual inspection (audible listening for the "hissing" sound), ultrasonic acoustic detectors, and periodic pressure decay tests. Ultrasonic leak detection devices are commonly used to find small leaks that are not audible, by sensing high-frequency sound emissions at leak sites. While these methods can be effective for spot-checking a system, they are labor-intensive and not continuous. In a large or complex pneumatic installation, leaks may develop at any time in hoses, fittings, valves, and other connections. A more automated, continuous monitoring approach is desirable for early leak detection without requiring frequent manual audits. [2]

One way to achieve automated leak monitoring is to leverage the sensors and control infrastructure already present in modern pneumatic systems. Many pneumatic machines and workstations are equipped with pressure sensors, flow sensors, or can be retrofitted with such instrumentation. By analyzing sensor data in real time, it is possible to detect anomalies indicative of leaks. Prior research has explored analyzing system pressure patterns to infer leaks – for instance, using an accumulator pressure drop profile and advanced signal processing or machine learning to detect small leaks. However, because pressure in a regulated pneumatic system may remain relatively stable even as air escapes (until the leak becomes large), purely pressure-based diagnostics struggle with detecting anything but major leaks. In contrast, measuring airflow consumption provides a more direct indication of leakage. A leak

creates an additional airflow demand on the compressor or supply line, which can be observed as an increase in flow rate drawn by the system. Recent industrial solutions for smart leak detection indeed utilize flow sensors on main supply lines to continuously monitor for unexplained air usage spikes. [3]

In this paper, we present an automated leak detection system for a pneumatic manipulator station that employs both pressure and flow sensing. The work is based on a master's thesis project in which a real pneumatic workstation was instrumented for self-diagnostics of air leakages. The main contributions of our study are: (1) a comparative evaluation of three sensing approaches – motion timing, pressure, and flow – for detecting pneumatic leaks, and (2) an assessment of simulation modeling for predicting leak behavior versus actual physical experiments. The focus is on experimental findings: we performed controlled leak tests on a laboratory pneumatic station and also created a corresponding simulation model in Automation Studio to replicate the system's behavior under leak conditions. By comparing the simulated and real-world results, we validate the reliability of the detection methods and identify practical considerations for implementation

2 Methodology

2.1 Pneumatic Station and Leak Simulation Setup

The experimental testbed is a pneumatic manipulator workstation (Figure 1) consisting of multiple pneumatic actuators (cylinders) and a valve manifold (valve island) controlled by a PLC. The station is supplied with compressed air regulated to 4 bar. For the purposes of this research, we focused on a single axis of motion (the Y-axis linear actuator of the manipulator) as the primary point of investigation. This choice was made to simplify the experiments, since instrumenting every actuator and potential leak point in the system would require a large number of sensors. By monitoring one representative actuator motion in detail, we can still glean insights that are extendable to other parts of the system.

To induce and measure leaks, we introduced calibrated orifice leaks at a specific location in the pneumatic circuit. A T-fitting was installed near the Y-axis cylinder's supply port, with an interchangeable plug that has a small hole to simulate a leak. Four leak orifice sizes were tested: diameters of 0.5 mm, 1 mm, 2.5 mm, and 5 mm. These sizes were chosen to represent a range from a very small pinhole leak (0.5

mm) to a quite severe leak (5 mm). The orifice diameters and corresponding leak flow rates (theoretical, at 4 bar pressure) are summarized in Table 1. The leak orifice plug is only installed on one side of the cylinder (for example, the extension side); when that side is pressurized during the actuator's stroke, air will continuously escape through the orifice.

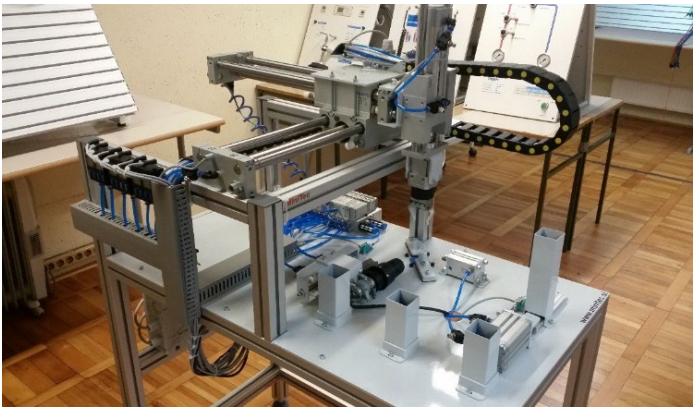

Figure 1: The experimental testbed – a pneumatic manipulator workstation.

Table 1: Theoretical leak flow rates for various orifice sizes at 4 bar

Leak orifice diameter	Leak flow (theoretical)
0.5 mm	~0.013 m³/min (13 L/min)
1.0 mm	~0.053 m³/min (53 L/min)
2.5 mm	~0.230 m³/min (230 L/min)
5.0 mm	~1.314 m³/min (1314 L/min)

These flow values were computed using standard orifice flow equations for compressible flow. As expected, leak flow increases rapidly with orifice size – a 1 mm leak passes roughly 4x the airflow of a 0.5 mm leak, and a 5 mm break could leak over 1000 L/min (which in practice would overwhelm a typical compressor). In fact, at 2.5 mm our leak flow was already comparable to the capacity of the air supply, meaning the system could no longer maintain the nominal pressure.

2.2 Instrumentation and Data Acquisition

Three types of measurements were leveraged to detect leaks: motion timing, pressure, and flow. For motion timing, a laser distance sensor (Omron ZX1 laser displacement sensor) was mounted to track the position of the Y-axis carriage over

time. The idea was to see if a leak (which might reduce the effective force/pressure available) slows down the actuator's movement, thereby increasing the stroke time. The laser provided a real-time analog distance reading of the moving part; by capturing this signal, we could compute the velocity profile or total time of travel for the axis under normal and leak conditions. The laser sensor was positioned such that its zero-point was set at the fully extended position of the axis (a calibration was done to offset the initial distance). In practice, as will be seen, the motion timing method proved to be the least sensitive, because the pneumatic regulator largely compensates to keep the motion speed consistent (until very large leaks occur).

For pressure measurement, we utilized the station's existing pressure sensors (Festo SDE1 series pressure transducers) which were installed on the pneumatic supply lines of the actuators. These sensors output an analog voltage corresponding to the local line pressure. We connected the pressure sensors to the PLC's analog input card (Beckhoff EL3124) to record the pressure in the cylinder's chamber during operation. One important consideration discovered was that the pressure regulator on the supply maintained the line pressure so effectively that small drops due to leaks were quickly compensated. Thus, to get a meaningful pressure reading, the sensor needed to be placed as close as possible to the leak point, ideally on the same segment of tubing. In our setup, the pressure sensor was attached via the T-fitting directly adjacent to the leak orifice plug. This way, the sensor would register a pressure drop whenever air escaped through the orifice. If the sensor were farther away (e.g., only at the regulator or main header), the local pressure drop might be completely flattened out by the regulator response and system volume, making the leak undetectable. Even with the sensor close by, as we will show, the pressure dips due to the smaller leaks were very subtle.

For flow measurement, two mass flow sensors were installed: one on the main air inlet to the Y-axis actuator circuit, and another on the branch feeding the Y-axis cylinder itself. The inlet flow sensor (Festo SFAM model) had a range of 20–200 L/min, suitable for measuring the total airflow into the entire station or the selected manifold. The cylinder branch flow sensor (SMC miniature flow sensor) had a much smaller range (0.2–10 L/min) to measure the actuator's own air consumption with high resolution. The rationale for using two flow sensors was to have a reference vs. localized measurement: the flow into the overall system vs. the flow into the actuator. In the absence of leaks, these two should match when the only air consumption is the actuator's motion. If there is a leak anywhere in the system (in

our case, intentionally on that actuator's line), then the total flow at the inlet will exceed the flow that actually went into moving the actuator. By comparing the two, one can not only detect that a leak exists (inlet flow > actuator flow), but also quantify it by the difference of the readings.

All sensor signals (laser displacement, pressure, and flow sensors) were interfaced to a Beckhoff CX5130 PLC running TwinCAT 3. The PLC was programmed to execute the pneumatic cylinder's motion sequence (extend and retract in a cycle) and simultaneously log the analog sensor values. We utilized the TwinCAT Measurement functionality (TwinCAT 3 Scope) to record and visualize the data in real-time. The sampling rate for data logging was set to 100 Hz, which was sufficient to capture the dynamics of the cylinder motion (which lasts on the order of 0.5–1 s). The data was later exported for analysis and plotting. Additionally, a simple Human–Machine Interface (HMI) was built using TwinCAT HMI tools to remotely monitor the sensor readings and leak detection status. This could allow an operator to see live information about potential leaks (e.g., an alarm if a leak is detected by the system logic comparing inlet vs. actuator flow)

2.3 Automation Studio Simulation Model

In parallel to the physical experiments, we developed a simulation model of the pneumatic system using Automation Studio. The simulation aimed to replicate the Y-axis cylinder behavior under the same conditions (including leaks) to verify if the model predictions agree with real measurements. The model included a double-acting pneumatic cylinder, 5/2 directional control valve, pressure regulator, and connecting pneumatic lines. We calibrated the component parameters using manufacturer data sheets for things like cylinder bore and stroke, valve flow coefficients, and line volumes. The leak was introduced in the simulation by adding a flow resistance path (an orifice to atmosphere) on the cylinder's line, with an opening diameter equal to the physical leak orifice. For example, a 1 mm leak was modeled as a 1 mm diameter orifice to ambient, placed in the same location in the circuit as the real leak. To mimic the fact that in the real setup the leak exhausts directly to atmosphere (very short path), we set the "leak" outlet tube length to only 1 mm in the simulation model. This ensures the simulated leak does not have any significant flow resistance beyond the orifice itself (i.e., no long pipe that could restrict it).

The simulation was run for each leak size as well as for the no-leak case. We recorded the simulated cylinder chamber pressure and flow rates through the cylinder's inlet. One nuance of the simulation is that it can directly provide the leak flow value as a separate variable (since we can measure flow through the leak orifice element in the model). This is useful for analyzing how much of the air is going into useful work versus being lost. In contrast, on the real system we infer the leak flow only by subtraction of sensor readings (inlet minus actuator flow). In the simulation, however, one must be careful: if one only looks at the flow into the actuator component, the presence of a leak on that line might not obviously show up in that measurement. In our model, the "actuator flow" monitoring block measures flow into the cylinder itself; the leak path branches off, so from the cylinder's perspective, it may still consume the same amount of air to move (until the point pressure drops too much). The leak flow is then seen separately. Therefore, to make meaningful comparisons, we consider both the total flow drawn from the supply and the distribution of that flow into the cylinder vs. out the leak. The Automation Studio model was executed with the same cycle timing as the real machine (extend and retract motions with similar load conditions) so that we could directly overlay simulation results with experimental data.

3 Results and Discussion

3.1 Baseline Operation (No Leak)

We first consider the normal operation of the pneumatic axis with no leak present. In this scenario, the Y-axis cylinder executes an extend and retract cycle, and the sensor readings serve as a baseline. The laser displacement sensor showed a smooth motion profile, with the carriage moving a fixed distance in roughly 2.0 s (extend) and similarly 2.0 s to retract. The pressure in the cylinder (on the extending side) during extension typically rose to ~4 bar and remained near constant until the end of stroke (when the pressure spiked slightly as the piston hit the end stop). The flow sensor on the actuator line indicated a transient air flow peak during the initial filling of the cylinder at the start of motion, followed by a drop to near zero when the piston reached full extension and the valve closed. The inlet flow sensor, which measures total flow into the system, showed essentially the same profile in the no-leak case – all the air drawn from the supply went into the cylinder's movement.

3.2 Effects of Leaks on Measured Signals

When a leak is introduced, the impact on the system measurements is immediate. Qualitatively, even a small leak creates an additional steady airflow during and after the cylinder motion which was not present in the no-leak case.

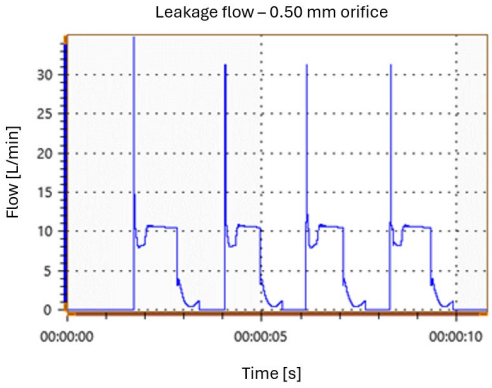

Figure 2: Simulated air flow rate in the case of a 0.5 mm diameter leak.

The Figure 2 shows simulated air flow rate through the orifice in the case of a 0.5 mm diameter leak (simulation data is shown). During the motion, the flow drawn from the supply is higher than before because it must simultaneously fill the cylinder and satisfy the continuous leak. Once the cylinder stops moving, in the no-leak case the flow would drop to zero, but with the leak, a constant flow continues as air escapes through the orifice.

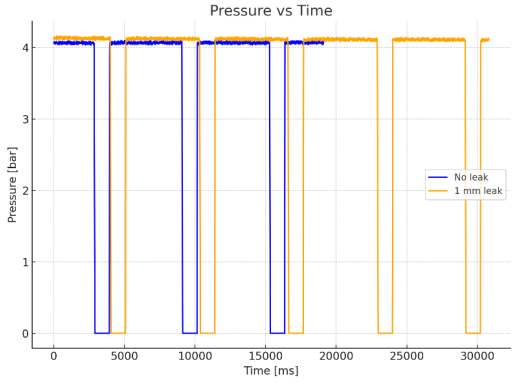

Figure 3: Measured pressure on the system inlet.

The pressure measurements showed practically no changes. Figure 3 illustrates the pressure on the system inlet, both without leak and with a 1 mm leak. In the no-leak case (blue curve), the pressure rises to ~4 bar and stays nearly flat during the stroke. With a leak (orange curve), one might expect the pressure to drop – however, up to moderate leak sizes (≤1 mm) the regulator and valve were actually able to maintain almost the same pressure profile. In both simulation and real tests, the pressure drop in the cylinder due to a 0.5 mm or 1 mm leak was almost imperceptible. Only when we tested a very large leak (2.5 mm) did the pressure traces start to show a noticeable decay during the motion, and at 5 mm the system could not sustain 4 bar at all (pressure collapsed, as expected when leak flow exceeded compressor capacity). This confirms that relying on pressure sensors alone for leak detection in a regulated supply can be unreliable – small leaks do not create enough of a pressure disturbance to be distinguished from normal operation, especially if the sensor is not extremely close to the leak point.

In terms of the motion timing, we measured the time taken for the cylinder to extend under each leak condition. Interestingly, up to the 1 mm leak, there was no appreciable difference in the stroke time or velocity. The laser displacement data over time yielded virtually identical speed profiles for the no-leak, 0.5 mm leak, and 1 mm leak cases. This indicates that the closed-loop pressure regulation (and the inherent oversizing of the pneumatic supply) can compensate for a fair amount of leakage without slowing down the actuator's performance. The operators or control system would not notice any slowdown until the leak becomes quite severe. Indeed, in our experiments only the 2.5 mm leak started to produce a slightly slower motion (and by 5 mm leak, the motion was significantly affected or failed to complete at speed). These findings align with practical experience: a machine might operate seemingly "fine" while wasting compressed air through moderate leaks, until a tipping point is reached. Thus, using motion speed as an indicator of leaks proved to be the least sensitive method – it can only detect very large leaks that already cause performance degradation.

Quantitatively, the flow-based detection was the most sensitive. Even the smallest leak (0.5 mm) caused a clear change in the flow sensor readings.

Figure 4 shows a set of real recorded flow sensor traces for three scenarios – no leak, 0.5 mm leak, and 1 mm leak – on the Y-axis extend stroke (normalized to the same cycle timing). The inlet flow (primary sensor) in the no-leak case (blue line) peaked

around ~120 L/min and returned to zero. With a 0.5 mm leak (orange line), the peak was slightly higher (~160 L/min) and after the motion a ~10 L/min flow continued to be present on smaller actuator sensor (a flat line indicating the leak). With a 1 mm leak, the peak was higher still and the flow after motion was ~>50 L/min, which in fact maxed out the smaller secondary sensor on the actuator line. The difference between the inlet flow and actuator flow corresponds exactly to the leak flow; for 1 mm this difference was so large that the actuator sensor could not capture it beyond 10 L/min (saturation). Despite the secondary sensor's saturation, the presence of the leak is unequivocal from the inlet sensor alone – seeing a nonzero flow when the actuator is static is a red flag. In a practical implementation, one could set a threshold: for example, after an actuator completes its motion, the flow reading should drop near zero within a certain short time. If instead a sustained flow above some small threshold is measured, a leak alarm can be triggered.

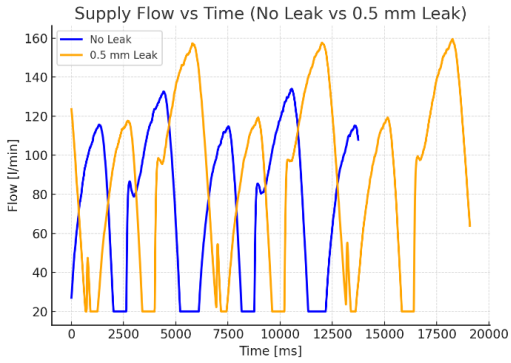

Figure 4: Flow rate profile without any leak (blue) and with 0.5 orifice leak (orange).

3.3 Comparison of Simulation and Real Results

The simulation model outputs were compared to the real measurements to verify their agreement. Overall, the trends matched well: both simulation and experiment showed that flow is a reliable leak indicator while pressure is not very sensitive to small leaks. The simulation's flow values for the leak were within ~10% of the calculated values and what was inferred from real sensor data. For instance, simulation of a 1 mm leak gave a leak flow of ~55 L/min, whereas the theoretical was ~53 L/min and the experiment indicated >50 L/min (consistent with sensor limits). The pressure curves in simulation also mirrored the shape of the measured pressure transients. Up to a 2.5 mm leak, neither showed significant pressure drop

during motion, maintaining a "step-like" pressure profile. At the 2.5 mm leak, both simulation and real began to show a sag in pressure, and at 5 mm, neither could hold full pressure.

3.4 Discussion of Detection Methods

From the results above, we can conclude that among the three measured modalities, air flow monitoring is the most effective for leak detection in pneumatic systems. Even minor leaks produced distinct changes in flow that are easy to detect with a simple threshold or by comparing reference vs. local flow readings. Pressure monitoring can play a supporting role, especially if one wants to pinpoint where the leak is (by placing pressure sensors near suspected locations), but it is not as universally reliable for initial detection of small leaks. The motion timing approach, while conceptually straightforward (no extra sensors needed if one monitors actuator cycle times), was essentially ineffective for early leak detection in our tests – leaks that didn't affect motion speed still caused significant air loss. Only when a leak becomes severe enough to drop pressure and slow the actuator would the timing method catch it, at which point a lot of energy may have already been wasted. This outcome underscores the importance of direct leak monitoring rather than relying on secondary effects like performance degradation.

Another practical observation is the influence of sensor placement and range. We encountered an issue where our chosen flow sensor on the actuator line maxed out at 10 L/min, which was too low once leaks exceeded 1 mm. In a real deployment, one must choose sensors with appropriate range (or use multiple ranges) to cover the expected leak sizes. The use of a higher-range sensor on the main inlet was a good solution in our case, since the main sensor (20–200 L/min range) easily captured the larger flows. For pressure sensors, as mentioned, distance from the leak matters. If deploying pressure-based leak detectors, they should ideally be integrated into each critical segment (for example, built into valve manifolds or cylinder ports) to catch local pressure drops that a central sensor might miss. Nonetheless, given our findings, a more cost-effective strategy is likely to put a few flow sensors on major branches and use those to monitor overall consumption balance.

It is also worth putting the magnitude of losses in perspective: using our experimental data and calculations, a 1 mm diameter leak at 4 bar consumes on the order of 3.15 m^3 of air per hour (≈ 53 L/min). Over a full day of continuous

operation, this amounts to ~75 m³ of air lost, and in a year (assuming 8,000 operating hours) nearly 28,000 m³ of air wasted. In terms of energy cost, if we assume typical compressor efficiency and electricity price, this single 1 mm leak could cost around €800 per year in electricity. Larger leaks of course cost exponentially more (a 2.5 mm leak was estimated around €4,800/year). Therefore, even "small" leaks that do not hinder machine function can have significant economic impact – justifying the implementation of automatic leak detection and timely maintenance.

4 Conclusion

In this work, we developed and tested an automated leak detection approach for a pneumatic station using readily available sensors and simulation tools. The experimental results clearly demonstrated that flow-based sensing is the superior method for detecting compressed air leaks in pneumatic systems. Even the smallest induced leak (0.5 mm orifice) was readily identified through an increase in airflow consumption, whereas pressure measurements showed virtually no change and the machine's operation was unaffected (same cycle time). The pneumatic pressure regulator was effective enough that it masked small leaks from a pressure standpoint, highlighting why leak detection should not rely solely on noticing pressure drops or reduced performance. By placing a flow sensor on the main air supply line and comparing it with the expected actuator consumption (or with additional flow sensors on sub-circuits), the system can automatically detect when extra air is being used that does not correspond to productive work. This enables real-time leak monitoring and could be used to alert maintenance personnel or trigger corrective actions (e.g. stopping the machine for inspection if a severe leak is detected).

Pressure-based leak detection can still be useful for locating leaks or as a redundancy. Our tests showed that if a pressure sensor is very near the leak (such as a sensor mounted in a tee at a cylinder port), it will register a pressure drop when that segment is active. Thus, one strategy could be to use flow sensors for system-wide leak detection and pressure sensors at critical components for isolation – for example, detect via total flow that "some leak" exists, and then check individual line pressures to narrow down the location. The motion timing method was proven to be largely ineffective for proactive leak detection in our case; it might only be viable in scenarios where adding sensors is impossible and only major leaks are of interest.

The simulation model built in Automation Studio was beneficial in understanding the system behavior and correlating it with theory. It allowed us to simulate various leak sizes and confirm that the trends (negligible pressure change, significant flow change) align with the real-world outcomes. Simulation can be a useful design tool for predicting how a leak detection system will perform, and for setting appropriate thresholds. For instance, one could simulate a range of leak scenarios to determine what flow increase is expected for a given leak size, thereby tuning the sensitivity of detection algorithms to catch leaks above a certain threshold.

In conclusion, implementing automated leak detection using sensors in pneumatic stations is both feasible and highly beneficial. With the rising costs of energy and the push for efficient Industry 4.0 operations, such self-diagnostic capabilities can save substantial costs and prevent unplanned downtime. Our work contributes an experimental validation that simple sensor-based approaches (particularly airflow monitoring) can reliably detect leaks in real time. Future work may involve scaling the system to monitor multiple actuators simultaneously, integrating machine learning to distinguish leak signatures from other anomalies, or exploring wireless IoT sensors for retrofitting existing industrial equipment-

References

[1] D'Alessio, B. (2023). The Hidden Cost of Compressed Air Leaks in Bulk Solids Handling Systems. AZO Materials Handling Blog. WWW: https://www.azo-inc.com/blog/compressed-air-leaks

[2] Taylor, K. (2025). Seven Ways to Reduce Compressed Air Costs. Fluid-Aire Dynamics Blog. WWW: https://fluidairedynamics.com/blogs/articles/reduce-air-compressor-operating-costs

[3] Desmet, A., & Delore, M. (2017). Leak detection in compressed air systems using unsupervised anomaly detection techniques. Proceedings of the Annual Conference of the PHM Society 2017, 9(1).

[4] Baligač, A. (2024). Avtomatizirano zaznavanje napak pri delovanju pnevmatske postaje (Master's thesis, University of Maribor, Slovenia).

Conference sponsors

General sponsor

HAWE Hidravlika d.o.o.

Social event sponsor:

LA & CO d.o.o.

Conference organization has been sponsored by:

OLMA d.o.o.

BECKHOFF Avtomatizacija d.o.o.

HAINZL Motion & Drives d.o.o.

TESNILA Bogadi d.o.o.

Dravske elektrarne Maribor d.o.o.

POCLAIN Hydraulics d.o.o.

UNIFOREST d.o.o.

NOO University of Maribor, Ministry of Higher Education, Science and Education

Media sponsors:

VENTIL **UM Press** **IRT3000**

We would like to thank all the sponsors for their support and contribution to the organization of the conference!

Smart Hydraulics.
Easy Business.

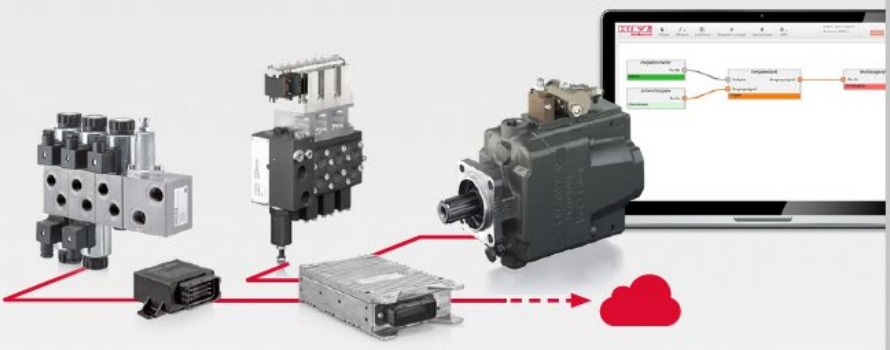

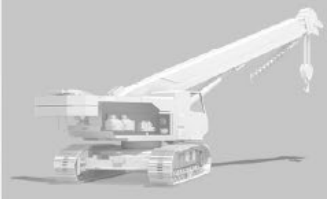

SAFETY

Varnostne funkcije

Povezljivost

Modularni sistemi

Pametna povezljivost:
S HAWE hidravličnimi rešitvami vedno dobite točno to, kar potrebujete: aktuator, krmilni sistem, senzorje in aplikacijsko programsko opremo – vse na enem mestu.

www.hawe.com

HAWE HYDRAULIK

Smart Hydraulics.
Easy Business.

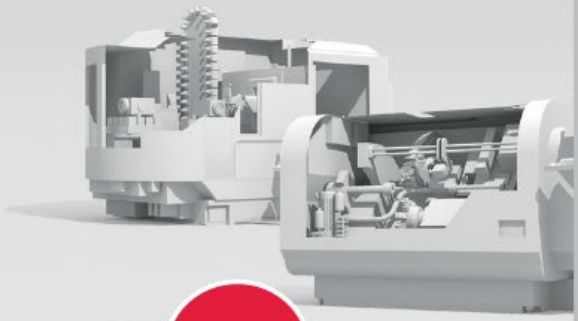

Modularna zasnova

Učinkovitost

Nadzor stanja

Produktivnost

Fleksibilnost je naš standard:
S HAWE hidravličnimi agregati vedno dobite točno to, kar potrebujete: modularno konfiguracijo, integrirane senzorje in krmilnike ter programsko opremo prilagojeno posamezni napravi.

www.hawe.com

HAWE HYDRAULIK

la&co

Certified Excellence
rexroth
A Bosch Company

Sinergija premikanja. *Hidravlika. Pnevmatika. Linearna tehnika.*

Specializirani smo za razvoj in implementacijo hidravličnih, pnevmatskih ter linearnih sistemov. Naše rešitve temeljijo na visoki zanesljivosti, natančnosti in dolgoročni učinkovitosti, kar zagotavlja optimalno delovanje tako v industrijskih kot mobilnih aplikacijah.

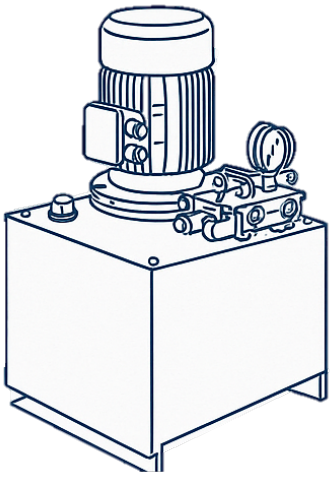

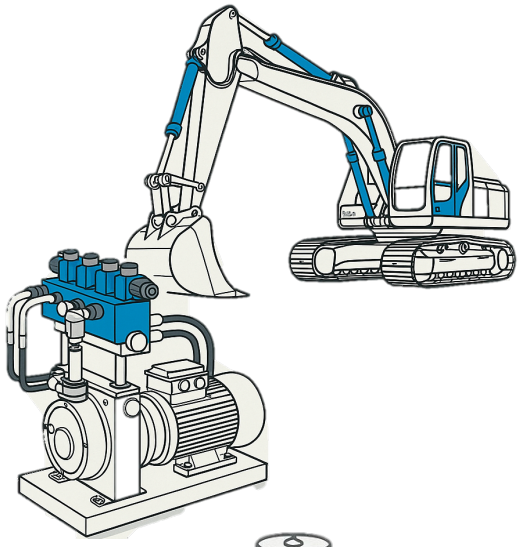

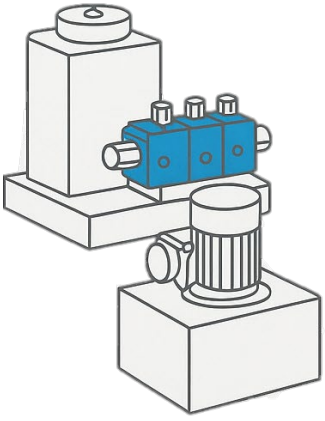

OLMA®
www.olma.si
SINCE 1947

ENERGOLUBRIC
New generation hydraulic oils

Discover the Future of Hydraulic Oils

Naziv izdelka	Protiobrabni aditivi	Vsebuje cink	Odlična oksidacijska stabilnost	Visok indeks viskoznosti	Detergentni aditivi
ENERGOLUBRIC 40XY	•		•	•	
ENERGOLUBRIC 30XY ZF	•		•	•	
ENERGOLUBRIC 30XY	•	•	•	•	
ENERGOLUBRIC 20XY ZFS	•		•	•	
ENERGOLUBRIC 20XY ZF	•		•		
ENERGOLUBRIC 20XY S	•	•	•	•	
ENERGOLUBRIC 20XY	•	•	•		
HYDROLUBRIC HEES	•			•	
HYDROLUBRIC VG BR	•				
HYDROLUBRIC HVLPD	•			•	•
HYDROLUBRIC VGS PLUS	•	•		•	
HYDROLUBRIC VGS	•	•		•	
HYDROLUBRIC HVLP	•	•		•	
HYDROLUBRIC VG D	•				•
HYDROLUBRIC VG	•	•			
HYDROLUBRIC HD	•	•			
HYDROLUBRIC HLP	•	•			

Olma d.o.o., Poljska pot 2, 1000 Ljubljana, Slovenija, EU , phone.:+386 (01) 58 73 600, email: order@olma.si

EtherCAT in tehnologija PC krmilnikov: New Automation Technology

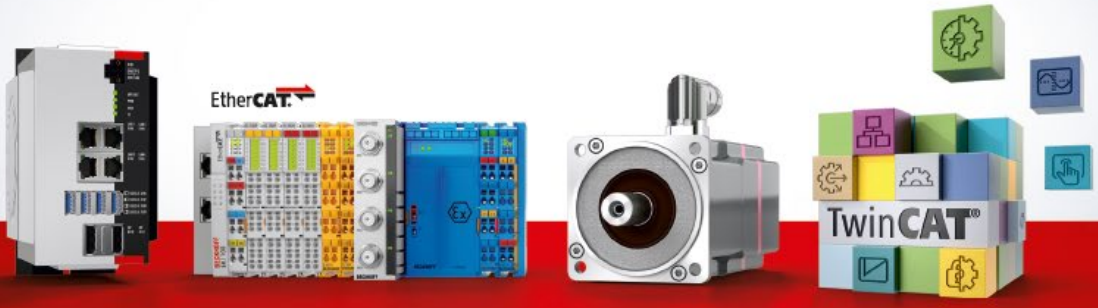

EtherCAT in tehnologija PC krmilnikov postavljata standarde po svetu:

- vse komponente za industrijske računalnike, V/I periferijo, pogonsko tehniko in avtomatizacijo
- uveljavljeni mejniki v avtomatizaciji na globalni ravni: Lightbus, V/I moduli, programska oprema TwinCAT
- maksimalna skalabilnost in odprti sistemi za avtomatizacijo
- na osnovi visoko zmogljivega področnega vodila EtherCAT
- združevanje ključnih funkcij naprave ali sistema na eni krmilni platformi
- univerzalne rešitve za avtomatizacijo za prek 20 različnih tipov industrije: od CNC obdelovalnih strojev do pametne avtomatizacije zgradb

Beckhoff Avtomatizacija d.o.o.
Zbiljska cesta 4, 1215 Medvode
Slovenija
Telefon: +386 1 36130-80
info@beckhoff.si

Skenirajte za več informacij o sistemu Beckhoff

New Automation Technology **BECKHOFF**

DINAMIKA PREMIKANJA

HAINZL MOTION & DRIVES SLOVENIJA

Vaš partner za hidravlične in električne sisteme ter pogonske rešitve za mobilne in industrijske aplikacije.

// Uradni zastopnik podjetja Danfoss Power Solutions
// Načrtovanje, svetovanje in posodobitev sistemov
// Vzdrževanje in testiranje hidravličnih komponent

www.hainzl.si

Danfoss

HAINZL
MOTION & DRIVES

www.bogadi.si

TESNILA BOGADI d.o.o.

Izdelava tesnil in hidravličnih cilindrov po meri /
Servis in obnova hidravličnih cilindrov /
Izdelki iz gume in poliuretana / Obnova koles /




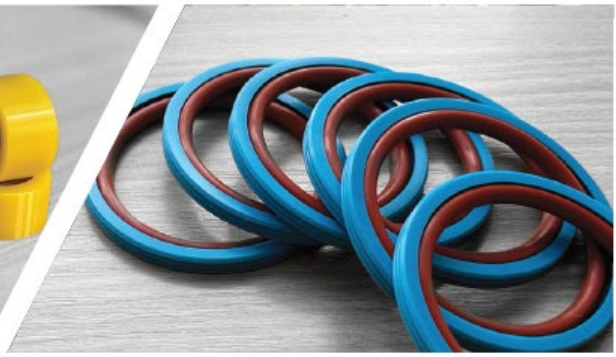

Izzivi naših naročnikov nas ženejo k
najboljšim rešitvam – **osebno, strokovno in zanesljivo.**

info@bogadi.si / +386 (0)2 426 04 50

Tesnila Bogadi d.o.o.
Karantanska ulica 21, 2000 Maribor
W: www.bogadi.si / **T:** +386 2 426 04 50 / **E:** info@bogadi.si

POCLAIN Hydraulics

ŠIROK IZBOR VENTILOV

ZA HIDRAVLIČNE POGONE VOZIL IN NJIHOVA HIDRAVLIČNA ORODJA

Izmenjevalni ventil

Ventil za hidravlično zaporo koles

4/3 Potni ventil

6/2 Potni ventil

ZASNOVANI IN PROIZVEDENI V SLOVENIJI

Poclain Hydraulics d.o.o.
Industrijska ulica 2, 4226
Žiri, Slovenija
+386 (0)4 51 59 100

www.poclain-hydraulics.com

UNIFOREST®

NOVI PROFI VITLI

S proporcionalno zavoro.

GX/GKX

70GX

65 kN
Vlečna sila

90GX

85 kN
Vlečna sila

90GKX

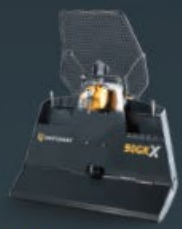

85 kN
Konstantna vlečna sila

2x90GX

2x85 kN
Vlečna sila

2x90GKX

2x85 kN
Konstantna vlečna sila

www.unlforest.sl

Vodilni proizvajalec električne energije iz obnovljivih virov

Z energijo narave ustvarjamo zeleno prihodnost.

Zavezani trajnostnemu razvoju ter zanesljivim in strateškim rešitvam postavljamo temelje energetske prihodnosti – odgovorni do okolja, predani družbi.

FS Fakulteta za strojništvo

AKTUALNA IZOBRAŽEVANJA ZA INDUSTRIJO

Na Fakulteti za strojništvo Univerze v Mariboru ponujamo krajša strokovna izobraževanja, prilagojena potrebam gospodarstva. Omogočajo hitro pridobivanje specifičnih znanj za vaše izzive v praksi.

Materiali

Tekstilije, procesi in zeleni prehod

Hidravlika in pnevmatika

Vzdrževanje

Pametna tovarna

Napredne izdelovalne tehnologije

Numerično modeliranje in računalniške simulacije

Ergonomija ter snovanje in oblikovanje izdelkov

Zagotavljanje kakovosti

Organizacijska znanja

Procesna tehnika

Vas zanima več?

www.cvu.fs.um.si/ponudba-izobrazevanj

NOO NAČRT ZA OKREVANJE IN ODPORNOST

Univerza v Mariboru

REPUBLIKA SLOVENIJA
MINISTRSTVO ZA VISOKO ŠOLSTVO, ZNANOST IN INOVACIJE

Financira Evropska unija
NextGenerationEU

REVIJA ZA FLUIDNO TEHNIKO, AVTOMATIZACIJO IN MEHATRONIKO

VENTIL

ISSN 1318 - 7279 Letnik 30

- Strokovni in znanstveni prispevki
- Iz prakse za prakso
- Ventil na obisku
- Novice - zanimivosti
- Aktualno iz industrije
- Novosti na trgu
- Podjetja predstavljajo
- Ali ste vedeli
- Dogodki
- Intervju

revija Ventil

Univerza v Ljubljani, Fakulteta za strojništvo, Aškerčeva 6, 1000 Ljubljana
Tel.: 01/ 4771 704, Faks: 01/ 4771 772
E-pošta: ventil@fs.uni-lj.si, Internet: www.revija-ventil.si

Spoštovani!

Ventil je znanstveno-strokovna revija in objavlja prispevke, ki obravnavajo razvojno in raziskovalno delo na Univerzi, inštitutih in v podjetjih s področja fluidne tehnike, avtomatizacije in mehatronike. Revija želi seznanjati strokovnjake z dosežki slovenskih podjetij, o njihovih izdelkih in dogodkih, ki so povezani z razvojem in s proizvodnjo na področjih, ki jih revija obravnava. Prav tako želi ustvariti povezavo med slovensko industrijo in razvojno in raziskovalno sfero ter med slovenskim in svetovnim proizvodnim, razvojnim in strokovnim prostorom. Naloga revije je tudi popularizacija področij fluidne tehnike, avtomatizacije in mehatronike še posebno med mladimi. Skrbi tudi za strokovno izrazoslovje na omenjenih področjih.

Revija Ventil objavlja prispevke avtorjev iz Slovenije in iz tujine, v slovenskem in angleškem jeziku. Prispevkom v slovenskem jeziku je dodan povzetek v angleščini, prispevki v angleščini pa so objavljeni z daljšim povzetkom v slovenskem jeziku. Člani znanstveno strokovnega sveta so znanstveniki in strokovnjaki iz Slovenije in tujine. Revijo pošiljamo na več naslovov v tujini in imamo izmenjavo z drugimi revijami v Evropi. Revija je vodena v podatkovni bazi INSPEC.

Tridesetletno izhajanje revije Ventil pomeni, da je v prostoru neprecenljiva za razvoj stroke. Uredništvo si skupaj z znantveno strokovnim svetom prizadeva za visokokvalitetno raven in relevantnost objav, ki bosta v prihodnosti vse napore usmerila v to, da bo kvalitetna raven še višja. V ta namen vključuje v znanstveno strokovni svet priznane znanstvenike, raziskovalce in strokovnjake, ki s svojim znanjem vspodbujajo vsak na svojem področju objavljanje rezultatov razvojnega in raziskovalnega dela. Uredništvo spremlja razvoj stroke in znanstveno raziskovalno delo doma in v tujini preko konferenc, delavnic in seminarjev ter z izmenjavo tuje periodike.

Revija je priznana v tujini, še posebno na področju fluidne tehnike, kar želimo doseči tudi na področju mehatronike in avtomatizacije. Preko objav v reviji se promovirajo dosežki slovenske znanosti in industrijske proizvodnje. Revija je in bo tudi v prihodnje prostor za predstavljanje kvalitetnih razvojnih in raziskovalnih dosežkov slovenske industrije in raziskovalne sfere na področju fluidne tehnike, avtomatizacije in mehatronike.

Uredništvo

IRT 3000
INOVACIJE • RAZVOJ • TEHNOLOGIJE

SPLAČA SE BITI NAROČNIK

IRT 3000

ZA SAMO 70€ DOBITE:

- celoletno naročnino na revijo IRT3000 (10 številk)
- strokovne vsebine na več kot 140 straneh

IRT 3000 ADRIA — Revija v hrvaškem jeziku

ZA SAMO 28€ DOBITE:

- celoletno naročnino na revijo IRT3000 ADRIA (4 številke)
- strokovne vsebine na več kot 200 straneh

IRT 3000 АДРИА — Revija v srbskem jeziku

ZA SAMO 28€ DOBITE:

- celoletno naročnino na revijo IRT3000 АДРИА (4 številke)
- strokovne vsebine na več kot 200 straneh

• vsakih 14 dni e-novice IRT3000 na osebni elektronski naslov

DIGITALNA NAROČNINA

Na voljo je tudi digitalna različica revije, obogatena s povezavami in video vsebinami.

STROKOVNA LITERATURA

V naši spletni trgovini je na voljo širok nabor kakovostne strokovne literature.

Spletni nakup:

NAROČITE SE!

051 322 442
info@irt3000.si
www.irt3000.si/narocilo-revije

WWW.IRT3000.COM

University of Maribor Press

HALF A CENTURY OF SCHOLARSHIP AND RESEARCH

PRESS.UM.SI

International Conference Fluid Power 2025: Conference Proceedings

Darko Lovrec, Vito Tič (eds.)
University of Maribor, Faculty of Mechanical Engineering, Maribor, Slovenia
darko.lovrec@um.si, vito.tic@um.si

The International Fluid Power Conferences are a two day event, intended for all those professionally-involved with hydraulic or pneumatic power devices and for all those, wishing to be informed about the 'state of the art', new findings and innovations within the field of hydraulics and pneumatics. All papers included in the conference program are reviewed and collected in the conference proceedings. The gathering of experts at this conference in Maribor has been a tradition since 1995, and is organised by the Faculty of Mechanical Engineering at the University of Maribor, in Slovenia. Fluid Power conferences are organised every second year and cover those principal technical events within the field of fluid power technologies in Slovenia, and throughout this region of Europe. This year's conference FT2025 is taking place on the 17th and 18th September in Maribor, at Congress centre Habakuk.

DOI
https://doi.org/10.18690/um.fs.7.2025

ISBN
978-961-299-049-7

Keywords:
international conference, fluid power, science and profession, inovations, achievements

University of Maribor Press

University of Maribor

Faculty of Mechanical Engineering

FT2025

30